

DISSERTATION ZUR ERLANGUNG DES DOKTORGRADES DER FAKULTÄT CHEMIE UND PHARMAZIE  
DER LUDWIG-MAXIMILIANS-UNIVERSITÄT MÜNCHEN

**Mesoporous silica nanoparticles  
as drug delivery  
platforms**

**Drug loading, pore sealing, targeting and controlled  
drug/endosomal release**

Veronika Ortrud Sophie Weiß

aus

Landshut, Germany

2014



### **Erklärung**

Diese Dissertation wurde im Sinne von §7 der Promotionsordnung vom 28. November 2011 von Herrn Prof. Dr. Christoph Bräuchle betreut.

### **Eidesstattliche Versicherung**

Diese Dissertation wurde eigenständig und ohne unerlaubte Hilfe erarbeitet.

München, den .....

Veronika Ortrud Sophie Weiß

Dissertation eingereicht am 24.06.2014

1. Gutachter Prof. Dr. Christoph Bräuchle

2. Gutachter Prof. Dr. Thomas Bein

Mündliche Prüfung am 17.07.2014



# Summary

Nano-sized mesoporous silica particles (MSN) with high colloidal stability attract growing interest as drug delivery systems for targeted cancer treatment and as bioimaging devices. MSN nanoparticles can feature a well-defined and tunable porosity at the nanometer scale, high loading capacity, and multiple functionality for targeting and entering different types of cells. In order to examine the functionality of the particles, highly-sensitive fluorescent live-cell imaging is a powerful method. It enables the possibility to follow the nanoparticle uptake, intracellular fate and drug release. With the knowledge gained by means of live-cell imaging experiments improvement on the synthesis side is possible. This thesis is based on a close collaboration between the groups of T. Bein and C. Bräuchle, whereas the synthesis part takes place in the group of T. Bein and the (live-cell) imaging in the group of C. Bräuchle. The biocompatibility (especially the studies in mice) of selected MSN was investigated in the group of E. Wagner. The goal of this thesis was to study the uptake behavior of targeted MSN and various controlled (endosomal) release mechanism.

To prevent drug-leakage out of loaded mesopores capping systems were installed. Three possibilities, namely surface coating, internal pore modification and molecular/particle pore gating, were examined.

First surface coating with the already established supported lipid bilayer (SLB) was investigated. Here a system published previously in our groups [1] was further improved by attaching targeting ligands (folic acid or epidermal growth factor) to the supported lipid bilayer (SLB) surrounding mesoporous silica nanoparticles and exchanging the on-board photosensitizer to a red-shifted one with an easier synthesis route. Efficient receptor-mediated cell uptake was demonstrated after 3 h of incubation, whereas in this time range only a small amount of unspecific uptake seems to take place. This nanoparticle system was shown to provide spatial and temporal control of cargo release (in this case calcein and a rhodamine derivative) into the cytosol of cancer cells.

The second surface coating approach was carried out by means of a pH-responsive polymer (poly(2-vinylpyridine) (PVP)). Thereby the outcome was a highly stable modular toolbox for targeted drug delivery, based on the sequential covalent attachment of different functionalities to the surface of core-shell MSN. In the system presented here, PVP was used as a pH-responsive cap system, with a shell of poly(ethylene glycol) (PEG) as solubilizing polymer. Additionally, folic acid and a photosensitizer were attached to the PEG block for cell targeting and endosomal escape, if needed. Uptake of the folic acid receptor targeted MSN was achieved with a high amount of internalized MSN after 2 h, especially compared to unspecific uptake. It could be demonstrated *in vitro*, that membrane permeable cargos (colchicine, DAPI) can be delivered without further attachment of endosomal escape mechanisms, whereas for membrane-impermeable cargos (calcein) the photosensitizer was needed as endosomal escape trigger. The designed systems exhibited a very high stability in bio-fluids at different pH-values. Intravenous administration of the MSN in mice showed good tolerance *in vivo* without any associated acute toxicity, and preferred localization in the liver.

Furthermore internal pore modifications were studied as capping systems. Controlled release was

achieved by covalent linking of cargo with the MSN pore through a disulfide bond, which was cleaved in a controlled manner. Additionally, a polymer with high buffering capacity (poly(amidoamine) (PAMAM)) was attached on the particle surface for achieving endosomal escape over the proton sponge effect. The particles need to get in contact with the cytoplasmic reducing milieu of the target cells in order to reduce the disulfide bond. Different cargos (propidium iodide, 5(6)-carboxy-X-rhodamine, colchicine and DAPI) were tested. We were able to show, that the charge of the cargo molecule has to be considered, as the positively charged polymer forms a barrier for particle loading. For uncharged molecules the time-dependent release behavior was investigated. The process starts after approximately 10 h of incubation and it continued over the monitored time of 60 h. With a control experiment, in which the buffering polymer was omitted, it could be proven that PAMAM was the reason for endosomal release. Furthermore, the biocompatibility was examined and also receptor-mediated cellular uptake, provided through attachment of the targeting ligands in a last synthesis step.

Finally, molecular pore gating was investigated by attaching the enzyme carbonic anhydrase (CA) to the surface of the MSN. This project was in an additional collaboration with the group of T. Carell. The particle surface was equipped with an inhibitor for the enzyme, namely silaic acid. The usage of this system is advantageous because of the following two aspects. First, CA is abundant in the blood system and hence there would be supply, if a few enzymes got lost. Second the inhibitor-enzyme binding is pH-responsive. In the neutral regime binding is favored, whereas in the acidic compartments (e.g. in the endosomes) the inhibitor-enzyme binding breaks up. While the cargo diffuses inside the pores of the MSN, like in the surface coated examples, the drug is released when the particle reaches the acidic compartments. For a membrane-permeable cargo (DAPI) efficient release into the cell could be detected. The localization of the particles after one day of incubation with early/late endosomes or lysosomes proves the presence of an acidic milieu, as the particles show exclusive co-localization with acidic compartments (late endosomes, lysosomes). Additionally, targeting moieties can be attached on chemically modified carbonic anhydrase to achieve targeted delivery.

The size of the pores used so far is rather small ( $\sim 2.5\text{-}5\text{ nm}$ ), therefore newly prepared particles with pores up to 13 nm were synthesized. Further already established strategies for controlled release were tested. It was discovered that the coating with a supported lipid bilayer or PVP works as predicted by our earlier experiments. However, the attachment of the photosensitizer AlPcS<sub>2a</sub> revealed an unexpected behavior. After activation of the covalently attached photosensitizer spreading of the photosensitizer over the whole cell was observed, contrary to experiments conducted in our groups before with smaller pore size MSN. A first investigation of this behavior revealed no reasonable explanation. Thus an intense follow-up study might be advisable. Nevertheless we were able to demonstrate the release of different cargos (calcein, propidium iodide, alexa fluor dextran (10.000 Da) out of these particles.

It has been further examined whether fusion (as release mechanism) of SLB coated MSN with cells

can be revealed. To induce fusion two different peptides were applied, namely a reduced form of SNARE (soluble N-ethylmaleimide-sensitive factor attachment protein receptor) peptides and H5WYG (obtained from the fusion-inducing sequence in influenza viruses). The reduced SNARE-model, established in the group of A. Kros, was investigated in collaboration with the group of A. Kros. The first challenge, incorporating the peptides into the SLB, was successfully accomplished. The first steps towards the release of model-drugs into cells were carried out. The overcome of the final hurdles provides material for further investigations.



# Contents

<b>Summary</b>	<b>v</b>
<b>1 Introduction</b>	<b>1</b>
<b>2 Drug delivery with mesoporous silica nanoparticles</b>	<b>3</b>
2.1 Targeting and cellular uptake . . . . .	4
2.2 Endosomal escape . . . . .	7
2.3 Controlled release of cargo . . . . .	10
2.3.1 External Stimuli . . . . .	10
2.3.2 Internal stimuli . . . . .	11
2.4 Biological and pharmaceutical relevance . . . . .	13
<b>3 Multifunctional mesoporous silica nanoparticles</b>	<b>17</b>
3.1 Synthesis of inorganic silica cores . . . . .	17
3.2 Modification of silica cores . . . . .	19
<b>4 Fluorescence live cell-imaging</b>	<b>23</b>
4.1 Fluorescence principle . . . . .	23
4.2 Requirements for used dyes . . . . .	24
4.3 Spinning disc microscope . . . . .	26
4.4 Imaging . . . . .	28
<b>5 Experimental methods and data analysis</b>	<b>33</b>
5.1 Chemicals . . . . .	33
5.2 Cell culture . . . . .	33
5.3 Microscopy in live cells . . . . .	34
5.3.1 Uptake studies . . . . .	35
5.3.2 Controlled release of cargo and endosomal escape with photoactivation . . . . .	36
5.3.3 Elevation of pH induced controlled endosomal release . . . . .	36
5.3.4 Endosomal compartment staining. . . . .	37
5.3.5 LPK-Ecf staining . . . . .	37
5.3.6 SNARE-peptide mediated fusion experiments . . . . .	37
5.4 UV-VIS spectroscopy . . . . .	38

## Contents

<b>6 Targeted drug delivery with red light photoactivated mesoporous silica nanoparticles</b>	<b>39</b>
6.1 Synthesis and Characterization . . . . .	41
6.2 Targeting <i>in vitro</i> . . . . .	45
6.3 Cargo Release by Photoactivation . . . . .	47
6.4 Summary . . . . .	51
<b>7 Polymer pore closing with pH depending polymer and photoinduced opening mechanism</b>	<b>53</b>
7.1 Synthesis and Characterization . . . . .	55
7.2 Targeting <i>in vitro</i> . . . . .	57
7.3 Externally triggered release of membrane impermeable cargo <i>in vitro</i> . . . . .	58
7.4 Internally triggered release of membrane permeable cargo <i>in vitro</i> . . . . .	61
7.5 Stability . . . . .	62
7.6 Experiments <i>in vivo</i> . . . . .	64
7.7 Summary . . . . .	67
<b>8 Dendrimeric shell and disulfide binding of cargo - proton sponge effect</b>	<b>69</b>
8.1 Synthesis and characterization . . . . .	71
8.2 Release - <i>in vial</i> . . . . .	75
8.3 Cytotoxicity . . . . .	76
8.4 Release of different cargos - <i>in vitro</i> . . . . .	78
8.5 Targeting <i>in vitro</i> . . . . .	85
8.6 Summary . . . . .	86
<b>9 Enzyme based pH-sensitive cap system for MSNs</b>	<b>89</b>
9.1 Synthesis and characterization . . . . .	91
9.2 Dye release - <i>in vitro</i> . . . . .	95
9.3 Targeting - <i>in vitro</i> . . . . .	98
9.4 Summary . . . . .	99
<b>10 Outlook: Modifications of surface coated MSN</b>	<b>101</b>
10.1 Large pore MSN . . . . .	101
10.1.1 Synthesis and characterization . . . . .	102
10.1.2 LP-MSN-AIPcS <sub>2a</sub> : removal of free photosensitizer . . . . .	109
10.1.3 Delivery of different sized cargos with LP-MSN . . . . .	110
10.2 Membrane-fusion inducing peptides - reduced SNARE peptides . . . . .	116
10.3 Membrane-fusion inducing peptides - fusion peptide H5WYG . . . . .	121
10.4 Summary . . . . .	125
<b>11 Perspective</b>	<b>127</b>
<b>List of abbreviations</b>	<b>129</b>
<b>Bibliography</b>	<b>133</b>

<b>Appendix</b>	<b>165</b>
1 Details for Chapter 6: Red light photoactivated mesoporous silica nanoparticles . . .	165
2 Details for Chapter 7: Polymer-Capped Mesoporous Silica Nanoparticles . . . . .	176
3 Details for Chapter 8: Dendrimeric shell functionalized MSN . . . . .	187
4 Details for Chapter 9: CA-capping for MSN-phSA . . . . .	197
5 Details for Chapter 10: Modifications on SLB-coated MSN . . . . .	201
5.1 Chapter 10.1: Large pore MSN . . . . .	201
5.2 Chapter 10.2: Fusion-SNARE . . . . .	205
5.3 Chapter 10.3: Fusion-H5WYG . . . . .	205
<b>Acknowledgments</b>	<b>207</b>
<b>List of publications</b>	<b>209</b>
<b>Curriculum Vitae</b>	<b>213</b>



# 1 Introduction

According to the “Deutsches Krebsforschungszentrum”, cancer is the second most common cause of death in Germany, only exceeded by deceases of the circulatory system. [2] As cancer is a disease of the body’s own cells, in other words an abnormal cell growth beyond the usual boundaries, it is challenging to treat. Since cancer cells are no foreign material in the body, the immune system does not recognize them as a diseases. The common treatment consists of surgery, radiation, and chemotherapy, mostly in a combined manner. However these methods seriously affect the health of the whole body. Moreover, metastasis often can’t be efficiently treated especially with local therapies like surgery and radiation. Thus the main challenge is to find a drug or drug formation that kills cancer cells but does not affect any other cell.

Currently, various promising approaches for cancer therapy are investigated, such as immunotherapy, targeted cancer therapy, angiogenesis inhibition, hypothermia and photodynamic therapy. [3] Whereby, immunotherapy aims at activating the immune system against the tumor [4], and was announced to be the “turning point in cancer” by *Science* this year. [5] Targeted cancer therapy focuses at blocking signaling pathways and inducing apoptosis by interfering with specific molecules involved in cancer growth. [6] The formation of new blood vessels, which are needed for supply in tumor formation are inhibited with angiogenesis inhibitors. [7] Hypothermia can be used in combination for example with radiation and induces cell-damage and subsequently cell death. [8] Especially for the upper layers of tissue the photodynamic therapy is promising, where a photosensitizing agent is used to induce cell-damage after light activation. [9] While clinical trials for immunotherapy and hypothermia are in progress, some targeted cancer therapies, angiogenesis inhibitors and photodynamic therapies are already approved for several types of cancer. [3]

The use of individual aspects of nanotechnology is another promising approach in cancer therapy research, and is also the area of this thesis. With the help of nanotechnology nanodevices can be created, that provide a broad field of application possibilities for cancer treatment, like gene therapy, photodynamic therapy, radiotherapy/radiofrequency therapy, drug delivery or cancer theranostics (combination of diagnosis and therapy). [10] The nanodevices that are generally investigated include liposomes, nanoparticles, polymeric micells, dendrimers, carbon nanotubes and quantum dots. [10] Most of the above mentioned nanotechnology derived systems aim to conceal and protect the drug until it reaches its destination, the cancer, and are intended for an intravenous application. By means of nanotechnology the properties of cancer therapeutics could be altered in order to increase the solubility, decrease the degradation during the blood circulation and concentrate the drug at the desired site of action. [11] There are several requirements such particles have to fulfill. First, they should be nontoxic, also in its degradation products. Second the size is important. Particles that are below 5-6 nm will get excreted very quickly by means of the renal filtration [12] whereas big particles,

## 1 Introduction

$\geq 200$  nm, are more likely to be taken up by the reticuloendothelial system (RES). [13] Further, the particle should have a decent clearing mechanism after fulfilling its work (long clearance time preferred) and should be colloidally stable in physiological conditions. [11] Last but not least, the particles should be able to encapsulate the drug, provide a controlled release of the therapeutic agent and preferentially can be targeted to the cells or tissue of interest. [11] Especially these requirements are investigated in this work. The focus lies on mesoporous silica nanoparticles (MSN) with several different modifications as possible new systems in drug delivery for cancer therapy.

An overview over the MSN systems, that have been studied in recent years in cooperation between the groups of Prof. Bein and Prof. Bräuchle, will be provided. The thesis is organized in the following way. After this short introduction (**chapter 1**) the theoretical background and the *state in the art* of the research field of drug delivery with MSN (**chapter 2, 3**) are presented. The chapters were published in *Chemistry of Materials*. [14] These chapters on the background of the work are followed by the theory on fluorescence microscopy, imaging possibilities for MSN (**chapter 4**) and the experimental methods used in this work (**chapter 5**).

In **chapter 6** a surface coated MSN system is described. The MSN are coated with a supported lipid bilayer, targeting moieties are attached, and their release behavior due to a covalently linked photosensitizer was investigated. With the help of *in vial* and various *in vitro* (which include experiments in living cells) experiments the functionality of the system was proven. The focus was to investigate a system that could be used as a platform, as loading and targeting ligands can be easily varied. The results presented in this chapter are published in *Nano Letters*. [15]

**Chapter 7** describes a MSN-system with a pH-dependent polymer cap. This is another surface coated system that this time is investigated *in vial*, *in vitro* (including live-cell-experiments) and *in vivo* (animal experiments, here especially mice). Here the focus is laid on the pH-dependent release behavior of the particles inside living cells as well as the bio-compatibility and targeting strategies. The main part of the presented results are part of a submitted manuscript.

**Chapter 8** discusses the possibility of internal pore modification (drug immobilization with the help of disulfid-bridges) combined with a dendrimeric surface coating. The dendrimer-coating is believed to provide another strategy beside photoactivation to rupture the endosomal membrane and provides an endosomal escape strategy. Another aspect is the toxicity of the particles and the ability to functionalize them with targeting-ligands.

In **chapter 9** the molecular/particle pore gating approach is examined. In this case carbonic anhydrase (CA) was used. It was attach to the MSN by modifying their particle surface with silaic acid, which functions as CA-inhibitor in an neutral pH-regime. As silaic acid is provided at the outer particle surface the binding enzyme blocks the pore entrances until the system reaches acidic compartments and the reversible binding is cleaved. The release behavior after uptake into cells is investigated, as well as the attachment of a targeting ligand to the chemically modified enzyme.

Parts of the last two chapters are in preparation for publication.

The last chapter (**chapter 10**) provides insight into other MSN-modifications. First the improvements and difficulties in increasing the pore size are discussed. Afterwards, experiments with fusion inducing peptides, namely SNARE-peptides and fusion peptide H5WYG, are depicted.

## 2 Drug delivery with mesoporous silica nanoparticles

This chapter is adapted from the publication “Multifunctional Mesoporous Silica Nanoparticles as a Universal Platform for Drug Delivery”, published in *Chemistry of Materials*, written in collaboration with C. Argyo from the group of T. Bein. [14]

Multifunctional mesoporous silica nanoparticles (MSNs, size typically  $< 500$  nm) have attracted substantial attention in recent years due to their advantageous structural properties, such as a high internal surface area and pore volume, tunable pore sizes, colloidal stability, and the possibility to specifically functionalize the inner pore system and/or the external particle surface. These highly attractive features make MSNs a promising and widely applicable platform for diverse biomedical applications including bioimaging for diagnostics [16, 17], biosensing [18, 19], biocatalysis [20–22], bone repair and scaffold engineering [23–25], and drug delivery. [26–28] Caruso and co-workers established another interesting approach using mesoporous silica particles as templates to create submicrometer-sized polymer capsules for drug delivery used in cancer therapy. [29–31]

Periodically ordered mesoporous silica, created by combining surfactant micellar aggregates with reactive silica precursors, was discovered about 20 years ago by researchers at Mobil. [32, 33] In particular, inorganic-organic (hybrid) core-shell nanoparticles based on mesoporous silica have received great attention as drug delivery vehicles, where the decoration of the inner or outer surface of the particles with organic molecules can impart important features for successful drug delivery. MSNs have first been proposed around 2001 as nanocarriers for transporting therapeutics. [34] Inspired by this simple concept (at that time still lacking control over cargo uptake or release), many efforts were made in recent years to create multifunctional stimuli-responsive nanocarrier systems consisting of MSNs as host materials. [35] This is based on the excellent material properties of MSNs such as good biocompatibility, high loading capacity, and efficient encapsulation of cargo molecules in their mesopores. Additional benefits include the possibility to design stimuli-responsive mechanisms with spatiotemporal control of release of the cargo, and the efficient attachment of organic surface functionalities including hydrophilic polymers, gate keepers, and targeting ligands, respectively. [15, 36–41]

The delivery of anticancer therapeutics into cancer cells by employing nanoparticle carriers has made significant progress in recent years. Here, the intention is to overcome common issues of conventional systemic drug supply such as poor solubility, limited stability, rapid metabolization and excretion of the drug, undesired side effects, and the lack of selectivity toward specific cells types. [42–44] The encapsulation of therapeutics within nanocarriers that selectively target certain cell types or tissues

## 2 Drug delivery with mesoporous silica nanoparticles

represents a promising strategy to address these problems.

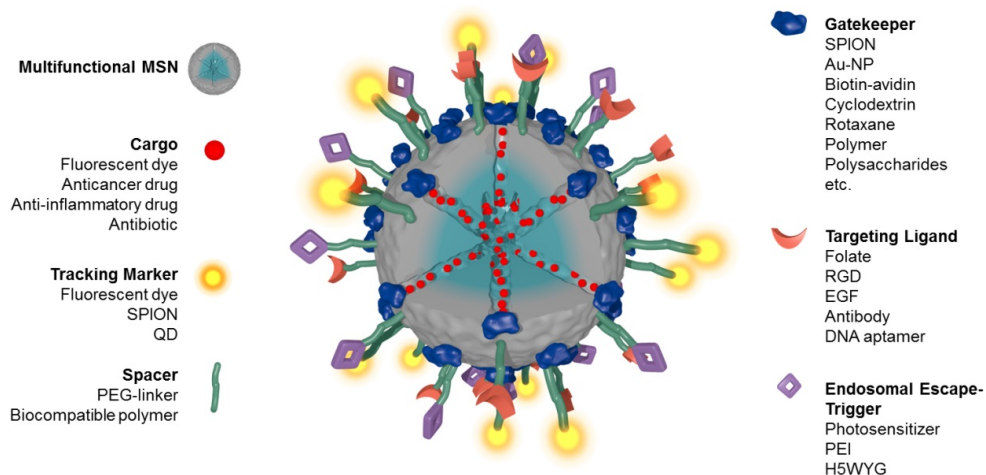


**Figure 2.1:** Schematic illustration of a multifunctional mesoporous silica nanoparticle (MSN) containing the necessary features for a stimuli-responsive controlled release of the loaded cargo into the cytosol of a targeted cell (SPION: superparamagnetic iron oxide nanoparticle, QD: quantum dot, PEG: poly(ethylene glycol), Au-NP: gold nanoparticle, RGD: Arg-Gly-Asp amino acid sequence, EGF: epidermal growth factor, PEI: poly(ethylene imine), H5WYG: endosomolytic peptide).

MSNs can be designed as a multifunctional platform for different *stimuli-responsive trigger systems* for a specific drug release. Moreover, different strategies for achieving *controlled endosomal escape* are discussed. Coating the nanoparticles with different organic shells improves *biocompatibility*, facilitates attachment of targeting ligands for specific cellular recognition, and can be utilized for the effective encapsulation of cancer therapeutics. Investigation of *in vitro* behavior of colloidal particles, often fluorescently marked to track the particles in cells, with *live-cell imaging* serves to evaluate *targeting specificity* and efficient delivery. The implementation of the above strategies and features into one multifunctional drug delivery vehicle provides a promising basis for wide-ranging applications in cancer therapy and diagnosis. These key prerequisites for efficient drug delivery nanocarriers based on MSNs are schematically presented in Figure 2.1. They will be discussed in more detail in the following sections.

### 2.1 Targeting and cellular uptake

**Targeting.** Insufficient target selectivity of drugs can cause unfavorable side effects and reduce therapeutic efficacy. Especially in anticancer chemotherapy, limited selectivity of cytostatics and cytotoxins toward tumor cells is responsible for many undesired side effects. The efficacy of the treatment can be affected when nonspecific toxicity to normal cells prevents an effective dose that is necessary to eradicate malignant cells. [45, 46] Extensive studies showed passive targeting of nanocarriers in tumor tissue. [47, 48] Well-stabilized nanoparticles with optimal size and appropri-

ate antifouling surface can remain in blood vessels long enough to accumulate at the tumor site. Passive targeting relies on the enhanced permeability and retention (EPR) effect. This effect is described as the tendency of particles of certain sizes, such as liposomes, nanoparticles, and macromolecular drugs, to preferentially accumulate in tumor tissue. Tumor vasculature typically exhibits an increased permeability and is lacking effective lymphatic drainage. [49] Enhanced passive bioaccumulation via the EPR effect could be achieved by neutralizing the MSN surface with positively charged groups. [50] However, the EPR effect is not universal for all types of tumor cells, and a lack of cell-specific interactions might decrease therapeutic efficacy and induce multiple drug resistance (MDR). [49, 51, 52]

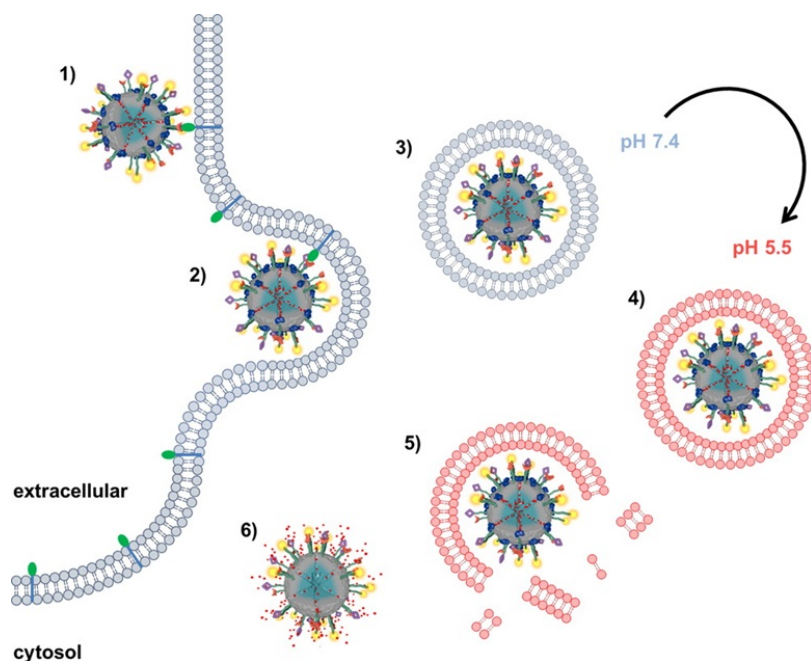


**Figure 2.2:** Schematic representation of different stages of a targeted cellular uptake of a multifunctional MSN and controlled release of the cargo into the cytoplasm of cancer cells. (1) Active docking to cell surface receptor of a nanocarrier via targeting ligands; (2) Process of ligand/receptor-mediated endocytosis; (3) MSN entrapped in endosome; (4) Intracellular transport and acidification of endosome; (5) Triggered endosomal escape of nanocarrier, thus obtaining access to the cytoplasm; (6) Controlled delivery of the cargo inside the cell.

In contrast, employing targeting ligands such as folic acid or macromolecules, like the epidermal growth factor (EGF), in order to exploit the overexpression of certain receptors on tumor cell surfaces can promote specific and active nanocarrier binding and cellular uptake. Active targeting can be accomplished by covalent attachment of targeting molecules (ligands) to the particle surface. The main challenge for targeted nanocarriers is to achieve high targeting specificity and drug delivery efficiency simultaneously, while avoiding nonspecific binding and activation of immunogenic effects. A recent advance has been reported by Brinker and co-workers, who combined a porous, inorganic MCM-41-type silica core coated with a supported lipid bilayer to prevent cargo leakage by means

## 2 Drug delivery with mesoporous silica nanoparticles

of a short targeting peptide (SP94). [51] This small peptide was identified by phage display to bind efficiently to hepatocellular carcinoma cells. The complementary receptor is still unknown. In this study, a ligand recruitment procedure was described leading to efficient receptor-mediated endocytosis of the nanocarriers.

**Table 2.1:** Diverse Targeting Ligands Used for Active and Specific Cell Recognition of Nanocarrier Based on MSNs.

targeting ligand	cell membrane receptor	targeted cell line	ref.
Folic Acid (FA)	folate receptor (FR- $\alpha$ )	HeLa, KB	[15, 53–62]
RGDmotiv	integrins	HeLa, MCF-7,U87-MG, HZ29, SCC-7	[63–66]
antibody ME1	mesothelin	MM	[67]
antibody ab2428	ErbB 2	MCF-7	[68]
antibody Herceptin	HER2/neu	BT-474	[69]
aptamer AS 1411	nucleolin	MCF-7, MDA-MB-231	[70]
mannose	mannose receptor	MDA-MB-231	[71]
galactose	galactose receptor	HCT-116, Capan-1, MDA-MB-231	[72]
hualuronic acid	CD44 (RHAMM, HARE)	CD168, MDA-MB-231	[73]
anisamide	Sigma-receptor	ASPC-1	[74]
EGF	EGF-R	HuH-7	[15]
SP94	unknown	Hep3B	[51]
FA, TEM-7, CD31	FR- $\alpha$ , TEM-7 antibody, CD31 antibody	MCF-7,HUVEC	[75]

The small molecule folic acid (FA) has been widely investigated as targeting ligand and causes a notable enhancement in uptake efficiency of MSN nanocarriers when attached to them (for References, see Table 2.1). Often, long spacers, e.g., PEG chains, are used for the covalent attachment of the targeting ligands to the external surface of the MSNs. This linkage provides high flexibility to obtain efficient binding of the targeting ligands to the cell membrane receptors. Ligands such as FA, mannose, hyaluronic acid, and EGF (among others) used as targeting devices are abundantly present in organisms. Moreover, the associated receptors are widely present on many eukaryotic cells. This implies concerns about the achievable targeting specificity. In those cases, the significant overexpression of receptors on cancer cells has been exploited. Extensive efforts have been made to create actively targeted nanocarrier vehicles using ligands for specific recognition of the cell-surface receptors as well as antibodies and DNA aptamers. Important examples are summarized in Table 2.1. Studies on antibodies attached to the nanoparticle surface via either electrostatic interactions

or covalent linkage showed highly specific binding with high affinity to antigens overexpressed on different cancer cell lines. [67, 68] MSN bioconjugates with DNA-aptamers were also investigated and showed specific binding to nucleolin, a cell membrane protein overexpressed on breast cancer cells. [70] However, concerns may arise about the stability of these systems in body fluids due to potential degradation of the targeting ligands by extracellular nucleases or proteases, which may reduce targeting efficiency of antibody- and aptamer-aided delivery concepts.

**Endocytosis.** In general MSNs are internalized into the cells via endocytosis. [27] For illustration, a typical sequence of cytosolic delivery of therapeutics to cancer cells with mesoporous silica nanocarriers is depicted in Figure 2.2. The endocytic pathway is the most common uptake mechanism of cells for many different nanoparticles and macromolecules. Endocytosis is a very complex process by which cells absorb such particles by engulfing them with lipid bilayer forming vesicles. For this purpose, a part of the cell membrane is used for creating an endosome. [76] Size and morphology of the silica nanoparticles and functional groups on the external particle surface influence the ability of MSNs to be internalized via endocytosis. [77–82] Utilizing such modifications of the MSNs can aid in specific cellular uptake in a precisely controlled manner. In a study of Slowing *et al.*, [83] endocytosis of aminopropyl-functionalized MSNs was shown to be affected by caveolar inhibition suggesting a cellular uptake via a caveolae-mediated mechanism. However it can be imagined that also other cellular uptake mechanism, like the clathrin dependent endocytosis [84], play an important role in cellular MSN uptake. Endocytosis of MSNs can be investigated via flow cytometry, transmission electron microscopy, confocal microscopy, and other techniques. [85]

## 2.2 Endosomal escape

Recent studies have demonstrated that MSNs are able to undergo smooth cell internalization, but endosomal escape has been identified as a bottleneck for the efficient delivery of macromolecular substances or nanoparticles. [86] The entrapment in the endosomes could lead to degradation of the nanocarriers and their cargo molecules by specific digestive enzymes when fusion with a lysosome occurs. Thus, an important step in achieving an appropriate therapeutic effect is to facilitate the endosomal escape and to ensure cytosolic delivery of the therapeutics.

Many anticancer therapeutics such as doxorubicin (DOX) feature cell membrane permeability, and consequently, a trigger for endosomal escape is not required. These permeable drugs only require a means of preventing premature release from the nanocarrier to avoid global distribution in the organism and targeted transport into cancer tissue to achieve a sufficiently high local drug concentration. Nevertheless, a large number of molecular and macromolecular therapeutics are either hydrophobic or membrane impermeable. Therefore, the multifunctional nanocarrier vehicles should provide an efficient endosomal escape mechanism for the local delivery of the drug molecules into the cytoplasm, thus gaining access to the targeted cell compartments or to the nucleus.

Excellent strategies for achieving endosomal escape are provided by nature. Evolution created bacteria and viruses, which are able to penetrate membranes via different mechanisms to escape the endosomal pathway and to reach their target sites. Thus, it would be desirable to transfer

## 2 Drug delivery with mesoporous silica nanoparticles

these very efficient natural mechanisms to the drug delivery vehicles. Different mechanisms such as pore formation in the endosomal membrane, pH-buffering effects of protonable groups (“proton sponge”), or fusion into the lipid bilayer of endosomes have been proposed to facilitate the endosomal escape. [87]

In addition, photochemical methods to rupture the endosomal membrane have been introduced to MSNs. [1, 15, 86] In a study by Sauer *et al.*, [86] MSNs were taken up into cells and transported within endosomes, but no release of the cargo into the cytoplasm could be detected during incubation. In order to overcome the barrier of endosomal entrapment, photoinduced endosomal release via excitation of a photosensitizer (PS) was employed. Photochemical internalization (PCI) using PS that generate reactive oxygen species upon photoactivation is a powerful tool to overcome trapping by the endosomal membrane. [88] Initial approaches of combining PS with mesoporous silica as a drug carrier did not provide a covalent bond of the PS to the particles. This could lead to uncontrolled spreading of the compounds and toxic effects on the cells. To achieve a more spatially controlled activity of nanodevices operating with PS, it is desirable to bind the PS directly to the surface of the mesoporous particles. Thus, a mesoporous core-shell system with covalently surface-linked PS was designed that provides an on-board trigger for light-activated endosomal membrane rupture. [1] The nanocarriers can be loaded with model drugs in a broad size-range and are encapsulated by a SLB. The controlled release mechanism in living cells operates in a two-step cascaded manner, where the SLB is disintegrated by singlet oxygen in a first step and, second, the endosomal membrane is ruptured causing efficient cytosolic drug release. This nanodevice for drug delivery is capable of stimuli-responsive and localized endosomal escape and drug release without the systemic cell toxicity exhibited by common (dissolved) PS. In order to create a general photoactivatable drug delivery platform being applicable in biological environments, such as cancer tissue, further improvements have to be accomplished. Strategies for red-light activation have already been investigated. [15, 72] The activation of the photosensitizer with low energy light reduces the phototoxicity and significantly increases the depth of tissue penetration, which will be crucial when activation *in vivo* is required.

Another promising endosomal release strategy is based on the proton sponge effect, in which osmotic swelling and membrane rupture of endosomes is initiated by macromolecules with high buffering capacities. [89] This mechanism does not require an external stimulus, and custom-made nanocarriers can activate an “automatic” pathway for endosomal escape. Several cationic lipids and polymers, such as poly(ethylene imine) (PEI), possess substantial buffering capacity below the physiological pH which is a potential trigger to escape the endosomal entrapment. [91, 92] The cationic polymers or particles enter the cell via endocytosis, subsequently being entrapped in the endosome. Upon intracellular trafficking to late endosomes or lysosomes, the compartment is acidified from an initial physiological pH value of 7.4 to around 5 (see also Figure 2.3). [90] Thus, the overall protonation level for PEI increases drastically. [93] The accumulation of positive charge inside the endosome is coupled with a passive influx of chloride anions through ion channels to maintain electroneutrality. The large increase of ion concentration within the endosome in turn results in an inflow of water molecules, which causes osmotic swelling and subsequent membrane rupture. Employment of the

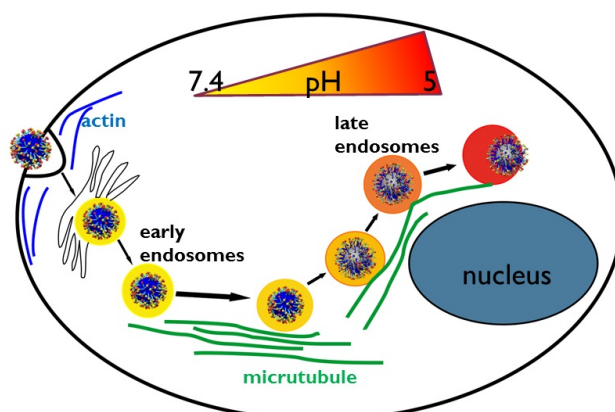


**Figure 2.3:** Schematic illustration of the acidification process inside cells after endocytosis. After reaching the cell, particles are uptaken via endocytosis and passed on, from early endosomes with a pH around 7.4 to late endosomes, and finally lysosomes with a pH around 5. [90]

proton sponge effect would provide an elegant solution for the problem of endosomal entrapment of MSNs. However, the exact mechanism is not fully understood. It is still an open question whether there has to be a high-capacity buffering agent present that is subsequently protonated and highly charged or if an already highly charged surface of particles is also sufficient to cause counterion influx, endosome swelling, and rupture. Lin and co-workers reported on MSNs with negatively charged surface functionalization achieving endosomal escape via the proton sponge effect. [83] More negatively charged nanoparticles would escape more easily from endosomes of cancer cells owing to their high buffering capacity. The zeta potential of the silica nanoparticles seems to have a great impact on the ability of particles to escape the endolysosomal pathway. However, such highly negatively charged nanoparticles exhibit unfavorable cellular uptake behavior due to electrostatic repulsion with the negatively charged cell membrane. Nanocarriers providing protonable groups at mildly acidic conditions should result in much more efficient cellular uptake and subsequent drug release to the cytosol. In general, the proton sponge effect is a promising intrinsic endosomal escape pathway that should be further investigated.

An alternative mechanism uses endosomolytic peptides to achieve endosomal release. [94] The lipid bilayer-enclosed MSNs established by Brinker and co-workers were equipped with such an endosomolytic peptide (H5WYG) (Figure 2.4). [95] This peptide sequence is a subunit of the glycoprotein hemagglutinin of the influenza virus A and undergoes a conformational change upon protonation. H5WYG peptides were often employed in combination with nanocarriers, but experimental evidence for the exact molecular mechanism was not provided so far. [96–98] It is speculated, that different endosomal escape pathways take place, such as the proton sponge effect (protonation of the histidin residues of the peptide) or fusion of the endosomal membrane with the SLB. Further investigations are needed to evaluate the exact mechanism, which could lead to the full exploitation of this endosomal escape pathway. In general, endosomal entrapment was found to be a bottleneck in efficient cytosolic delivery of nonpermeable drug molecules and additional efforts have to be made

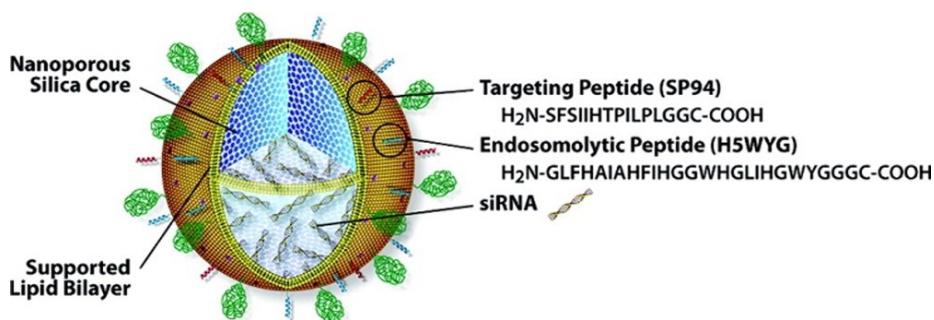


**Figure 2.4:** “Protocell” consisting of MSN-supported lipid bilayers with targeting peptides (SP94) and endosomolytic peptides (H5WYG) attached to the outer periphery of the nanoconstructs. [99]

to overcome this entrapment. A complete understanding of the diverse escape mechanisms is highly desirable.

## 2.3 Controlled release of cargo

Extensive *in vitro* studies have been performed to gain insights regarding the feasibility of employing MSNs as drug nanocarriers. Cargo release in a controlled manner is highly desirable, since side effects can be drastically reduced by locating delivery to single cells or target tissue and since the optimal amount of drug can be liberated.

As discussed above, MSNs serving as drug delivery vehicles can be functionalized on the external particle surface with stimuli-responsive molecules, nanoparticles, polymers, and proteins acting as caps and gatekeepers for such a controlled release of various cargos. Delivery of antitumor drugs and other pharmaceutical cargos such as enzymes or oligonucleotides requires effective protection from undesired degradation in harsh environments, such as the stomach and intestines. On the other hand, when injected into the bloodstream, such a drug delivery device should offer perfect enclosure of the cargo to prevent undesired premature release and systemic distribution before reaching the targeted tissue or cells. The most common pore sealing strategies can be classified into three different types of gatekeepers, i.e. molecular/particle pore gating, coating of the external particle surface, and internal pore binding. Reported *in vial* and *in vitro* studies and the diverse opening mechanisms based on external or internal stimuli are presented in Tables 2.3.1 and 2.3.2, respectively.

### 2.3.1 External Stimuli

A broad spectrum of triggers for specific cargo release has been described. Triggers such as light, external magnetic fields and temperature require activation of the release mechanism from the outside. [101, 113, 116] These systems provide perfect control over temporal and spatial release of the drugs into the targeted tissue or cells, but tissue penetration in *in vivo* studies can limit performance. Temperature changes have also been investigated to release encapsulated molecules. [116, 119]

**Table 2.2:** Controlled Cargo Release Mechanisms Triggered by External Stimuli.

external stimulus	gating system	opening mechanism	cargo	release experiments	ref.
UV-vis light ( $\lambda = 240\text{-}639$ nm)	<b>Molecular Pore Gating</b>				
	thymidine dimers	cleavage	dye	<i>in vial</i>	[100]
	cyclodextrin (CD)	dethreading	dye	<i>in vial</i>	[101]
	cucurbit[6]uril	photothermal dethreading	dye	<i>in vial</i>	[102]
	nitroveratryl carbamate	cleavage	anticancer drug	<i>in vial</i>	[103]
	<b>Coating</b>				
	polymer shell	photolysis, dethreading	dye	<i>in vial</i> <i>in vitro</i>	[104, 105]
	SLB	photolysis	dye, therapeutic	<i>in vitro</i>	[1, 15, 106]
	<b>Internal Pore Modification</b>				
	coordinative bonds	cleavage	dye	<i>in vial</i>	[107]
IR-light ( $\lambda = 808$ nm)	<b>Coating</b>				
	aptamer DNA shell	photothermal dehybridization		<i>in vitro</i>	[108]
				<i>in vitro</i>	[108]
	<b>Pore Modification</b>				
	coordinative bonds	photothermal cleavage	anticancer drug	<i>in vitro</i>	[109]
Magnetic field + absorber	<b>Molecular/Particle Pore Gating</b>				
	DNA	thermal cleavage	dye	<i>in vial</i>	[110]
	SPIONs	heat-shock induced cleavage of disulfide linker	dye	<i>in vitro</i>	[111]
	Au-NPs	cleavage of boroester linker	dye	<i>in vial</i>	[112]
	<b>Coating</b>				
PEI/NIPAM	thermal phase transition	dye, enzyme	<i>in vial</i>	[113]	
Temperature	<b>Molecular/Particle Pore Gating</b>				
	biotin-avidin	cleavage of DNA linker	dye	<i>in vial</i>	[114]
	Au-NPs	cleavage of DNA linker	dye	<i>in vial</i>	[115]
	<b>Coating</b>				
	paraffin	melting	dye, anticancer drug	<i>in vitro</i>	[116]
	polymer	phase transition	dye, antibiotic, anticancer drug	<i>in vial</i> <i>in vitro</i>	[117–119]
Molecules	<b>Molecular Pore Gating</b>				
	DNA	competitive displacement	dye	<i>in vial</i> <i>in vitro</i>	[120–122]
	glycoprotein	cleavage of boroester linker	dye, antifungal drug	<i>in vitro</i>	[123]
	18-crown-6	competitive displacement	anti-inflammatory drug	<i>in vitro</i> <i>in vial</i>	[124]
	SLB	lysis	dye, colchicine	<i>in vitro</i>	[39]

Light can also be used to activate various opening mechanisms. [100, 102] Recently, Bein, Bräuchle and co-workers could demonstrate an improved system consisting of MSNs coated with an SLB and equipped with a covalently attached PS. [15] The SLB was shown to seal the pores and to prevent premature release of the loaded cargo. Upon photoactivation of the PS with red light, generation of reactive oxygen species initiated cargo release due to rupture of the SLB. Photosensitizers are promising components of nanocarrier systems for efficient drug delivery because they can simultaneously serve as a means for endosomal escape and for triggering controlled release in combination with SLB-coated MSNs.

### 2.3.2 Internal stimuli

In contrast to external stimuli, internal stimuli like changes in pH, enzymatic reactions, and reducing agents can provide intrinsic and autonomous release of the loaded cargo molecules from the mesoporous host system. Many mechanisms for controlled closure and release have been developed in

## 2 Drug delivery with mesoporous silica nanoparticles

**Table 2.3:** Controlled Cargo Release Mechanisms Triggered by Internal Stimuli.

internal stimulus	gating system	opening mechanism	cargo	release experiments	ref.
pH (acidic)	<b>Molecular/Particle Pore Gating</b>				
	SPIONs	cleavage of borooester linker	anti-inflammatory drug	<i>in vitro</i>	[125]
	Au-NPs	cleavage of borooester linker	dye	<i>in vial</i>	[112, 126]
	CD	dethreading	dye, anticancer drug	<i>in vial, in vitro</i>	[127–130]
	[2]pseudorotaxane	dethreading	dye	<i>in vial</i>	[131]
	curcubit[6]uril	dethreading	dye	<i>in vial</i>	[132, 133]
	<b>Coating</b>				
	saccharides	cleavage of borooester linker		<i>in vial</i>	[134]
	layered double hydroxides (LDH)	dissolution	dye	<i>in vial</i>	[135]
	polymer	phase transition	anticancer drug, insulin, dye	<i>in vial, in vitro</i>	[95, 117, 136] [103, 137–140]
	coordination polymer	cleavage	anticancer drug	<i>in vitro</i>	[141]
	chitosan	phase transition	anti-inflammatory drug, anticancer drug	<i>in vial, in vitro</i>	[68, 142, 143]
	<b>Internal Pore Modification</b>				
	coordinative bonds	cleavage	anticancer drug	<i>in vial, in vitro</i>	[109, 144]
	acetal linkage	cleavage	peptide	<i>in vitro</i>	[145]
electrostatic interactions	cleavage	anticancer drug	<i>in vitro</i>	[146]	
template	extraction	anticancer drug	<i>in vitro, in vivo</i>	[147]	
hydrazone linkage	cleavage	anti-inflammatory drug	<i>in vitro</i>	[148]	
pH (basic)	<b>Molecular Pore Gating</b>				
	$\beta$ -lactoglobulin	phase transition	dye, anti-inflammatory drug	<i>in vial</i>	[149]
	lysozyme	detaching	dye	<i>in vitro</i>	[150]
	sulfophenyl isothiocyanate	cleavage	anti-inflammatory drug	<i>in vial</i>	[41]
enzymes	<b>Molecular Pore Gating</b>				
	azopyridine derivatives	cleavage	dye, anticancer drug	<i>in vitro</i>	[151]
	cucurbit[7]uril	competitive displacement	dye	<i>in vial</i>	[152]
	[2]pseudorotaxane	cleavage of ester linker	dye	<i>in vial</i>	[153]
	biotin-avidin	enzymatic digestion	dye	<i>in vial</i>	[40]
	<b>Coating</b>				
	hyaluronic acid	cleavage	dye, anticancer drug	<i>in vitro</i>	[73]
	ethylene glycol ester	cleavage	dye, anticancer drug	<i>in vitro</i>	[154]
	peptides	cleavage	dye	<i>in vial</i>	[155]
starch derivatives	enzymatic digestion	dye, anticancer drug	<i>in vitro</i>	[156]	
lactose derivatives	enzymatic digestion	dye	<i>in vial</i>	[157]	
reducing agent	<b>Molecular Pore Gating</b>				
	CD	cleavage of disulfide linker	dye	<i>in vial</i>	[130]
	ssDNA	cleavage of disulfide linker	anticancer drug, ssDNA	<i>in vitro</i>	[158]
	collagen	cleavage of disulfide linker	dye, ssDNA	<i>in vial</i>	[159]
	polymer	cleavage of disulfide linker	dye	<i>in vial, in vitro</i>	[105, 140, 160]
	<b>Internal Pore Modification</b>				
	disulfide linkage	cleavage	enzyme, cysteine	<i>in vial, in vitro</i>	[86, 161]
molecules	<b>Molecular Pore Gating</b>				
	ATP aptamer	competitive displacement	dye	<i>in vial, in vitro</i>	[162–164]
	insulin derivatives	competitive displacement	insulin, cAMP	<i>in vial</i>	[165]
	Au-NPs	dehydrogenation of DNA linker	dye	<i>in vial</i>	[166]
	<b>Coating</b>				
	enzyme multilayers	phase transition	insulin	<i>in vial</i>	[167]

recent years, often with a view on utilizing such biologically relevant changes in the cell environment encountered by the particles upon endocytosis.

Thus, pH changes have been used to open gates at the pores of the mesoporous nanoparticles, and changes in redox potential could be used to cleave disulfide bridges. pH-responsive nanocarriers have been designed to achieve a site-selective controlled release, because tumor and inflammatory tissues are more acidic than normal tissue and blood. Importantly, the acidification of endosomes inside targeted cells can be utilized to trigger pH-responsive intracellular release of the cargo molecules. [68, 141, 148] Zink and co-workers have described a pH-responsive dethreading of bulky  $\beta$ -cyclodextrin molecules upon protonation of a complementary stalk located at the pore entrances and the resulting efficient DOX release *in vitro*.

In the context of oral administration, nanocarrier systems have been designed with acid-stable gatekeepers to be able to pass the stomach without premature release. After passing the acidic environment, pH-responsive caps can be cleaved in the basic milieu of the intestines to efficiently release the loaded pharmaceuticals. [41, 149, 150] Enzyme-responsive controlled release can be highly efficient once the nanocarriers have entered the cancer tissue or the cytosol of targeted cells. Many intracellular and extracellular enzymes are overexpressed in cancer tissue and exhibit increased activity, resulting in preferential cargo release at those locations. [151, 155] Summarizing, molecular and particle-based pore gating or coatings, removable by either intracellular or external triggers, can provide exquisite control over the location and time of cargo release during drug delivery.

## 2.4 Biological and pharmaceutical relevance

On-demand cargo release from the mesopores of silica nanoparticles has been proven to be feasible. To understand the biological and pharmaceutical activity of the MSN drug delivery systems *in vitro* and *in vivo*, it is useful to investigate the response of cells, such as knock-down of certain genes, stimuli-responsive labeling of cell compartments, destruction of the microtubule network, or apoptosis of cancer cells. [1, 39, 168, 169] Depending on the charge of the cargo, the surface of the nanocarriers has to be tuned and the release systems need to be adjusted to the scope of the application. Diverse model systems have been developed to learn more about the complex processes during cellular uptake of MSNs and subsequent drug release. The focus of this work is not on discussing the challenges of preclinical studies but to provide information about the mode of operation of multifunctional MSNs in the biological environment. For instance, attaching fluorescent dyes to the MSNs provides the possibility to directly observe the behavior of the nanocarriers and the cells. Common dyes include rhodamine or fluorescein derivatives, as well as ATTO or ALEXA dyes. [59, 80, 86, 170] Fluorescent cargo and/or labeling of cell compartments also aids in the examination of the intracellular processes.

Drug loading of small anticancer therapeutics can be achieved by simple immersion of the particles into a concentrated solution of the desired drug, followed by sealing with the gating mechanism under study. Efficient loading was shown by Bein, Bräuchle and co-workers upon adsorbing colchicine, propidium iodide, phalloidin, chromobodies, calcein, or a rhodamine derivative into MSNs, which

## 2 Drug delivery with mesoporous silica nanoparticles

were subsequently sealed by an SLB. [1, 15, 39] Doxorubicin (DOX) is a commonly used anticancer therapeutic due to its efficient induction of apoptosis in cancer cells, and it is fluorescent, thus enabling direct microscopic observation. [171] Several DOX-containing systems have been investigated, ranging from  $\text{Fe}_3\text{O}_4@\text{mSiO}_2$  nanocapsules [172] to hollow MSNs, [173–175] to mesoporous silica-coated gold nanorods, [108] and to MSNs including targeting functionalities like aptamers. [70] Imaging the release of various cargos from MSN with different capping and release systems was a main goal of this work. *In vitro* methods can verify the encapsulation of a large amount of

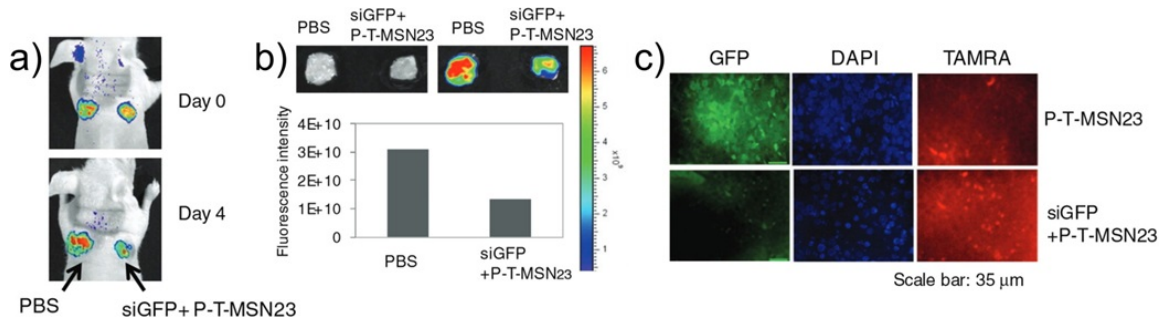


**Figure 2.5:** Knockdown of GFP genes with siRNA-loaded, PEGylated (P), and carboxy-tetramethylrhodamine-labeled (T) MSN with a pore diameter of 23 nm (P-T-MSN23) *in vivo*. *In vivo* optical images before (a) and after (b, top) removal of tumors and quantitative analysis of GFP-expressing tumors (b, bottom). (c) Optical microscopic images of a tissue section after 4',6-diamidino-2-phenylindole (DAPI) staining show considerable reduction in GFP expression in the siGFP-P-T-MSN23-treated tumor, compared with tissue treated with P-T-MSN23. [169]

drug molecules in MSN carriers, which increases their efficiency. This was proven in a study of Tian and co-workers. [168] They demonstrated a significant increase of early and late apoptosis of paclitaxel-loaded MSNs on MCF-7 cells compared to free drug molecules. Gene transfection or oligonucleotide delivery with MSNs has not been studied to a large extent yet, and in most reported cases, the oligonucleotides are only adsorbed on the external surface of the MSNs or incorporated in a polymer shell of coated MSNs. [176] Milligan and co-workers used so-called “protocells” for GFP and IL-10 gene delivery *in vitro* and *in vivo*, but no proof of gene adsorption inside the pores was provided. [176, 177] Tamanoi and co-workers attached siRNA to the external surface of coated MSNs with the aid of PEI and observed gene silencing of EGFP. [178] Attachment of the oligonucleotides exclusively on the external particle surface could cause concerns about premature degradation via abundantly available ribonucleases. Therefore, controlled loading of siRNA into large pores of MSNs is a highly desirable approach that is expected to provide efficient protection from bioerosion.

In addition to extensive *in vitro* investigations, the first *in vivo* application of MSNs was reported in 2008. [179] Recently, Nel and co-workers presented a successful proof of principle aimed to overcome DOX resistance in a mouse xenograft model with PEI-PEG functionalized MSNs. [180] Unfortunately, heterogeneity in the tumor microenvironment, such as differences in the vascularity, possibly influences the efficacy of drug delivery *in vivo*. Further research is necessary to evaluate the MSN distribution in tumor models, particularly with targeting ligands to ensure the capability of the

## 2.4 Biological and pharmaceutical relevance

delivery systems to efficiently reach all cells within the tumor tissue. Nevertheless, these early experiments provide strong evidence that MSNs are promising candidates for improved cancer therapy and that they are able to reduce side effects for healthy tissues. [181, 182] Furthermore, very promising results for siRNA delivery were obtained by Min and co-workers. [169] They showed successful delivery of GFP downregulating siRNA in a tumor xenograft mouse model (Figure 2.5). The reduction of GFP fluorescence could be observed with optical imaging *in vivo* (Figure 2.5 a,b) and more clearly in tissue sections (Figure 2.5 c). Although the results demonstrate the feasibility of this approach, the system is still lacking control over pore sealing and a release mechanism.

In addition to possible cancer therapeutics and gene delivery, there are also studies for inhibitor delivery and delivery of cytokines. [59, 183] A detailed overview on *in vivo* biosafety evaluations and diagnostic/therapeutic applications of MSNs has recently been provided by Shi and co-workers. [184]



# 3 Multifunctional mesoporous silica nanoparticles

This chapter is adapted from the publication “Multifunctional Mesoporous Silica Nanoparticles as a Universal Platform for Drug Delivery”, published in *Chemistry of Materials*, written in collaboration with C. Argyo from the group of T. Bein. [14]

## 3.1 Synthesis of inorganic silica cores

MSNs acting as host systems for therapeutics provide high loading capacity within the porous system and protection of the guest molecules from degradation and from detection by the immune system. Furthermore, the nanocarrier systems can be utilized for the transport of hydrophobic molecules through biological media, thus increasing the therapeutic effect at the desired location.

The synthesis of ordered mesoporous silica materials has been extensively studied in recent years, [185–188] including sol-gel processes to create MCM-41 [189] and SBA-15, [190] among various different structure types. [191–193] Fine-tuning of the reaction parameters such as concentrations, pH value, chemical nature of the surfactants, temperature, and time allows for a precise adjustment of size, morphology, and pore structure of the mesoporous silica.

The scope of conventional mesoporous materials such as MCM-41 for applications in drug delivery is limited due to their relatively large particle sizes in the micrometer range. Cellular uptake studies of nanoparticles showed that particle sizes less than 120 nm are preferred for endocytic uptake. [194] Thus, efforts have been made to obtain spherical MSNs in that size range. [195–199] For example, a standard synthesis route, following addition of surfactant template, silica source, and organotrialkoxysilanes to a highly basic aqueous solution at elevated temperatures to create MCM-41-like nanoparticles, is used by many research groups. [142, 181, 200–203] Another versatile approach for obtaining stable suspensions of MSNs in high yields was developed in our group. Here, triethanolamine is exploited as base and as complexing ligand for the silica precursor and is used to tune the particle size (to about 80 nm). [36, 204] Their worm-like pore structure with pores growing from the center to the periphery suggests a seed-growth mechanism (Figure 3.1 c). Interest in the delivery of large cargo molecules, such as enzymes or oligonucleotides, leads to a growing research activity in the synthesis of MSNs with large pores (10–20 nm, Figure 3.1 d). [205, 206]

In order to gain access to the pores, the templating surfactant molecules have to be removed. This can be achieved either by calcination or with extraction methods. To overcome impediments such

### 3 Multifunctional mesoporous silica nanoparticles

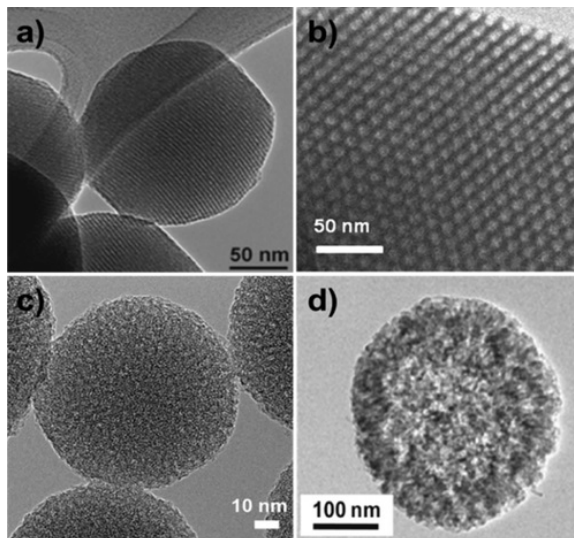


**Figure 3.1:** Transmission electron micrographs of (a) MCM-41-type nanoparticles ref [207], (b) micrometer-sized SBA-15 material ref [208] ), (c) colloidal MSNs with worm-like pore structure (Bein and co-workers), and (d) monodispersed MSNs with large pores ( $>15$  nm). ref [205]

as reduction in pore size, particle agglomeration, removal of organic moieties, or low degree of condensation of the silica network, Cauda *et al.* established a new approach that combines the advantages of both aforementioned methods for template removal. [209] Here, a liquid-phase high temperature “calcination” of MSNs is performed in a high-boiling organic solvent leading to a higher degree of silica condensation while maintaining the colloidal nature of the nanoparticles.

In order to exploit the whole potential of MSNs for drug delivery applications, it is desirable to add functionality to the silica scaffold. Molecular functionality attached to the surfaces of inorganic silica can dramatically change the properties of the obtained material, which is important in host-guest interactions with the cargo. The incorporation of organic moieties at specific locations is intended to fine-tune surface and materials properties and is a subject of current research. [210, 211] The spatially selective modification of the internal pore system and the external particle surface with organic and inorganic moieties is often an essential requirement for these materials to operate as multifunctional drug carriers exhibiting the required features. External surface functionalization is particularly important for colloidal and chemical stability as well as for interactions with the environment, such as modifying the particles for specific cell targeting or attaching large molecules for pore gating and improving biocompatibility. [83, 212–215] On the other hand, internal organic moieties can supply enhanced interaction or covalent binding sites for cargo molecules, such as drugs or proteins, which allows for control over diffusional transport, delivery kinetics, and stability of the therapeutic molecules. [136, 216, 217]

In general, there are several approaches to achieve functionalization of silica materials. The most important functionalization strategies are via postsynthetic grafting and via co-condensation, besides the synthesis of periodic mesoporous organosilicas (PMO) and employment of metal organic

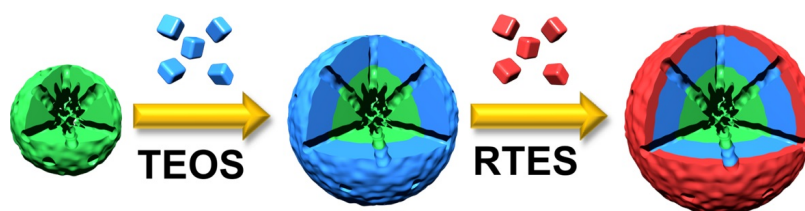


**Figure 3.2:** Site-selective delayed co-condensation approach for creating bifunctional MSNs. In a first step, a mixture of organosilane (green) and tetraethylorthosilicate (TEOS) in an aqueous solution containing template and base catalyst creates a functionalized nanoparticle core. Subsequently, the nanoparticle growth is completed by addition of pure TEOS (blue) resulting in an unfunctionalized silica shell around the core. Finally, the addition of another organotriethoxysilane (RTES, R represents an organic moiety, red) and TEOS forms an external skin with different functionality.

reagents. [189, 218–220] In order to gain control over the location of the functional groups in silica nanoparticles, Bein and co-workers established a site-selective delayed co-condensation approach. [37, 221] Here, bifunctional MSNs with a selective functionalization of the interior and an orthogonal functionality at the external particle surface in different onion-like shells can thus be prepared (Figure 3.2). This strategy opens new possibilities for the design of numerous highly functionalized porous nanoparticles with applications in controlled drug delivery.

## 3.2 Modification of silica cores

Surface modification with organic and inorganic species can introduce a large variety of functionalities for controlling diffusion and release of cargo molecules and cell surface recognition, among others. The potential to design biocompatible external surfaces of nanoparticles providing tunable interactions with the biological environment by attachment of molecular or macromolecular moieties for biomedical applications has been recently demonstrated. [40, 41, 86] The combination of the properties of such an external functional shell and the advantageous structural properties of the mesoporous silica core can create multifunctional drug carriers, making the delivery process highly controllable.

**Gating** One of the important functionalities in this context is triggered release of the cargo through specially designed gating concepts. In general, gatekeepers can be classified into three different types, namely molecular/particle pore gating, surface coating, and internal pore modifications (cf. Figure 3.3). Pore gating systems can consist of either bulky molecular groups or nanoparticles, such as proteins, superparamagnetic iron oxide nanoparticles (SPIONs), or gold nanoparticles (Au-NPs) which block the pore entrances for efficient sealing of the interior mesoporous environment. [40, 111, 166] These macromolecular structures are either degradable or attached to the silica particle surface via linkers that are cleavable upon exposure to certain stimuli. [125, 156] Very good pore sealing can also be achieved by a complete coating of the MSNs. For instance, polymers, oligonucleotides, or supported lipid bilayers (SLB) have been shown to prevent premature

### 3 Multifunctional mesoporous silica nanoparticles

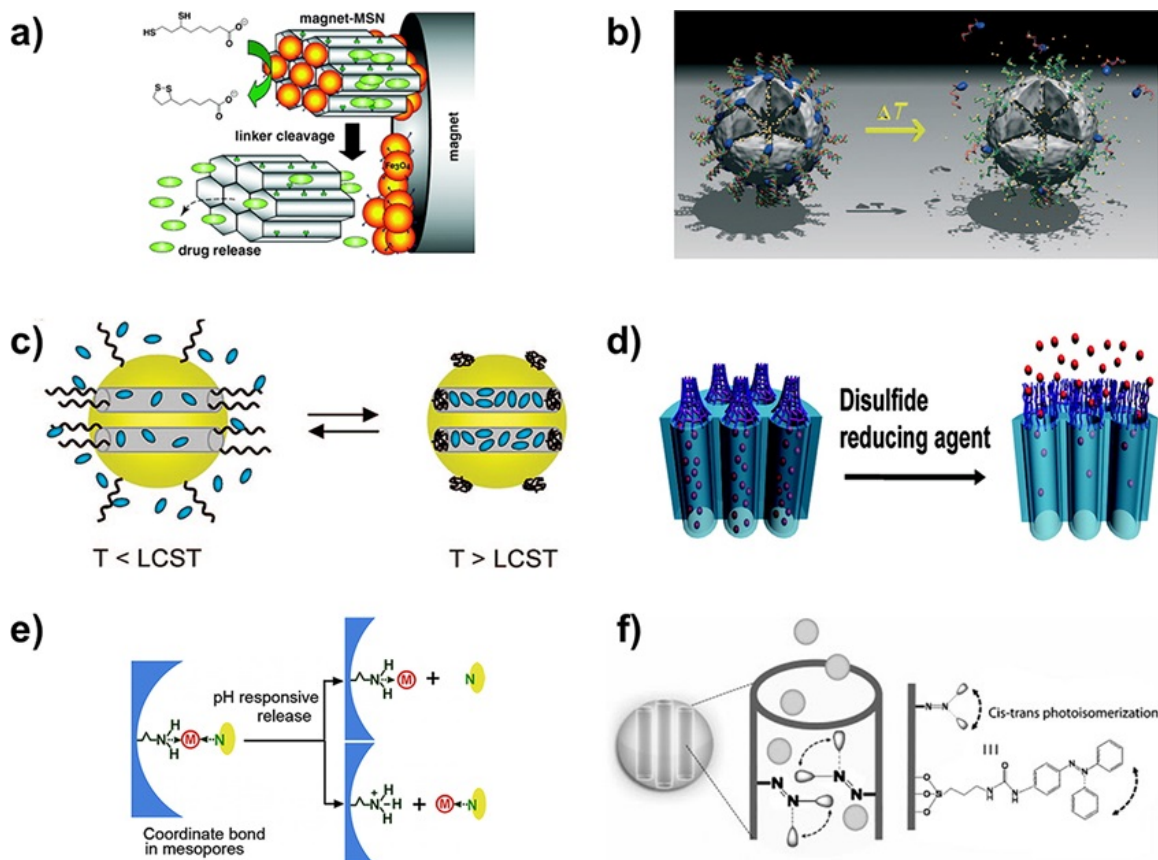


**Figure 3.3:** Strategies for controlled release can be classified into three different types, molecular/particle pore gating (a,b), surface coating (c,d), and internal pore modification (e,f). (a) Mesoporous silica nanorods capped with superparamagnetic iron oxide nanoparticles (SPIONs) containing redox-responsive cleavable disulfide linkers; [111] (b) temperature-dependent programmable molecular valve system consisting of avidin caps being opened by melting the DNA linkers; [114] (c) temperature-dependent phase transition of PNIPAM-coating on MSNs; [118] (d) disulfide-linked polymeric network at the outlet of mesoporous silica allowing redox-responsive controlled release of the cargo [160] (e) schematic release mechanism for a pH-responsive system based on coordination bonding in mesopores; [144] and (f) light-activated cis/trans isomerization of azobenzene groups inside mesopores expels the cargo. [222]

cargo release. [15, 39, 51, 53, 95, 99, 108, 177, 223, 224] Often, phase transitions or competitive displacement reactions lead to opening of the pores and efficient cargo delivery. [117, 120] The third strategy for controlled cargo release involves attachment of the cargo molecules in the porous system of the silica nanocarriers. Coordinative or covalent bonds can be cleaved by certain stimuli such as competitively binding molecules or reducing agents to activate cargo release. [107, 109, 161] Zink and co-workers have presented different nanocarriers with on-demand controllable release mechanisms, including nanoimpellers consisting of azobenzene groups that have been described to trigger UV-light-activated release of a cell membrane-impermeable dye. [222]

**Biocompatibility and Stability** For applications of MSNs as nanocarriers, biocompatibility and

low toxicity are required. A modification of the nanoparticle surface with functional shells, such as polymer coatings, charged groups, or a supported lipid bilayer was found to decrease particle aggregation and improve stability in biological media. For instance, functionalization of the particle surface with phosphonate groups was shown to improve the stability and dispersibility of MSNs in aqueous media. [128, 225] This modification helped to prevent interparticle aggregation, and redispersion after a drying process was highly improved. [16] In general, MSNs provide good biocompatibility, but the high surface area and a low degree of condensation of the silica framework can promote a high rate of dissolution. [226, 227] Bare, nonfunctionalized MSNs featuring silanol groups at their surface dissolve fairly rapidly in simulated body fluid under physiological conditions and produce soluble silicic acid species (which are found to be nontoxic). [228] The rate of silica dissolution is dependent on particle size, functionalization, degree of silica condensation, and pore morphology. A surface functionalization can prevent fast degradation and provide prolonged stability of MSNs in biological media. For example, a hydrophilic polymer shell such as poly(ethylene glycol) (PEG) or an SLB on colloidal MSNs improves stability in water, maintains monodispersity, and can minimize nonspecific adsorption of proteins on the nanoparticle surface. [35, 53, 128] Such a polymer coating provides a protective shell for the silica surface, which is important when prolonged circulation time in an organism is required for effective drug delivery. PEGylation can hinder capture by organs of the reticuloendothelial system (RES) and consequently slow down biodegradation. [229] Hemocompatibility is another important attribute of MSNs. Surface functionalization of bare MSNs can reduce or even completely prevent thrombogenic effects and nonspecific protein adsorption on MSN surfaces. [230] For example, heparin-coated core-shell MSNs have recently been described. [231] Heparin is a highly sulfated, anionic polysaccharide, known for its anticoagulant properties. This novel nanoscale system combines the efficiency of heparin in preventing blood-clotting with multifunctional core-shell MSNs featuring excellent structural properties and colloidal stability. In general, MSNs with organic shells offer multifunctionality and improved biocompatibility and hemocompatibility and are expected to have potential as blood-stream-injectable drug-delivery systems offering new options for cancer therapy.



## 4 Fluorescence live cell-imaging

A common technique to perform live-cell imaging is fluorescence microscopy because it offers the ability to monitor cell interactions after the cells were labeled, with fluorescent dyes. Nowadays, many site-specific fluorescent dyes to mark defined cell compartments are commercial available. [232] Furthermore nanostructures such as mesoporous silica nanoparticles can be marked with fluorescent dyes and the interaction of particles with cells can then be monitored. [1, 14, 39, 86, 233] These experiments lead to a better understanding of the interaction between nanoparticles and cells, and are an important first step in developing new materials for medical applications.

In this thesis live-cell imaging was employed to observe the uptake and cellular fate of functionalized mesoporous silica nanoparticles, their release behavior as well as for the activation of the photoinduced endosomal escape.

The following section aims to give a general introduction to fluorescence principles on the basis of the Jablonsky-Diagram. Furthermore, requirements for dyes used in live cell imaging and related problems are discussed. Finally, the utilized spinning disc setup is described along with the principal for confocal microscopy.

### 4.1 Fluorescence principle

The basic physical principles behind fluorescent microscopy [234, 235] can be described by a look at the Jablonsky-Diagram (Figure 4.1). A fluorescent molecule is capable of gaining energy by absorption of photons if the energy of the photon is equal the energy difference of its energetic levels. From the electronic ground state  $S_0$  the molecule gets excited to a higher (electronic) state (e.g.  $S_1$ ,  $S_2$ ) and therein in vibrational and/or rotational excited states by absorbing a photon. Internal conversion, vibrational relaxation and intersystem crossing can then take place or relaxation by emission of a photon.

For live-cell fluorescent microscopy the energy of absorbed and emitted photons is normally in the visible light range. The energy  $E$  is inversely related to the wavelength ( $\lambda$ ) of the absorbed photon's:

$$E = \frac{h \cdot c}{\lambda} \quad (4.1.1)$$

Hereby,  $h$  is the Planck's constant and  $c$  is the speed of light in vacuum.

To come from higher energy levels back to the ground state the molecule can emit a photon with the corresponding wavelength (fluorescence), which normally takes place in the nanosecond range. Beside the singlet excited states also triplet excited state can be reached. This process is called intersystem crossing and is more likely if the triplet state vibrational energy levels overlap with

#### 4 Fluorescence live cell-imaging

lowest energy levels in  $S_1$ . In this case the electron undergoes a forbidden transition (spin transition) and owing to this, it can take microseconds for the electron to come back to the singlet ground state which involves another spin transition. Meanwhile it is also possible, that another photon excites a triplet-triplet transition and it would take even longer to come back to the ground state.

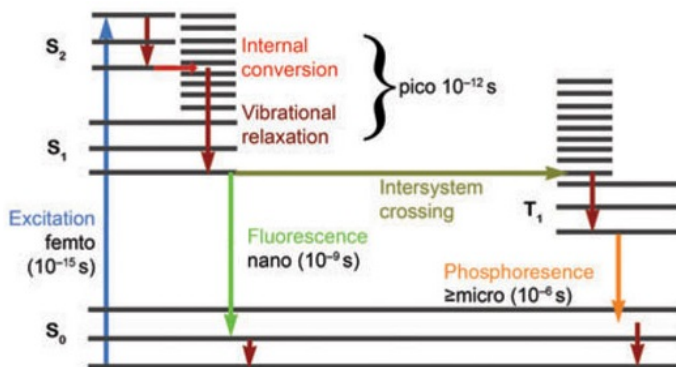


**Figure 4.1:** Jablonsky-Diagram displaying the energy states of a molecule and the times that the various steps in the fluorescence excitation and emission and phosphorescence take. The diagram is taken from ref. [234].

In addition to the light emitting processes also emission-free possibilities for returning to a favorable lower energy level. The vibrational energy is then transferred e.g. to neighboring molecules and lost for fluorescence. But it is unlikely for a fluorescent molecule to get back to the ground level only using vibrational relaxation. Beside vibrational relaxation internal conversion plays a role. In the case of internal conversion the system changes between electronic states without energetic loss, by going from a low vibrational state of a higher electronic state to a high vibrational state of a lower electronic state. Internal conversion can also be followed by vibrational relaxation. Within picoseconds a molecule is able to come to the lowest energy level of  $S_1$ .

Because of the energy difference between the vibrational modes of the electronic ground state and the first singlet excited state, normally a total relaxation, without any photon emission, to the ground state is not preferred.

Due to the non-radiant relaxation behavior there is a shift to lower energy in the maximum of the emission wavelength in comparison to the maximum in the absorption wavelength, the so called "Stokes shift". Apart from that, the emission and absorption spectra exhibit a symmetry due to the similarity of transitions. Depending on the electronic, vibrational and rotational states of a fluorophore the excitation spectra a broader or smaller.

## 4.2 Requirements for used dyes

A suitable fluorescent dye is pivotal for fluorescence microscopy. In the following several requirements for the fluorescent dye will be presented. Prerequisite for a high fluorescence is a dye which has a

high quantum yield and a long lifetime. The quantum yield  $\Phi_{Fl}$  hereby is defined as [235]:

$$\Phi_{Fl} = \frac{\text{Number of photons emitted as fluorescence}}{\text{Number of absorbed photons}} \quad (4.2.1)$$

A higher quantum yield means an increase in fluorescence intensity and alternative competing photochemical processes like bleaching and free radical formation become less likely. [234] Especially for cell experiments it is often useful to have dyes with a high quantum yield because one wants to observe processes over a longer time range and it wouldn't be of advantage if the bleaching of the dye takes place too fast. An example for such an experiment would be the observation of cargo release out of endosomes, as the dye is highly concentrated inside the endosome and after release into the cytosol it gets highly diluted. If the dye also bleached fast there wouldn't be a chance to detect the spreading inside the cytosol.

Photobleaching normally occurs due to destruction of the dye, mostly because of the generation of reactive oxygen species (ROS) like singlet oxygen ( $^1O_2$ ). As a result the total number of ground state molecules is permanently reduced, the higher the light intensity, the faster this process will take place. With laser light as excitation source photobleaching can occur within a few microseconds. [236] The less dye molecules are present, the faster there will be no fluorescence left to detect, and for example spreading of a dye could not be observed. Thus in most cases, photobleaching is undesirable. Nevertheless there are cases like the photoactivated endosomal escape where the generation of reactive oxygen species is desired. These dyes are used on purpose which are known to generate a high amount of singlet oxygen, for example porphyrine or phthalocyanine derivatives. [237] The produced singlet oxygen destroys selectively the surrounding environment of the activation area like cancer tissue.

Another useful property in fluorescence microscopy is fluorescence enhancement that may occur because of environment changes, like intercalation into special structures (e.g. DNA or RNA), binding to ions (like calcium ions) or changes in pH. [238–240]

An effect that can be used in order to easily image spreading of a dye inside cells is the use of so called “quenchable” dyes. Quenching is the reversible loss of fluorescence due to non-covalent interactions between a fluorophore and its surrounding. It can occur due to e.g. *förster resonance energy transfer* (FRET) charge transfer reaction, biochemistry or static quenching, if ground-state fluorophores associate to other molecules (in the case of identical molecules this is called “self-quenching”). [234] Calcein represents a suitable quenchable dye, because of its self-quenching abilities, at a concentration of about 30  $\mu\text{M}$  the fluorescence intensity of calcein decreases already. [241] Therefore calcein is often used e.g. in liposome-fusion experiments.

Furthermore it is possible to combine two or three dyes for one measurement. However before doing so it is of great importance to check their fluorescence excitation and emission spectra, in order to avoid overlapping which would lead to cross-fluorescence. Particular the excitation spectra would be problematic, if they possess a broad spectral range and therefore the dye could be excited with various wavelength. To circumvent the problems that would arise from broad fluorescent emission spectra it is often useful to use alternating excitation in order to separate the images from each

other.

### 4.3 Spinning disc microscope

To study living cells with fluorescence microscopy a high spatial resolution in 3D and a high time resolution is crucial to gain new insights and answer open questions for example in regard to drug delivery as will be presented in the chapter 6 - 10. The best tool for this is a spinning disc microscope. Lateral resolution for optical microscopes is expressed by the Rayleigh criterion: [242]

$$d_{\text{lateral}} = \frac{0.61\lambda}{\text{N.A.}} \quad (4.3.1)$$

where  $\lambda$  is the wavelength of the light and N.A. the Numerical Aperture, defined as follows:

$$\text{N.A.} = n \cdot \sin\phi \quad (4.3.2)$$

with  $\phi$  being the half-angle of the light cone entering the microscope objective and  $n$  the refractive index of the medium, between objective and sample. [235]

The Rayleigh criterion states, that two objects can be laterally resolved if the central maximum of one point-object overlaps with the first minimum of the other one. The axial resolution  $d_{\text{axial}}$  is then given by: [242]

$$d_{\text{axial}} = \frac{2n\lambda}{\text{N.A.}} \quad (4.3.3)$$

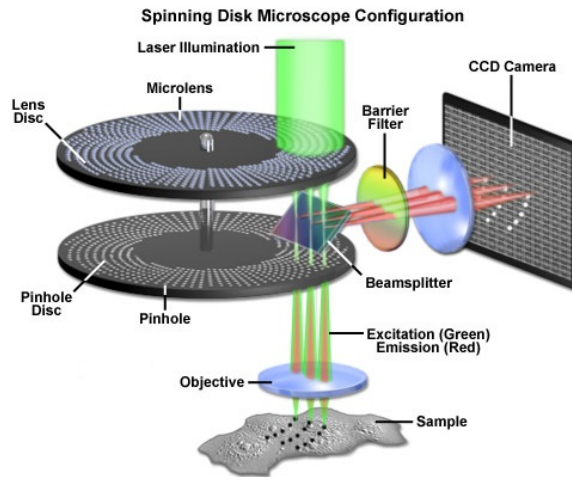


**Figure 4.2:** Schematic representation of a spinning disc setup. Picture is taken from ref. [243]. Laser light, crosses both rotating discs, is focused on the sample with confocal illumination and subsequently fluorescence passes back through the pinhole disc and reflected by a beamsplitter onto the detector, usually a CCD camera.

A confocal microscope is improved in comparison to a simple fluorescence microscope by introducing

### 4.3 Spinning disc microscope

pinholes in the excitation and detection pathway. The function of the pinholes is to block the out of focus fluorescence, and thereby increase the resolution, especially in the axial direction, as the width of the point spread function is reduced, as well as the intensity of the side lobes. By varying the size of the pinholes one can further influence the diffraction.

Confocal microscopes can be further improved, leading to spinning disc confocal microscopes, by substituting the pinholes with a spinning disk unit consisting of two fast rotating discs. On one disc there are multiple lenses, concentrically arranged and on the other one pinholes are installed, allowing for multiple simultaneously scans. With these discs it is now possible to screen many confocal spots over the sample and perform a faster imaging compared to a scanning confocal microscope, leading to a high time resolution. A disadvantage is however, that strong lasers are needed, as much light gets lost while passing the pinhole. Nevertheless the above mentioned advantages justify the usage of these kind of microscopes.

A schematic figure of the optical configuration of a Yokogawa spinning disc unit is given in Figure 4.2. The laser light first passes a lens disc with Fresnel microlenses. With these lenses the laser beams

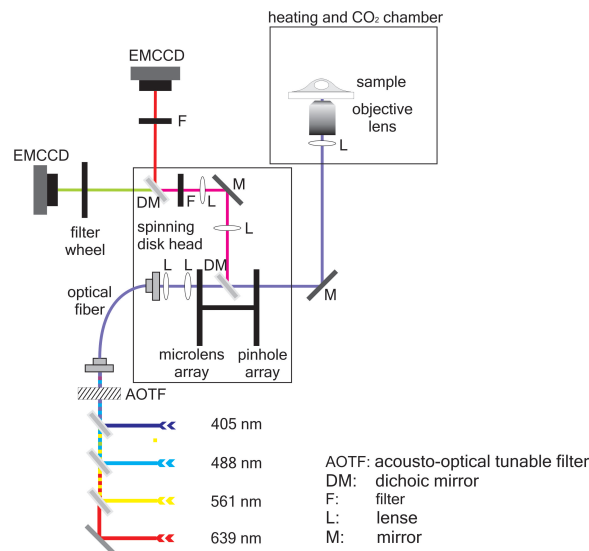


**Figure 4.3:** Schematic representation of the Zeiss Cell Observer SD, utilizing a Yokogawa spinning disc unit CSU-X1. The laser light enters the spinning disc head and is further directed to the microscope to illuminate the sample. The emitted fluorescence again passes the spinning disc head, a dichroic mirror separates the signal spectrally and is imaged onto two EMCCD cameras.

are perfectly aligned to the following pinhole disc. Both Discs are rotating (max. 10.000 revolutions per minute) so that the specimen must not be scanned for acquiring a picture, contrary to confocal microscopy. An objective ensures the beam to be focused on the specimen. The fluorescent light then comes back through the objective and passes the pinhole disc, where again out of focus light is cut off. After the pinhole disc a dichromatic beam-splitter separates the fluorescent from the excitation light since they have different wavelengths. The fluorescence can go through filter sets, corresponding to the spectra of the used dyes, to the detection EMCCD-camera. [243]

#### 4 Fluorescence live cell-imaging

In this work all measurements were performed on the commercially available Zeiss Cell Observer SD, utilizing a Yokogawa spinning disc unit CSU-X1. A schematic representation of the beam path can be seen in Figure 4.3. Four lasers (405, 488, 561 and 639 nm), that can be selectively chosen in desired combinations over an acousto-optical-tunable-filter (AOTF), are available. Over a single-mode optical fiber the lasers are directed into the spinning disk unit. The laser beam passes the rotating microlense and pinhole arrays and enters the microscope, where it illuminates the sample through an objective. A motorized stage controls the position of the sample in x-/y- position and a piezo-stage controls the z-position. The emitted fluorescence goes back through the objective, passes the pinhole array and by means of an dichroic mirror is directed to the EMCCD cameras. Appropriate dichroic mirrors and filters, that are located in front of the cameras, split the emission light.

### 4.4 Imaging

This section is adapted from the publication “Multifunctional Mesoporous Silica Nanoparticles as a Universal Platform for Drug Delivery”, published in *Chemistry of Materials*, written in collaboration with C. Argyo from the group of T. Bein. [14]

The imaging possibilities for MSNs and their combinations with other materials range from optical microscopy to magnetic resonance imaging and to ultrasonic imaging, near-infrared imaging, and other techniques. In this thesis, we will focus on optical microscopy and its applicability to gain real-time observation of MSNs in cell cultures and tissues. Other imaging techniques and the preparation methods for functionalized hybrid nanoparticles, such as silica nanoparticles containing magnetic cores, have been extensively discussed elsewhere. [17, 184, 244, 245] In this context, MSNs are being developed as a platform for incorporation of nanocrystals or for doping with active species including iron oxide nanocrystals, quantum dots, gold nanoparticles, and manganese or gadolinium ions. These types of multifunctional nanocarriers attract great interest with a view on theranostic applications.

There are different possibilities to fluorescently label MSNs. Depending on the desired type of labeling (removable or not), fluorescent dye molecules can be attached to the inner and outer particle surface by covalent linkage via postsynthetic grafting, incorporation into the silica framework, or pH-/redox-sensitive linkage. Diffusion of dye molecules or nanoparticles like quantum dots inside the pores has been investigated as well. [246] In that case, efficient enclosure of the fluorescent cargo in the mesopores can be achieved by an SLB or other bulky molecules used as valves. Diffusion dynamics of fluorescent molecules in porous silica materials were intensively studied with fluorescence microscopy. Bräuchle and co-workers could image single dye molecules [247–249] as well as the anticancer agent DOX [233] moving inside mesoporous channels of silica materials. Such studies are crucial for understanding diffusion processes and confirm the need for defined surface modifications for controlling adsorption and desorption processes of the cargo molecules in the mesoporous system. Functionalization of the mesoporous interior with amino-groups in order to achieve positively charged

surfaces resulted in preferential and increased uptake of negatively charged siRNA constructs. [250] Issues of cargo loading efficacy may arise due to electrostatic repulsion when negatively charged molecules like double stranded DNA should be absorbed into nanocontainers featuring negative surface charge. [251] On the other hand, electrostatic interactions may not be too strong; otherwise, they can cause entrapment in the porous system, and consequently, cargo release is inhibited. The stability of the cargo to be transported is a key factor in particle design, especially if the goal is to efficiently deliver sensitive cargos like siRNA. Fluorescent donor-acceptor pairs offer the possibility to investigate the stability of oligonucleotides inside the pores by measuring the Förster resonance energy transfer (FRET). [250, 251] Thus, the stability of oligonucleotides in specifically functionalized mesopores after adsorption was demonstrated. Since nanocarriers provide protection against diverse biological attacks, incorporation of oligonucleotides into the mesopores of silica materials is very promising for future experiments in gene delivery, especially because previous efforts in delivery so far have focused on oligonucleotides attached to the external particle surface. [176, 178]

Another useful method to monitor the release of payload from the pores of MSNs in real-time is FRET. For that purpose, Lee and co-workers attached a FRET donor-acceptor pair of coumarin and fluorescein isothiocyanate (FITC) to the cap system  $\beta$ -cyclodextrin located at the pore entrances of MSNs. After light activation, cleavage of the gatekeepers occurred and subsequently the FRET-signal vanished due to great distance of the donor-acceptor pair. [252]

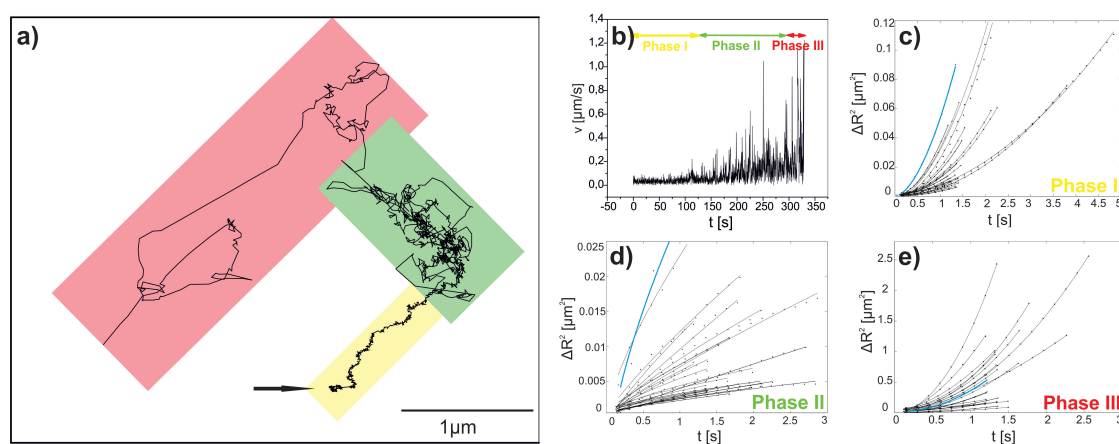


**Figure 4.4:** Internalization of epidermal growth factor receptor (EGFR) targeted MSNs with supported lipid bilayer. [15, 253] (a) Trajectory of an MSN during uptake into HuH7 cells. The particle was tracked 4 min after addition of the particles on top of the cells, for 5 min and 50 s at a temporal resolution of 150 ms/frame. Three phases are typically observed during the internalization process. [254] The starting point of the trajectory is indicated with an arrow. The overlying color boxes indicate the three phases. Yellow: phase I, slow active transport; green: phase II, anomalous and confined diffusion; red: phase III, active transport with back and forth movement. (b) Instantaneous velocities of the trajectory shown in (a) and (c-e) the mean square displacement (MSD) plots of the three phases obtained from several trajectories. The corresponding plots from the trajectory are indicated in blue. The analysis of the trajectories was performed with the help of the viro-tracker developed by Godinez *et al.* [255] to localize the xy-coordinates and with the help of the transport-program developed by Arcizet *et al.* [256] to calculate MSD plots. [253]

#### 4 Fluorescence live cell-imaging

Optical imaging is also the most widely used technique to study the feasibility of custom-made drug nanocarriers based on MSNs. The direct release and distribution of cargo inside cells can be monitored via fluorescence microscopy. Furthermore, precise investigations of uptake behavior and cellular internalization mechanisms of MSNs in single cells can be realized. Methods that were developed to evaluate the uptake behavior of viruses and single polymeric gene carriers (polyplexes) were extensively exploited by Bräuchle and co-workers. [254, 257–259] Subsequently, the internalization

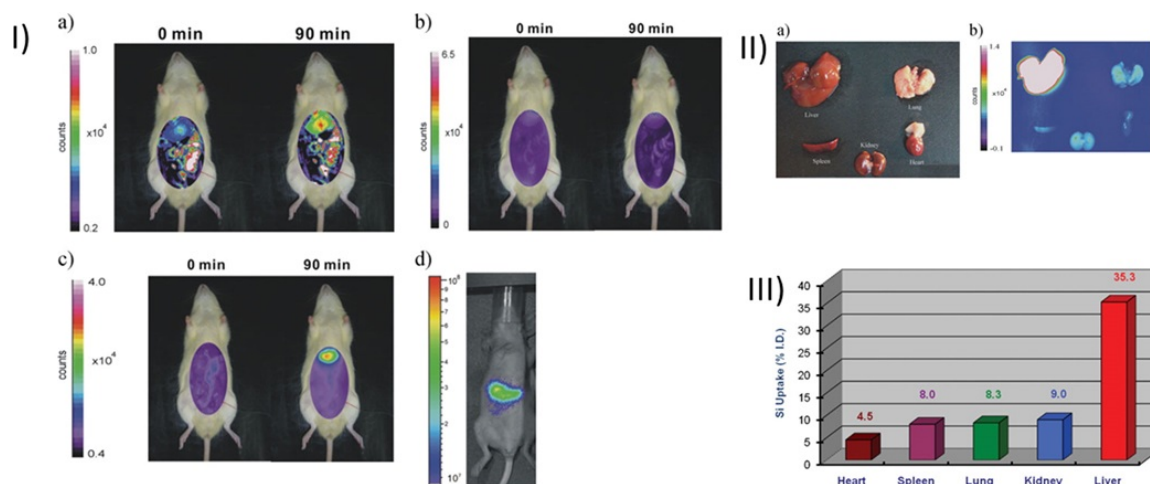


**Figure 4.5:** (I) Comparison of FITC-tagged MSN with ICG-tagged MSN (50-100 nm). (a, b) Biodistribution of MSN-NH<sub>2</sub>-FITC in an anesthetized rat before and after (90 min) i.v. injection. The experimental conditions were set at 492 nm (excitation) and 518 nm (emission) and (a) a longer shutter time (60 s) for a visible imaging and (b) 30 s shutter time. (c) Biodistribution of MSN-TA-ICG in an anesthetized rat before and after i.v. injection for 90 min. MSN-TA-ICG sample showed less interference of autofluorescence in a shorter shutter period (30 s). (d) MSN-TA-ICG in nude mice after i.v. injection for 3 h. (II) Dissected organs from a rat sacrificed after i.v. injection of MSN-TA-ICG for 3 h. (a) representative white-light and (b) fluorescent images. (III) *In vivo* biodistribution of silicon percentage in various organs of rat after i.v. injection of MSN-TA-ICG for 6 h. [260]

of epidermal growth factor receptor (EGFR) targeted MSNs into living cells was also investigated. Detailed information on the internalization pathway, the behavior of the MSNs inside the cells, and information on unexpected interactions between the particles and the cell can be gathered by life-cell imaging, and consequently, possible challenges can be monitored. Similar to the behavior of polyplexes, it was observed that porous silica nanoparticles exhibit three phases of motion during their internalization (Figure 4.4). The particle motion was measured on a sensitive fluorescence wide field microscope and analyzed with single particle tracking methods. In the first phase, the particles attach to the cell membrane and consequently show a slow directed movement, provoked by movement of the subjacent actin cytoskeleton mediated by the EGF receptor and linker proteins. With the transition to phase II, the particles are internalized into the cells. Phase II consists of either normal, anomalous, or confined diffusion or a combination of all three. Normal diffusion is often hindered in the cytoplasm by the local microenvironment (cytoskeleton, organelles, large molecules, etc.). Phase III shows much faster, active transport of the particles entrapped inside

endosomes along the microtubule network via motor proteins with velocities up to 2  $\mu\text{m/s}$ .

Optical microscopy also provides the capability to image *in vivo*. However, attenuation of photon propagation and a poor signal-to-noise ratio due to autofluorescence of the tissue can cause difficulties and should be considered in the selection of the type of dye and its concentration. Nevertheless, the high loading capability of MSNs makes them promising candidates to overcome this problem. Thus, Lo and co-workers could study the spatial distribution of MSNs with positive surface charge and loaded with indocyanine green (ICG) via near-infrared microscopy inside anesthetized rats. [260] In that case, the biodistribution of the optical MSN probe was evaluated in comparison to FITC-labeled MSNs. FITC seems to be not appropriate for *in vivo* optical imaging, since tissue penetration depth of the fluorescent signal of this dye is too small and consequently not detectable. NIR fluorescent dyes can be clearly detected after intravenous injection for evaluating particle accumulation inside the liver and kidney and partially in lungs, spleen, and heart. Further verification of the biodistribution in the dissected organs can be seen in Figure 4.5.

Optical microscopy utilizing NIR fluorescent dyes offers the possibility to investigate long-term biodistribution of nanocarrier systems, since it is a noninvasive method and animal models do not need to be sacrificed. As observed in such experiments, bare MSNs seem to face the problem of being cleared through the reticuloendothelial system (RES), such as spleen or liver, and the EPR effect is decreased. [47, 228, 260] Further modifications of the particle surface including PEGylation of the MSNs are needed to avoid the activation of the immune system. [261]



# 5 Experimental methods and data analysis

## 5.1 Chemicals

The following chemicals were used as received without further purification: Alexa Fluor 488 Dextran (AFD, MW 10 kDa, Invitrogen); Alexa Fluor®568 Phalloidin (Invitrogen); Al(III) phthalocyanine chloride disulfonic acid (AlPcS<sub>2a</sub>, Frontier Scientific); calcein (Sigma-Aldrich, ≥ 90 %); CellLight®Early Endosomes-GFP/ Lysosomes-GFP/ Tubulin-GFP, BacMam 2.0 (Invitrogen); collagen A (Biochrom AG); colchicine (Sigma-Aldrich); dextran, fluorescein (10.0000 MW, Invitrogen); 1,2-distearoyl-sn-glycero-3-phosphoethanolamine-N-[folate(polyethylene glycol)-2000] (ammonium salt) (DSPE-PEG<sub>2000</sub>-FA, Avanti Polar Lipids); DPBS (no calcium, no magnesium, Invitrogen); dulbecco's modified eagle's medium : F12 (1:1) (Invitrogen); dulbecco's modified eagle's medium (DMEM):F12 (1:1) (Invitrogen) with Glutamax I; epidermal growth factor (EGF, Pepro-Tech, > 98 %); fetal bovine serum (Invitrogen); FITC-H5WYG (Enzo Life Science, ≥ 88 %); folic acid (FA, Sigma, > 97 %); folic acid deficient roswell park memorial institute 1640 medium (RPMI 1640, Invitrogen); hank's balanced salt solution (HBSS; calcium, magnesium, no phenol red, Invitrogen); H5WYG (Enzo life science, ≥ 88 %); LysoTracker®Red DND-99 (Invitrogen); propidium iodid (Sigma-Aldrich); wheat germ agglutinin (WGA) Alexa Fluor 488/ 647 conjugate (Invitrogen). DOPE-PEG<sub>4</sub>-(KIAALKE)<sub>3</sub> (LPK, 50 μM), DOPE-PEG<sub>4</sub>- (EIAALEK)<sub>3</sub> (LPE, 50 μM), cholesterol-PEG<sub>12</sub>- (KIAALKE)<sub>3</sub> (CPE, 50 μM), (EIAALEK)<sub>3</sub>- carboxyfluorescein (E-cf, 50 μM) and (KIAALKE)<sub>3</sub>- carboxyfluorescein(K-cf, 50 μM) were provided by the group of Prof. Kros (University of Leiden). Doubly distilled water from a Millipore system (Milli-Q Academic A10) was used. All cell or cell compartement staining reagents were applied as proposed by the producer.

## 5.2 Cell culture

KB cells were grown in folic acid deficient Roswell Park Memorial Institute 1640 medium (RPMI 1640, Invitrogen) supplemented with 10 % fetal bovine serum (FBS). HeLa cells were cultivated in Dulbecco's modified Eagle's medium (DMEM):F12 (1:1) (Invitrogen) with Glutamax I medium supplemented with 10 % FBS. Tubulin-GFP expressing HuH7 cells and wildtype HuH7 cells were grown in Dulbecco's modified Eagle's medium : F12 (1:1) (Invitrogen) supplemented with 10 % FBS. All cells were cultured at 37°C in a 5 % CO<sub>2</sub> humidified atmosphere. PCR was routinely performed in order to guaranty mycoplasma infection free cells.

KB cells were seeded on ibidi-Treat μ-Slides (IBIDI), HeLa and tubulin GFP expressing HuH7 cells on collagen A - coated LabTek chambered cover glass (Nunc). For live cell imaging the cells were

seeded 72, 48 or 24 h before measuring, at a cell density of  $0.75 \times 10^4$ ,  $1 \times 10^4$  or  $2 \times 10^4$  cells /  $\text{cm}^2$  respectively.

### 5.3 Microscopy in live cells

Live-cell imaging was performed on a confocal setup based on the Zeiss Cell Observer SD, utilizing a Yokogawa spinning disc unit CSU-X1 (cf. Chapter 4). The system was equipped with a 1.40 NA 100x or 63x Plan apochromat oil immersion or a 0.45 NA 10x air objective from Zeiss. 3D images were acquired with an axial distance of  $0.2 \mu\text{m}$ .

**Table 5.1:** Filter-dye combinations used in the measurements described in Chapters 6 - 10.

Fluorophor	$\lambda_{abs}[nm]$	$\lambda_{fl}[nm]$	$\lambda_{exc}[nm]$	Detection BP filter	ref.
DAPI	356	500	405	525/50	[262]
AFD 488	495	519	488	525/50	[263]
bodipy	$\sim 500$	$\sim 510$	488	525/50	[264]
Calcein	470	509	488	525/50	[265]
carboxyfluorescein	492	517	488	525/50	[266]
FITC	490	520	488	525/50	[267]
GFP	488	510	488	525/50	[268]
WGA 488	495	519	488	525/50	[269]
LysoTracker Red DND-99	577	590	561	629/60	[270]
Propidium Iodide	535	617	561	629/60	[271]
5(6)-Carboxy-X-rhodamine (RD)	570	595	561	629/60	[272]
AlPcS <sub>2a</sub>	$\sim 650-700$	$\sim 690$	639	690/60	[273]
Atto 633	629	657	639	690/60	[274]

The exposure time was 0.1 s for all experiments and the frame rate varied in the range from 3 to 0.03 Hz, depending on the experiment. In the excitation path a quad-edge dichroic beamsplitter (FF410/504/582/669-Di01-25x36, Semrock) was installed. For two or three-color detection a dichroic mirror (560 or 660 nm, Semrock) and band-pass filters 525/50, 629/60 and 690/60 (Semrock) were placed in the detection path depending on the used dyes (Table 5.1). Separate images for each fluorescence channel were acquired by using two separate electron multiplier charge coupled devices (EMCCD) cameras (Photometrics Evolve™).

The used lasers for an excitation of the single dyes, their maximum excitation and emission wavelength and the associated filters are listed in Table 5.1, the applied laser-power densities which vary for the experiments described in Chapter 6 - 10 are displayed in Table 5.2.

**Table 5.2:** Laser Power densities used for the experiments listed for each Chapters in W/mm<sup>2</sup>.  
\* 0.12 and 0.06 W/mm<sup>2</sup> for imaging and 1.2 W/mm<sup>2</sup> for photoactivation.

$\lambda_{exc}[nm]$	Fluorophor	Chapter						
		6	7	8	9	10.1	10.2	10.3
405								
	DAPI	-	0.16	0.16	0.16	-	-	-
488								
	AFD488	-	-	-	-	0.39	-	-
	bodipy	-	-	-	-	-	0.62	1.1
	Calcein	0.39	0.39	-	-	0.29	-	0.39
	carboxy-fluorescein	-	-	-	-	-	1.1	-
	FITC	-	-	-	-	0.37	-	0.62
	GFP	0.62	1.1	6.6	0.48-1.1	-	-	-
	WGA488	0.39	0.29	0.14		-	-	-
561								
	Lysotracker Red	-	-	-	-	-	-	0.042
	PI	-	-	0.39	-	0.39	-	-
	RD	1.2	-	2.1	-	-	-	-
639								
	AlPcS <sub>2a</sub> *	0.12/ 1.2	0.12/ 1.2	- -	0.06/ 1.2	- -	- -	
	Atto633	-	0.011-0.12	0.011-0.12	0.011-0.011	-	0.012-0.12	0.012-0.10

### 5.3.1 Uptake studies

To evaluate the functionality of the folic acid ligand, KB cells were incubated with nanoparticles for 2-5 h at 37°C under a 5 % CO<sub>2</sub> humidified atmosphere. In the case of live cell imaging the cell membrane was stained afterwards by adding a final concentration of 10  $\mu\text{g}/\text{mL}$  wheat germ agglutinin Alexa Fluor 488 conjugate (WGA488, Invitrogen) to the cell medium. After 1 min, the cell medium was removed, the cells were washed twice with cell medium, and imaged immediately. In the case of fixed cells the latter were washed three times after the 2-5h incubation time with PBS (Invitrogen). Afterwards 200  $\mu\text{L}$  of 4 % paraformaldehyde (PFA, Science Service) were added for

## 5 Experimental methods and data analysis

15 min. After removing the PFA, the cells were washed three times with PBS and stained with a final concentration of 10  $\mu\text{g}/\text{mL}$  WGA488 in cell medium. After 1 min the cell medium was removed, the cells were washed twice with PBS and imaged.

In control experiments, the FA receptors on the KB surface were blocked by pre-incubation of the cells with 3 mM folic acid (Sigma) for 2 h at 37°C under a 5 % CO<sub>2</sub> humidified atmosphere, bprior to addition of particles.

In case of EGF, instead of staining the cell membrane HuH7 cells with GFP tagged tubulin were used for live cell imaging. The wildtype HuH7 cells were treated equivalent to the live cell imaging of the KB cells. When applying HuH7 tubulin the cell medium was exchanged with CO<sub>2</sub>-independent medium (Invitrogen) after the incubation time and imaged immediately. For control experiments, EGF receptors on the HuH7 surface were saturated by pre-incubating the cells with 0.2  $\mu\text{M}$  EGF for 2 h at 37°C under a 5 % CO<sub>2</sub> humidified atmosphere, before adding particles.

### 5.3.2 Controlled release of cargo and endosomal escape with photoactivation

Cells were incubated with the corresponding particles 16 - 22 h prior to the measurements at 37°C under a 5 % CO<sub>2</sub> humidified atmosphere. Shortly before imaging, the medium was replaced by CO<sub>2</sub>-independent medium (Invitrogen). During the measurements all cells were kept on a heated microscope stage at 37°C. The photosensitizer AIPcS<sub>2a</sub> was activated by 1.2 W/mm<sup>2</sup> of 639 nm light for 1 min.

### 5.3.3 Elevation of pH induced controlled endosomal release

The release of cell-membrane permeable cargo due to pH-dependent opening of the PVP-coating inside the endosomes was measured by incubating cells with particles for several hours.

**MSN-PVP-PEG-NH<sub>2</sub>:** In the case of colchicine-release, tubulin GFP expressing HuH7 were incubated with colchicine loaded particles (100  $\mu\text{g}/\text{mL}$ ) for 18 h at 37°C under a 5 % CO<sub>2</sub> humidified atmosphere. For DAPI-release HeLa cells were incubated with DAPI-loaded particles (25  $\mu\text{g}/\text{mL}$ ) for 15 min, 15 h and 46 h at 37°C under a 5 % CO<sub>2</sub> humidified atmosphere.

**MSN-D3:** Cells were incubated 5 - 48 h prior to the measurements at 37°C under a 5 % CO<sub>2</sub> humidified atmosphere. Shortly before imaging, the medium was replaced by a CO<sub>2</sub>-independent medium (Invitrogen). In order to clearly show the tubulin-structures the pictures were specially processed: a rolling ball background subtraction (rolling ball radius:500 for tubulin structures and 300 for zoom in on tubulin structures) was used to remove the background and the z-stack could be depicted as a z-projection of the standard deviation.

**MSN-phSA-CA:** HeLa cells were incubated 7 - 24 h prior to the measurements with DAPI-loaded particles (33  $\mu\text{g}/\text{mL}$ ) at 37°C under a 5 % CO<sub>2</sub> humidified atmosphere.

#### Nuclei staining kinetics with DAPI.

HeLa cells were measured 5, 11, 24, 33, 49, and 61 h after incubation with the samples MSN-D3-MTS-DAPI, MSN-NH<sub>2</sub>-MTS-DAPI and the supernatant of MSN-D3-MTS-DAPI (after particle

separation). Each time point was measured with an independently incubated set of cells. In order to evaluate the fluorescence of the nucleoli, the z-stack position was set exclusively in the region of the nuclei. The integrated intensity of a region of interest (ROI) around the nuclei was determined (44 - 104 nuclei for each data point) and divided by the area of the ROI. Consequently, the average integrated density per nuclei area ( $\pm$  standard deviation, represented by error bars) could be plotted dependent on the incubation time.

Shortly before imaging, the medium was replaced by a CO<sub>2</sub>-independent medium (Invitrogen). During the measurements all cells were kept on a heated microscope stage at 37°C. The subsequent imaging was performed as described in the Spinning disk confocal microscopy section.

#### 5.3.4 Endosomal compartment staining.

The staining of the early/late endosome or the lysosome with GFP, commercially available CellLight<sup>®</sup> staining from Invitrogen was used (CellLight<sup>®</sup> Early Endosome-GFP, Late Endosome-GFP, and Lysosome-GFP, BacMam 2.0). The cells were simultaneously incubated with MSNs and the BacMam 2.0 reagent. The concentration of the labeling reagent has been chosen with 25 particles per cell (PCP) of the BacMam 2.0 reagent (cf. staining protocol [275]). For incubation, the cells stayed at 37°C under 5 % CO<sub>2</sub> humidified atmosphere for 21 - 24 h until the measurement.

#### 5.3.5 LPK-Ecf staining

The incorporation of the lipid-PEG-peptideK construct into the SLB of SLB@MSN the freshly prepared particles were mixed with the fluorescent-labeled counter-peptide E. In those experiments 15  $\mu$ L of MSN ( $\sim$  1 mg/mL) were mixed with 12  $\mu$ L carboxy-fluorescein-labeled E-peptide (E-cf, 50  $\mu$ M) and the co-localization was measured on cover-slip.

#### 5.3.6 SNARE-peptide mediated fusion experiments

Experiments without nanoparticles have been performed with HeLa cells in order to test the functionality of CPE and LPK in terms of membrane incorporation and binding to K/E-cf.

Hereby the cell medium was replaced by 100  $\mu$ L HBSS (or in a control with CO<sub>2</sub>-independent medium (Invitrogen) supplemented with 10 % FBS). 10  $\mu$ L CPE/LPK (50  $\mu$ M) were added directly on top of the cells without medium, followed by HBSS.

After 1 min incubation the cells were washed once with HBSS, followed by 10  $\mu$ L carboxy-fluorescein-labeled peptide (K-cf/E-cf) again to the top of the cells without medium and HBSS afterward. Again after 1 min incubation the cells were washed three times with HBSS and imaged in HBSS.

For the investigation of MSN with cells, the pretreatment of the cells was the same, CPE was used to introduce a SNARE-motive to the cell surface. Instead of K/E-cf, SLB@MSN-LPK were incubated with the cells. Depending on the desired incubation time HBSS or RPMI 1640 medium without FBS was used for the incubation of the cells. Incubation times longer than half an hour were performed in RPMI 1640 medium without FBS at 37°C under a 5 % CO<sub>2</sub> humidified atmosphere.

## **5.4 UV-VIS spectroscopy**

UV-VIS spectra were recorded with a NanoDrop ND 1000 spectrometer. Usually, 2  $\mu\text{L}$  of sample were used and all presented spectra are background corrected for water absorption.

In the following chapters all of the above presented methods have been employed. The following chapters discuss research of various aspects where fluorescence microscopy and cell culture were applied to answer some questions in the field of drug delivery.

## 6 Targeted drug delivery in cancer cells with red light photoactivated mesoporous silica nanoparticles

This project was performed in collaboration with Dr. Stephan Mackowiak, Alexandra Schmidt, Christian Argyo and Constantin von Schirnding, Prof. Thomas Bein and Prof. Bräuchle. The Particle Synthesis and Characterization was mainly performed by Alexandra Schmidt (group of T. Bein). The Chapter is adapted from and based on the publication “Targeted Drug Delivery in Cancer Cells with Red-Light Photoactivated Mesoporous Silica Nanoparticles”, published in *Nano Letters* [15].

The delivery of large amounts of cancer therapeutics specifically into the cytosol of cancer cells still faces significant challenges. Beside the lack of specificity in uptake by cancer cells these challenges include delivery of a large amount of cargo, release of the cargo into the cytosol and an easy synthesis in only one delivery system. Notably, release of the drug from the endosome poses a significant hurdle on the way toward drug delivery with high efficacy. In this Chapter, we will present a system that provides solutions for all of these aspects by externally triggering the release with a photosensitizer. In particular, a photoactivatable drug delivery system based on core-shell colloidal mesoporous silica nanoparticles (MSN) was employed, which allows exact spatial and temporal control of the release of the cargo from both the MSN and the endosome. [39, 221] Core-shell MSN are more suitable than regular MSN for this task because they can have different functionalizations in the core and the shell. This allows us to optimize the core functionalization, for example, for cargo uptake or covalent binding of the cargo to the core by disulfide bridges. [86] Moreover, the surface functionalization can be chosen to implement various gating mechanisms, such as surrounding the MSN with a lipid bilayer to enclose the cargo in it. [1, 39] Previously, our groups published a photoactivatable drug delivery system performing some of the above-mentioned tasks. [1] The current system, as can be seen in Figure 6.1 is improved in three key areas. The used photosensitizer (PS) will be activated by red light instead of blue light; the synthesis is significantly simplified, and targeting ligands have now been added to the system. The function of the photosensitizer is to solve the problem of endosomal entrapment. Other approaches addressing this issue such as taking advantage of the proton sponge effect, [89, 276] employing fusogenic or endosomolytic peptides, [51, 99, 277, 278] and the drop in pH inside the endosome will be discussed in the following Chapters. The photoactivation approach offers a solution for a defined and located initiation of the cargo release through an external stimulus in the form of a laser beam. The laser beam can be directed into the cancer tissue and

## 6 Targeted drug delivery with red light photoactivated mesoporous silica nanoparticles

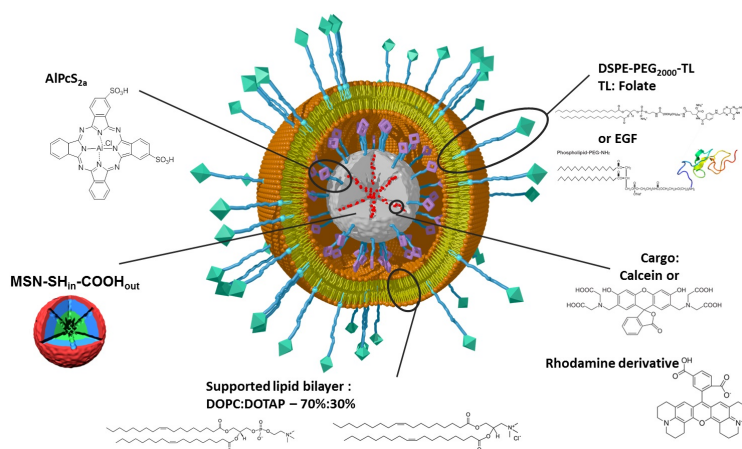


**Figure 6.1:** Schematic illustration of the multifunctional mesoporous silica nanoparticle (MSN-SH<sub>in</sub>-COOH<sub>out</sub>) surrounded with a supported lipid bilayer (SLB) containing the necessary features for a stimuli-responsive controlled release (photosensitizer) of the loaded cargo (calcein, rhodamine derivative) into the cytosol of a targeted (folic acid to FA receptor, EGF to EGF receptor) cell .

activated at the right time point. The activation of the photosensitizer with red light instead of blue light reduces the phototoxicity and significantly increases the depth of tissue penetration, [279] which will be crucial when activation *in vivo* is required as shown by the Kataoka group. [280] In comparison to regular photochemical internalization and other photoactivatable systems our system exhibits specific uptake by cancer cells due to the presence of targeting ligands. Schlossbauer *et al.* [1] presented MSN with photosensitizers that allowed free choice and controlled release of the cargo. However, the issue of the targeting capability of the system was not addressed. Febvay *et al.* [281] used MSN with photosensitizers in their studies as well, but the cargo had the role of the photosensitizer; that is, the cargo selection was very limited. Moreover, the photosensitizer, that is, cargo, was covalently bound to the MSN core, and hence a suitable release mechanism was not present. Yang *et al.* [282] used lipid-coated mesoporous silica nanoparticles as carriers for photosensitizers but aimed at improving photodynamic therapy (PDT). Gary-Bobo *et al.* [72] also used their combination of PS and MSN to enhance PDT by a combination of photosensitizer and cancer drugs. In the case of Lee *et al.*, [283] the photosensitizer served as a gate-opening mechanism. However, the PS was adsorbed inside the pores, and the cargo was attached on the surface via singlet oxygen-sensitive linkage, and therefore the key feature of MSN having a high internal loading capacity was not utilized here. In most of these systems the MSN served as improvement of PDT, whereas in our system the photosensitizer specifically serves as gate-opening mechanism and as a trigger for endosomal escape. In the current approach, we covalently link the photosensitizer molecule (PS) to the MSN surface and encapsulate the MSN with a supported lipid bilayer (SLB) to retain the drug. This allows for choosing a drug different from the PS and implementing a gating mechanism as well. Furthermore, the targeting mechanism presented by Febvay *et al.* was based on a streptavidin-coated nanoparticle and a cell surface that was stained with the antibody P-gp. [281]

While this demonstrates the targeting effect in principle, this specific targeting system is rather rare for cancer cells. Here we introduce the choice between two targeting ligands to our MSN, namely, folic acid (FA) as an example of a small molecule ligand and epidermal growth factor (EGF) as an example for a protein ligand. Both ligands are relevant for cancer cell targeting. For this purpose, targeting ligands (TL) are inserted into the SLB by diffusion to achieve specific uptake of the drug delivery vehicle by cancer cells.

In the following, first the synthesis and characteristics of our drug delivery system are discussed. Subsequently, live cell microscopy studies will be presented to evaluate the functionality of the employed targeting ligands and the release of the cargo from the MSN by photoactivation.

## 6.1 Synthesis and Characterization

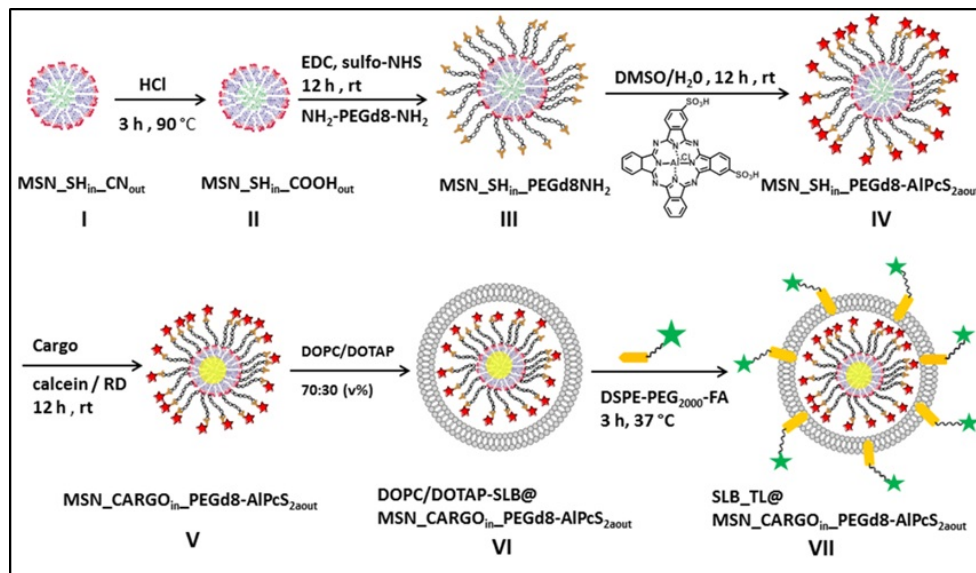


**Figure 6.2:** Synthesis pathway of core (Green) shell (Red) MSN with covalently linked AlPcS<sub>2a</sub> (Red Star) via PEG-linker (Black Chain) and surrounded by DOPC/DOTAP supported lipid bilayer with targeting ligand (Green Star, TL), before the formation of the SLB, the MSN core is loaded with a cargo (yellow), in our case calcein or a rhodamine derivative. Drawing is not to scale.

The core-shell MSN were synthesized via a sol-gel method using tetraethylorthosilicate (TEOS) as a silica source and CTAC as a pore template (cf. appendix Chapter 1 for details and ref. [221]). The MSN core was functionalized with thiol groups and the surface with cyano groups. The transmission electron microscope (TEM) image of the MSN (MSN-SH<sub>in</sub>-CN<sub>out</sub>) shows spherical particles with a mean diameter of 70 nm (Figure 6.3 a). The mesoporous channel structure radiating from the particle center is apparent in the image. From dynamic light scattering (DLS) and nitrogen sorption experiments a mean particle size of 69 nm and a mean pore size of 5.2 nm was determined (black squares in Figure 6.3b and c). To promote endosomal escape and subsequent delivery of the cargo

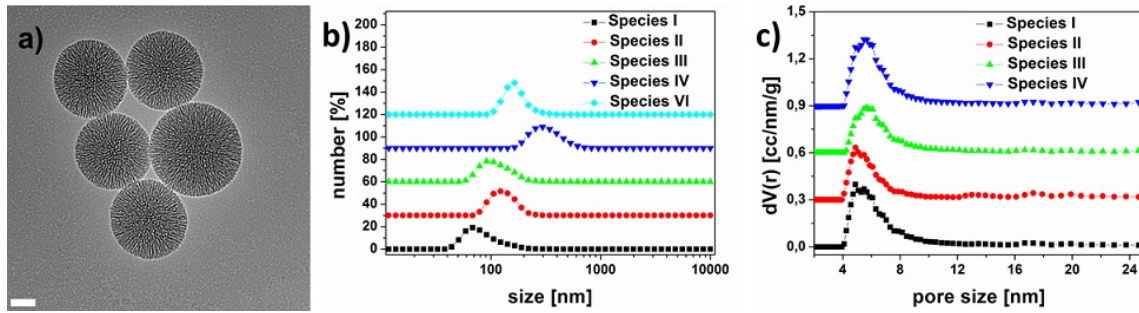


**Figure 6.3:** (a) TEM image showing bare MSN (I). The scale bar is 20 nm. (b) Particle sizes of species I-IV in Figure 6.2 obtained by DLS measurements. All curves, except of species I (black curve), are shifted by a value of 30 along the y-axis for clarity. (c) Pore size distributions of species I-IV. The exact values of the maxima are given in Table 2 in the appendix. Data are shifted by a value of 0.3 along the y-axis for clarity. Species I (black curve) represent  $\text{MSN-SH}_{in}\text{-CN}_{out}$ , species II (red curve) are  $\text{MSN-SH}_{in}\text{-COOH}_{out}$ , species III (green curve) are  $\text{MSN-SH}_{in}\text{-PEGd8NH}_2$ , species IV (blue curve) are  $\text{MSN-SH}_{in}\text{-PEGd8-AIPcS}_{2aout}$ , species VI (cyan curve) are  $\text{DOPC/DOTAP-SLB@MSN-CARGO}_{in}\text{-PEGd8-AIPcS}_{2aout}$ .

into the cytosol, we employ a photoactivation approach. Therefore, a red-light sensitive photosensitizer, aluminum phthalocyaninedisulfonate ( $\text{AIPcS}_{2a}$ ), is covalently linked to the surface of the MSN via an octamer PEG-linker. The PEG-linker is functionalized with amino groups on both ends. In the first reaction step, the surface cyano groups of the MSN ( $\text{MSN-SH}_{in}\text{-CN}_{out}$ ) are hydrolyzed to carboxyl groups ( $\text{MSN-SH}_{in}\text{-COOH}_{out}$ ), and subsequently the PEG-linker is attached to the MSN surface via EDC amidation ( $\text{MSN-SH}_{in}\text{-PEGd8-NH}_2$ ). The  $^{13}\text{C}$  solid state NMR (ssNMR) shows the successful implementation of these three steps (Figure 6.4 a). The resonance of the carboxyl group appears at 180 ppm upon hydrolysis of the cyano groups (red trace in Figure 2a). Following EDC amidation, the carboxyl group disappears, and the C-O and  $\text{CH}_2$  resonances, both from the PEG-linker, appear at 70 and 42 ppm, respectively (green trace in Figure 6.4 a). The other resonances originate from the functionalized silanes of the MSN (cf. appendix for details). The different surface functionalizations, including the attachment of the PEG-linker, are apparent in the final relative mass levels of the thermogravimetric analysis (TGA) curves as well (Figure 6.4 b and Table 2). Species  $\text{MSN-SH}_{in}\text{-PEGd8-NH}_2$  with the PEG-linker has a significantly greater mass loss than species  $\text{MSN-SH}_{in}\text{-CN}_{out}$  and  $\text{MSN-SH}_{in}\text{-COOH}_{out}$ . The slightly lower mass loss of species  $\text{MSN-SH}_{in}\text{-COOH}_{out}$  in comparison to species  $\text{MSN-SH}_{in}\text{-CN}_{out}$  originates from a more stable silica network that is formed during the 3 h heating in HCl, where the cyano is converted to carboxylic acid groups. The more stable silica network is apparent from the reduced BET surface area, as measured by  $\text{N}_2$  sorption experiments, as well (cf. appendix for details). Subsequently,  $\text{AIPcS}_{2a}$  is attached to the free remaining amino group of the PEG-linker by linking the PEG- $\text{NH}_2$  group with one of the two sulfonate groups of  $\text{AIPcS}_{2a}$  ( $\text{MSN-SH}_{in}\text{-PEGd8-AIPcS}_{2aout}$ ). The PEG-linker is required here because direct attachment of the  $\text{AIPcS}_{2a}$  to the MSN surfaces results in a significantly reduced pore accessibility and particle aggregation. The successful attachment of  $\text{AIPcS}_{2a}$  is inferred from the IR spectrum (cf. appendix Figure 6) and the TGA (blue curve in Figure 6.4 b). The mass

loss for species  $\text{MSN-SH}_{in}\text{-PEGd8-AIPcS}_{2aout}$  is comparably large due to the high molecular mass of  $\text{AIPcS}_{2a}$ . In particular, the ratio of the mass loss going from species  $\text{MSN-SH}_{in}\text{-PEGd8-NH}_2$  to  $\text{MSN-SH}_{in}\text{-PEGd8-AIPcS}_{2aout}$  and from species  $\text{MSN-SH}_{in}\text{-COOH}_{out}$  to  $\text{MSN-SH}_{in}\text{-PEGd8-NH}_2$  is 2. This can be related to the molecular mass ratio of the PS and the PEG, which is 2 as well.

To utilize the above multifunctional nanoparticles as drug delivery vehicles, a cargo was loaded into the MSN pores, and the entire nanoparticle was enclosed by a supported lipid bilayer to prevent premature release of the cargo from the MSN core. The cargo was loaded into the MSN by incubating them in a concentrated solution of the cargo overnight. In our system different types of cargo can be loaded. Here we show two examples, calcein and a rhodamine derivative. After the loading of the cargo the SLB is formed around the nanoparticle via the solvent exchange method as published by Cauda *et al.* [39] The SLB consists of a lipid mixture of 70 vol% of 1,2-dioleoyl-sn-glycero-3-phosphocholine (DOPC) and 30 vol% of 1,2-dioleoyl-3-trimethylammonium-propane (DOTAP). We note that the length of the PEG-linker, as described above, should not be too long because otherwise the formation of the SLB around the nanoparticle can be difficult. The DLS data (Figure 6.3 b) show that the modifications of the MSN surface, the attachment of the PEG-linker, the linking of the photosensitizer, and the formation of the 70 vol% DOPC/30 vol% DOTAP shell (SLB) result in colloidal systems with slightly varying hydrodynamic particle sizes (Figure 6.3 b and Table 2 in appendix, respectively). We note that the hydrodynamic sizes can also reflect a weak agglomeration behavior. In particular, it appears that the presence of carboxyl- or sulfonyl groups, either directly

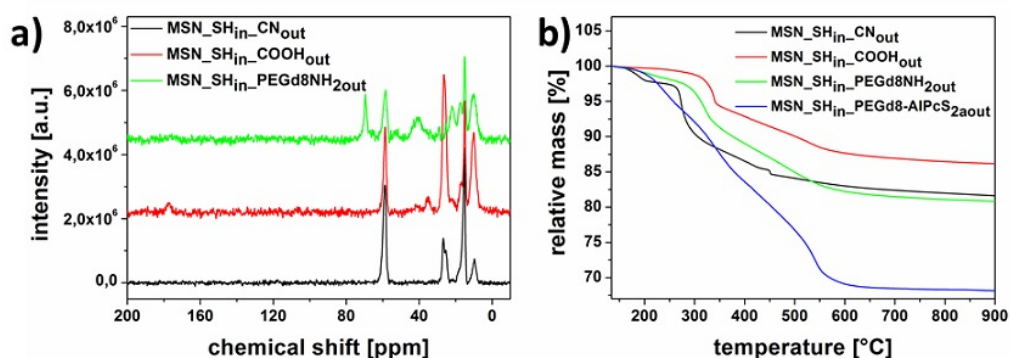


**Figure 6.4:** (a) Solid state  $^{13}\text{C}$  NMR spectra of species  $\text{MSN-SH}_{in}\text{-CN}_{out}$ ,  $\text{MSN-SH}_{in}\text{-COOH}_{out}$ ,  $\text{MSN-SH}_{in}\text{-PEGd8-NH}_2$ . It shows the successful conversion of the surface cyano groups to carboxyl groups and the subsequent linkage of the PEG8 linker to the MSN shell. Spectra for  $\text{MSN-SH}_{in}\text{-COOH}_{out}$  (red) and  $\text{MSN-SH}_{in}\text{-PEGd8-NH}_2$  (green) are shifted by a value of  $2 \times 10^6$  each for clarity reasons. (b) Thermogravimetric analysis of species  $\text{MSN-SH}_{in}\text{-CN}_{out}$ ,  $\text{MSN-SH}_{in}\text{-COOH}_{out}$ ,  $\text{MSN-SH}_{in}\text{-PEGd8-NH}_2$  and  $\text{MSN-SH}_{in}\text{-PEGd8-AIPcS}_{2aout}$ . The relative mass losses are given in Appendix, Table 2.

on the MSN surface or on the  $\text{AIPcS}_{2a}$ , results in an increase of the effective particle size (red circles and blue inverse triangles in Figure 6.3 b, respectively). In contrast, the presence of PEG molecules on the MSN surface as well as the presence of the SLB results in a decrease of the effective particle size (green triangles and cyan diamonds in Figure 6.3 b). In both cases, the origin of the size decrease can be attributed to the weaker interactions between the particles caused by steric or

## 6 Targeted drug delivery with red light photoactivated mesoporous silica nanoparticles

electrostatic stabilization. The accessible pore size as obtained by nitrogen sorption measurements is barely affected by the various surface modifications, as expected for particles that feature true core-shell spatially distributed functionalities (Figure 6.3 c and cf. appendix for details). The permeability of the SLB and the opening of the SLB by photoactivation were examined *in situ* with a cuvette, containing a semipermeable membrane (for details see appendix). Figure 6.5 shows the release of cargo, either calcein (blue triangles) or a rhodamine derivative (RD) (black squares), from the MSN-PS-SLB (DOPC/DOTAP-SLB@MSN-CARGO<sub>in</sub>-PEGd8-AIPcS<sub>2aout</sub>). The amount

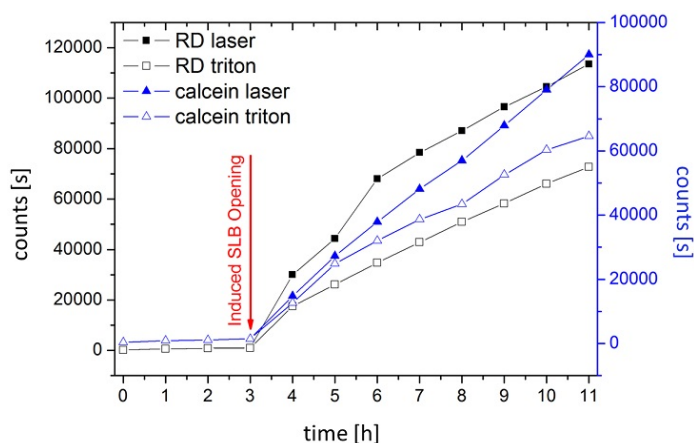


**Figure 6.5:** Release kinetics of calcein (solid blue triangle) and a rhodamine derivative (RD, solid black squares) before and after photoactivation at 3 h with light of  $\lambda = 639$  nm and  $0.55$  mW/mm<sup>2</sup> for 1 min of MSN-PS-SLB measured *in situ*. Only after photoactivation a significant amount of cargo is released, demonstrating the impermeability of the SLB before. Analogously, the SLB can be opened by addition of triton to the MSN solution after a 3 h time period. For both calcein (open blue triangles) and the RD (open black squares) the release by triton is slower as compared to the opening of the SLB by photoactivation.

of released cargo over a 3 h time period before opening the SLB is minimal, demonstrating the integrity of the SLB. After 3 h in the cuvette the SLB was opened either by photoactivation or triton addition. To open the SLB through photoactivation the MSN-PS-SLB particles were exposed to 639 nm light with a power density of  $0.55$  mW/mm<sup>2</sup> for 1 min, resulting in an activation of the photosensitizer and singlet oxygen production. The singlet oxygen reacts with the double bonds of the DOPC and opens the SLB. This is apparent from the strong increase of fluorescence starting after 3 h, originating from the release of the cargo from the MSN core (solid symbols in Figure 6.5). Alternatively, the SLB can be opened by triton addition (open symbols in Figure 6.5). A strong increase of fluorescence for calcein (open blue triangles) and RD (open black squares) is apparent. However, the SLB opening via photoactivation seems to be more efficient, judging from the release rate of the cargos after induced SLB opening. Besides the prevention of premature release of the cargo from the MSN core, the SLB offers the opportunity to add various targeting ligands to our nanoparticle system. In the following section, we will discuss how our MSN-PS-SLB system can be modified with two different targeting ligands, namely, folic acid (FA) and epidermal growth factor (EGF). The efficient modification of our drug delivery system with various targeting ligands as the

final step in the synthesis allows for tuning of our multifunctional nanoparticles for a wide range of cell types without constructing a completely new system for each cell type.

## 6.2 Targeting *in vitro*

Most cancer cells have specific receptors overexpressed on their surface. These receptors are only present in small concentrations or not at all on the surface of healthy cells. Ideally, a drug delivery system can be easily modified to make it specific for multiple cancer cell types. The system presented above offers this opportunity because the MSN-PS-SLB (DOPC/DOTAP-SLB@MSN-CARGO<sub>in</sub>-PEGd8-AIPcS<sub>2aout</sub>) is only modified at the very end of the synthesis for a specific targeting ligand (TL). The basic building block for adding the targeting ligand to the MSN-PS-SLB (VI) is a DSPE-PEG<sub>2000</sub>-TL conjugate molecule. This building block is inserted into the SLB by incubating the MSN-PS-SLB (DOPC/DOTAP-SLB@MSN-CARGO<sub>in</sub>-PEGd8-AIPcS<sub>2aout</sub>) with DSPE-PEG<sub>2000</sub>-TL at 37°C for 3 h (FA) and 12 h (EGF), respectively (final step in Figure 6.2).

In the studies presented here, we chose FA and EGF as targeting ligands because their receptors are commonly overexpressed on a wide range of cancer cells. [284, 285] FA receptors are overexpressed on various cell lines such as HeLa cells and KB cells, [284] and the EGF receptor is abundant on HuH7 cells, for example. [258] The functionality of the targeting ligands on our nanoparticle system was evaluated by performing competition experiments and by evaluating the MSN-PS-SLB-TL (SLB-TL@MSN-CARGO<sub>in</sub>-PEGd8-AIPcS<sub>2aout</sub>) uptake with live cell confocal fluorescence microscopy. In a competition experiment the MSN-PS-SLB-TL are incubated with cells that were either previously incubated with free targeting ligand or not. Preincubation of cells with free targeting ligand will block the specific receptors on the cell surface. Consequently, uptake of the MSN-PS-SLB-TL should only happen unspecific and therefore is expected to take much longer than receptor-mediated endocytosis.

To evaluate the functionality of the FA ligand, KB cells were used. In the experiments shown in Figure 6.6a the cells were preincubated with FA for 2 h at 37°C before the MSN-PS-SLB-FA particles were added to the cells and incubated for 3 h at 37°C. Recording z-stacks of the cells with a spinning disk confocal fluorescence microscope allows us to indicate MSNs inside or outside the cell. A typical cut through the cell is shown in Figure 6.6. It shows that in KB cells only a few individual particles are present inside the cell (Figure 6.6 a), whereas full stacks emphasize the quasi absence of nanoparticles inside the cell, independent of the chosen focal plane. In contrast, incubation of MSN-PS-SLB-FA with KB cells that were not preincubated with FA before resulted in significant uptake of particles (Figure 6.6 b). The nanoparticles appear in the single representative z-slice as well as in the full stack, through the entire height of the cell. This clearly demonstrates that the particles are taken up by receptor-mediated endocytosis and that unspecific uptake of the particles by KB cells is small after 3 h incubation time (see also in Figure 7 in the appendix). In the case of the EGF ligand, we synthesized the DSPE-PEG<sub>2000</sub>-EGF conjugate as described in the appendix. Similar to the FA experiments, we performed competition experiments with the EGF ligand. Experiments were performed with HuH7 cells, which are known to overexpress the

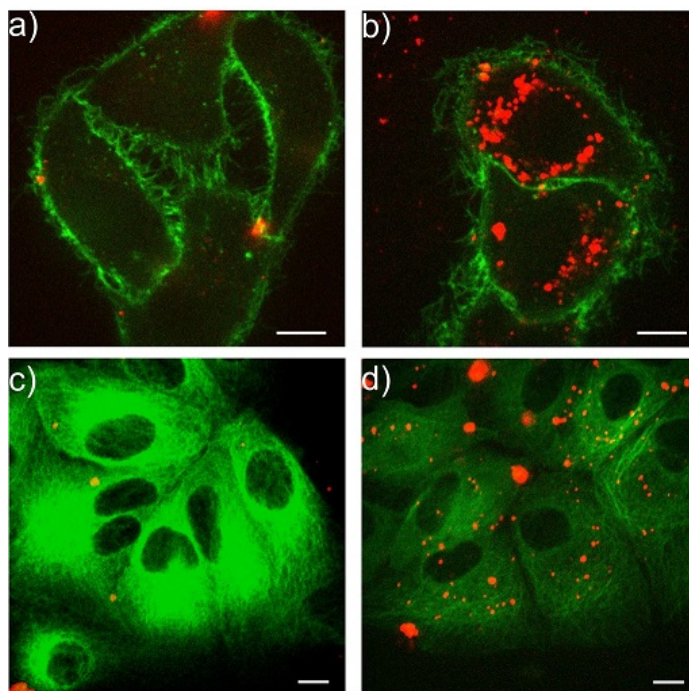


**Figure 6.6:** Unspecific and receptor-mediated endocytosis of MSN-PS-SLB particles with folic acid ligand (MSN-PS-SLB-FA) by KB cells and MSN-PS-SLB particles with EGF ligand (MSN-PS-SLB-EGF) by HuH7 cells with GFP tagged tubulins (HuH7tub), respectively. (a) Incubation of MSN-PS-SLB-FA particles with FA preincubated KB cells for 3 h at 37°C . (b) Incubation of MSN-PS-SLB-FA particles with KB cells, not FA preincubated, for 3 h at 37°C . (c) Internalization of MSN-PS-SLB-EGF particles by HuH7tub with EGF preincubated and (d) non pre-incubated HuH7tub cells. The KB cell membrane is shown in green and the particles in red. For HuH7tub the GFP tagged tubulins are shown in green and the particles in red. Images were taken with live KB cells and HuH7tub cells. The scale bar represents 10  $\mu\text{m}$ .

EGF receptor. [258] Figure 6.6 c shows that in the case of pre-incubation of HuH7 cells with EGF almost no MSN-PS-SLB-EGF particles are endocytosed by the HuH7 cells after 3 h. In contrast, a significant number of the particles is present inside the cells when the cells were not preincubated with EGF (Figure 6.6 d). Again typical slices of the z-stacks are shown in Figure 6.6 c,d (see also Figure 8 in appendix). The above results demonstrate that our MSN-PS-SLB nanoparticles can be modified efficiently to meet the specific requirements of various cancer types and to ensure a specific receptor-mediated uptake. In addition, in the two cell types discussed here the unspecific uptake of the NPs is very small after 3 h. Both are important factors for successful drug delivery vehicles in order to prevent damage of healthy cells by cancer therapeutics. Furthermore, the targeting ligand is introduced after the completion of the synthesis of the actual nanoparticle system. This offers more flexibility to separately synthesize both the nanoparticle system and the DSPE-PEG<sub>2000</sub>-TL because possible incompatible reaction conditions can be avoided. This allows for selecting the synthesis strategies for both components more freely, which is considered a significant advantage for the incorporation of fragile peptides into these systems. Besides the specific uptake of the drug

delivery vehicle by cancer cells, it is of key importance for efficient drug delivery to release the drug into the cytosol, and ideally to do so with spatial and temporal control. In the following, we will show that our system provides the means to achieve this.

### 6.3 Cargo Release by Photoactivation

One of the main challenges for drug delivery with high efficacy is to overcome the endosomal entrapment in order to release the drug into the cytosol. In combination with MSN, three strategies have been pursued so far to solve this issue, namely, employing polycations, [54] fusion or endosomolytic proteins, [51, 99, 278] or photosensitizers. [1, 280, 281] In the case of MSN coated with a polycation, targeting capabilities were shown, but release of cargo was not, and no gating mechanism, to keep the drug enclosed, was presented. [54] The fusion or endosomolytic protein approach is a rather complicated and costly strategy, but it works well as has been demonstrated. [51, 99, 277] However, for both methods an external control of the exact location and time of the cargo release is not possible. A photoactivation approach provides both of these capabilities. In the studies where MSN and photosensitizers were used, the photosensitizer was either loaded as a cargo into MSN [281] or covalently attached to them. [1] The covalent attachment of the photosensitizer is advantageous compared to loading it into the MSN pores. The ratio of MSN to photosensitizer is more easily controlled, the loading capacity of the MSN can be completely used for the drug, and a spatial separation between drug and photosensitizer exists. This could be important considering that the singlet oxygen, produced by photoactivation of the photosensitizer, will most likely damage the drug when not spatially separated from it. In previous work from our group, [1] the photosensitizer had to be excited by blue light, which cannot penetrate the tissue very deeply. [279]

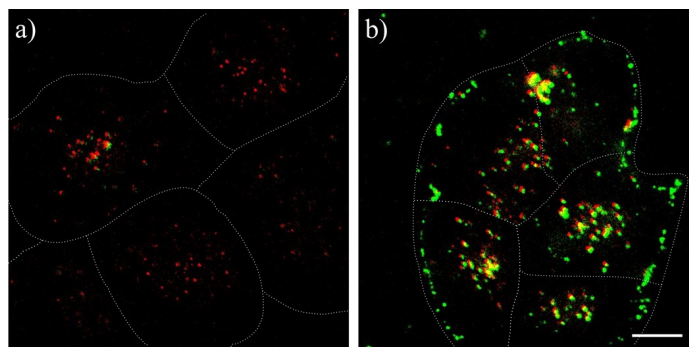


**Figure 6.7:** (a) Uptake of free calcein (green) and free AlPcS<sub>2a</sub> (red) by KB cells after 20 h incubation at 37°C under 5 % CO<sub>2</sub> humidified atmosphere. (b) Uptake of MSN loaded with calcein (green), covalently attached AlPcS<sub>2a</sub> (red) and SLB after 20 h incubation at 37°C under 5 % CO<sub>2</sub> humidified atmosphere. Intensity scale is the same in both images. The fluorescence of calcein and AlPcS<sub>2a</sub> is slightly shifted against each other to show the colocalization clearer. Calcein is only transported into the cell in significant amounts when it is loaded into the MSN. Scale bar represents 10 μm.

Moreover, the attachment of the used photosensitizer to the MSN surface was synthetically more

## 6 Targeted drug delivery with red light photoactivated mesoporous silica nanoparticles

involved. Here we have improved both of these aspects by using a different photosensitizer, namely, AlPcS<sub>2a</sub>. First, it is photoactivatable with red light, and thereby the phototoxicity caused by light activation with blue light is reduced. Additionally, the potential depth of tissue penetration of the activation laser is increased by a factor of about 5. The latter feature will become important if this drug delivery system is tested *in vivo*. Nishiyama *et al.* demonstrated this by using AlPcS<sub>2a</sub> for a transfection of the conjunctival tissue in rat eyes. [280] Finally, AlPcS<sub>2a</sub> can be more easily attached to the MSN surface than the previously used photosensitizer because a sulfonate group can be directly linked to an amino group.

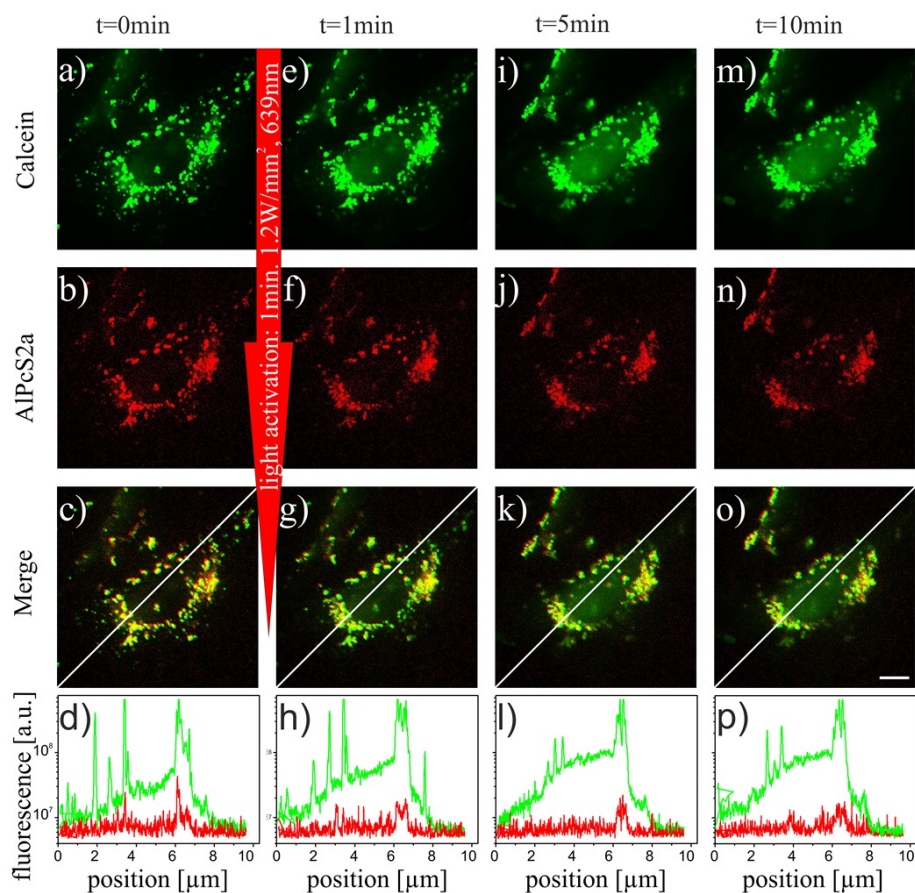


**Figure 6.8:** Fluorescence microscopy of MSN-PS-SLB-FA nanoparticles loaded with calcein inside HeLa cells, after an incubation time of 16 h. (a-c) Calcein (green) and AlPcS<sub>2a</sub> (red) are colocalized (yellow) prior to photoactivation. (d) Intensity profile along the white line in the merged image for both. (e-h) 1 min, (i-l) 5 min, and (m-p) 10 min after photoactivation. The scale bar represents 10  $\mu\text{m}$ .

To verify that the drug delivery mechanism works *in vitro*, we incubated MSN-Calcein-PS-SLB-FA nanoparticles for 3 h with HeLa cells. In comparison to the incubation with free calcein, the incubation of the nanoparticles containing calcein as a cargo produces a significantly higher calcein concentration inside the cell (Figure 6.8 a). The uptake of free calcein by KB cells is negligible

(Figure 6.7). This demonstrates that our drug delivery system can be used to efficiently transport membrane impermeable cargos into the cell. Before photoactivation, calcein and the photosensitizer are colocalized (yellow color in Figure 6.8 c) and exhibit a dot-like pattern, indicating that calcein and the MSN-PS-SLB-FA particles are still inside the endosomes (Figure 6.8 a-c). This demonstrates that the escape from the endosome does not happen automatically and that a mechanism is required to overcome this key challenge in the field of drug delivery.

To induce the opening of the SLB coat around the MSN and the following endosomal escape in a cascaded manner, we activated the integrated photosensitizer AlPcS<sub>2a</sub> with 1.2 W/mm<sup>2</sup> of 639 nm light for 1 min, at similar conditions as those used for the *in situ* experiment in Figure 6.5. As a result, 1 min after activation an increase of the green fluorescence caused by calcein through the entire cell and in particular in the nucleus can be observed (Figure 6.8e/h). In contrast, no change of the red fluorescence pattern originating from the photosensitizer is observed; only a small decrease in fluorescence can be seen due to photobleaching during the photoactivation step. This trend continues over time as is apparent from the images taken at 5 min (Figure 6.8 i-k) and at 10 min (Figure 6.8 m-o) after photoactivation. In the merged image after 1, 5, and 10 min (Figure 6.8 g/k/o), the presence of the green signal becomes dominant, indicative of a lower colocalization between calcein and photosensitizer due to the spreading of calcein in the cell. The green fluorescence is observed in particular inside the cell nucleus. This time-series of images shows that photoactivation can open the SLB and the endosome via an activation cascade, resulting in the release of calcein into the cytosol. While the green fluorescence from calcein is present through the entire cytosol after photoactivation (Figure 6.8 e/i/m), the dot-like pattern of the red fluorescence, caused by the PS on the MSN, does not change (Figure 6.8 f/j/h). This shows that, in contrast to calcein, the MSN does not escape from the endosomes. The reason for this behavior is unknown but has been observed before. [281] However, we note that free PS in endosomes does spread after photoactivation (see Figure 6.9) in

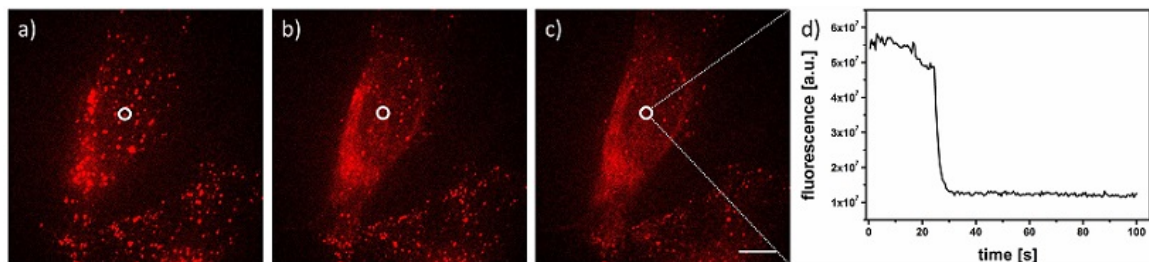


**Figure 6.9:** Uptake of free AlPcS<sub>2a</sub> by HeLa cells after 20 h incubation at 37°C under 5 % CO<sub>2</sub> humidified atmosphere. (a) Before photoactivation (b) 50 s after photoactivation with 1.2 W/mm<sup>2</sup> of 639 nm light (c) 100 s after photoactivation. The spreading of the AlPcS<sub>2a</sub> is apparent. (d) Intensity trace of one endosome marked by white circle in a - c. Scale bar represents 10 μm.

contrast to particle bound PS, and it is therefore not believed that particle bound PS causes much damage to the cell. We also paid particular attention to the fact that there remained no free PS left in the particle solution after the photosensitizer-attachment. Monitoring with Nanodrop UV-VIS spectroscopy revealed, that it takes several washing steps, even after the human eye can not detect

## 6 Targeted drug delivery with red light photoactivated mesoporous silica nanoparticles

any left PS, to remove unbound PS. As can be seen in Figure 6.10a already supernatant 4, i.e. after four washing steps, should be PS-free. But the supernatant is not PS-free before 8 washing cycles (Figure 6.10 b). The destruction of cells through photosensitizers is also discussed in the literature,

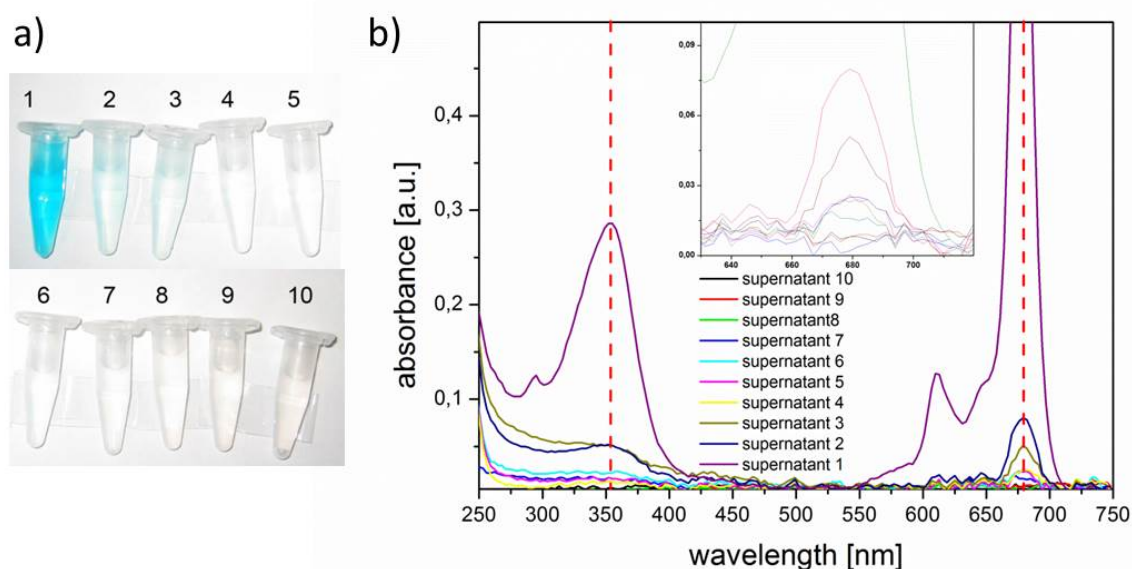


**Figure 6.10:** (a) Supernatants of the washing procedure of the sample  $\text{MSN-SH}_{in}\text{-PEGd8-AIPcS}_{2aout}$ . (b) UV-VIS data taken from the supernatants of the washing procedure of the sample  $\text{MSN-SH}_{in}\text{-PEGd8-AIPcS}_{2aout}$ . No free photosensitizer could be detected in supernatants 8-10.

and if the photosensitizer is not located close to the cell membrane it cannot cause necrosis. [286] The induction of apoptosis is dependent on the cell line, the overall light dose, the localization, the type of photosensitizer, concentration of the photosensitizer, and many more parameters, and therefore it should be subject of continuing intensive studies. However, for the intensities in the range of  $0.12\text{-}1.2\text{ W/mm}^2$ , which were used in this work, the system works without observable damage. Furthermore, the lifetime of singlet oxygen is relatively short (around  $2 \times 10^{-7}\text{ s}$  [287]). We emphasize that the cargo is located in the channels of the MSN, whereas the photosensitizer is clearly separated from the pores via a PEG-linker and located at the outside of the MSN. Consequently the singlet oxygen cannot destroy much of the cargo or of the cell membrane during the activation, as it cannot diffuse inside the pores or too close toward the cell environment in this short time. In addition to calcein, our multifunctional system can be loaded with various cargos. For example, we loaded the MSN core ( $\text{MSN-SH}_{in}\text{-PEGd8-AIPcS}_{2aout}$ ) with a rhodamine derivative (RD). Subsequently, the loaded MSN core ( $\text{MSN-CARGO}_{in}\text{-PEGd8-AIPcS}_{2aout}$ ) was surrounded by an SLB, and FA was inserted into the SLB, resulting in  $\text{MSN-RD-PS-SLB-FA}$  ( $\text{SLB-TL@MSN-CARGO}_{in}\text{-PEGd8-AIPcS}_{2aout}$ ). The nanoparticles were incubated on KB cells for 22 h at  $37^\circ\text{C}$  under a 5 %  $\text{CO}_2$  humidity atmosphere. Similar to calcein, the fluorescence from RD-loaded particles in the cells exhibits a dot-like pattern before photoactivation (Figure 6.11 a). Ten min after the photoactivation, an evenly spread fluorescence in addition to the dot-like pattern is observed (Figure 6.11 b). The

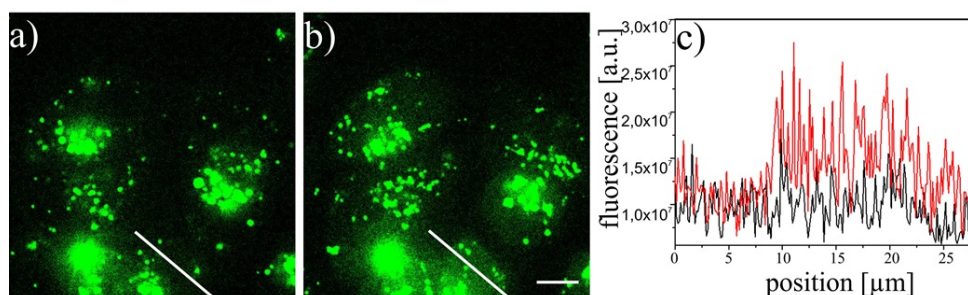


**Figure 6.11:** MSN-PS-SLB-FA nanoparticles loaded with RD (green) inside KB cells. (a) Before and (b) 10 min after photoactivation. (c) Intensity profile along the white line in a and b. Postphotoactivation (red line) a significantly higher fluorescence signal is apparent in the positions 10-20  $\mu\text{m}$  in comparison to pre-photoactivation (black line). The scale bar represents 10  $\mu\text{m}$ .

increase of the evenly spread fluorescence is apparent when measuring the intensity profile in a region that had low fluorescence before photoactivation. Figure 6.11 c shows the fluorescence intensity along the white line in Figure 6.11 a/b. After photoactivation, a strong increase of the fluorescence is observed. Thus, we conclude that 10 min after photoactivation some of the RD has been released from the MSN core and from the endosome as well and subsequently has spread through the cytosol. For both types of cargo the release into the cytosol occurs shortly after photoactivation, emphasizing the precise temporal control that is provided by the photoactivation approach. In addition, before photoactivation no spreading of the cargo is observed; that is, photoactivation is required for the release of cargo into the cytosol. As a result, our system provides a means to spatially control the release of cargo by applying laser light at specific areas, in particular the cancer tissue. This spatial control is available in addition to the ligand-based targeting ability of our particles and should further reduce unintentional exposure of healthy cells to cancer therapeutics. Therefore, the selectivity of drug release should be enhanced in comparison to the cases where only the proton sponge effect or fusogenic/endosomolytic peptides are used.

## 6.4 Summary

In conclusion, we have developed a drug delivery system based on mesoporous silica nanoparticles that addresses some of the key issues in the field of drug delivery. In particular high selectivity and high efficacy is achieved with this system. Furthermore, a combination of the high loading capacity of MSN, the supported lipid bilayer for controlled release, the addition of targeting ligands, and overcoming of endosomal entrapment by photoactivation makes this system a potent drug delivery vehicle. Employing fluorescence microscopy, we were able to demonstrate the selective uptake of our nanoparticles by various cancer cell lines and the release of different cargos *in vitro*. Furthermore, we have demonstrated that the red-light-based photoactivation approach has many advantages compared to other approaches used in the field so far. In particular, by covalently linking

## 6 Targeted drug delivery with red light photoactivated mesoporous silica nanoparticles

the PS to the MSN surface and using a PS that can be excited by red light, negative side effects of the PS can be minimized, and activation of the PS *in vivo* is feasible. Moreover, photoactivation for cargo release enhances the spatial selectivity of where the drug is released as compared to using targeting ligands only. With this new system we have created a platform for drug delivery based on MSN that is flexible regarding the loaded type of drug as well as regarding the employed targeting ligand (implying the desired cell type for drug delivery). We anticipate that the integration of all these strategies into one multifunctional drug delivery vehicle as well as the efficient synthesis and modification of the nanoparticles for multiple cell types will hold promise for wide-ranging applications, especially in cancer therapy.

In the subsequent chapter we will describe a polymeric surface coating, taking advantage of its pH - dependent solubility behavior. Similar aspects as in this chapter, like targeting and overcoming the endosomal entrapment with and without photosensitizer will be discussed.

## 7 Polymer pore closing with pH depending polymer and photoinduced opening mechanism

This project was performed in collaboration with Dr. Stefan Niedermayer, Alexandra Schmidt and Stefan Datz from the group of Prof. Thomas Bein; Annika Herrmann from the group of Prof. Ernst Wagner. The particle synthesis and characterization was mainly performed by Stefan Niedermayer and mice experiments by Annika Herrmann. The Chapter is adapted from and based on the manuscript “Multifunctional Polymer-Capped Mesoporous Silica Nanoparticles for targeted Drug Delivery” which is being prepared for submission.

In the following, a multifunctional drug delivery vehicle that combines the high loading capacity of a mesoporous silica core with the environmental sensitivity of a pH-responsive polymer is described. The system takes advantage of the pH-changes inside tumor tissue and especially during endocytosis to trigger internally the release of loaded cargo. For this purpose a polymer is used that changes its water solubility due to de-/protonation.

Polymers can be attractive for biological applications due to their biocompatibility, tuneable properties and production from sustainable sources. [288, 289] Therefore, polymers are widely used as responsive coatings of surfaces for selective ion-permeability [290], surface patterning [278], and drug delivery with polyplexes [258, 278, 288], hybrid dendrimers [291–293], and other drug-polymer conjugates. [38, 294] Regarding drug-polymer conjugates, which offer relatively small particle sizes and good biocompatibility, possible issues may arise from low loading capacities and potentially poor stability, depending on the strength of the drug-polymer interactions. [295] The drug-polymer interactions need to be optimized for different kinds of drugs to ensure stable drug-polymer conjugates.

Combining the high loading capacity and stability of mesoporous nanoparticles with the biocompatibility and tuneable properties of polymers offers the possibility to create stimuli-responsive and reversible delivery systems. For instance, You *et al.* showed the release behavior of poly(N-isopropylacrylamide) coated mesoporous silica at different temperatures. [118] Drug delivery vehicles based on nanoparticles in a size range of around 100 nm are likely to be taken up by cells via endocytosis. [296] During this process, the endosome is being acidified by the action of proton pumps. [87, 297] Therefore, pH-responsive polymer coatings around mesoporous silica nanoparticles offer the possibility to use the changes in pH during endocytosis as trigger for controlled release. For

## 7 Polymer pore closing with pH depending polymer and photoinduced opening mechanism

instance, attachment of poly(acrylic acid) [298] or poly(2-(diethylamino)ethyl methacrylate) [299] showed the ability of pH-responsive functional polymer coatings around mesoporous silica nanoparticles for release applications. Liu *et al.* reported on different release kinetics from mesoporous silica by the use of poly(4-vinylpyridine) as pH-responsive shell created by multipoint anchoring. [300] Poly(2-vinylpyridine) (PVP) has also been used for the pH-sensitive functionalization of surfaces, due to the pronounced transition between hydrophilicity and hydrophobicity upon protonation and deprotonation. [301]

As shown in Figure 7.1, at low pH, the protonated polymer is in a hydrophilic state and therefore, cargo molecules are able to diffuse into and out of the mesoporous silica nanoparticle. At pH values around 5.5 or higher, deprotonation of the polymer takes place, producing a hydrophobic state followed by a collapse of the polymer onto the silica surface, thus preventing premature release of the cargo. The pH-responsive switching behavior of the polymer introduces a site-specific release mechanism to the delivery vehicle. After endocytic uptake of the particles by a cell, the endosomes are acidified by proton pumps present in the endosomal membrane. [297] The change in pH can automatically lead to a switch of the particle into its open state, and subsequently trigger the release of cargo into the endosomal compartment. A major advantage of this delivery vehicle is the reversibility of the cap system. Once the particles have been exocytosed by the cell, before having released all of their cargo, the cap system will return into the closed state due to the environment ( $\text{pH} > 7$ ) outside of the cell. [297] To maintain colloidal dispersibility, even in the hydrophobic closed state, poly(ethylene glycol) blocks were attached to the ends of the PVP cap system. In this context, the use of  $\alpha$ -,  $\omega$ -bis-functionalized polymers offers the possibility for anchoring any functionality of interest (photosensitizers, targeting ligands) step by step (Figure 7.1).

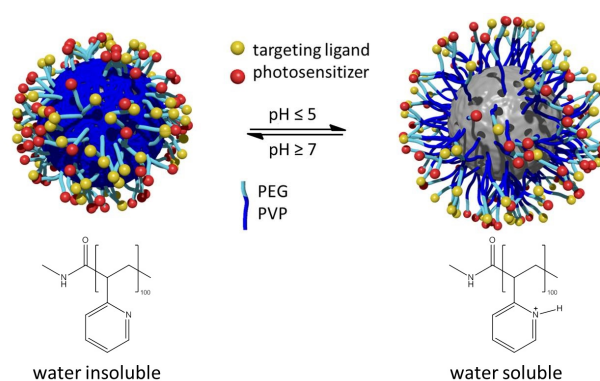


**Figure 7.1:** Concept of the pH-responsive delivery system. The pores can be reversibly opened and closed through changes in the water solubility of the polymer.

## 7.1 Synthesis and Characterization

According to transmission electron microscopy (TEM), the shell functionalized mesoporous silica nanoparticles (synthesis described in the Appendix) show an average particle diameter of 90 nm with a wormlike pore structure (Figure 7.9). The stepwise functionalization with poly(2-vinylpyridine) and PEG was monitored with several methods and is discussed in the following (DLS, zeta potential, TGA, nitrogen adsorption, IR and Raman spectroscopy, Figure 7.2).

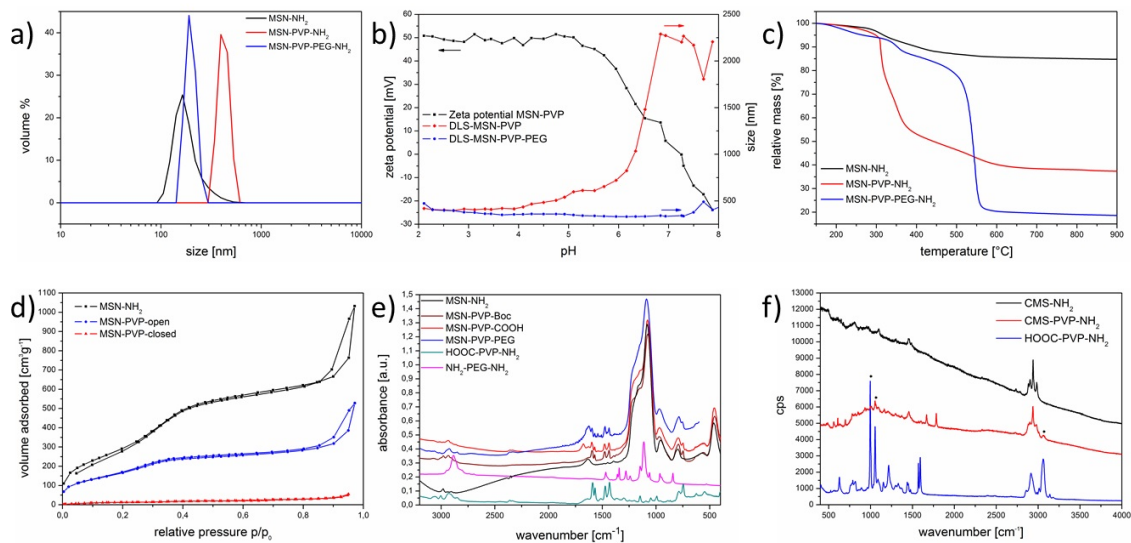


**Figure 7.2:** Different characterization methods of MSN: a) Dynamic light scattering, b) Titration experiments showing the zeta potential of MSN-PVP (black), of MSN-PVP (red) and MSN-PVP-PEG (blue), c) TGA data for MSN-NH<sub>2</sub> (black), MSN-PVP-NH<sub>2</sub> (red) and MSN-PVP-PEG-NH<sub>2</sub> d) Nitrogen sorption and e) IR spectra of MSN-NH<sub>2</sub> (black), MSN-PVP-Boc (brown), MSN-PVP-COOH (red), MSN-PVP-PEG (blue), HOOC-PVP-NH<sub>2</sub> and NH<sub>2</sub>-PEG-NH<sub>2</sub>, f) Raman spectra of MSN-NH<sub>2</sub> (black), MSN-PVP-NH<sub>2</sub> (red) and HOOC-PVP-NH<sub>2</sub> (blue).

DLS measurements revealed the need for PEG as stabilizing agent. The hydrodynamic diameter of shell-functionalized MSN in water was 160 nm (Figure 7.2 a). MSN nanoparticles functionalized with PVP show strong aggregation in aqueous media due to their hydrophobicity at pH 7 indicated by an apparent size increase to 550 nm. However, the attachment of PEG blocks to the end groups of the PVP blocks recovers the colloidal nature of the system (DLS reveals a size of around 200 nm again). Titration experiments are shown in Figure 7.2 b. The high zeta potential (+50 mV) of MSN-PVP at low pH reflects the polymer cap system in its fully protonated and thus open state. At pH = 5.5, close to the  $pK_a$  value of protonated pyridine, deprotonation of the polymer cap system occurs, leading to a significant drop in zeta potential with increasing pH. Together with the zeta potential, DLS measurements were performed simultaneously at the same pH values. For MSN-PVP the particles showed good colloidal dispersability as long as the polymer remained in its protonated state (Figure 7.2 a). Upon deprotonation, the polymer collapses at the particle surface, forming a hydrophobic shell around the particles, which is revealed in the increase in size due to agglomeration.

## 7 Polymer pore closing with pH depending polymer and photoinduced opening mechanism

In contrast attachment of PEG blocks tho the PVP-functionalized particles led to the suppression of aggregation, as no changes in size were observed over the whole pH-range for MSN-PVP-PEG (Figure 7.2).

The functionalization of the mesoporous silica nanoparticles was also monitored with TGA (Figure 7.2 c). While the shell functionalized nanoparticles (MSN-NH<sub>2</sub>) show a relative mass loss of 14.6 % (2.97 mmol per gram silica), the relative mass loss of 61.6 % for MSN-PVP-NH<sub>2</sub> corresponds to 0.14 mmol PVP per gram silica. Only 4.7 % of the amino-groups present at the surface have reacted with the polymer. Based on the mass loss of 80.4 % in the sample MSN-PVP-PEG, the amount of 1.3 mmol PEG per gram silica could be determined. This result shows that additional attachment of PEG to the shell of the MSN must have occurred besides the attachment to the end of the polymer cap system.

In order to show the ability of poly(2-vinylpyridine) to act as a pH responsive cap system, nitrogen sorption measurements were performed (Figure 7.2 d, Table 7.1). To observe the open form (MSN-PVP<sub>open</sub>) the particles where dried from a 0.01 M HCl dispersion at 60°C, this was expected to keep the protonated PVP functionalized MSN in an open state. The closed state could be realized through drying from a dispersion in Millipore water (pH 7). It can be seen that in the open state, the pores are accessible, whereas in the closed state, the polymer completely blocks the pores. The BET surface area of 51 m<sup>2</sup>/g in the closed state is in very good agreement with an estimated external BET surface area of 45 m<sup>2</sup>/g of spheres with similar density and diameter. The BET surface area of 51 m<sup>2</sup>/g for MSN-PVP<sub>closed</sub> corresponds to a reduction in surface area of 95 % compared with MSNs without polymer cap system (MSN-NH<sub>2</sub>), indicating that the surface of the pore walls after blocking is not even accessible for nitrogen.

**Table 7.1:** Summary of nitrogen sorption measurements

Sample	BET surface area [m <sup>2</sup> /g]	NLDFT pore size [nm]	NLDFT pore volume [cm <sup>3</sup> /g]
MSN-NH <sub>2</sub>	1097	3.78	0.79
MSN-PVP <sub>open</sub>	617	3.42	0.36
MSN-PVP <sub>closed</sub>	51	-	-

IR spectroscopy served to follow each step of the synthesis (Figure 7.2e). The signals at 1590 cm<sup>-1</sup> and 1570 cm<sup>-1</sup> correspond to the C=C stretch vibrations of the aromatic pyridine ring and can be found in all spectra after attachment of PVP to MSN. Additionally, in these spectra the C=N stretch vibrations of the aromatic ring can be observed at 1474 cm<sup>-1</sup> and 1430 cm<sup>-1</sup>. After deprotection of MSN-PVP and conversion of the amino group into a carboxy functionality with oxalic acid, a peak at 1677 cm<sup>-1</sup> appears which can be attributed to the asymmetric C=O stretching vibration of MSN-PVP-COOH. This peak vanishes after the addition of poly(ethylene glycol) bisamine, which underlines the successful attachment of PEG. In addition, Raman spectroscopy was used to monitor the attachment of HOOC-PVP-NH<sub>2</sub> (Figure 7.2 f, blue curve) to MSN-NH<sub>2</sub> (Figure 7.2 f, black

curve) resulting in MSN-PVP-NH<sub>2</sub> (Figure 7.2 f, red curve). Bands at 3062 cm<sup>-1</sup> (\*) (C-H stretching vibration of aromatic rings (pyridine)) and 1054 & 995 cm<sup>-1</sup>(\*) (ring stretching vibration of monosubstituted pyridines) are typical for the pyridine groups of poly-2-vinylpyridine. The signals from the polymer appear in the MSN sample after attachment of PVP to MSN and are marked with an asterisk.

## 7.2 Targeting *in vitro*

To design an effective drug delivery system, a targeting system is highly desirable. Generally one can distinguish between passive and active targeting. Modifications such as attaching PEG at the surface of the delivery system provide shielding against undesired interactions, and therefore, favor the enhanced permeability and retention effect (passive targeting). Active targeting, on the other hand, takes advantage of the overexpression of certain receptors on diseased cells by attachment of the corresponding targeting ligand to the delivery vehicle. [302] Accordingly, the biocompatibility and effectiveness of the PEGylated multifunctional MSN was tested further in an *in vivo* setting in mice. Moreover active targeting was shown *in vitro* and *in vivo* using the example of folic acid (FA) receptor targeting on KB-cells.

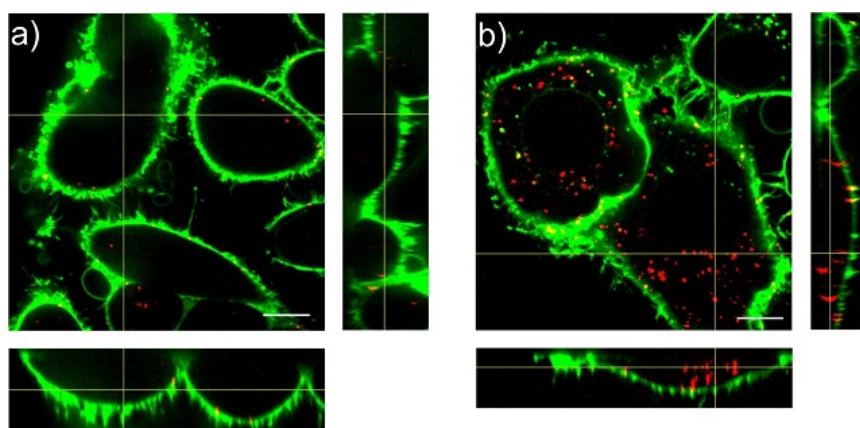


**Figure 7.3:** Unspecific and receptor-mediated uptake of MSN-PVP-PEG-FA particles by KB cells. a) Incubation of MSN-PVP-PEG-NH<sub>2</sub>-FA particles with FA pre-incubated KB cells for 2 h at 37°C. b) Incubation of MSN-PVP-PEG-NH<sub>2</sub>-FA particles with KB cells, no free FA in cell culture medium, for 2 h at 37°C. The KB cell membrane is shown in green (dye WGA488) and the particles in red (dye Atto633). Orthogonal views are given to illustrate the uptake more clearly. The scale bars represent 10 μm.

The attachment of active targeting ligands is important for creating a functional drug delivery system. [302] Folic acid was chosen as targeting ligand because it is an ideal model system for targeting with a small molecule and is also believed to be a promising candidate for clinical applications. [303] Furthermore, the covalent binding of folic acid to the particles can be achieved with an EDC-mediated coupling and could be easily substituted by other targeting ligands without changing the coupling chemistry. To demonstrate the functionality of the particles, they were incubated

## 7 Polymer pore closing with pH depending polymer and photoinduced opening mechanism

with KB-cells, which are known to overexpress FA-receptors. [303] In a competition experiment, with either free folic acid to block the FA-receptors or with uninhibited FA-receptors, the uptake of MSN-PVP-PEG-NH<sub>2</sub>-FA particles and hence the targeting abilities were monitored. For the visualization of nanoparticle-uptake, z-stacks of the cells were recorded with a spinning disk confocal fluorescence microscope, which allows us to detect MSNs inside or outside the cells after staining the cell membrane.

In Figure 7.3, typical confocal cuts through the cells together with the orthogonal projection are shown. In the case of pre-incubation with free folic acid, only a few individual particles are present inside the cells (Figure 7.3 a), and also in the full stacks the quasi-absence of nanoparticles is noted, independent of the chosen focal plane. In contrast, incubation of MSN-PVP-PEG-NH<sub>2</sub>-FA on KB-cells without pre-incubation of FA resulted in significant uptake of particles (Figure 7.3 b). The particles appear in the representative z-slice as well as through the entire height of the cell as shown in the orthogonal views. In the case of blocked receptors, only unspecific uptake is expected to occur, therefore the results demonstrate the specific folate-receptor mediated endocytosis within two hours with only a minor rate of unspecific uptake.

### 7.3 Externally triggered release of membrane impermeable cargo *in vitro*

To verify the release properties of the particle-system several experiments were performed. First, the pH dependency was tested *in vial*, in a cuvette system, at pH 7 and pH 5 (Figure 7.2 b). Second, the particles were tested *in vitro*, for this purpose they were incubated with cells to clarify if the acidification of the endosome is efficient enough to deliver the cargo. For that purpose the MSN were loaded with membrane-permeable and membrane-impermeable cargos and incubated with cells for several hours. Because membrane-impermeable cargos did not show endosomal escape, a photosensitive molecule was introduced to the system in order to trigger the endosomal escape externally. [1, 15]

**In vial.** The pH-responsive opening of the polymer cap system was demonstrated by quantification of released calcein molecules with fluorescence spectroscopy (Figure 7.2 b). All intensity values are normalized to the highest obtained fluorescent counts of the respective sample. Therefore, the highest amount released is set to 100 % relative release. The pH-dependent release curves show the striking capping effect of the poly(2-vinylpyridine) cap system. At pH 7, the polymer is in its hydrophobic state and thus successfully blocks the pores of the MSN until the release is triggered by decreasing the pH. In acidic media, the polymer changes into its water soluble hydrophilic state through protonation, which allows the cargo to diffuse out of the pores. As seen in Figure 7.2 b, no significant changes in release kinetics are observed through further attachment of PEG compared with sample MSN-PVP. The total amount of cargo loaded into the MSN could be calculated to 20.4  $\mu\text{g}$  dye per mg MSN. Long-term release experiments showed that even after 16 h, the premature release is less than 4 % (see Appendix Figure 13).

**In vitro.** The controlled release of cargo inside the desired tissue is one of the greatest challenges

### 7.3 Externally triggered release of membrane impermeable cargo *in vitro*

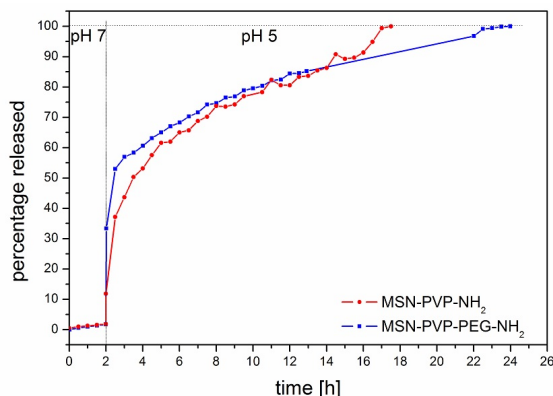


**Figure 7.4:** Release curve for fluorescein out of MSN-PVP-NH<sub>2</sub> and MSN-PVP-PEG-NH<sub>2</sub> with a change in pH after 2h from pH5 to pH7 (normalized fluorescence intensity).

in drug delivery. Many systems have been developed and characterized, including fusion, redox-sensitive systems and photoactivation. [87] Some of these systems exhibit already a good temporal and spatial control of the cargo-release. But once they are activated, the release of the cargo is unstoppable, even if the particles leave the tissue of interest. One advantage of our newly developed system is the reversibility of the pore opening. If the pH of the environment turns neutral again, PVP will close the pores and the delivery system can safely circulate inside the blood system.

**By photoactivation.** In the first experiments, MSN-PVP-PEG particles, loaded with calcein were incubated on HeLa cells for 20 h. The incubation time is long enough to allow the endosomal acidification. [287] However as seen in Figure 7.5, the fluorescence colocalization of the membrane-

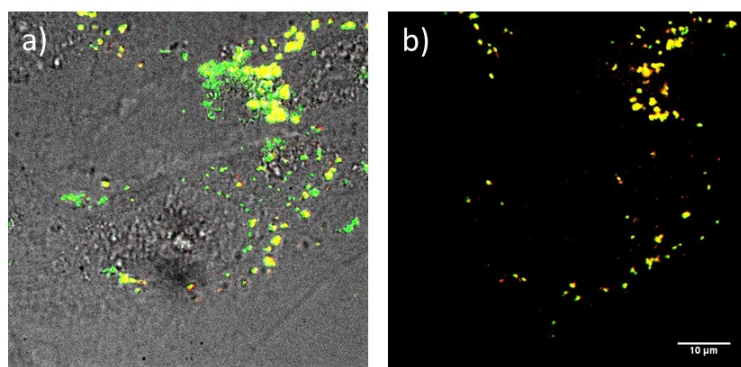


**Figure 7.5:** Fluorescence microscopy of MSN(Atto633)-PVP-PEG (25 μg/mL) nanoparticles loaded with calcein inside HeLa cells after 20 h incubation. a) merge of brightfield image and fluorescence image. b) fluorescence image of calcein (green) and Atto633 (red) are co-localized (yellow), no spreading of calcein can be observed, thus no endosomal escape has occurred. The scale bar represents 10 μm.

impermeable cargo calcein and the covalently bound dye Atto633 remained. Calcein is a membrane impermeable cargo and therefore is not able to exit intact endosomal compartments without external

## 7 Polymer pore closing with pH depending polymer and photoinduced opening mechanism

trigger, but it should be released inside the endosomal compartment. For membrane-impermeable cargos the system had to be further enhanced to induce endosomal escape. Thus the photosensitizer AlPcS<sub>2a</sub> (PS) was covalently linked to the PEG-chains, in addition to the pH-sensitive polymer on the particle surface. Endosomal escape was expected to occur after acidification of the endosomes and activation of the photosensitizer with red laser light. After activation with red laser light (639 nm, 1.2 W/mm<sup>2</sup>) singlet oxygen is produced, which can destroy the endosomal membrane. We emphasize that the lifetime of the singlet oxygen is very short (around  $2 \times 10^{-7}$  s [304]), thus its diffusion range is limited and therefore the cargo and also the cell membrane should stay intact, due to the spatial separation of cargo, cell membrane and PS. Moreover, the red light used for activation of the photosensitizer is in a useful region for medical applications and is already used in photodynamic therapy. [305] For the photoactivated release experiment, MSN-PVP-PEG-

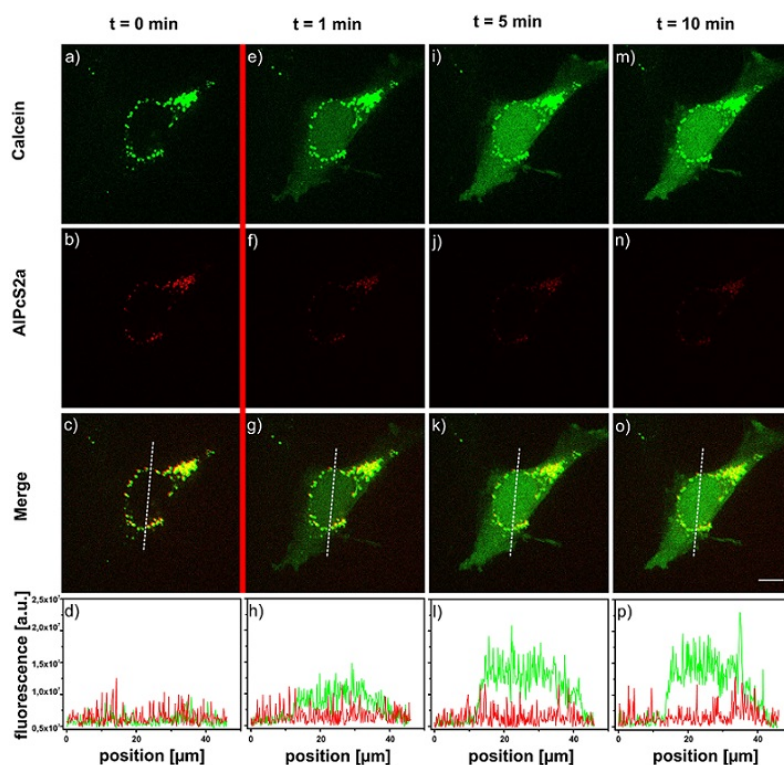


**Figure 7.6:** Fluorescence microscopy of MSN-PVP-PEG-AlPcS<sub>2a</sub>-FA nanoparticles loaded with calcein after 18 h incubation on a HeLa cell. a-c) Calcein (green) and AlPcS<sub>2a</sub> (red) are co-localized (yellow) prior to photoactivation. d) Intensity profile along the white line in the merged image. The red line indicates photoactivation with 1.2 W/mm<sup>2</sup> of red light (639 nm). e-h) after 1 min. photoactivation, i-l) 5 min. after photoactivation, m-p) 10 min. after photoactivation. The scale bar represents 10  $\mu\text{m}$ .

AlPcS<sub>2a</sub>/FA particles were incubated on HeLa cells for 18 h. As seen in Figure 7.6, calcein and PS are co-localized (yellow spots, Figure 7.6). Directly after 1 min photoactivation with 1.2 W/mm<sup>2</sup> of 639 nm light, calcein-spreading over the whole cell can be observed, and the calcein-fluorescence

#### 7.4 Internally triggered release of membrane permeable cargo *in vitro*

gets brighter over time due to de-quenching of the dye upon escape from the MSN host (Figure 7.6 e/i/m). In comparison to the emission from calcein the fluorescence of the photosensitizer stays localized in the same dot-like pattern as prior to the photo-activation, only the intensity is reduced because of photo-bleaching effects after the activation (Figure 7.6 f/j/n). The intensity profile along the white line, indicated in the merged pictures, depicts the fluorescence increase due to calcein more clearly (Figure 7.6 d/h/l/p). The cargo release can also be visualized with a constant PS-activation and simultaneous observation of calcein fluorescence. (over a period of 8 min; Figure Appendix 9). Strikingly, a significant part of the cargo appears to be released inside the cell already within two minutes. The above results were compared to those of incubation experiments of cells with a solution of free calcein and PS. As seen in Figure Appendix 9, the amount of internalized calcein is negligible. We also observe that the free PS is spreading over the whole cell, as already described in Chapter 6.3. If the PS is not covalently bound to an MSN, the molecules can diffuse inside the whole cell and can cause much more damage to the cell membrane and other organelles due to their greater proximity.

### 7.4 Internally triggered release of membrane permeable cargo *in vitro*

To safely deliver membrane-permeable cargos like DAPI [305] or colchicine [306] inside cells with our newly developed system the implementation of additional endosomal escape mechanisms is not necessary. It is anticipated that the particles will be taken up in endosomal compartments, and in the following the endosomes get acidified. This drop in pH from around 7 to approximately 5 results in the solvation of poly(2-vinyl pyridine) and thus in release of the cargo from the pores into the endosome, and consequently into the cytosol if it diffuses through the endosomal membrane. On the other hand, if the particles get exocytosed the pH will increase and poly(2-vinyl pyridine) will turn insoluble again. In this case the cargo will stay inside the particles and the latter can circulate again and possibly find a new target cell. DAPI and colchicine were used as model systems to examine the delivery of membrane permeable cargo. DAPI preferentially stains dsDNA and thereby produces a fluorescence enhancement of around 20-fold. [307] Figure 7.7 shows the staining of the nucleus after several time intervals. Shortly after incubation only a weak staining of the nucleus can be seen, after 15 h the nucleus is clearly visible and after 46 h even the region of the endoplasmic reticulum gets stained. Because of the slowly increasing and very strong DAPI-fluorescence signal after several hours of incubation, it could be excluded that the staining is due to free DAPI in the particle solution. In the case of free DAPI in the solution, the staining would be expected to be detectable shortly after addition, as the typical incubation time for nucleus staining with free DAPI in solution is only between 1-5 minutes. The second cargo colchicine hinders the polymerization of microtubuli as it binds to free tubulin. [306] It is blocking the formation of the mitotic spindle but not the mitosis itself. For this study stable GFP-transfected liver carcinoma cells (HuH7) were used, such that GFP is attached to the tubulin network. In Figure 7.8a a picture of untreated HuH7 cells with GFP tagged on the tubulin network is depicted; one can clearly see the fibrous tubulin

## 7 Polymer pore closing with pH depending polymer and photoinduced opening mechanism

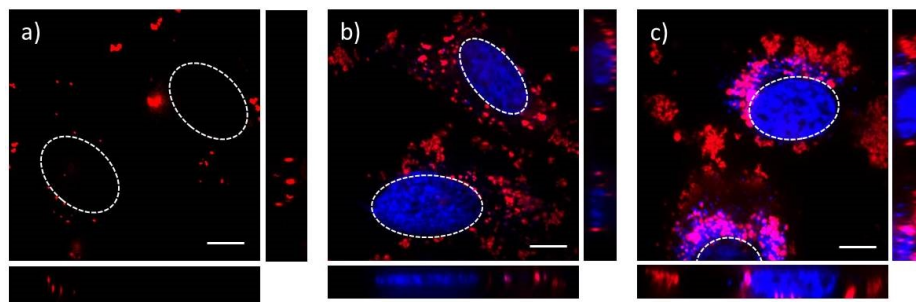


**Figure 7.7:** Fluorescence microscopy of HeLa cells incubated with MSN-PVP-PEG nanoparticles loaded with DAPI (blue) and labeled with Atto633 (red) after a) 15 min b) 15 h and c) 46 h incubation with the cells. The nucleus region is indicated with dashed white lines. The scale bar represents 10  $\mu\text{m}$ .

network. As shown in Figure 7.8 b, MSN-PVP-PEG particles loaded with colchicine were incubated

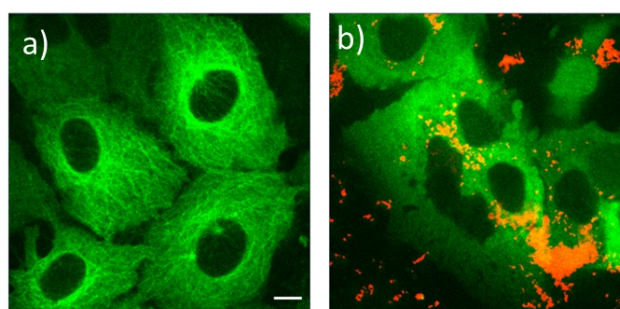


**Figure 7.8:** Fluorescence microscopy of HuH7 cell expressing tubulin GFP (green). a) untreated cells. b) MSN-PVP-PEG nanoparticles loaded with colchicine and labeled with Atto633 (red) after 18 h incubation with the cells. The scale bar represents 10  $\mu\text{m}$ .

for 18 h, and as clearly seen, the fibrous structure has vanished completely, because the formation of the tubulin network is hindered.

## 7.5 Stability

### Stability tests in artificial cell media.

The stability of the MSN was tested i) in bio-fluids and ii) for storage purposes in order to get an idea for the shelf-lifetime. Biostability assays were performed to test whether the polymer cap system will prevent the mesoporous silica nanoparticles from degradation. This was done using Dulbecco's Modified Eagle's Medium (DMEM) at 37°C at two different pH values (5 and 7). As a widely used basal medium for growing many mammalian cells, DMEM contains various amino acids, vitamins and inorganic salts, amongst others and is used here to simulate a biological environment. Samples were removed after specific times, washed and dried. The nanoparticles were then characterized with

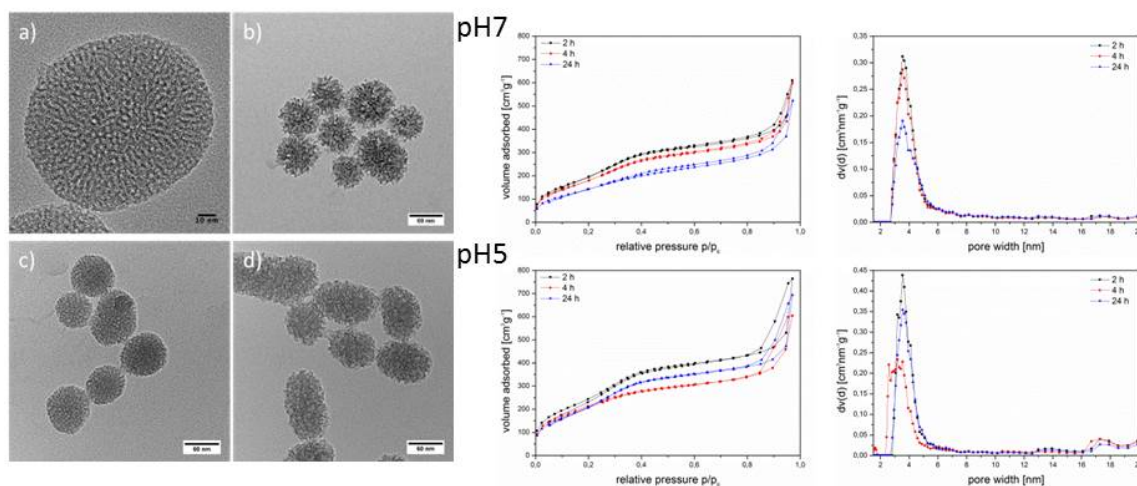


**Figure 7.9:** TEM images showing a) as synthesized MSN-NH<sub>2</sub>, and MSN after 24 h incubation in DMEM media: (b) MSN pH 7, (c) MSN-PVP-PEG pH 7, (d) MSN-PVP-PEG pH 5. Nitrogen sorption isotherms (left) and pore size distributions (right) for different immersion times in DMEM at pH 5.

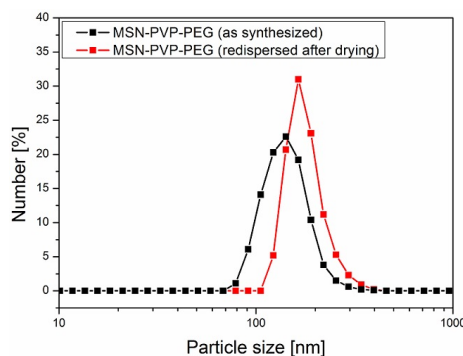


**Figure 7.10:** Dynamic light scattering of MSN-PVP-PEG as synthesized (black curve) and after drying the particles followed by redispersion in water (red curve). There is only a small size increase from around 142 nm to around 164 nm, which is in the range of measuring inaccuracy and demonstrates a good redispersion.

transmission electron microscopy and nitrogen sorption. TEM images show significant degradation of the nanoparticle structure for unfunctionalized MSN after 24 h immersion at pH 7 (Figure 7.9), which is in good agreement with results of similar experiments reported earlier. [38] In contrast, nanoparticles functionalized with PVP offer very good stability in DMEM at pH 7. At this pH, the polymer cap system forms a tight, hydrophobic, and therefore impermeable envelope for water, proteins and salts around the MSN.

Additionally, the polymer shell improves the stability of the MSN in DMEM at pH 5, where the cap system is in its open state. In comparison with uncoated nanoparticles, MSN-PVP particles show less degradation, which was also confirmed by nitrogen sorption experiments (Figure 7.9). In both

## 7 Polymer pore closing with pH depending polymer and photoinduced opening mechanism

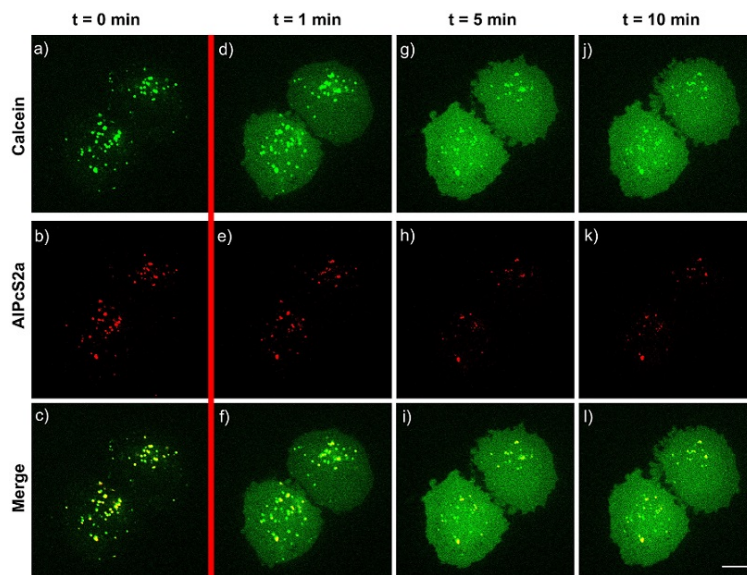


**Figure 7.11:** Fluorescence microscopy of MSN-PVP-PEG-AIPcS<sub>2a</sub>-FA nanoparticles loaded with calcein inside KB cells, particles have been stored three weeks at 4°C. a-c) Calcein (green) and AIPcS<sub>2a</sub> (red) are co-localized (yellow) prior to photoactivation. The red line indicates photoactivation with 1.2 W/mm<sup>2</sup> of red light (639 nm). d-f) after 1 min. photoactivation, h-i) 5 min. after photoactivation, j-l) 10 min. after photoactivation. The scale bar represents 10 μm.

cases, in the open and the closed state of the cap system, no changes in the pore size distribution were observed, indicating that the pores are not affected by the medium. In order to test the stability of the MSN regarding storage possibilities the functionality of 4-week-old particles (stored at 4°C) could be verified with *in vitro* release experiments (Figure 7.11). After storage in water and (therefore in a closed state of the PVP) the particles retain the same calcein release behavior in cells as was already seen in Figure 7.6. Drying and re-dispersion of MSN-PVP-PEG-NH<sub>2</sub> in water exhibits no significant agglomeration of the particles or any other visible change of their solution behaviour (DLS measurements in Figure 7.10). According to the redispersibility of the nanoparticles after drying a long shelf lifetime of the nanoparticles can be expected.

Cell experiments also revealed the good stability of the system. Even after storage of the ready-for-use particles for four weeks at 4°C the release behavior stays the same as can be seen in Figure 7.11. This test is in good agreement with the stability tests that are described above. It clearly demonstrates the good shielding of the silica core by the polymer layer.

## 7.6 Experiments *in vivo*

**Biodistribution and biocompatibility upon intravenous injection in mice.** In a next step, the biodistribution of unfunctionalized MSNs and MSNs functionalized with FA and the cap system was evaluated *in vivo*. Cy7-loaded MSNs were injected in mice (n=3) via the tail vein. Near infrared

fluorescence imaging revealed short circulation times for both particle types. Preferred accumulation in the liver was observed for several days (Figure 7.12). Importantly, both particle types were well tolerated by the mice. To rule out toxic effects of the Cy7-loaded MSN clinical chemistry parameters

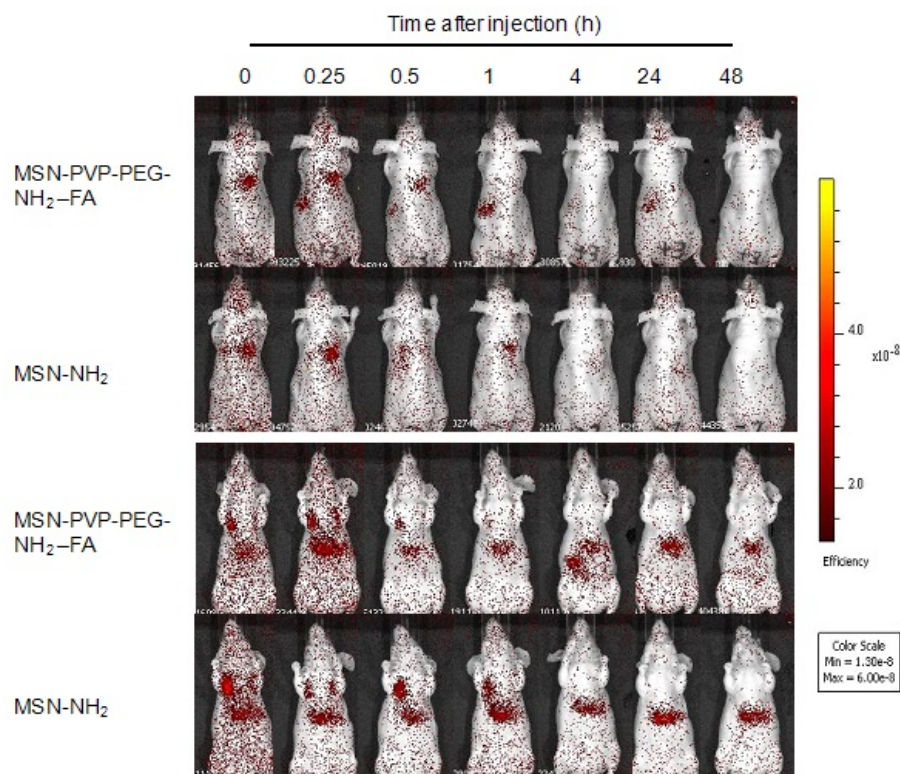


**Figure 7.12:** Intravenous administration of MSN in mice examined through near infrared fluorescence imaging. Time dependent distribution of 100  $\mu\text{g}$  per animal Cy7-loaded MSN-PVP-PEG-NH<sub>2</sub>-FA or unfunctionalized MSN (MSN-NH<sub>2</sub>) over 48 h. Upper panel: ventral position. Lower panel: dorsal position. Experiments were performed in triplicates; a representative mouse of each group is shown.

were investigated. Serum parameters of 3 mice per group are shown in Figure 7.2. Treatment with functionalized and unfunctionalized particles showed no deviations from the alanine transaminase (ALT) and aspartate transaminase (AST) levels compared to the control group treated with pure HBG indicating intact liver function. Besides, serum creatinine levels and blood urea nitrogen (BUN) were also unaffected, confirming that kidney function was not compromised by the treatment. Additionally, histopathological examinations of liver, lung, spleen and kidney were carried out and there were no histological disturbances for both particle types compared to the HBG treated group (Figure 7.13).

**Prolonged retention in (subcutaneous) tumors of mice.** In first experiments we tested targeting to a MDA-MB-231-tumor model in mice after systemic application. The tumor231 is known to overexpress FA-acid receptors as was already shown in literature. [308, 309] In this experiment tissue sections of the tumor, liver, spleen, lung and kidney were imaged with confocal microscopy to

## 7 Polymer pore closing with pH depending polymer and photoinduced opening mechanism

**Table 7.2:** Clinical chemistry parameters of mice 48 h after treatment with HBG (control), MSN-PVP-PEG-NH<sub>2</sub>-FA or unfunctionalized MSN. Values shown: alanine transaminase (ALT); aspartate transaminase (AST); creatinine; blood urea nitrogen (BUN).

Treatment group	ALT (U/I) ± SD	AST (U/l) ± SD	Creatinine (mg/dl) ± SD	BUN (mg/dl) ± SD
control	33.9 ± 12.9	54.7 ± 14.1	0.3 ± 0.0	47.3 ± 8.5
MSN-PVP-PEG-NH <sub>2</sub> -FA	43.2 ± 13.6	59.2 ± 12.1	0.3 ± 0.0	43.9 ± 6.7
MSN-NH <sub>2</sub>	32.5 ± 2.5	51.9 ± 2.1	0.3 ± 0.0	47.4 ± 6.5

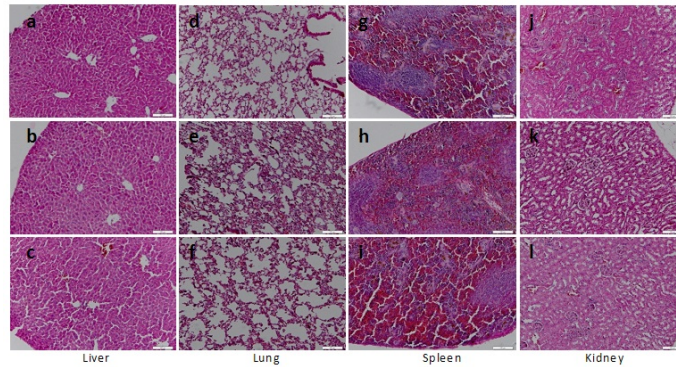


**Figure 7.13:** 48 h after treatment with HBG (control), MSN-PVP-PEG-NH<sub>2</sub>-FA or unfunctionalized MSN the organs were dissected and fixed in formalin, embedded into paraffin and stained with eosin and hematoxylin. Images were taken on an Olympus BX41 microscope. Histopathological sections of: a) liver of the control (HBG), b) animals treated with functionalized MSN and c) treated with unfunctionalized MSN; d) lung after treatment with HBG, e) functionalized MSN or f) unfunctionalized MSN; g) spleen after treatment with HBG, h) functionalized MSN or i) unfunctionalized MSN; j) kidney after treatment with HBG, k) functionalized MSN or l) unfunctionalized MSN

evaluate the distribution of MSN after intravenous injection. Additionally the particles were loaded with calcein in order to monitor model-drug release. But the detection of calcein inside the tissue sections was not possible due to auto-fluorescence of the tissue below 600 nm. [310] As can be seen in Figure 7.14 the particles can be found mainly inside the spleen and liver, also in the lung but almost no particles are found in the kidney. MSN-PVP-PEG-NH<sub>2</sub>/MSN-PVP-PEG-FA particles are able to reach the tumor tissue, presumably because of the EPR-effect. If also active targeting takes place is hard to distinguish out of the performed experiments, as the uptake of the particles into the cells is not clearly evaluable.

For a clear result studies with therapeutic loading have to be performed. Then the effect of therapeutic loaded particles can be compared to unloaded particles and to free therapeutics. If the targeting works the therapeutics loaded particles should give the best results.

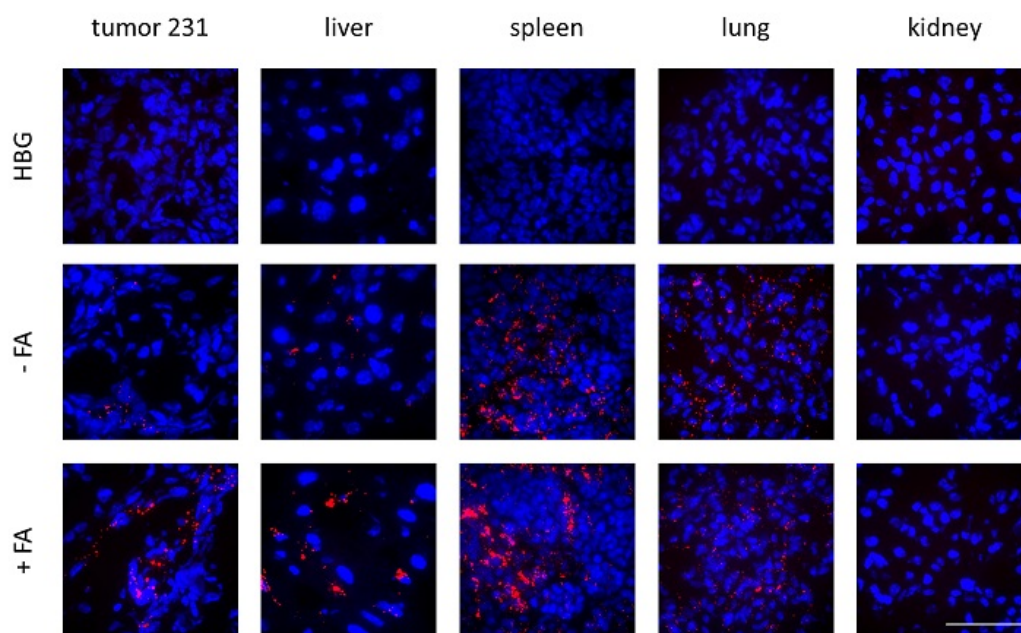


**Figure 7.14:** Systemic administration of MSN in MDA-MB-231-tumor (tumor231) bearing mice. The cell nuclei are stained with DAPI (blue), MSN-PVP-PEG-NH<sub>2</sub> are labeled with Atto633 (red). 3 mice per group, one representative mouse of each group is shown. The mice were injected with HBG as control (upper panel), MSN-PVP-PEG-NH<sub>2</sub> (middle) and with MSN-PVP-PEG-FA (lower panel). Accumulation inside spleen and liver can be clearly detected, also inside the lung, but almost no particles can be found in the kidney. The scale bar represents 50 $\mu$ m.

## 7.7 Summary

In this work, we have developed a multifunctional drug delivery vehicle based on polymer-functionalized mesoporous silica nanoparticles. This system combines attractive features such as the high loading capacity of MSNs with the tunable functionality of a polymer. The use of bis-functionalized polymers blocks allowed us to covalently attach step-by-step many functionalities of interest. We demonstrate that covalently bound poly(2-vinylpyridine) in combination with a PEG-block acts as a pH-responsive cap system for MSN. With this system, we show the successful delivery of different cargos into cells. Membrane permeable cargos were delivered without any external trigger, because such cargos could penetrate the endosomal membrane. Covalent attachment of a red-light-photosensitizer offered the possibility to open the endosome through irradiation with laser light, and to deliver membrane-impermeable cargos. Effective targeting of folic acid receptor expressing cells was enabled by the covalent attachment of folic acid. Stability tests revealed the effectiveness of poly(2-vinylpyridine) not only as cap system, but also as a highly effective protecting agent for MSNs against aggressive body fluids. In addition good storage stability for the dried particles can be expected. Biodistribution experiments *in vivo* revealed no particle agglomeration and showed preferred liver accumulation. The modified and unmodified MSN particles were well tolerated in

## 7 Polymer pore closing with pH depending polymer and photoinduced opening mechanism

mice without causing side effects. First *in vivo* targeting experiments revealed passive targeting of MSN to a tumor mouse model providing a huge range of further investigations on cancer treatment. With this new system we have developed a multifunctional toolbox based on MSNs that is able to open and close its cap system depending on the environment. One major advantage of our system derives from the covalent attachment of all components which allows the system to operate for several cycles. We anticipate that the possible integration of almost any functionality of interest, as well as the efficient synthesis make this system promising for wide-ranging biological and medical applications, especially in cancer therapy.

In the following chapter again the decrease in endosomal pH will be used to achieve endosomal release, but this time the proton-sponge effect will be investigated.

## 8 Dendrimeric shell and disulfide binding of cargo - proton sponge effect

This project was performed in collaboration with Dr. Stephan Mackowiak and Adriano de Andrade Torrano from the group of Prof. Bräuchle, Christian Argyo and Tim Gatzemeier from the group of Prof. Thomas Bein and Claudia Strobel from the group of Prof. Ingrid Hilger. Whereby the Particle Synthesis and Characterization was mainly performed by Christian Argyo, [311] cytotoxicity studies by Claudia Strobel and the quantification of particle uptake by Adriano de Andrade Torrano. The Chapter is adapted from the publication “Investigation of the Endosomal Escape via the Proton Sponge Effect with Dendron-Functionnalized Mesoporous Silica Nanoparticles”, which is in preparation for submission.

In a recent publication, the problem of endosomal entrapment has already been investigated in a joint project of Bräuchle, Bein and coworkers, showing no efficient cytosolic delivery of the cargo cysteine after endocytosis for multifunctional MSNs designed for a redox-driven disulfide cleavage based drug release system. [86] In order to overcome this barrier, photo-induced endosomal release via excitation of co-incubated photosensitizer was employed causing rupture of the endosomal membrane upon singlet oxygen generation. The system was further improved by adding “on-board-photosensitisers” (cf. Chapter 6). Compared to the photoactivation pathway, requiring an external stimulus to induce endosomal escape and the pH-responsive polymer approach presented in Chapter 7, the proton sponge effect is another promising “automatic” strategy to achieve endosomal release of nanocarriers. The proton sponge effect describes an intrinsic osmotic swelling induced by the buffering capacity of the modified nanocarriers, and consequently results in rupture of the endosomal membrane. [89] In detail, after endocytosis of cationic polymers these act like a proton trap preventing a drop in pH. [93] The intracellular trafficking of endosomal vesicles to late endosomes or endolysosomes normally leads to an acidification of the endosomal compartment by proton pumps ( $H^+$ -ATPase) causing a decrease of the internal pH value from 7.4 to 5.5. [90] However, when cationic polymers are present, the overall increased protonation level leads to a continuous inflow of protons coupled simultaneously to a passive influx of chloride anions to maintain electron neutrality within the compartment. Subsequently, an osmotic swelling and rupture of the endosomal membrane is caused by the substantial increase of the ion concentration within the endosome.

Several cationic lipids and polymers [91, 92], such as poly (ethyleneimine) (PEI), with high buffering capacities were examined as potential proton sponges, whereupon poly-(amidoamines) (PAMAM) dendron structures have attracted great interest due to their high amino group content, simple and variable synthesis as well as biomimetic structure. [291, 312–314] Dendrons represent a struc-

## 8 Dendrimeric shell and disulfide binding of cargo - proton sponge effect

tural component of a parent dendrimer structure, which are highly ordered, monodisperse, three-dimensional, tree-like polymers comprising specific size and shape characteristics. [315] Due to their high positive surface charge at physiological pH, PAMAM dendrimers exhibit extraordinary stability forming complexes with DNA. *In vivo* experiments demonstrated that the use of high PAMAM dendrimer generations (G7-10) as transfection agent for DNA is highly efficient. [316, 317] The resulting transfection was explicitly attributed to an activated proton sponge mechanism. Experiments on PAMAM coating of carbon nanotubes further indicate that PAMAM structures are substantially beneficial for cellular uptake and provide a reduction of cytotoxicity compared to uncoated nanotubes. [318] Lin and co-workers investigated a gene transfection nanocarrier system based on MCM-41-type mesoporous silica nanospheres containing covalently attached second generation (G2) PAMAM dendrimers. [319] An intracellular delivery of plasmid-DNA complexed by the PAMAM dendrimers and a fluorescent dye encapsulated in the mesopores could be observed. But as the dye is not covalently bound inside the pores and the plasmid DNA is complexed with the dendrimeric shell, the systems provides only an endosomal escape route, but a controlled release cannot be expected. The stability of the system over multiple hours or even in the blood flow is doubtful.

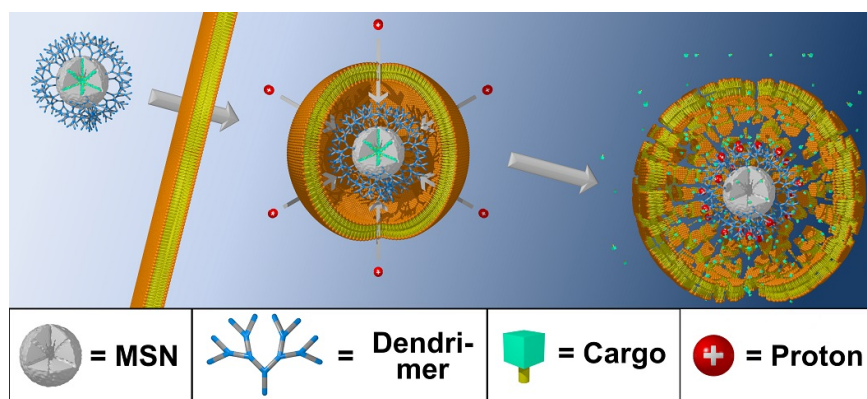


**Figure 8.1:** Schematic illustration of the proposed proton sponge effect. MSN-D3 approach a cell and are uptaken into endosomes. Endosome acidification leads to intrinsic osmotic swelling caused by the buffering capacity of the dendrimer-coated MSN. Finally endosomal rupture takes place and the cargo can be set free in the cytosol (reducing milieu).

In the present work, we established newly designed multifunctional core-shell MSNs coated with poly (amidoamine) (PAMAM) dendron structures on the outer surface, which feature a high buffering capacity acting as a potential trigger for endosomal escape. Covalent binding sites (mercapto groups) exclusively inside the mesopores can form disulfide bridges for immobilization of cargo molecules. Cytotoxicity studies suggest good biocompatibility of this system. Subsequently, this nanocarrier system offers controlled cargo release upon redox-driven cleavage of disulfide bridges when entering the reductive milieu of the cytosol. Additionally, the external PAMAM dendron shell of the nanocarriers offer high buffering capacity to generate a pH-dependent intrinsic endosomal escape mechanism via the proton sponge effect (Figure 8.1). Further attachment of the targeting ligand folate at the outer periphery of the nanocarriers results in specific receptor-mediated cellular uptake.

Our nanocarrier system can be modified at the very last synthesis stage with various ligands for a specific targeting of cancer cells. It is anticipated that the combination of all these important requirements for an efficient drug delivery makes the mesoporous silica nanocarriers a promising platform for specific cancer therapy.

## 8.1 Synthesis and characterization

The synthesis of PAMAM dendron-coated MSNs was carried out in three steps. First, propargyl-PAMAM dendron in the third generations (D3) was obtained by iterative steps of Michael additions and amidations following a previously described procedure. [320] The synthetic route using the reagents methyl acrylate and 1,2-ethylenediamine alternately for a stepwise creation of increasing PAMAM dendron generations is shown in the Appendix, Figure 20.

For a convergent synthesis route to covalently attach the PAMAM dendrons at the external MSN surface, a PAMAM dendron silane precursor was synthesized in a second step. The PAMAM dendron silane was synthesized by performing a Huisgens click reaction to attach azidopropyl trimethoxysilane to the propargyl-PAMAM dendrons. According to a previous report, [321] the azidopropyl trimethoxysilane was synthesized and subsequently reacted with alkyne-PAMAM dendrons to gain triazole-linked PAMAM moieties by using azide-alkyne click chemistry. In a last step, this silane linker was used in a delayed co-condensation approach to create core-shell functionalized MSNs via a sol-gel process, as described previously. [37, 38] Specifically, bifunctional MSNs (MSN-SH<sub>IN</sub>-N<sub>3</sub><sub>OUT</sub>) equipped with dendrons generation 3 on the external surface was prepared via a delayed co-condensation approach. The MSNs consisted of a thiol-functionalized particle core and additionally PAMAM dendrons were present exclusively on the outer particle surface. The nitrogen sorption measurements showed type IV isotherms indicating a mesoporous structure of the nanoparticles with typical inflection points at about 0.3 p/p<sub>0</sub> (Figure 8.2 a). At higher partial pressures (about

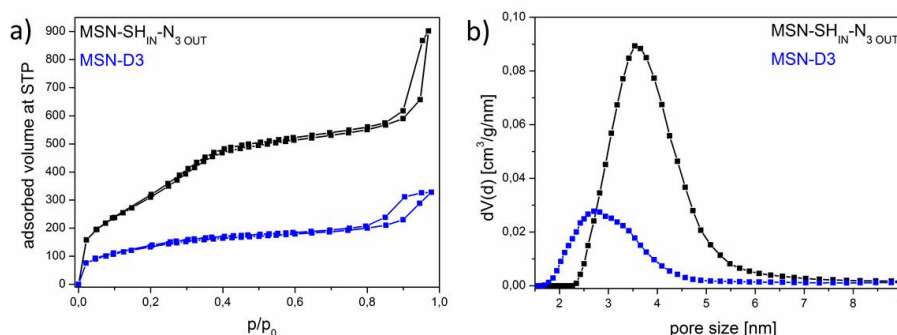


**Figure 8.2:** a) Nitrogen sorption isotherms and b) DFT pore size distribution of functionalized MSNs. MSN-SH<sub>IN</sub>-N<sub>3</sub><sub>OUT</sub> (black), and MSN-D<sub>3</sub> (blue).

0.9 p/p<sub>0</sub>) a second hysteresis loop arose for both samples, which can be related to interparticle textural porosity. For the reference sample MSN-SH<sub>IN</sub>-N<sub>3</sub><sub>OUT</sub> a relatively high BET surface area and

## 8 Dendrimeric shell and disulfide binding of cargo - proton sponge effect

pore volume was observed (data summarized in Table 8.1). The structural parameters of MSN-D3 are significantly reduced compared to MSN-SH<sub>IN</sub>-N<sub>3OUT</sub>. This is attributed to an increasing sample mass due to the non-porous organic polymer. Furthermore, there is the possibility that the large PAMAM dendron caused clogging of some pore entrances at the low measurement temperatures (−196°C) of the nitrogen sorption measurements. The slight decrease in pore size could be related to a partial pore blocking caused by the PAMAM dendron. Also we assume that the mesopores are still accessible for the incorporation of cargo molecules. Transmission electron microscopy im-

**Table 8.1:** Structural parameter of functionalized MSNs.

<sup>a</sup> Pore volume is calculated up to a pore size of 8 nm to remove the contribution of interparticle porosity.

<sup>b</sup> DFT pore size refers to the range of the pore size distribution with sufficient percentage.

Sample	BET surface area (m <sup>2</sup> /g)	Pore volume <sup>a</sup> (m <sup>3</sup> /g)	DFT pore size <sup>b</sup> (nm)
MSN-SH <sub>IN</sub> -N <sub>3OUT</sub>	1190	0.74	2.5 - 5.0
MSN-D3	497	0.24	2.0 - 4.0

ages showed spherically shaped nanoparticles with sizes of about 70 nm in diameter for PAMAM dendron-coated MSNs (Figure 8.3 c, MSN-D3). Furthermore, a worm-like porous structure consisting of radially grown mesoporous channels was present for all samples. Additionally, dynamic light scattering (DLS) measurements were performed to determine obtained particle sizes for the samples and the particle size distribution is shown in Figure 8.3 a. Both samples featured a narrow size distribution with an average particle size of about 122 nm. This indicated good colloidal stability and no tendency for agglomeration in aqueous solution was observed. Zeta potential measurements showed drastic changes in the surface charge of PAMAM dendron-coated MSNs (Figure 8.3 b). At acidic pH values highly positive surface charge was observed for MSN-D3, a zeta potential of about +60 mV at pH 2 was obtained. This sample exhibited high amino group content leading to such a high positively charged particle surface. PAMAM dendron-coated MSNs showed a significant difference of the zeta potential values compared to the reference sample MSN-SH<sub>IN</sub>-N<sub>3OUT</sub>. Here, the isoelectric point (IEP) was close to pH 2, which resulted in a negatively charged particle surface over the full pH range. Furthermore, MSNs functionalized with aminopropyl groups (MSN-SH<sub>IN</sub>-NH<sub>2OUT</sub>) featured only slightly positive surface charge with an IEP of about 4.2. The IEPs for the PAMAM derived particles were significantly shifted to higher pH values (about 6.7). These highly positively charged particle surfaces in acidic milieu gave evidence for a high proton acceptance of the polymer shell resulting in a high buffering capacity.

For a more detailed investigation of the buffering capacity of PAMAM dendron-coated MSNs, both samples were titrated against an aqueous solution of NaOH (0.01 M). As depicted in Figure 8.4, PAMAM derived samples featured a significant increase in required volume of NaOH solution to be neutralized (pH 7). This suggested a high tendency for proton uptake MSN-D<sub>3</sub> indicating a great potential to act like a proton sponge showing optimal buffering behavior in the pH range 5.5 to 6.5 which perfectly fits the endosomal acidification range. In general, a high buffering capacity in the

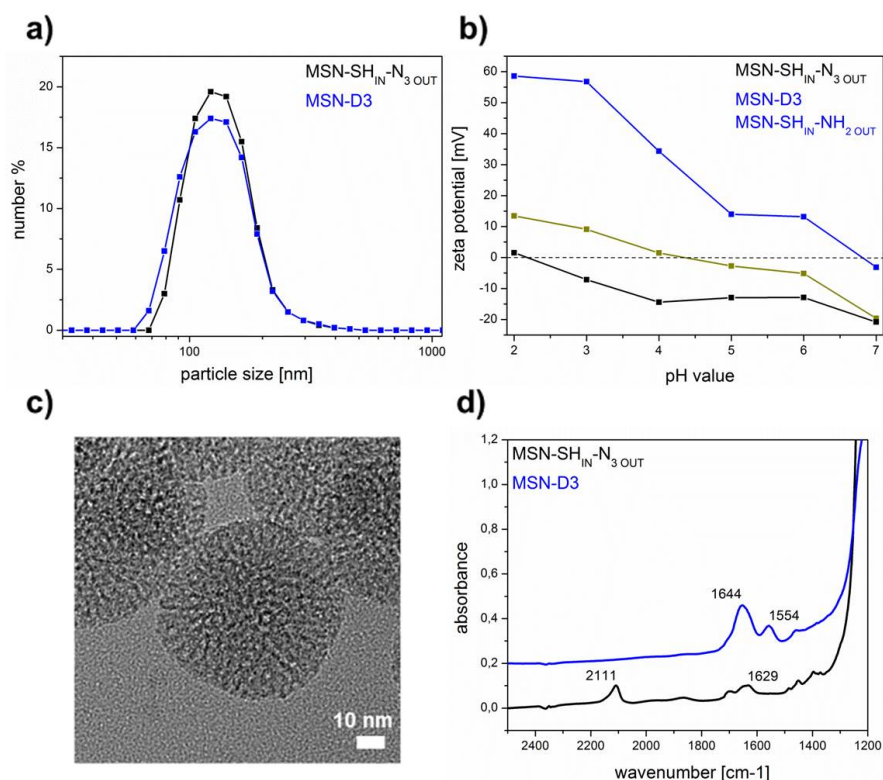


**Figure 8.3:** a) Dynamic light scattering (DLS) measurements, b) Zeta potential measurements, c) Transmission electron micrograph, and d) IR spectroscopy of functionalized MSNs. MSN-SH<sub>IN</sub>-N<sub>3OUT</sub> (black), MSN-D3 (blue), and MSN-SH<sub>IN</sub>-NH<sub>2OUT</sub> (brown). The TEM image belongs to MSN-D3. For clarity reasons, the curves of IR spectroscopy are shifted along the y-axis by 0.2 units.

physiological range (pH 5 - 7) is desirable to enable endosomal release via proton sponge effect. In the literature, titrations of amino-terminal PAMAM generations with 0.1 M HCl gave sharp breaks at pH 3.86 and pH 6.85, respectively.[312] This provided information about the  $pK_a$  values for the tertiary amino groups (pH  $\sim$  5) and for the terminal primary amino groups (pH  $\sim$  9). Conclusively, the tertiary amino groups are significantly less basic than the terminal primary amino groups, which were completely protonated already at pH 7.4. In contrast, the tertiary amino groups were unprotonated at neutral pH values. Acidification (pH  $\sim$  5.5) causes an almost exponential increase of the buffering capacity with the number of PAMAM generations. [322] In consequence, the buffering activity of PAMAM dendrimer or dendron structures in the pH region of interest (pH 7 - 5) is mainly provided by the tertiary amino groups. Elementary analysis provided information about the quantitative organic functionalization degree of modified MSNs. The measured data is shown in Table 8.2 (aminopropyl functionalized MSNs (MSN-SH<sub>IN</sub>-NH<sub>2OUT</sub>) have been used as a reference). The nitrogen content (wt% N) of the samples directly correlates with the amount of PAMAM functionalization, since nitrogen atoms were only present in the PAMAM dendron structures. The measured values for PAMAM dendron coated MSNs were significantly higher compared to the

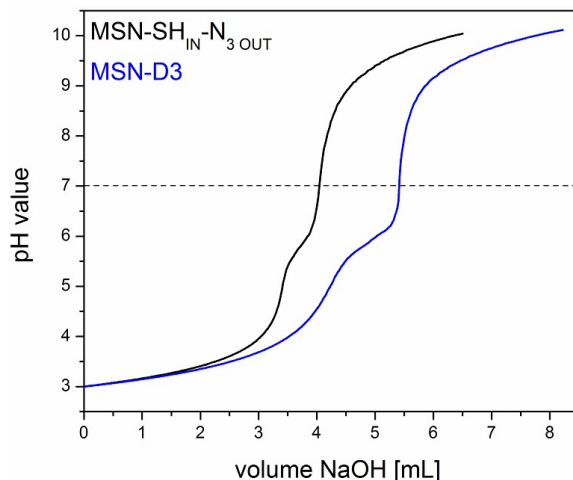


**Figure 8.4:** Titration data of functionalized MSNs. MSN-SH<sub>IN</sub>-N<sub>3OUT</sub> (black) and MSN-D<sub>3</sub> (blue).

reference samples MSN-SH<sub>IN</sub>-N<sub>3OUT</sub> and MSN-SH<sub>IN</sub>-NH<sub>2OUT</sub>. These high nitrogen contents may allow a high protonation level in acidic milieu. In terms of IR spectroscopy, organic functional groups

**Table 8.2:** Elemental analysis data for functionalized MSNs.

Sample	MSN-SH <sub>IN</sub> -N <sub>3OUT</sub>	MSN-D <sub>3</sub>	MSN-SH <sub>IN</sub> -NH <sub>2OUT</sub>
wt% N	0.860	2.47	0.350

were determined (Figure 8.3, for full range IR spectra see also Appendix Figure 3). All samples featured typical bands of the silica framework appearing at 1240 - 1050 cm<sup>-1</sup> (asymmetric stretching vibration of Si-O-Si), and at 964 and 796 cm<sup>-1</sup> (asymmetric bending and stretching vibration of Si-OH). The reference sample MSN-SH<sub>IN</sub>-N<sub>3OUT</sub> showed a characteristic signal at 2111 cm<sup>-1</sup> which was related to the azide vibration mode (asymmetric stretching vibration of -N=N<sup>+</sup>=N<sup>-</sup>). Additionally, a band at 1629 cm<sup>-1</sup> indicated the bending modes of physisorbed water. This band was present in all spectra but was partially covered by other, more intensive bands for the PAMAM dendron-coated particles. The nanoparticles MSN-D<sub>3</sub> showed two additional bands at 1644 cm<sup>-1</sup> (C=O stretching vibration) and 1554 cm<sup>-1</sup> (N-H deformation and C-N stretching vibration), which were attributed to the amide bonds of the PAMAM dendron moieties. An increase in intensity of these signals was observed with increasing PAMAM dendron generations indicating increasing amounts of functional groups within the samples. Further characterization of the attached functional groups was performed by <sup>13</sup>C solid state NMR analysis (Appendix Figure 18). MSN-SH<sub>IN</sub>-N<sub>3OUT</sub> showed distinct signals for the propyl chains of the mercaptopropyl- and azidopropyl- moieties which have been incorporated into the silica framework during the co-condensation approach at 53 ppm (-CH<sub>2</sub>-N<sub>3</sub>), 27 ppm (-CH<sub>2</sub>-SH), 22 ppm (CH<sub>2</sub>-CH<sub>2</sub>-CH<sub>2</sub>-), and 10 ppm (Si-CH<sub>2</sub>-). Additional peaks of high intensity at 58 ppm (O-CH<sub>2</sub>-CH<sub>3</sub>) and 15 ppm (O-CH<sub>2</sub>-CH<sub>3</sub>) were present in all samples and

were related to ethoxy groups resulting from the extraction steps in ethanolic solution. PAMAM dendron functionalized MSNs featured characteristic peaks for the amide groups of the PAMAM dendrons at 173 ppm (C=O). Furthermore, weak signals at 144 ppm and 125 ppm derived from the two carbon atoms in the triazole ring which provided evidence for a successful click reaction of the PAMAM dendron silane precursor. Various strong signals in the range between 60 to 10 ppm corresponded to different types of methylene groups which belong to the PAMAM moieties (52 and 40 ppm (N-CH<sub>2</sub>-R), 21 and 10 ppm (R-CH<sub>2</sub>-R)).

From all these results, we conclude a successful synthesis of core-shell functionalized MSNs with the third generation of PAMAM dendron (D3) via the delayed co-condensation approach. The PAMAM moieties are exclusively located at the external particle surface resulting in an organic polymer coating of MSNs featuring a high buffering capacity. The sample MSN-D3 showed optimal properties and might have a great potential to generate the proton sponge effect. Therefore, we investigated the MSN-D3 particles in the following for cargo release, cytotoxicity, cell uptake and cell targeting experiments.

## 8.2 Release - *in vial*

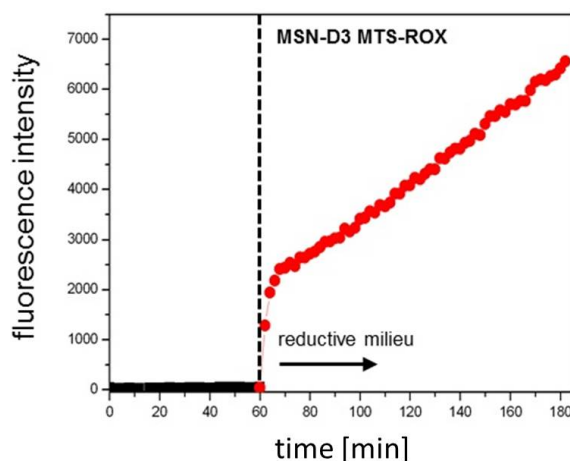


**Figure 8.5:** Redox-responsive release kinetics of 5(6)-carboxy-X-rhodamine (MTS-ROX) before (black) and after (red) addition of dithiothreitol (DTT) to simulate the reductive milieu of the cytosol. Before medium change, MSN-D<sub>3</sub> shows no premature release of the fluorescent cargo molecules, which are attached to the mesopores via disulfide bridges. Only in a reductive milieu a significant increase in fluorescence intensity can be observed, demonstrating a redox-responsive release behavior of the MTS-ROX due to cleavage of the disulfide bridges.

To prove a stimuli-responsive cargo release behavior of the PAMAM dendron-coated MSNs we performed time-based release experiments of the fluorescent model drug 5(6)-carboxy-X-rhodamine (ROX). The thiol-functionalization of the particle core offers the possibility to covalently attach cargo molecules to the internal pore surface via disulfide bridges. In a reductive milieu (simula-

tion of the cytosol), disulfide bridges can be cleaved causing a release of the cargo molecules from the mesopores. [86] A derivative of the fluorescent dye ROX (containing the thiol-reactive group methanethiosulfonate, MTS) was covalently attached to the particle core in a one-step synthesis at mild conditions (1 h, room temperature, dark). The presence of non-bound dye was excluded due to extensive washing steps before the release experiments. A custom-made two-compartment release set-up was used to perform the *in vial* release experiments (Figure 8.5), as previously described. [40] The PAMAM dendron-functionalized MSNs with immobilized MTS-ROX in the mesopores showed no cargo release in aqueous solution under oxidative conditions within the first hour. The cargo molecules were covalently attached via disulfide bridges preventing premature leakage of the dye. Only upon addition of a reducing agent (dithiothreitol, DTT) an increase in fluorescence intensity was shown. This indicated a redox-responsive cleavage of the disulfide bridges and subsequently a specific stimuli-responsive release of the fluorescent model drug occurred. In conclusion, the redox-responsive behavior provides great potential for a specific cargo release once the mesoporous silica nanocarriers have escaped from the endosomes and entered the cytosol of the targeted cell.

### 8.3 Cytotoxicity

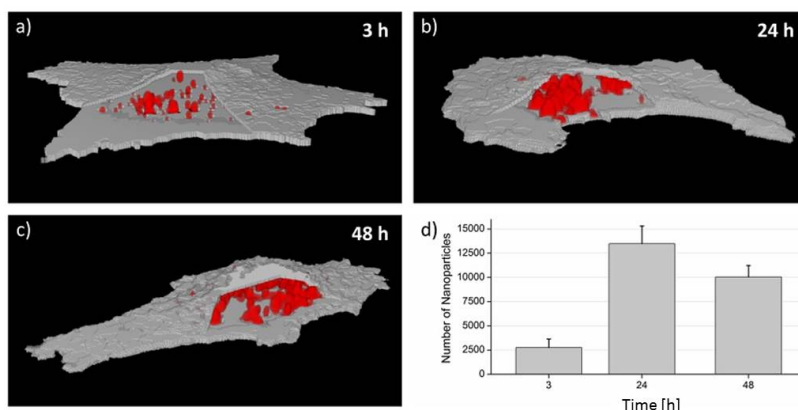


**Figure 8.6:** Cellular uptake kinetics of PAMAM dendron-coated MSNs. Panels (a-c) show representative 3D images of single cells (in gray) and intracellular MSNs (in red) after 3 h, 24 h and 48 h. (d) The absolute number of nanoparticles internalized by single cells increases steeply within the first 24 h and reaches more than 13000 nanoparticles. Remarkably, the number decreases to around 10000 PAMAM dendron-coated MSNs per cell after 48 h. The histogram depicts the mean  $\pm$  standard error of two independent experiments ( $n = 15$ ).

The decision which dendrimer generation we used was partially based on the result of cytotoxicity studies. It was shown, that high generation denrimers (starting with the fourth generation), due to their high cationic charge, exhibit a high toxicity, whereby low generation denrimers are believed to be more biocompatible. [323] In order to elucidate for the first time the toxicity of PAMAM dendrimers in combination with MSN we determined the uptake kinetics and the relative cellular

dehydrogenase activity (rcDH, in order to assess the cell viability) of immortalized human microvascular endothelial cells (HMEC-1), modeling an important cell barrier after intravenous application.

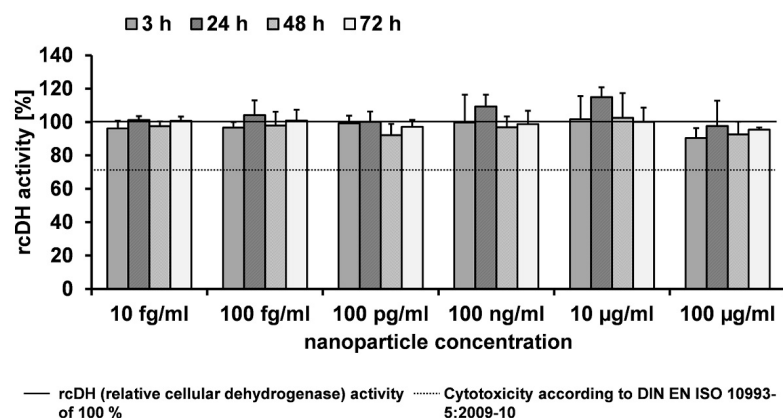


**Figure 8.7:** Relative cellular dehydrogenase activity of human microvascular endothelial cells (HMEC-1) after exposure to PAMAM dendron-coated MSNs. PAMAM dendron-coated MSNs revealed no cytotoxic impact.  $n = 3$  independent experiments.

To gain detailed information about the dose of MSNs effectively internalized by cells at defined incubation times, we investigated the nanoparticle uptake kinetics (Figure 8.6). HMEC-1 were exposed to a concentration of  $100 \mu\text{g/ml}$  PAMAM dendron-coated MSNs for 3 to 48 h and subsequently imaged by live-cell fluorescence microscopy. Confocal stack images of single cells (stained plasma membrane, WGA488) interacting with fluorescent-labeled nanoparticles were acquired and evaluated with Particle\_in\_Cell-3D, a custom-made ImageJ image analysis method [324]. In order to reach an absolute quantification of nanoparticle, the intensity of each object (nanoparticle or agglomerate) is compared to the intensity of a single nanoparticle previously measured in a calibration procedure. Image analysis revealed that around 2500 nanoparticles are inside each cell after just three hours. This number increases and reaches more than 13000 nanoparticles per cell after 24 h. Interestingly, intracellular particles are *diluted* by the natural cell division process [325], and the number decreases to approximately 10000 MSNs after 48 h. This interpretation is in line with the reported doubling time of HMEC-1 cells, 28.6 h [326]. The relative cellular dehydrogenase activity (rcDH) of HMEC-1 cells after exposure to PAMAM dendron-coated MSNs is presented in Figure 8.7. Although the cells were shown to internalize thousands of nanoparticles, PAMAM dendron-coated MSNs revealed no adverse effects over all investigated concentrations ( $10 \text{ fg/ml}$  to  $100 \mu\text{g/ml}$ ) and exposure times (3 to 72 h). For data interpretation the cytotoxic threshold giving by DIN EN ISO 10993-5:2009-10 was used. Therefore, PAMAM dendron-coated MSNs can be considered as highly biocompatible.

## 8.4 Release of different cargos - *in vitro*

We investigated the potential of freshly prepared PAMAM dendron-coated MSNs to achieve endosomal escape via the proton sponge effect by performing *in vitro* cell experiments. Fluorescent live-cell imaging with high-resolution spinning-disk confocal microscopy is a versatile technique to examine the cellular uptake of nanocarriers and the intracellular cargo release. (cf. Chapter 5) For the cell experiments we tried four drug-models, propidium iodide (PI), a rhodamine derivative (ROX), colchicine and DAPI, that all can be chemically modified with the thiol-reactive group methanethiosulfonate (MTS) in order to create disulfid-bridges with the thiol-functionalization of the MSN. Here PI and ROX are not able to cross intact endosomal membranes, Colchicine and DAPI molecules in contrast would be able to diffuse through the cell-membrane in case they are not particle-bound. All four molecules exhibit features that makes them good model cargos for small drugs. Propidium iodide is a positively charged fluorescent dye that binds to nucleic acids and its fluorescence is increased 20-30 fold after intercalation therein. [271] DAPI is just as PI a stain for nucleic acids and usually used to stain the cell nucleus of living/fixed tissues or cells. [262] Both dyes are very useful as they exhibit an enhancement in fluorescence after intercalation into nucleic acids and they can stain a MSN-free region inside the cell (nucleus), which is favorable as in this way also dim fluorescence can be detected without cross-talk from the MSN-label. Rox however could be used to demonstrate the delivery of the cargo inside the whole cytosol, as it isn't supposed to cross an intact cell membrane. It would only spread inside the cytosol after release, and is also good to use in *in vial* experiments, as it doesn't need a binding partner for fluorescence enhancement. Colchicine is a non-fluorescent molecule, used in medicine as treatment against gout, which binds to tubulin subunits and therefore hinders the polymerization of the tubulin-network. [327, 328] As the tubulin network can be easily stained with commercial available kits, it is easy to monitor the delivery of colchicine into the cytosol, as just the structure of the tubulin network has to be monitored. We excluded the possibility of free colchicine or DAPI molecules inside the particle solution (as they would be membrane permeable) with extensive washing steps and always used the last supernatant from the washing procedure to test its freedom of free molecules with cell experiments.

After endocytosis, the loaded nanocarriers need access to the reductive cytosol, which provides efficient redox potential to cause cleavage of the covalent linkage and successful cargo release. Today, due to limited understanding of cellular redox compartmentalization leads to controversial discussion about the redox potential of the endosomal environment in literature continue. [329]

FRET experiments with disulfide-bridged folate-dye conjugates showed a time-dependent reduction of the fluorescence signal after cellular uptake to KB cells suggesting to some extent a reductive milieu in the endosomes. [330] In contrast, Austin *et al.* showed that the pathway of endocytosis for antibody-drug conjugates, containing disulfide bridges, to breast carcinoma cells (SKBr3) provides a oxidizing environment and hence no significant disulfide cleavage could be observed. [331] Since the acidic milieu of lysosomes and late endosomes is not favorable for reducing agents such as glutathione (GSH), endolysosomal content could be mainly degraded by means of thiol reductases. [332] These enzymes are able to cleave disulfide bridges of free drug conjugates, but are too large to access the porous system of MSNs. Therefore, we assume that our nanocarrier system only provides efficient

cargo release only after endosome rupture, when the particles are freely distributed in the cytosol

### Propidium iodid

The first dye we used was propidium iodide, as it was already shown in our groups, that it can be delivered with MSN. [1] The MTS-functionalization was attached over an amino-group. First we

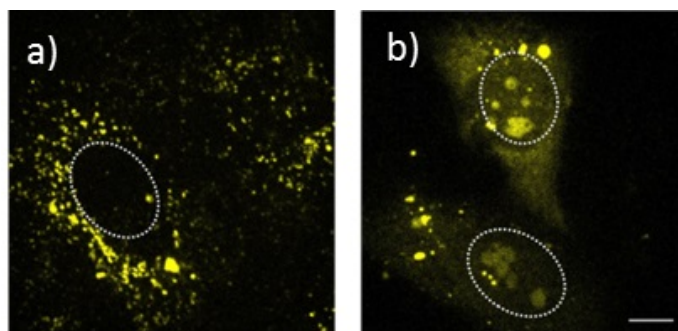


**Figure 8.8:** HeLa cells incubated for (a) 5 h with PI loaded MSN-D3 (same result for 40/72 h), (b) 16 h with pure PI and photoactivated release of PI from endosomes. In case of free PI staining of the nucleoli inside the nucleus (dashed white line) can be observed. The scale bar represents 10  $\mu\text{m}$ .

tested the functionalized propidium iodide, if it is still functional after attachment of the reactive group. For this purpose HeLa cells were incubated with the dye and free photosensitizer AlPcS<sub>2a</sub> for 16 h. The photosensitizer was used in order to provide endosomal escape route as PI can not pass the membrane of living cells. After 26 h the PS was excited as already described (Section 5.3). As can be seen in Figure 8.8 b the nucleoli of HeLa cells are clearly visible and we can presume that the dye is not damaged due to the binding procedure. Nevertheless, the dye-loading of the dendrimer-functionalized particles was not successful. In Figure 8.8 a again HeLa cells are depicted. In this case the cells are incubated for 5 h with PI-loaded MSN-D3. Contrary to the free PI/AlPcS<sub>2a</sub> the cell and nuclei remained unfluorescent and only the MSN can be excited whereas the nucleus remains dark. 40 and 72 h of incubation with PI-loaded MSN-D3 resulted in the same pictures. We assume that due to the positive charges of the dendrimer and the positive charges in the PI only a inefficient drug loading was possible and therefore no drug release could be detected.

### ROX

The next dye we tested was a methanethiosulfonate-functionalized rhodamine derivative (MTS-ROX). After an incubation time of 72 h of KB cells with MTS-ROX loaded MSN-D3 we could only observe a slight cell membrane staining (Figure 8.9 a), in this case we increase the contrast in a way that the particles seem overexposed. As it was possible, that the buffer capacity of MSN-D3 was not big enough to induce endosomal escape we added a second proton sponge inducing agent to the denrimer functionalization over an EDC amidation, polyhistidine (polyHIS). Again after 72 h of incubation a slight membrane staining could be observed (Figure 8.9 b). In Section 6.3 we already

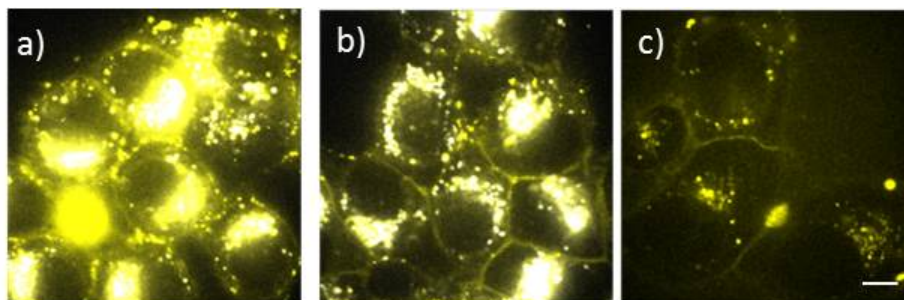


**Figure 8.9:** KB cells incubated for 72 h. (a) with ROX-loaded MSN-D3, (b) with ROX-loaded MSN-D3-polyHIS and (c) with pure ROX. In all three cases a slight staining of the membrane can be observed. The scale bar represents 10  $\mu\text{m}$ .

observed the delivery of a rhodamine derivative into the cytosol after photoactivation. In this case the rhodamine derivative spreaded inside the cytosol, but the membrane was not fluorescently labeled through the released dye. Because of this we also incubated a small amount of free MTS-ROX for 72 h and we could also observe the slight membrane-staining (Figure 8.9 c). It seems, that the release of the dye is very slow and not enough dye could be release in order to detect it over the background of the cell and the bright fluorescence of the MSN, also because of photobleaching.

## Colchicine

We also tested membrane-permeable cargos. Membrane permeable cargos would not need a delivery system to access the cells. But our goal is deliver the drug into a localized compartment and not in every available cell. The membrane-permeable cargos therefore are also attached into the MSN pores over disulfide bonds. It is therefore believed, that it needs first endosomal escape, provoked through the proton sponge effect, and afterward cleavage of the disulfide bond inside the cytosol in order to deliver the cargo. So the membrane permeability of the cargo itself is not believed to influence the experiment.

The intracellular release of the cell membrane-permeable anticancer drug colchicine causes inhibition of the microtubuli polymerization due to irreversible binding to tubulins. [333] The depolymerization of the microtubules, which are basic structural components of the cellular cytoskeleton, is still proceeding ultimately leading to cell death.

MTS-modified colchicine was immobilized at the inner mesoporous surface of the PAMAM dendron-coated silica nanoparticles and subsequently these loaded drug delivery vehicles were incubated with tubulin-GFP-transfected HuH7 cells. In Figure 8.10 a, the fluorescently-labeled microtubule network (green) of untreated HuH7 cells is depicted for comparison. After 9.5 h of incubation the tubulin network in this case is destroyed for MSN-D3 as well as for MSN-D3-polyHIS. A reproduction of this experiment with the same particles (after a storage time of the particles of one week at 4 °C) was not possible. Also experiments with the genetically modified HuH7 tubulin GFP cells were challenging, as they were infected with mycoplasma and after the treatment with antibiotics showed problems

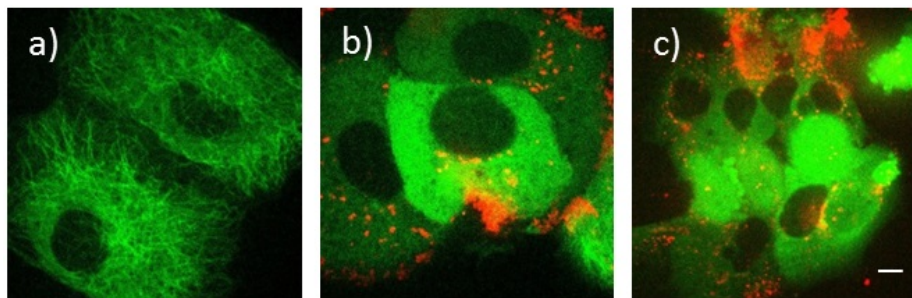


**Figure 8.10:** Fluorescence image of HuH7 tubulin GFP cells. a) untreated cells expressing GFP to the tubuline-network. b-c) HuH7 tubulin GFP cells incubated with MTS-Colchicine loaded MSN for 9.5 h. b) MSN-D3-polyHIS particles on the cells, tubuline network is destroyed. c) MSN-D3 particles on cells, tubulin network is also destroyed. The scale bar represents 10  $\mu\text{m}$ .

with the GFP fluorescence. That's why we changed the cell line finally to KB cells and GFP-stained the tubulin-network with an commercially available transfection reagent. Additionally, as we couldn't detect a difference in polyHIS modified MSN-D3 to unmodified MSN-D3 we exclusively used MSN-D3 for the experiments.

For the following experiments we always used particles not older than one week in order to be sure, that no alteration of the system had taken place. Again the MTS-modified colchicine was immobilized at the inner mesoporous surface of the PAMAM dendron-coated silica nanoparticles and subsequently these loaded drug delivery vehicles were incubated with tubulin-GFP-transfected KB cells. Already after 2 h of particle incubation (MSNs have been additionally labeled with Atto633, red), endocytosis occurred to a high degree (Figure 8.11 b). Importantly, the microtubule network seemed to be still intact, suggesting that no release of colchicine had occurred at this time point. A partial destruction of the microtubule network could be observed, measured after 7 h of incubation (Figure 8.11 c). After 22 h of incubation, cell death finally occurred which was indicated by vanishing of the tubulin structure, blurred green fluorescence signal and a round form of the cells. A delivery of free colchicine was excluded due to reference experiments with the sample supernatant after particle separation by centrifugation showing no effect to the microtubule network for 22 h (Figure 8.12). This destruction of the cytoskeleton due to colchicine has been observed by our groups before. Cauda *et al.* could show an efficient cell death triggered by colchicine after endocytosis of the drug-loaded MSN nanocarriers sealed with a supported lipid bilayer. [39] Despite of the enhanced therapeutic effect compared to free drug molecules, concerns about premature leakage from the lipid bilayer-coated nanocarriers may arise since colchicine features membrane permeability. In the study of Cauda *et al.* [39] colchicine leads to the destruction of the tubulin network after only 2 h of incubation. As the release mechanism in the previous study is believed to be simple diffusion out of the SLB and endosomal membrane, as no controlled release mechanism is included, it is in good agreement that in the present study, with a controlled release mechanism, it takes up to 22 h until the tubulin network is destroyed. Thus, an immobilization of the drug molecules to the internal mesoporous surface via stimuli-responsive cleavable linkers (e.g. disulfide bridges) as done in the

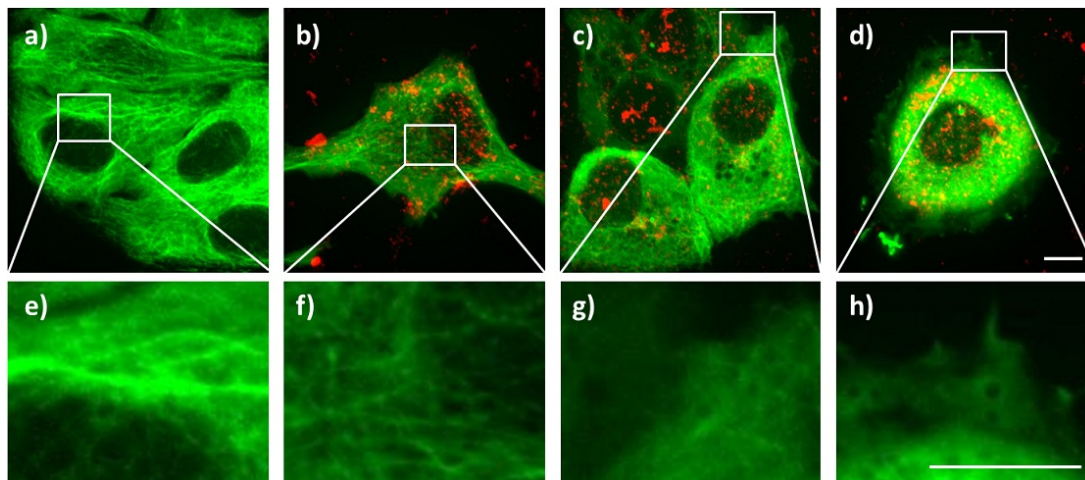


**Figure 8.11:** Fluorescence microscopy of a/e) KB cells with GFP tagged tubulins (green). The cells were incubated with MSN-D3 loaded with immobilized colchicine (MTS-Col) inside the mesopores and labeled with Atto633 (red) for b/f) 2 h, c/g) 7 h and g/h) 22 h. e-h) Zoom in on representative microtubule structures. A time-dependent destruction of the tubulin network can be observed finally causing cell death. The scale bar represents 10  $\mu\text{m}$ .

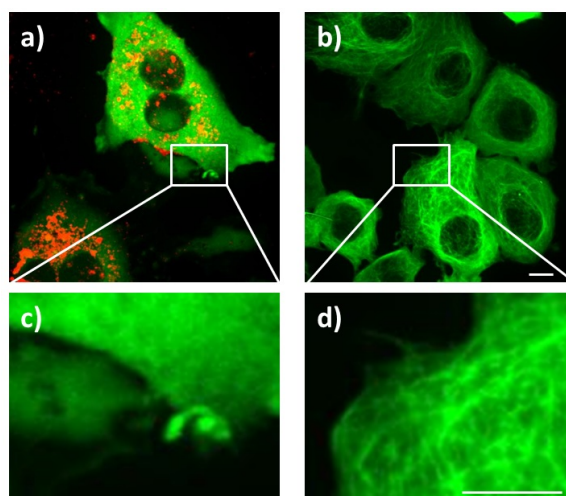


**Figure 8.12:** Fluorescence microscopy of KB cells with GFP tagged tubulins (green). a/c) The cells were incubated with MSN-D3 loaded with covalently attached colchicine (MTS-Col) in the mesopores and labeled with Atto633 (red) after 22 h incubation on the cells. b/d) Cells are incubated with sample supernatant after particle separation by centrifugation for 22 h. c-d) Zoom in on representative microtubule structures. A destruction of the tubulin network can only be observed for particle-incubated cells. The scale bar represents 10  $\mu\text{m}$ .

present work promises further improvement for a spatial-controlled cargo release. Conclusively, the present cell experiments suggest a time-dependent intracellular release of immobilized colchicine from the mesoporous drug delivery vehicles. We anticipate that the acidification of the endosomal

compartment while trafficking initiated the proton sponge effect. The high buffering capacity of the PAMAM dendrons caused high internal osmotic pressure subsequently leading to rupture of the endosomal membrane and access to the cytosol. Reducing agents present in the cytosol were able to cleave the disulfide bridges and colchicine has been efficiently released.

## DAPI

We further investigated the *in vitro* release of 4',6-diamidino-2-phenylindole (DAPI) on HeLa cancer cells. DAPI preferentially stains the nuclei of cells. The intercalation to dsDNA leads to a significantly enhanced fluorescent signal, which can be detected by fluorescence live-cell imaging microscopy (20-fold increase). [240, 334] PAMAM dendron-coated MSNs were immersed in a solution containing in situ synthesized DAPI derivatives with thiol-reactive methanethiosulfonate groups (MSN-D3-MTS-DAPI), which were subsequently covalently attached to the mercapto-functionalized mesopores of the silica nanoparticles. These established covalent disulfide bridges should be cleaved only when the proton sponge effect has achieved endosomal escape and the nanocarriers have reached the reductive milieu of the cytosol. HeLa cells were incubated with MSN-D3-MTS-DAPI for 5, 10

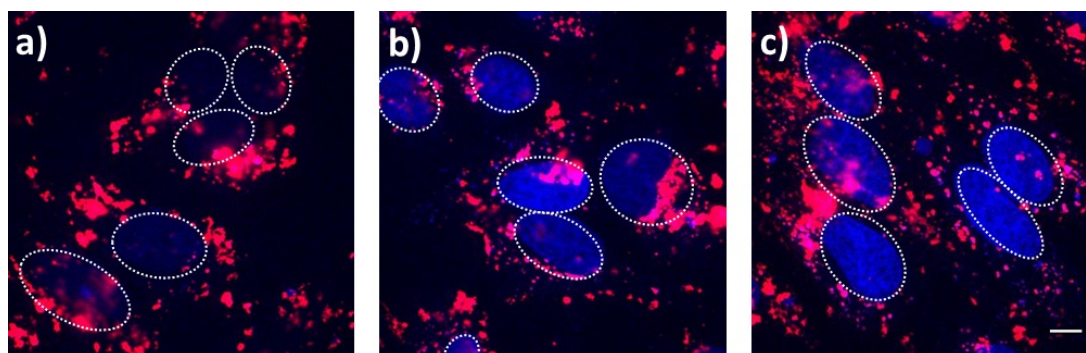


**Figure 8.13:** Fluorescence microscopy of HeLa cells incubated with MSN-D3 nanoparticles loaded with immobilized DAPI (MTS-DAPI, blue) inside the mesopores and labeled with Atto633 (red) after a) 5 h, b) 10 h and c) 22 h incubation on the cells. The nuclei are indicated with dashed circles. Time-dependent nuclei staining can be observed suggesting triggered release of the cargo molecules from the nanocarriers after endosomal escape via the proton sponge effect and excess to the cytosol. The scale bar represents 10  $\mu\text{m}$ .

and 22 h. Figure 8.13 shows an efficient cellular uptake behavior of the nanoparticles labeled with Atto633 (red) already after 5 h. Moreover, only weak staining of the nuclei (blue) has been observed at this time point. In contrast, free DAPI molecules are able to permeate through the cell membrane causing efficient nuclei staining already within a few minutes (1-5 min), as described by standard nucleus staining protocols. [262] Reference experiments with the sample supernatant after particle separation by centrifugation showed only a marginal staining of the nuclei which proves that only a small amount of free dye molecules was present in the particle solution. Therefore, we assume that the DAPI was released from the MSNs upon cleavage of the disulfide anchors. Over the entire time range a successive increase in fluorescence intensity of the DAPI-stained nuclei could be

## 8 Dendrimeric shell and disulfide binding of cargo - proton sponge effect

observed. We attribute this time-dependent release behavior of DAPI to the relatively slow process of the proton sponge effect which was caused by the PAMAM dendron content of our nanocarriers. Consequently, endosomal escape was provided for an efficient cytosolic delivery of the cargo molecules.

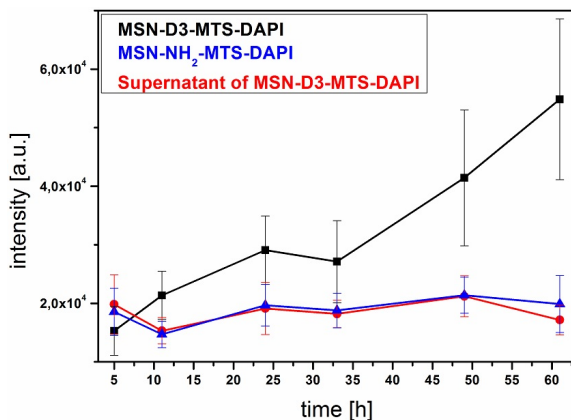


**Figure 8.14:** Nuclei staining kinetics of the DAPI delivery to HeLa cells from MSN-D3-MTS-DAPI (black), MSN-NH<sub>2</sub>-MTS-DAPI (blue), and the supernatant (red) of the MSN-D3-MTS-DAPI solution (after particle separation). The fluorescence intensity of distinct regions of interest (stained nuclei) has been evaluated after different time points of sample incubation. Data represents average fluorescence intensity  $\pm$  standard deviation. A time-dependent increase of fluorescence intensity can be observed for MSN-D3-MTS-DAPI suggesting an efficient DAPI release from the nanocarriers. In contrast, the fluorescence intensity remains constant at a marginal level for the reference samples. This indicates that negligible DAPI release occurred for MSN-NH<sub>2</sub>-MTS-DAPI and almost no free DAPI molecules have been present in the particle solution (supernatant).

For further monitoring of the proton-sponge induced cargo delivery, bare MSNs without dendron functionalization on the external surface have been loaded with DAPI (MSN-NH<sub>2</sub>-MTS-DAPI) for reference experiments. These nanoparticles only exhibit amino groups at the external surface. We monitored their release behavior in comparison to the sample MSN-D3-MTS-DAPI and its solution after particle separation (by centrifugation), denoted as supernatant (for fluorescence microscopy images refer to Appendix 19). HeLa cells have been incubated with the samples for a total time period of 61 h. The fluorescence intensity of DAPI-stained nuclei dependent on the incubation time has been investigated for all three samples (MSN-D3-MTS-DAPI, MSN-NH<sub>2</sub>-MTS-DAPI, and supernatant of MSN-D3-MTS-DAPI). The experimental findings are summarized in Figure 8.14 The nuclei areas have been selected as distinct regions of interest (ROI) and the fluorescence intensity has been evaluated at different time points for all samples. Sample MSN-D3-MTS-DAPI revealed a significant increase in fluorescence intensity over time, as has been discussed before (cf. Figure 8.13). This proves an efficient DAPI delivery to the cells shown by fluorescent nuclei staining. The supernatant of sample MSN-D3-MTS-DAPI exhibited no temporal increase of fluorescence intensity proving that only a small amount of free dye was present in the solution which was already completely incorporated into the nuclei after 5 h (first data point). Conclusively, DAPI needs to be released

from the mesopores of the dendron-coated silica nanoparticles. Importantly, the fluorescence intensity for the reference sample MSN-NH<sub>2</sub>-MTS-DAPI also remained constant at a marginal level comparable to the supernatant of sample MSN-D3-MTS-DAPI. Almost no nuclei staining could be observed for sample MSN-NH<sub>2</sub>-MTS-DAPI indicating that negligible amounts of DAPI have been released from these nanocarriers. This comparison demonstrates that the PAMAM dendron content of our drug delivery vehicles is crucial to achieve successful cargo delivery to cancer cells.

**Table 8.3:** Overview over cargos used for release experiments with MSN-D3.

Cargo	Membrane permeability	Cellular observation	Cell line
PI	non membrane-permeable	no release	HeLa
ROX	non membrane-permeable	membrane staining	KB
Colchicine	membrane-permeable	de-polymerizes tubulin structure	HuH7tub, HuH7, KB
DAPI	membrane-permeable	staining of nuclei	HeLa

Conclusively, these *in vitro* release experiments with different cell lines and different cargo molecules (overview given in Table 8.3) incorporated into the mesoporous system of PAMAM dendron-coated silica nanoparticles suggest an efficient endosomal escape followed by intracellular delivery caused by the proton sponge effect. In contrast to the recent literature we were able to show the time-dependent release of drug-models out of dendrimer-functionalized MSN, whereas other papers mainly show knockdown of certain genes with PAMAM gene-complexes after one defined time-point. [319, 335–337]

## 8.5 Targeting *in vitro*

Another key feature for a capable drug delivery vehicle is specific targeting of the desired tissue, mainly cancer cells. Many cancer cell lines were found to overexpress diverse cell membrane receptors due to increased metabolic activity. In contrast, healthy tissue features only small concentrations of such receptors on the cell membrane surface. A preferential targeting of cancer cells can be achieved by exploiting a receptor-mediated cellular uptake of the nanocarriers. Targeting ligands, such as folic acid, can be attached to the periphery of the PAMAM dendron-coated MSNs. The covalently bound FA moieties interact with the folic acid receptor FR- $\alpha$  resulting in a fast and specific endocytosis. [15, 54] Amino group terminated PAMAM dendrons offer the possibility to covalently attach folate via a short bifunctional PEG-linker. Atto633-labeled MSNs equipped with the folate targeting ligand were incubated for 5+h with KB cells to investigate a receptor-mediated endocytosis. In Figure 8.15 membrane-stained KB cells (WGA488, green) are depicted. Two cellular uptake experiments were performed simultaneously. On the one hand, KB cells were pretreated with free folate to gain full saturation and blocking of the cell receptors before particle incubation. Here, unspecific cell uptake could be observed only to a minor degree (Figure 8.15 b), which is commonly expected to take much longer than receptor-mediated endocytosis. Indication of the particle location

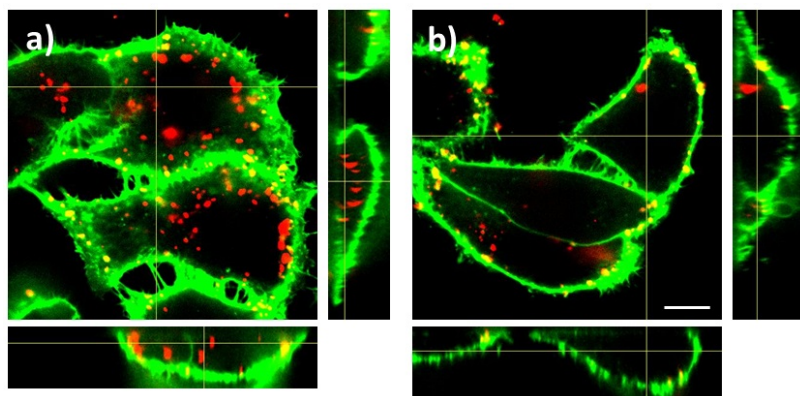


**Figure 8.15:** a) Receptor-mediated and b) unspecific endocytosis of MSN-D3 with targeting ligand folate (MSN-D3-FA, red) by KB cells (membrane staining, green). A specific receptor-mediated cell uptake can be observed for MSN-D3-FA with KB cells (not FA-preincubated) after 5 h incubation at 37°C (a). Incubation of MSN-D3-FA with FA-preincubated KB cells for 5 h at 37°C (b) shows significantly less internalized particles compared to (a). The scale bar represents 10  $\mu\text{m}$ .

(inside or outside the cell) can be received by evaluation of cellular z-stacks with a spinning disk confocal fluorescence microscope. A significantly higher efficiency of particle internalization to the cells occurred for KB cells without pretreatment with free targeting ligands (Figure 8.15 a). Here, the fast cellular uptake is attributed to the receptor-mediated endocytosis of MSNs with folate (MSN-D3-FA) which can also be seen in the orthogonal views.

## 8.6 Summary

In summary, the synthesis of PAMAM dendron-coated MSNs combines advantageous structural parameters such as high loading capacity and tunable functionality with the high tendency of PAMAM dendrons for proton absorption. The novel synthesis strategy, primarily creating PAMAM dendron silane precursors, which have been subsequently used in a delayed co-condensation approach, resulted in core-shell functionalized MSNs containing PAMAM dendron moieties exclusively at the external particle surface. Cytotoxicity tests suggest a very good bio-tolerability, since no adverse effects of the PAMAM dendron-coated MSNs on the cellular dehydrogenase activity of the cells were observed. Remarkably, under comparable experimental conditions, single cells were shown to be overloaded with more than ten thousand intracellular nanoparticles.

We could show that these multifunctional mesoporous silica nanocarriers provide triggered and efficient release of the fluorescent dye DAPI and the anticancer drug colchicine to cancer cells which is achieved by the high buffering capacity of the external PAMAM dendron shell causing the proton sponge effect. Conclusively, our drug delivery vehicles provide an intrinsic endosomal escape pathway for efficient intracellular release of immobilized cargo molecules. This technique prevents endosomal entrapment of nanocarriers and will also provide access for impermeable cargos to the cytosol or other targeted cell compartments. Furthermore, they feature optional attachment

of various cargos inside the mesopores via disulfide bridges and binding of different targeting ligands to the outer periphery of the nanoparticles which can be precisely tuned to target specific cancer cell lines. The multifunctional MSNs are viewed as a general platform for controlled drug delivery in various biomedical applications, in particular for cancer therapy.

In the following chapter another strategy in using the decreasing pH-value inside endosomes is investigated. We use the pH-dependent binding of an enzyme-inhibitor pair for closing the pore entrance of the MSN.



## 9 Enzyme based pH-sensitive cap system for MSNs

This Chapter is based on work in cooperation with: Christian Argyo [311], Michael Gattner, Stefan Datz, Thomas Carell, Thomas Bein, and Christoph Bräuchle. The particle synthesis and characterization was mainly performed by Christian Argyo and Stefan Datz, and carbonic anhydrase functionalization by Michael Gattner. The Chapter is adapted from the manuscript “Carbonic Anhydrase-Based pH-Responsive Cap System for Mesoporous Silica Nanoparticles” which is in preparation for submission.

Beside surface coating and internal pore modification, particle pore gating is another possibility for controlled release mechanism from MSNs. As already described in Chapter 3.2 diverse molecules can be used for particle pore gating. Besides SPIONs, [111, 125] Au-NPs, [112, 126] 18-crown-6 [124] and [2]-pseudorotaxane, [131] biological relevant molecules such as DNA, [110, 120–122] glycoprotein, [123] lysozyme [150] and ATP dependent aptamers, [162–164] provide high potential as bulky gatekeepers.

The idea is to use molecules that are already present in the blood stream or inside cells and therefore offer the opportunity of increased biocompatibility and improved prevention of an immune response. The influence of surface coatings of nanoparticles on the immune response is part of current research. [338] In this Chapter we investigated carbonic anhydrase (CA) as a cleaveable capping structure for MSNs. CA is a ubiquitous enzyme in animals, as it catalyzes the hydration of CO<sub>2</sub>/dehydration of bicarbonate, and is therefore a promising candidate.

The attachment of CA to MSNs was achieved by using benzene sulfonamide (phSA) groups as a functionalization of the external particle surface. Benzene sulfonamide groups are well described in the literature as inhibitors for CA. The binding behavior of phSA to the active site of CA is pH-dependent. [339] With this inhibitor-enzyme system we wanted to obtain a pH-sensitive gatekeeping system. Both, CA and phSA are often used as model systems for biophysical and physical-organic studies of proteins and protein-ligand binding. CA is a monomeric single chain protein of intermediate molecular weight (ca.30 kDa), its inexpensive, the amino acid sequence is known and it provides an excellent stability under laboratory conditions. [339] The inhibitors aryl-sulfonamides can be easily synthesized and possess a high binding affinity to CA (1  $\mu$ M to sub-nM) to the catalytic center. [339] In a pH region  $> 7$  the carbonic anhydrase is reversibly bound to benzenesulfonamide which are covalently attached at the external particle surface and therefore show high potential to block the pore entrances of the MSNs. A decrease in pH causes a cleavage of the coordination bond of the inhibitor to the active site of the enzyme. As the hydrodynamic diameter of CA is about 5.4 nm

## 9 Enzyme based pH-sensitive cap system for MSNs

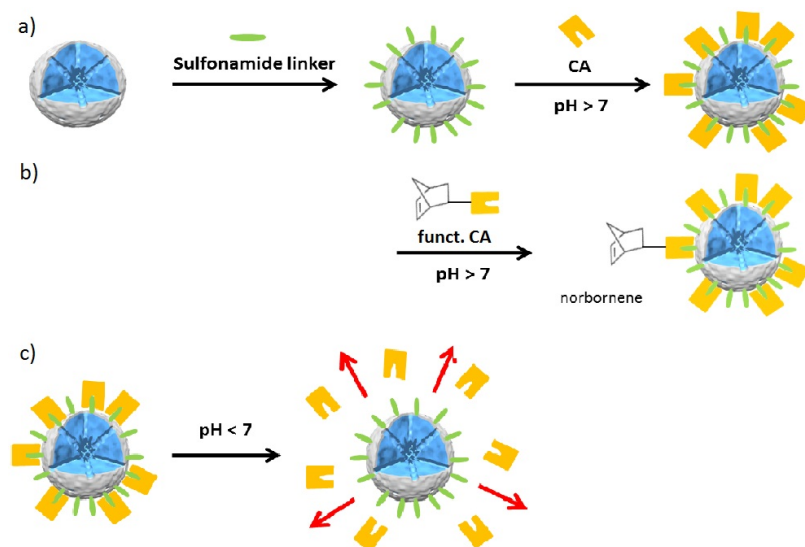


**Figure 9.1:** a) Covalent attachment of sulfonamide groups (green) at the outer MSN surface. In a second step, carbonic anhydrase (CA) enzymes (yellow) bind to the sulfonamide groups at  $\text{pH} > 7$  and consequently block the pore entrances. b) Carbonic anhydrase modified with norbornene binds also to the functionalized MSN surface. c) Decreasing the pH to slightly acidic values ( $\text{pH} < 7$ ) leads to a cleavage of the capping system and incorporated cargo molecules can be released.

and the MSN pores are around 4 nm the gatekeeper is in a suitable size range for closing the MSN pores efficiently.

With this system the incorporated cargo molecules should be concealed inside the MSN pores until the particles reach a region (e.g. late endosomes or lysosomes) with a slightly acidic pH values. Consequently the acidic environment triggers the cleavage of the capping system and the cargo can efficiently be released.

Beside this highly controllable release mechanism, the system can be further improved with targeting ligands, by a specific modification of the carbonic anhydrase. Therefore a unnatural amino-acid (norbornen-lysine) was introduced into the amino acid sequence. [340, 341] With the help of the unnatural amino-acid it is possible to attach one targeting molecule to one carbonic anhydrase. As the unnatural amino acid was placed on the opposite side of the catalytic center, the targeting ligand is presented exactly at the outer periphery of our drug delivery vehicles. The system described in this Chapter represents a novel pH-sensitive capping system additionally providing the possibility to attach targeting ligands at a defined exposed place of the carbonic anhydrase. We anticipate that these multifunctional nanocarriers offer high potential for applications such as controlled drug delivery.

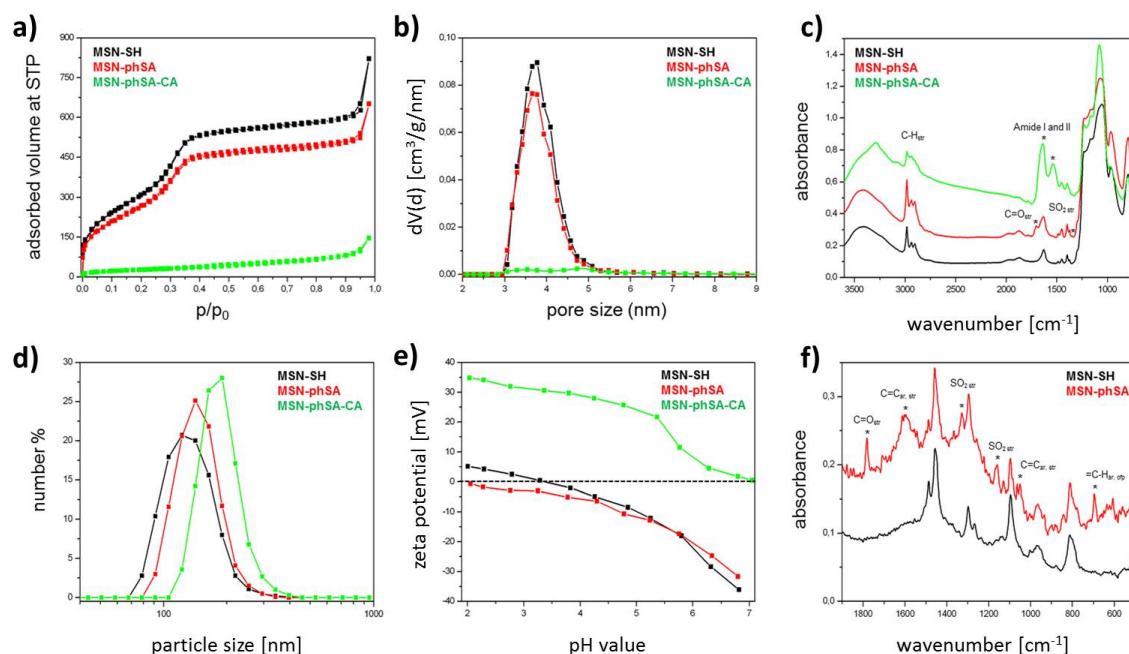


**Figure 9.2:** a) Nitrogen sorption isotherms. b) DFT pore size distributions of functionalized MSNs. c) Infrared (IR) data of functionalized MSNs. MSN-SH (black), MSN-phSA (red), and MSN-phSA-CA (green). For clarity reasons, the curves are shifted along the y-axis by 0.2 units. d) Dynamic light scattering (DLS). e) Zeta potential measurements of functionalized MSNs. f) Raman spectroscopy data of functionalized MSNs. MSN-SH (black), MSN-phSA (red), and MSN-phSA-CA (green). For clarity reasons, the curves are shifted along the y-axis by 0.1 units.

## 9.1 Synthesis and characterization

The synthesis of pH-responsive MSNs consisting of biomolecular valves based on the enzyme carbonic anhydrase (CA) was achieved in a two-step approach. First, MSNs containing thiol-functionality exclusively at the external particle surface were established, following a previously described delayed co-condensation approach. [37] In brief, the silica source tetraethyl orthosilicate (TEOS) and the template cetyltrimethylammonium chloride (CTAC) were mixed at elevated temperatures in an aqueous solution including the base triethanolamine (TEA) which additionally serves as a structure directing agent to form colloidal nanoparticles. A mixture of TEOS and mercaptopropyl triethoxysilane (MPTES) was added at the very last step of the silica framework formation to achieve a very thin external functional shell consisting of thiol groups (MSN-SH). This organic moiety offers the possibility to attach further functionality exclusively on the outer surface of the MSNs and not affecting the porous system. In a second step, benzene sulfonamide (phSA) groups have been covalently attached to the silica nanoparticles via a short bifunctional crosslinker (maleimide-C6-NHS) at mild reaction conditions (MSN-phSA). The particle sizes of functionalized MSNs has been determined with dynamic light scattering (DLS) measurements (Figure 9.2 d). All samples featured narrow

## 9 Enzyme based pH-sensitive cap system for MSNs

particle size distribution implying a good colloidal stability. No agglomeration occurred due to the additional attachment of organic moieties to the particle surface. Samples MSN-SH and MSN-phSA show a maximum for particles sizes at 122 and 142 nm, respectively. For enzyme-coated particles MSN-phSA-CA a slight shift to higher values can be observed (190 nm) due to the additional organic shell based on carbonic anhydrase macromolecules.

Furthermore, the first-order reflection of the mesoporous material observed with small-angle X-ray diffraction (XRD) suggests a non-ordered mesoporous structure (cf. Appendix Figure 21). The surface charge of silica nanoparticles, measured by zeta potential, is changed due to stepwise attachment of organic moieties (Figure 9.2 e). The isoelectric point (IEP) of MSN-SH (pH 3.6) is shifted to a more acidic pH values ( $<2$ ) for MSNs containing the benzene sulfonamide groups on the outer surface. The tendency for sulfonamide groups to be protonated is relatively low due to the stabilizing resonance effect, consequently causing a more negative surface charge since the influence of silanol groups is increased. After attachment of the carbonic anhydrase a drastic change can be observed. This enzyme consists of various amino acid residues which can be easily protonated, including arginine, histidine and lysine. Therefore, a highly positive surface charge occurs over the whole acidic pH range. MSN-phSA-CA features an IEP at neutral pH values (pH  $\sim 7$ ).

**Table 9.1:** Porosity parameters of functionalized MSNs.

<sup>a</sup> Pore volume is calculated up to a pore size of 8 nm to remove the contribution of interparticle porosity.

<sup>b</sup> DFT pore size refers to the peak value of the pore size distribution.

Sample	BET surface area (m <sup>2</sup> /g)	Pore volume <sup>a</sup> (m <sup>3</sup> /g)	Pore size <sup>b</sup> (nm)
MSN-SH	1170	0.83	3.8
MSN-pSA	1004	0.72	3.7
MSN-pSA-CA	99	0.07	-

Vibrational spectroscopy, including infrared (IR, Figure 9.2 c) and Raman (Figure 9.2 f) spectroscopy, were performed to investigate specific vibrational bands originating from organic groups. IR data for all samples show typical vibration bands of the silica framework (Figure 9.2 c). A broad peak in the range between 1300 and 1000 cm<sup>-1</sup> can be assigned to Si-O-Si stretching vibration modes. Two additional bands at 900 and 780 cm<sup>-1</sup> are related to asymmetric stretching and bending vibrations of Si-OH groups, respectively. Furthermore, a group of bands in the range between 3000 and 2800 cm<sup>-1</sup> can be observed which indicates C-H stretching vibration of methylene and methyl groups from the propyl chain of organosilane moieties and residual ethoxy silane groups. Sample MSN-SH features a band at 1633 cm<sup>-1</sup> which can be assigned to the bending modes of physisorbed water. This band is present in all spectra but partially overlapped by other more intensive bands for the coated particles. MSNs containing the benzene sulfonamide groups show additional C=O stretching vibration bands at 1700 and 1627 cm<sup>-1</sup> which can be referred to the carbonyl groups of the short maleimide-C6-NHS linker (maleimide and amide, respectively). Furthermore, a peak of weak intensity at 1340 cm<sup>-1</sup> is present in the spectrum of sample MSN-phSA which belongs

to the typical asymmetric  $\text{SO}_2$  stretching vibration modes derived from the sulfonamide groups. For the sample MSN-phSA-CA amide vibration bands (Amide I:  $1639\text{ cm}^{-1}$ , C=O stretching vibration; Amide II:  $1535\text{ cm}^{-1}$ , N-H deformation and C-N stretching vibration) of high intensity are all-dominant present in the range between  $1700$  and  $1500\text{ cm}^{-1}$  which are typical for enzymes. Raman spectroscopy provides complementary data to IR spectroscopy (cf. Appendix).

Nitrogen sorption measurements show type IV isotherms for MSN-SH and MSN-phSA confirming mesoporosity of the silica nanoparticles. The corresponding nitrogen sorption isotherms are depicted in Figure 9.2 a showing inflection points at  $p/p_0 = 0.3$ . Another hysteresis loop at about  $0.9 p/p_0$  is present for all samples which can be attributed to interparticle textural porosity. Relatively high surface areas (up to  $1200\text{ m}^2/\text{g}$ ) and pore volumes ( $0.8\text{ cm}^3/\text{g}$ ) can be observed for MSN-SH and MSN-phSA (Table 9.1).

The slight reduction in these porosity parameters for benzene sulfonamide-functionalized MSNs can be assigned to the increase of sample weight by additional non-porous organic moieties. Furthermore, the DFT pore size distribution (Figure 9.2 e) still shows accessible pores. The porous system is not affected by the attachment of the benzene sulfonamide linkers and no incorporation of organic groups inside the mesopores can be observed which is confirmed by a constant pore size distribution. The attachment of the bulky enzyme carbonic anhydrase results in a drastic reduction of the surface area and pore volume for sample MSN-phSA-CA. Enzyme-coated MSNs feature a type II isotherm which corresponds to non-porous materials. The carbonic anhydrase enzymes act like bulky biomolecular valves which are able to efficiently block the mesopores even towards the access of small nitrogen molecules.

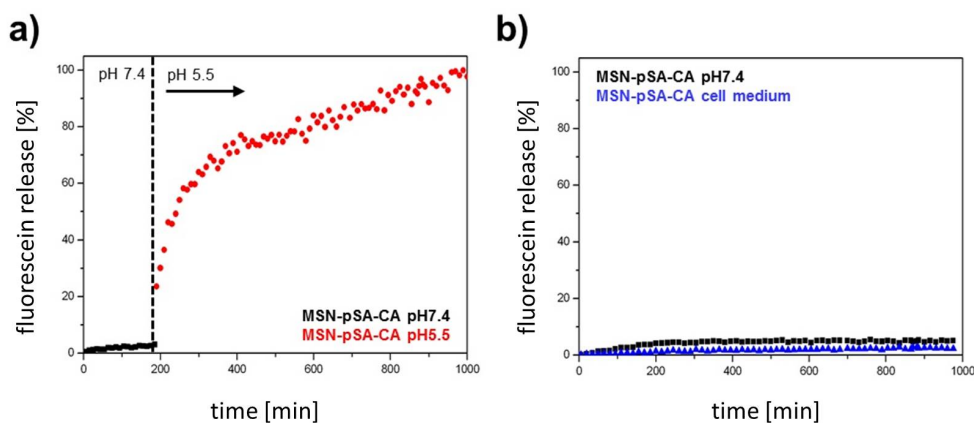


**Figure 9.3:** *In vial* release kinetics of fluorescein molecules from the enzyme-coated MSNs at different pH values. (a) Sample MSN-pSA-CA feature no premature release of the fluorescent cargo molecules in HBSS buffer solution at pH 7.4 (closed state, black curve). After 3 h the medium has been changed to slightly acidic milieu (CAP buffer, pH 5.5, red curve) resulting in a significant increase in fluorescence intensity. The gatekeepers are detached from the particle surface upon acidic pH values causing an efficient and precisely controllable release of the fluorescein from the mesoporous system. (b) Long-term stability of the capping system was investigated in HBSS buffer (pH 7.4, black curve) and cell medium (blue curve). No unmeant cargo release was observed within about 16 h.

## 9 Enzyme based pH-sensitive cap system for MSNs

With all these data, we assume a successful synthesis of carbonic anhydrase coated MSNs via benzene sulfonamide linkers. In order to investigate the pH-responsive secession of the bulky gatekeepers from the particles, *in vial* cargo release experiments were performed. We used a custom-made two-compartment system to analyze the time-based release of the fluorescent model drug fluorescein. [40] After incorporation of fluorescein molecules into the mesoporous system, carbonic anhydrase was added to block the pore entrances. An efficient sealing of the pores and no premature release of the cargo can be observed for the sample MSN-phSA-CA dispersed in HBSS buffer (pH 7.4) at 37°C (Figure 9.3 a, closed state, black curve). After 3 h the solution has been exchanged and the particles have been dispersed in CAP buffer (pH 5.5). The change to acidic milieu, which should simulated the acidification of endosomes, causes a significant increase in fluorescence intensity over time reaching its maximum after 18 h (open state, red curve). Furthermore, we could show a long-term stability of the capping system for more than 16 h in HBSS buffer and cell medium at pH 7.4 (Figure 9.3 b). These *in vial* release experiments demonstrates an efficient sealing of the pores with the carbonic anhydrase as bulky gatekeepers preventing premature cargo release and a stimuli-responsive release behavior upon acid-sensitive detachment of the capping system.

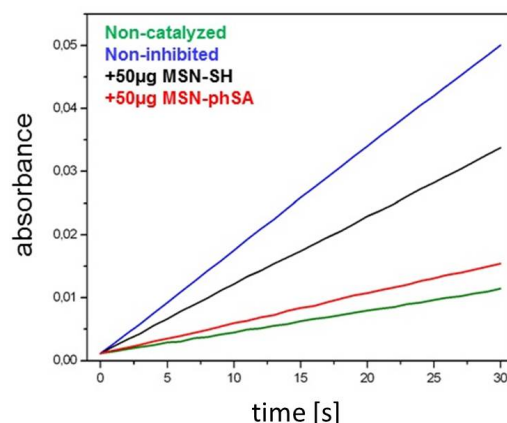


**Figure 9.4:** Enzyme activity assay of CA catalyzing the hydrolyzation of the chromogenic substrate p-nitrophenyl acetate measured by UV-Vis spectroscopy (absorbance at 400 nm). Non-catalyzed (green) and non-inhibited (blue) reaction and after addition of MSN-SH (black) or MSN-phSA (red).

Enzyme activity assays provide information about the binding affinity of carbonic anhydrase on the surface of sulfonamide-functionalized MSNs (Figure 9.4). The enzyme activity assay investigates the hydrolyzation of a chromogenic substrate (p-nitrophenyl acetate, NPA) in the presence of the enzyme generating nitrophenol in TRIS-buffered solution. By UV-Vis spectroscopy the resulting absorption maximum at 400 nm can be measured. Figure 9.4 shows the resulting curve for the non-catalyzed (no carbonic anhydrase) reaction which can be taken as baseline. The slight slope for this curve is due to the hydrolysis rate of the pure substrate in aqueous solution in the absence of catalytic enzymes. In presence of 100 nM enzyme (non-inhibited) the maximum conversion of the substrate can be obtained. By addition of 50 µg of MSN-SH particles a slight decrease in

conversion efficiency can be observed due to marginal reduction of enzyme activity in presence of silica nanoparticles. We assume that this effect corresponds to minor unspecific attachment of the carbonic anhydrase to the silica nanoparticles causing inaccessibility of the active site to some extent. In comparison, the addition of inhibitor-containing particles (MSN-phSA) a significant decrease of the slope of the resulting curve can be observed. Conclusively, the sulfonamide-functionalized MSNs are able to inhibit the enzyme carbonic anhydrase. At neutral pH values, the enzyme is specifically attached to the sulfonamide-functionalized particle surface resulting in an inhibition of the enzyme's active site. This leads to a drastic decrease in enzyme activity. With this, we further anticipate the confirmation of the pH-responsive gatekeeping concept of our mesoporous silica nanocarriers.

## 9.2 Dye release - *in vitro*

The *in vitro* release behavior of the sample MSN-phSA-CA was investigated with fluorescent live cell imaging. Instead of fluorescein (used *in vial*) we used 4',6-diamidino-2-phenylindole (DAPI) as cargo and studied the release behavior on HeLa cancer cells. Since DAPI and fluorescein molecules are of comparable size, the encapsulation behavior can be estimated the same. As already described in Chapter 8, DAPI is used for nucleic staining, is cell membrane permeable and the fluorescence intensity is about 20 fold enhanced after intercalation to DNA. [240] In order to keep track on the particles they were, additional to the DAPI loading, covalently labeled with Atto633. To seal the pores, the human carbonic anhydrase was added to the MSN solution after loading of DAPI. The

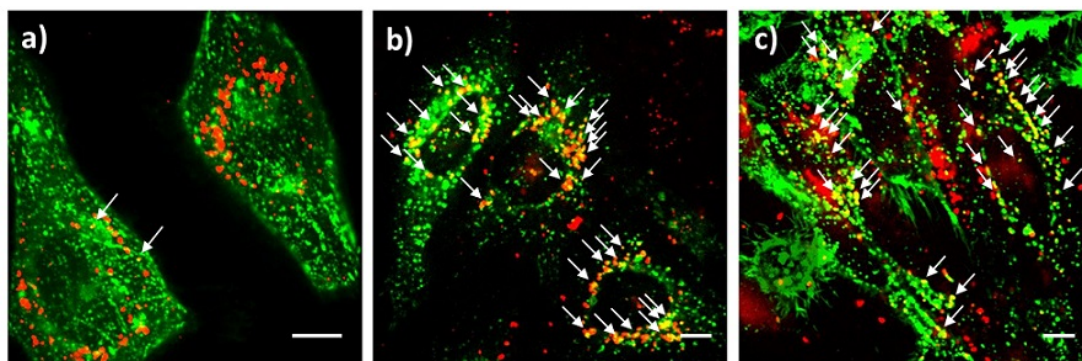


**Figure 9.5:** Fluorescence microscopy of HeLa cells incubated with Atto 633-labeled MSN-phSA-CA (red) after a) 24 h on GFP-early endosome (green) tagged cells, b) 21 h incubation on GFP-late endosome (green) tagged cells, and c) 21 h on GFP-lysosome (green) tagged cells. Co-localization (yellow) could be primarily observed for late endosomes and lysosomes (indicated with arrows) suggesting that the multifunctional MSNs are located in acidic compartments after endocytosis. The scale bar represents 10  $\mu\text{m}$ .

first step in testing the *in vitro* release behavior of carbonic anhydrase capped MSNs was to explore their fate inside HeLa cells. Therefore the early, late endosomes or lysosomes were stained with a fusion-constructs of green fluorescent protein (GFP) and the corresponding cell component marker. The cells were incubated simultaneously with the fusion construct and the Atto633 labeled, DAPI loaded MSNs for 21-24 h.

## 9 Enzyme based pH-sensitive cap system for MSNs

After 21-24 h the cells were imaged and co-localization between the GFP-marked cell compartments and the MSNs was investigated. In Figure 9.5 an exemplary section is depicted. After 24 h of incubation almost no co-localization (yellow) between early endosomes (green) and MSNs (red, Atto633) can be found (Figure 9.5a). After uptake of the particles they should be delivered relatively fast within minutes to a few hours to late endosomes. [303] The few yellow spots can be explained by endocytosis of MSNs at later time points which were not delivered to late endosomes so far. It can also be observed, that the MSNs are localized in the perinuclear region, which was already observed for other nanoparticles after an incubation time around 24 h. [342, 343] The co-localization

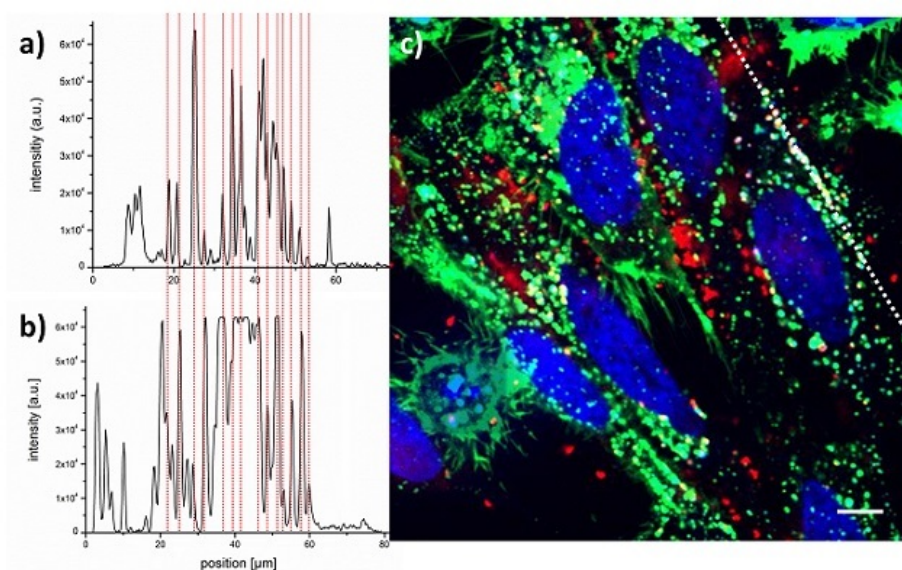


**Figure 9.6:** Colocalization of MSN-phSA-CA with GFP-stained lysosomes. The intensity profiles along the dashed white line in (c) is plotted for (a) MSN and (b) GFP-stained lysosomes, intensity maxima which occur in both profiles are marked with red lines. (c) Fluorescence microscopy of HeLa cells incubated with MSN-phSA-CA nanoparticles loaded with DAPI (blue) and labeled with Atto633 (red) after 21 h on GFP-lysosome (green) tagged cells. The white spots indicate co-localization between MSNs and lysosomes. A successful DAPI delivery is clearly visible by efficient nuclei staining (blue). The scale bars represent 10  $\mu\text{m}$ .

(yellow) between late endosomes/lysosomes (green, Figure 9.5b/c) and MSNs (red) after 21 h of incubation in contrast is clearly visible. The yellow spots are also indicated by arrows. In Figure 9.6 a more detailed analysis on the co-localization between lysosomes and MSNs is given. Along the dashed white line the intensity profiles of the MSNs (Figure 9.6a) and lysosomes (Figure 9.6 b) are graphically presented. The peaks (maxima) of all MSN can be assigned to a peak in the lysosome-profile, which is also indicated with red bars for a clear allocation. At some areas the lysosomes can not be clearly distinguished from another, because they lie very close together, in this cases no clear statement about co-localization can be drawn. Also not every lysosome contains MSNs, hence not every lysosome-peak has a corresponding MSN-peak. In Figure 9.6 c the same cells as in Figure 9.5 c is depicted, but in this case the released cargo DAPI (blue) is also included. We

summarize, that the MSNs are located in acidic compartments.

In a next step we took a closer look at the time-dependent release-behavior of DAPI from the CA capped MSNs. Therefore, we incubated HeLa cells with the particles for a total time period of 24 h. In Figure 9.7 exemplary cells after 7, 15 and 24 h (Figure 9.7 a-c) of incubation are depicted. Additionally the supernatant (after centrifugation) of the particle solution was incubated with the cells in order to exclude free DAPI molecules in the solution (Figure 9.7 d). After 7 h of incubation

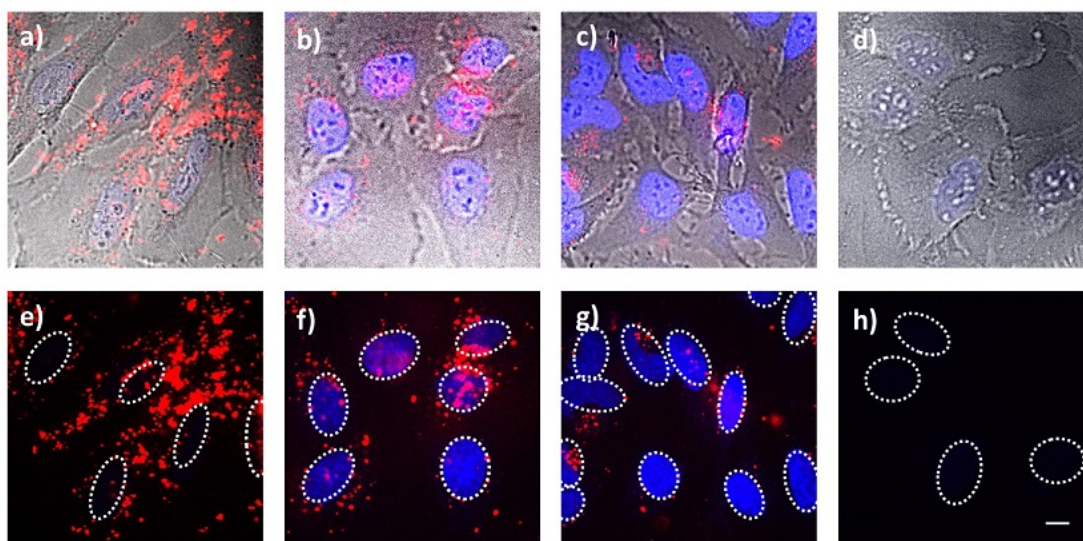


**Figure 9.7:** Fluorescence microscopy of HeLa cells incubated with MSN-phSA-CA nanoparticles loaded with DAPI and labeled with Atto633 (red) after (a/e) 7 h, (b/f) 12 h and (c/g) 24 h of incubation on the cells. The delayed nuclei staining with DAPI (blue) is caused by a time-dependent release of DAPI based on the need for an acidic environment. (d/h) As a reference, the incubation with the supernatant solution (without MSNs) showed no staining of the nuclei with DAPI after 24 h suggesting no free DAPI molecules in the particle solution. The nuclei are indicated with dashed circles. (a-d) Merge of brightfield image, MSN-fluorescence and DAPI. (e-h) Merge of MSN-fluorescence and DAPI. The scale bar represents 10  $\mu\text{m}$ .

the particles were efficiently uptaken by the cells, which is evident from the localization in the cells in the merge of particle fluorescence with brightfield images. However, a lack of nuclei staining after 7h indicates that the release needs some time to start (Figure 9.7 a/e). Only after 15 h (Figure 9.7 b/f) of incubation, the DAPI (blue) was efficiently released from the nanocarriers resulting in an significant nuclei staining (even more intensive after 24 h; Figure 9.7 c/g). These experiments in combination with the lack of DAPI fluorescence after incubation with the supernatant (particles separated by centrifugation; Figure 9.7 d/h) demonstrate a time-dependent release behavior without free cargo molecules in solution. Thus we anticipate, that the acidification process inside the endosomes destabilizes the binding between CA and particles and therefore efficiently releases the cargo DAPI which leads to a delayed nucleic staining.

### 9.3 Targeting - *in vitro*

For an efficient cell targeting a targeting ligand needs to be implemented. As the particle surface is covered with bulky enzymes (CA), the targeting moieties have to be attached directly onto the enzyme in order to be available for receptors. Furthermore, the site of targeting attachment on the enzyme is of key importance. It should be on the opposite of the active/binding site of the enzyme, to prevent blocking of the active site. However, site specific chemical modifications of proteins was found to be quite challenging. Different methods, such as the reaction of thiol groups with maleimide or lysine chains with activated esters, lack of specificity. A more precise method is the incorporation of unnatural amino acids (AS) into the protein. [340] The incorporation of unnatural AS bearing side-chains with alkyne, trans-cyclooctene, cyclooctyne or norbornene can be found in the literature. To

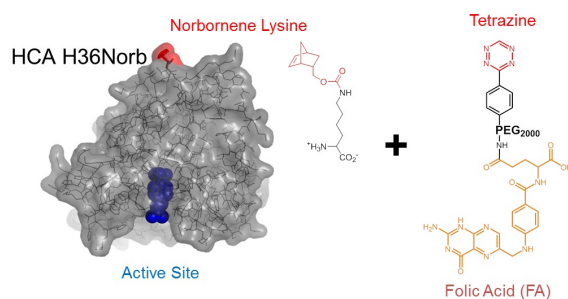


**Figure 9.8:** Norbornene functionalized carbonic anhydrase (HCA H36Norb) with indicated functionalization site (red) and active site (blue) is able to react in a reversed-electron-demand Diels-Alder reaction with a folic acid-PEG<sub>2000</sub>-tetrazine derivate to HCA-FA.

incorporate the genetically encoded non-natural amino acids bioorthogonal tRNA/rRNA-synthetase pairs are used. Especially the pyrrolysen systems is well studied. Previously a *Methyosarcina mazei* PylRS triple mutant (norb-PylRS:Y306G, Y384F, I405R) which accepts norbornene-containing Pyl analogue was identified by the group of Carell. [340, 341] The functionalization with norbonene is of interest as they react selectively with tetrazine.

The synthesis of the norbornene functionalized carbonic anhydrase was accomplished similar to the previously described procedure by the Carell-group [340, 341] gaining a human carbon anhydrase II (HCA) with H36Norb. The norbornene modified HCA then was reacted with a folic acid-PEG<sub>2000</sub>-tetrazine derivate as is schematically depicted in Figure 9.8. With this bio-orthogonal reversed-electron-demand Diels-Alder reaction we were able to gain a folic acid functionalized CA. The functionality of this modified enzyme as capping system was confirmed by another release experiment *in vial* and *in vitro* (data not shown).

The efficiency of the as synthesized targeting system was again tested as already described in the previous Chapters on KB-cells with free/blocked FA-receptors. In Figure 9.9 the result is shown. The cell membrane of the KB cells is stained with WGA488 (green) and the particles are labeled with Atto633 (red). In the first row (Figure 9.9 a-c) the folic acid receptor blocked cells are incubated 2-8 h. With increasing incubation time only a few particles get internalized. In contrast, the cells with

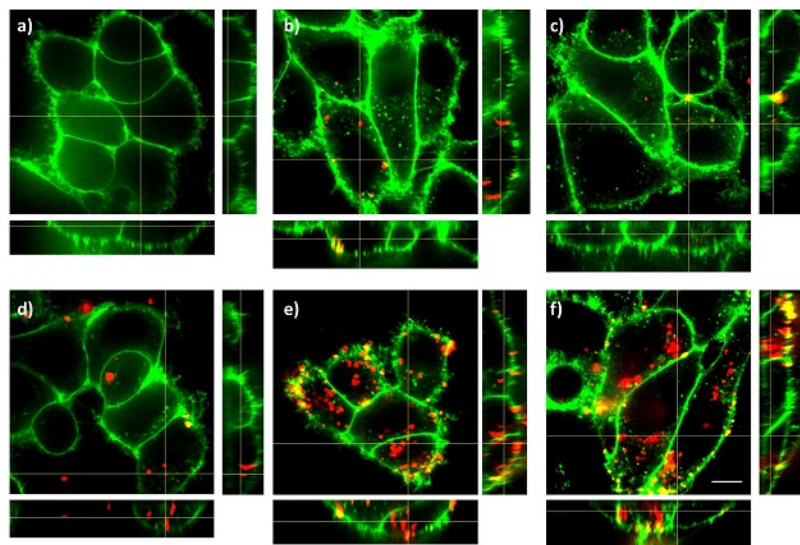


**Figure 9.9:** a-c) Unspecific and d-f) receptor-mediated endocytosis of MSN-HCA-FA (red) by KB cells (WGA488 membrane staining, green). A specific receptor-mediated cell uptake can be clearly observed for MSN-HCA-FA with KB cells (not FA-preincubated) after 5 and 8 h incubation at 37°C (e/f), whereby after 2 h of incubation no big difference to folic acid pre-incubated particles can be seen (d). Incubation of MSN-HCA-FA with FA-preincubated KB cells for 2, 5, 8 h at 37°C shows only a low amount of unspecific cellular uptake over all incubation times (d-f). The scale bar represents 10  $\mu\text{m}$ .

available folic acid receptor on their surface (Figure 9.9 d-f) exhibit an increasing uptake behavior and more important have many particles internalized and not only a few as in the case of blocked receptors.

## 9.4 Summary

In summary, we conclude that the novel capping system concept based on pH-responsive detachment of carbonic anhydrase is a suitable candidate for a highly controllable drug release from porous nanocarriers. Our drug delivery system provides an on-demand release mechanism shown by *in vivo* and *in vitro* cargo release experiments. The multifunctional MSNs are capable for efficient endocytosis by cancer cells and are subsequently located in acidic cell compartments including late endosomes and lysosomes. The acidic milieu caused cleavage of the coordination bond between the sulfonamide linkers and the bulky gatekeepers and a successful cargo release occurred which has been proven by the appearance of a strong fluorescent nuclei staining with DAPI. Also the specific attachment of targeting moieties on a modified human carbonic anhydrase II provides possibilities for applications *in vivo*, since the targeted delivery of drugs to the desired tissue is one of the critical parameters especially in cancer therapy. With this systems the drug could be selectively aimed at the desired tissue and only inside the cells the drug would be released. Consequently, spreading of chemotherapeutics in the organism is restrained and systemic side-effects can be further reduced.

### *9 Enzyme based pH-sensitive cap system for MSNs*

A detailed investigation of this valuable characteristic is part of future work. This newly developed concept for pH-responsive gatekeepers provide a promising basis for future work on mesoporous silica particles as a more powerful and versatile drug delivery platform.

In the last chapter the difficulties in increasing the pore size of MSN are discussed as well as nature derived strategies to overcome endosomal escape, namely fusion processes.

# 10 Outlook: Modifications of surface coated MSN

In the following Chapter some other modifications of mesoporous silica nanoparticles for drug delivery are described, which are based on the systems presented so far. First investigations on particles with increased pore size are presented. Furthermore, the incorporation of fusionogenic peptides into supported lipid bilayers around MSN was investigated.

## 10.1 Large pore MSN

This Chapter is based on the work in cooperation with: Alexandra Schmidt, Martina Lichtenecker [344], Katharina Braunger, Thomas Bein, and Christoph Bräuchle. The synthesis and characterization of the large pore system was mainly performed by Martina Lichtenecker.

In the previous Chapters promising post-synthesis functionalization methods for colloidal mesoporous silica nanoparticles, with pore sizes between 4 and 5 nm, are described in detail. These investigated systems are able to deliver membrane-permeable cargos as well as membrane-impermeable cargos to specific cells and release their cargo on external and internal stimuli. Often, the pore size of the MSN is the limiting factor for various cargos (e.g enzymes). With a pore size around 4 nm of standard silica nanoparticles (Chapter 6 - 9) only small molecules can be delivered, proteins normally need more space due to size and charge. Therefore it is desirable to develop MSNs with reproducible larger mesopores. [169, 184, 205, 345]

One of the most prominent mesoporous material is the Santa Barbara Amorphous 15 (SBA-15), introduced in 1998 in the group of Stucky. [190] Their pore size of this material can be modified in a broad size range (4.6-30 nm), but a particle size of 80  $\mu\text{m}$  [190, 346], and are already tested in various application fields like adsorption, host for (immobilized) catalysis or optical applications and drug delivery. [347–352] In addition to the above mentioned pore size, the particle size itself is of high importance for drug delivery applications. If the particles are too small (below 5-6 nm) they will most likely be cleared renal [12], in case of big particles ( $> 200$  nm) they are very likely taken up by the reticuloendothelial system (RES). [13] Because of this, SBA-15 particles can not be considered for drug delivery systems inside living systems, even though their synthesis is reproducible and their are well characterized.

Other approaches which were tested by Gao *et al.* [353] achieved smaller particles with pore sizes of around 20 nm and particle size between 70-300 nm. A dual surfactant system, consisting of the

## 10 Outlook: Modifications of surface coated MSN

triblock copolymer Pluronic F127 and Fluorocarbon Surfactant FC-4, together with the micellar expander TMB was employed at low temperatures. It was shown that FC-4 limits the particles growth whereas F127 acts as template for the mesoporous network. Additionally, the effect of distinct hydrothermal treatment steps was investigated. Until now, all mentioned LP-MSN systems lack introduced functionalization which is mandatory for the post-synthesis functionalization of the NPs (e.g. attachment of capping systems). In the following controlled release experiments with large-pore mesoporous silica nanoparticles (LP-MSN) synthesized in the Bein group are presented.

### 10.1.1 Synthesis and characterization

The LP-MSN particles investigated in this section were synthesized based on the modified procedure of Gao *et al.* [353] The reaction to create LP-MSN was performed under mild acidic conditions at low temperatures (30°C/ 10°C) in the presence of the dual surfactant system Pluronic® F127 and FC-4 (high and low amount). A co-condensation approach was pursued to introduce organic-functionalization within the mesoporous framework. (cf. details in Appendix Chapter 5.1) The

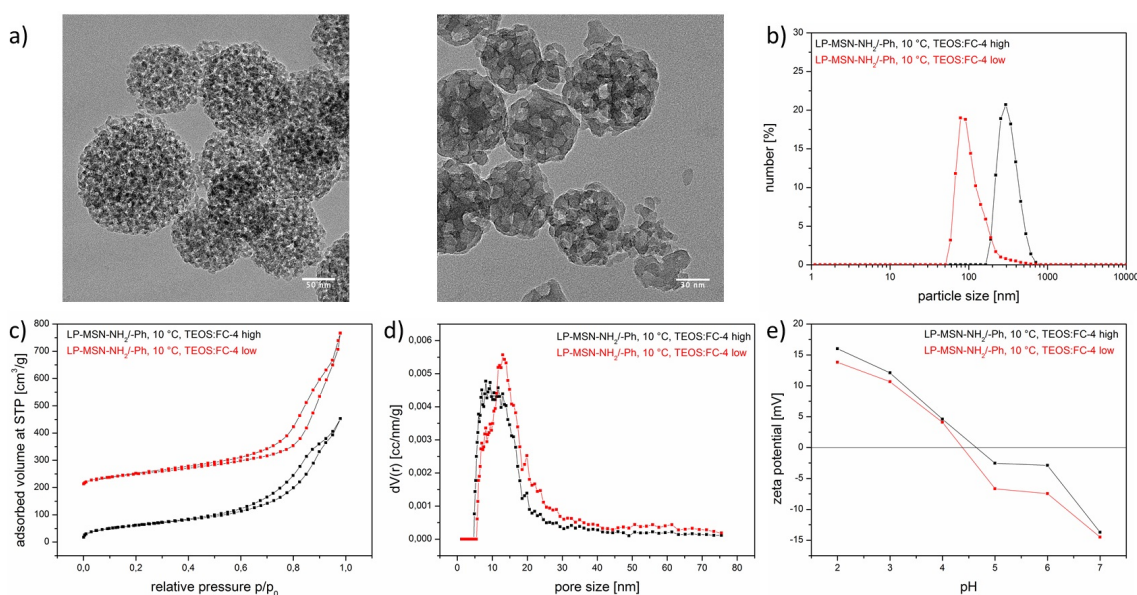


**Figure 10.1:** (a) TEM micrographs of LP-MSN-NH<sub>2</sub>/-Ph (10°C, TEOS:FC-4 high (left) and low (right)) after size-separation centrifugation. The scale bar represents 50 nm (left) and 30 nm (right). (b) DLS data of LP-MSN-NH<sub>2</sub>/-Ph (10°C, TEOS:FC-4 high, black) and LP-MSN-NH<sub>2</sub>/-Ph (10°C, TEOS:FC-4 low, red), measured after size-separation centrifugation. (c) Nitrogen sorption isotherms at 77 K and (d) calculated NLDFT pore size distribution of sample LP-MSN-NH<sub>2</sub>/-Ph (black, 10°C, TEOS:FC-4 high) and LP-MSN-NH<sub>2</sub>/-Ph (red, 10°C, TEOS:FC-4 low) For clarity reasons the isotherms are shifted along the y axis by a value of 200. (e) Zeta potential of sample LP-MSN-NH<sub>2</sub>/-Ph (10°C, TEOS:FC-4 high, black) and LP-MSN-NH<sub>2</sub>/-Ph (30°C, TEOS:FC-4 low, red).

transmission electron microscope (TEM) image of the LP-MSN (LP-MSN-NH<sub>2</sub>/-Ph, TEOS:FC-4 high and low, after size-separation-centrifugation) shows spherical particles with a fairly homogenous

particle size distribution within a size range of 100-200 nm (or around 60 nm for low FC-4) and significantly larger pore size of 7-9 (or 8-14) nm (Figure 10.1 a). LP-MSN-NH<sub>2</sub>/-Ph synthesized with higher amount of FC-4 feature a larger pore size (8-14 nm) compared to the low amount FC-4 synthesized particles (7-9 nm), in both cases the pores are evenly distributed over the entire nanoparticle. The particles with higher amount of FC-4 also exhibit a higher order in pore structure and lower average particle size. Both particle types possess suitable pore size for the intended application.

DLS measurements were performed to examine the particle size distribution after size separation centrifugation (Figure 10.1 b). Sample LP-MSN-NH<sub>2</sub>/-Ph (TEOS:FC-4 low) features particles with a size around 80 nm, LP-MSN-NH<sub>2</sub>/-Ph (TEOS:FC-4 high) around 300 nm. We attribute the slight increase compared to TEM measurements to the development of hydrodynamic shell.

Nitrogen sorption data of high and low FC-4 LP-MSN-NH<sub>2</sub>/-Ph revealed IUPAC type IV isotherms typical for mesoporous materials (see Figure 10.1 c/d). Sample LP-MSN-NH<sub>2</sub>/-Ph (TEOS:FC-4 low) exhibits a higher pore volume (0.8 cm<sup>3</sup>/g) and pore size (maximum at 13.0 nm) compared to LP-MSN-NH<sub>2</sub>/-Ph (TEOS:FC-4 high) with 0.6 cm<sup>3</sup>/g and 8.1 nm. The obtained data are in good agreement with the TEM measurements. Textural porosity or a small amount of impurities in both samples are probable causes for the lack of a saturation plateau of the isotherms at high p/p<sub>0</sub> values. But the N<sub>2</sub> adsorption measurements also reach their limitation within the large pore diameter of our LP-MSN-NH<sub>2</sub>/-Ph.

For charge-determination, zeta potential measurements were performed (Figure 10.1 e). Due to amino moieties present in both samples exhibit a positive zeta potential between pH 2-4. At pH 5-7 the NH<sub>2</sub> groups are deprotonated and the potential turns negative. This behavior is typical for amino-functionalized nanoparticles and indicates the successful functionalization of LP-MSN by co-condensation.

To achieve a controlled endosomal release system with LP-MSN the particles were post-synthetic modified with stimuli-responsive molecules, PVP/SLB for capping and AlPcS<sub>2a</sub> for endosomal escape. As capping systems we tested supported lipid bilayers (SLB) and the pH-dependent polymer poly(2-vinylpyridine) (PVP), which were already described with our established core-shell particles in Chapter 6 and 7. The LP-MSN were loaded with a selection of cargo molecules of a varying size, they are listed in Table 10.1. The release behavior was tested *in vial* and *in vitro*. Whereby for the PVP-capped LP-MSN only the cargo calcein was used. The release of small molecules (calcein, propidium iodide) was repeated in order to compare them with already performed experiments of core-shell particles (with smaller pores, 4-6 nm) in our groups. [1, 15] The larger dextran molecules (fluorescently labeled polysaccharides) were not used as model drugs so far, as their size exceed the capacity of conventional MSN.

### Supported lipid bilayer capped LP-MSN

In a first set of *in vial* release experiments the release behavior at physiological temperatures (37°C) of calcein (Figure 10.2 a) or FITC-dextran (3000-5000 Da, Figure 10.2 b; 10000 Da, Figure 10.2 c) without internal release mechanisms was monitored with the already described fluorescent release

**Table 10.1:** Properties of applied cargos in different size ranges.

size range	cargo	molecular weight [Da]	hydrodynamic radius [nm]
small size	calcein	623	ca. 0.6
	propidium iodide	668	ca. 0.6
medium size	FITC-dextran	3.000 - 5.000	ca. 1.2 - 1.4
	Alexa-Fluor-Phalloidin	1590	ca. 1.5
large size	FITC-dextran	10.000	ca. 2.3
	Alexa-Fluor-dextran	10.000	ca. 2.3

setup. The goal of this experiments was first to proof that the formation of the supported lipid bilayer works also with increased pore size and therefore decreased real surface volume. Second the incorporation of small, medium and large size cargos should be demonstrated. In a next step LP-MSN with covalently attached photosensitizer AIPcS<sub>2a</sub> and cargo calcein were investigated (Figure 10.2 d).

The SLB was disrupted in all cases after 3 h of monitoring the closed system. The release trigger for LP-MSN covered with SLB was the addition of Triton-X, which disintegrates the SLB. [39] This delay time is important to rule out free fluorescence molecules and secondly in case of wrong SLB-formation the fluorescence increase could be detected without inducing release. In the case of attached photosensitizer the release trigger was light activation and resulting singlet oxygen formation which then leads to membrane rupture. [15]

In case of calcein loading no premature release could be detected (Figure 10.2 a), indicating a successful capping of the particles with the SLB. In case of the FITC-dextran premature release up to 20% could be visible (Figure 10.2 b/c). This could be either indicating an insufficient washing step, so that free cargo molecules are in the solution or an insufficient sealing of the particles. In case of free cargo molecules in the solution only a limited amount of fluorescent molecules should pass the cuvette membrane, since the majority should be encapsulated inside the MSN by the supported lipid bilayer. In case of an insufficient SLB-formation the fluorescence would increase constantly, independent of the release trigger. Especially the small plateau that is reached after three hours in the case of the 10000 Da FITC-dextran (Figure 10.2 c) indicates the presents of free dye molecules, as otherwise the fluorescence would increase the entire time. Also the strong increase in fluorescence after the triggered release indicates a successful formation of the supported lipid bilayer. We assume that the polysaccharides of the dextrans interact with the SLB and can not be separated easily thereof.

To overcome the endosomal entrapment the red light sensitive photosensitizer AIPcS<sub>2a</sub> was attached onto the surface of LP-MSN. The functionality of the system in order to rupture the SLB was demonstrated with the in cuvette-release experiment (Figure 10.2 d). By formation of a sulfonamide bond, AIPcS<sub>2a</sub> was covalently attached to LP-MSN-NH<sub>2</sub>/-Ph. To remove excess AIPcS<sub>2a</sub>, the

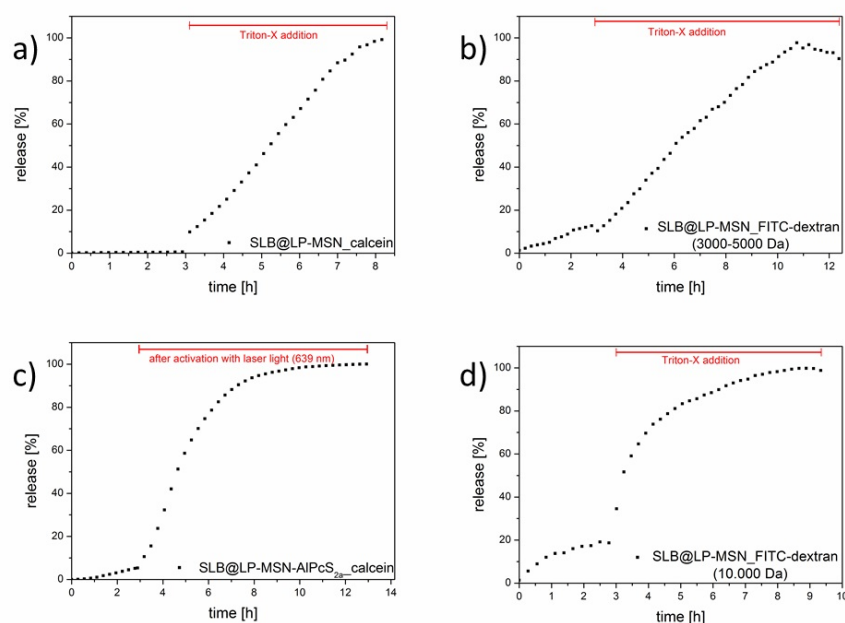


**Figure 10.2:** Dye release kinetics of SLB@LP-MSN-cargo as a function of time. After a three-hour release experiment (37°C) with SLB sealed LP-MSN-calcein, Triton-X (a/b/d) or photoactivation (c) was applied, resulting in a burst of dye release. (a) SLB@LP-MSN-calcein. 100 % was set for the amount released after 8 h. (b) SLB@LP-MSN-FITC-dextran (3000-5000 Da). The inflection of the curve after 11 h presumably is a result of photobleaching of FITC. The curve was normalized to 100 % for the amount released after 11 h. (c) SLB@LP-MSN-AIPcS<sub>2a</sub>-calcein. Photosensitizer AIPcS<sub>2a</sub> was activated by red laser light (639 nm, 1 min, 5.4 W/cm<sup>2</sup>). Saturation of released calcein was reached after 12 h. The release curve was normalized to the value obtained after 12 h. (d) SLB@LP-MSN-FITC-dextran (10,000 Da). Saturation of released FITC-dextran was reached after about 9 h. The curve was normalized to 100 % for the amount released after about 9 h.

particles were extensively washed with a DMSO/H<sub>2</sub>O mixture (1:1 vol%) after the synthesis.

The supernatants of the washing steps were investigated with UV-VIS, as small amounts cannot be detected by eye, but in spectroscopy/microscopy. For characterization of the attachment nitrogen sorption measurements were performed and the BET area was calculated for each sample. The results are given in Table 10.2. After attachment of AIPcS<sub>2a</sub> the BET-surface area increased slightly.

**Table 10.2:** Summary of nitrogen sorption measurements.

Sample	BET surface area [m <sup>2</sup> /g]	pore volume [cm <sup>3</sup> /g]	pore size [nm]
LP-MSN-NH <sub>2</sub> /-Ph	177	0.8	13.0
LP-MSN-AIPcS <sub>2a</sub>	246	0.9	13.0

## 10 Outlook: Modifications of surface coated MSN

Presumably the large steric hindered  $\text{AlPcS}_{2a}$  molecules resulting in interstitial pore volume. The pore size was not effected by the synthesis, indicating that the mesoporous framework was not affected by the reagents and that the attachment occurred predominantly on the outer surface of the LP-MSN. The amount of attached  $\text{AlPcS}_{2a}$  was determined with thermogravimetric analysis of the samples LP-MSN-NH<sub>2</sub>/-Ph and LP-MSN- $\text{AlPcS}_{2a}$  (Figure 10.3 a). The additional mass loss of 4.5 % for the sample LP-MSN- $\text{AlPcS}_{2a}$  is high, considering that the amount of organo-functionalization (APTES/PTES) was only 0.5 mol%. The amount of attached  $\text{AlPcS}_{2a}$  was calculated to 64  $\mu\text{mol}$  per g LP-MSN-NH<sub>2</sub>/-Ph.

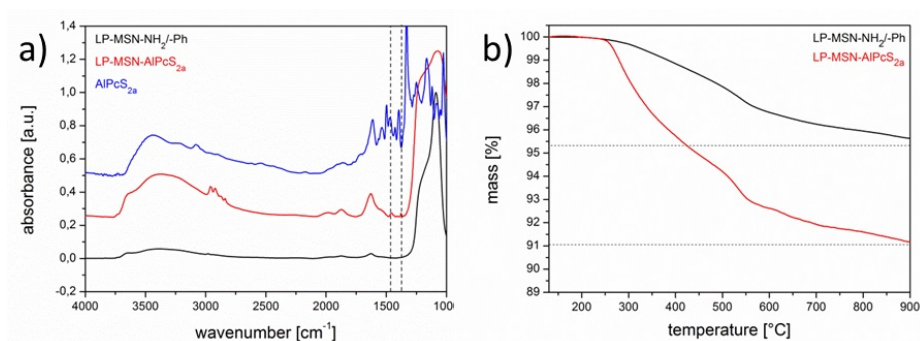


**Figure 10.3:** (a) IR spectra of LP-MSN-NH<sub>2</sub>/-Ph (black) and LP-MSN- $\text{AlPcS}_{2a}$  (red), normalized to silica peak (1087 nm), in blue: IR spectrum of  $\text{AlPcS}_{2a}$  (normalized to the strongest peak). The spectrum of LP-MSN- $\text{AlPcS}_{2a}$  was shifted along the y axis by a value of 0.25 and the spectrum of  $\text{AlPcS}_{2a}$  by a value of 0.5 for clarity reasons. (b) Thermogravimetric analysis of the samples LP-MSN-NH<sub>2</sub>/-Ph (black) and LP-MSN- $\text{AlPcS}_{2a}$  (red). The curves are normalized at 130°C. The mass loss is not easily evaluated as high temperatures can cause side reactions like dehydroxylation of the silanol-groups. For mass loss calculations the mass value at 900°C was used.

Infrared spectroscopy (Figure 10.3 b) also confirmed a successful attachment of  $\text{AlPcS}_{2a}$ . Peaks between 2959 and 2838  $\text{cm}^{-1}$  can be attributed to symmetric and asymmetric CH<sub>2</sub> stretching vibrations. The peak at 1678  $\text{cm}^{-1}$  with medium intensity can be attributed to the O-H vibration of small amounts of water in the sample. The aromatic stretching vibration of  $\text{AlPcS}_{2a}$  is outlined at 1456  $\text{cm}^{-1}$  (dashed line) and can be found in both spectra (LP-MSN- $\text{AlPcS}_{2a}$  and  $\text{AlPcS}_{2a}$ ). At 1377  $\text{cm}^{-1}$  (second dashed line) the asymmetric SO<sub>2</sub> stretching vibration of the newly formed sulfonamide bond is visible in the spectrum of LP-MSN- $\text{AlPcS}_{2a}$ . Below 1300  $\text{cm}^{-1}$  the vibrations of the silica framework arises with strong intensity, whereas the aromatic vibrations below 1000  $\text{cm}^{-1}$  could not be detected.

To conclude, the successful synthesis of large pore mesoporous silica nanoparticles could be demonstrated. Also the formation of a supported lipid bilayer around the particles was shown, and the covalently attachment of photosensitizer to LP-MSN as photoactivable release stimulus was achieved. In contrast to the standard MSN which are described in Chapter 6, the use of a PEG-spacer between LP-MSN and  $\text{AlPcS}_{2a}$  was not necessary in order to prevent pore clogging.

### Post-synthesis modified LP-MSN with PVP capping

Additionally to the supported lipid bilayer approach a polymeric capping system was tested with LP-MSN. The synthesis route was equal to the one described in Chapter 7. For all experiments the cell-membrane impermeable cargo calcein was used, making the employment of a photosensitizer for endosomal escape mandatory. (cf details in Appendix Chapter 5.1)

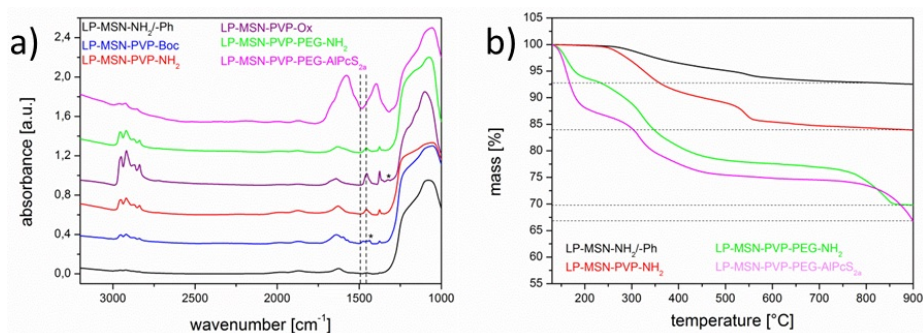


**Figure 10.4:** (a) IR spectra of LP-MSN-NH<sub>2</sub>/-Ph (black), LP-MSN-PVP-Boc (blue), LP-MSN-PVP-NH<sub>2</sub> (red), LP-MSN PVP-Ox (purple), LP-MSN-PVP-PEG-NH<sub>2</sub> (green) and LP-MSN-PVP-PEG-AIPcS<sub>2a</sub> (magenta). All spectra are normalized to the silica peak. The dashed lines indicate the C=C and C=N stretching vibration of the pyridine rings. The asterisked peak in the spectrum of LP-MSN-PVP-Boc can be attributed to the asymmetric CH<sub>3</sub> bending vibration of the Boc protecting group, the asterisked peak in the spectrum of LP-MSN-PVP-Ox can be assigned to the C-O stretching vibration. (b) Thermogravimetric analysis of the samples LP-MSN-NH<sub>2</sub>/-Ph (black), LP-MSN-PVP-NH<sub>2</sub> (red), LP-MSN-PVP-PEG-NH<sub>2</sub> (green) and LP-MSN-PVP-PEG-AIPcS<sub>2a</sub> (magenta), all curves were normalized at 130°C. The mass losses of the green and magenta curves are not easily evaluated as both curves are descending between 800°C and 900°C. This might be caused by side reactions like dehydroxylation of the silanol-groups.

In order to characterize the reaction TGA measurements and IR spectra were recorded. TGA measurements were performed for each reaction step to calculate the additional mass loss (Figure 10.4 a). From the mass loss of 7.5 % of LP-MSN-NH<sub>2</sub>/-Ph (Figure 10.4 a, black curve), the amount of aminopropyl moieties can be estimated at 0.56 mmol/g silica under the assumption that the molar ratio of aminopropyl to phenyl-moieties in the sample is 1:1 as employed during synthesis. After the attachment of the PVP polymer an additional mass loss of 8.2 % was measured, which equates to an estimated PVP-functionalization density of 6.9 μmol/g silica (Figure 10.4 a, red curve). This indicates that 1.2 % of all NH<sub>2</sub>-residues on the surface of LP-MSN have reacted with poly(2-vinylpyridine). This result can be explained by the large molecular dimension of the polymer (in coiled form) and the mutual shielding of the long polymeric chains. From the additional mass loss of 14.1 % of the sample LP-MSN-PEG-NH<sub>2</sub> (Figure 10.4 a, green curve) the amount of bound PEG can be estimated to 80 μmol/g silica. This implies that after attachment of oxalic acid about 14 % of all carboxy-groups within the LP-MSN have reacted with PEG. Thus it is assumed that the attachment of oxalic acid and PEG not only occurred at the N-terminal residues of PVP, but also on the amino moieties on the surface of LP-MSN. As the additional mass loss of LP-MSN-PVP-PEG-AIPcS<sub>2a</sub> was 3 % (Figure 10.4 a, magenta curve), the amount of attached AIPcS<sub>2a</sub> can

be calculated to 42  $\mu\text{mol}$  per gram silica.

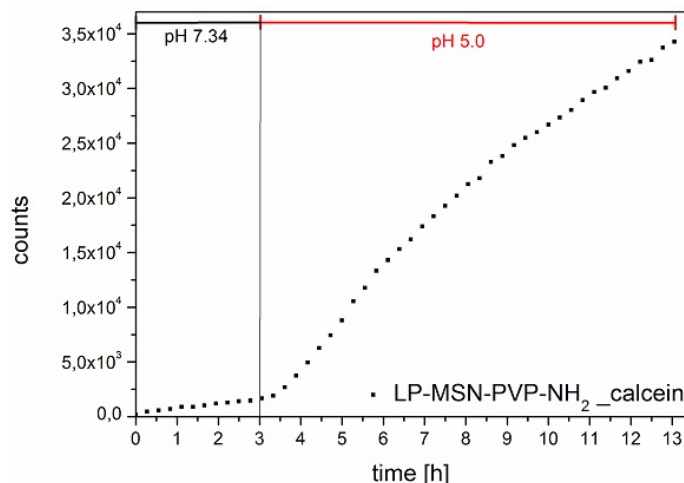


**Figure 10.5:** Time-based dye release kinetics of calcein loaded LP-MSN-PVP-NH<sub>2</sub> particles at pH 7.34 (SSC buffer, 1:40, particles completely closed by PVP) and pH 5.0 (McIlvaine buffer, PVP chains protonated, open state) 37°C.

IR spectra of all samples were measured for further analysis of the functional groups on the obtained samples (Figure 10.4). The peaks between 2950  $\text{cm}^{-1}$  and 2837  $\text{cm}^{-1}$  can be assigned to the symmetric and asymmetric CH<sub>2</sub>-stretching vibration of the vinyl groups in PVP and are present in all samples after the attachment of the polymer. A shoulder with very weak intensity is also visible in the spectrum of LP-MSN-NH<sub>2</sub>/-Ph due to the presence of propyl groups. The vibrations at 1455  $\text{cm}^{-1}$  and 1376  $\text{cm}^{-1}$  (dashed lines) can be attributed to C=C and C=N stretching vibrations of the pyridine rings. They appear in all spectra of PVP-containing samples. The asymmetric CH<sub>3</sub> bending vibration of the Boc protecting group is visible at 1438  $\text{cm}^{-1}$  in the spectrum of LP-MSN-PVP-Boc (asterisked peak), and disappears after de-protection with TFA. The peak at 1324  $\text{cm}^{-1}$  in the spectrum of LP-MSN-PVP-Ox (asterisked peak) can be assigned to the C-O stretching vibration, which disappears after the attachment of the PEG-linker. However, the C=O stretching vibration, which should arise within the range of 1685-1640  $\text{cm}^{-1}$ , could not be detected. In the spectrum of LP-MSN-PVP-PEG-AIPcS<sub>2a</sub> broad shoulders are visible in the range of 1573-1396  $\text{cm}^{-1}$  that presumably result from an overlay of aromatic ring stretching vibrations in AIPcS<sub>2a</sub> and C=C and C=N stretching vibrations of the pyridine rings. The peak at 1635  $\text{cm}^{-1}$  is visible in all spectra and can be attributed to residual water within the samples. Below 1300  $\text{cm}^{-1}$  the vibrations of the silica framework appear with strong intensities.

DLS measurement revealed a size increase after attachment of PVP (from 190 nm to 295 nm) and an additional increase after addition of the PEG-linker (to 342 nm). These results are in good accordance with the previously described system and are explained there (Chapter 7) After the successful synthesis calcein was adsorbed into the mesopores of the sample LP-MSN-PVP-NH<sub>2</sub> at acidic pH and a time-based release experiment at 37°C was performed (Figure 10.5). In the first

three hours the pH was set to pH 7.34 (SSC buffer) to measure the LP-MSN in closed state. After 3 h, the nanoparticles were separated by centrifugation and re-dispersed in McIlvaine buffer (pH 5.0) resulting in a protonation of the polymer chains, resulting in an opening of the pores. Immediately, a second release experiment was performed for additional 13 h.

The pH-dependent calcein-fluorescence was calibrated with the help of emission scans of a serial dilution of calcein in both buffers and the measured cps at pH 5.0 were multiplied with the obtained intercept of 1.35. The release experiment showed a small amount of premeasured calcein release. This most likely can be attributed to free calcein molecules that were attached to the polymer chains and then are diluted in the buffer. After the protonation of PVP at pH 5.0 a strong fluorescence increase could be observed.

### 10.1.2 LP-MSN-AIPcS<sub>2a</sub>: removal of free photosensitizer

In Chapter 6 it was already discussed, that the washing procedure is highly important after attachment of AIPcS<sub>2a</sub> to MSN. It was also shown, that free AIPcS<sub>2a</sub> is uptaken into cells and the release out of single endosomes can be monitored, followed by staining of the whole cell afterward with photosensitizer (Figure 6.9).

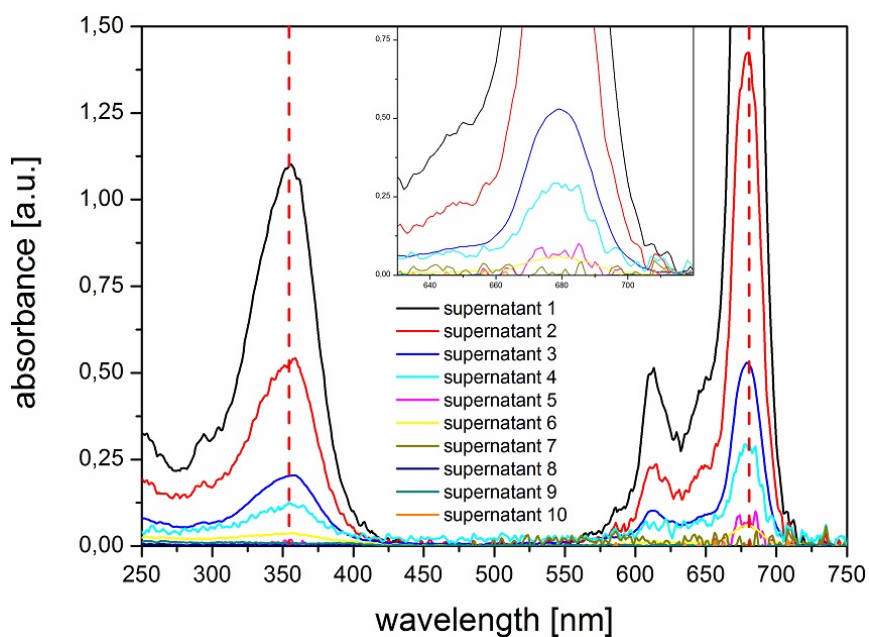


**Figure 10.6:** UV-Vis data taken from the supernatants of the washing procedure of the sample LP-MSN-AIPcS<sub>2a</sub>. No free photosensitizer could be detected in supernatants 9 and 10.

With the help of UV-VIS measurements the washing procedure of LP-MSN-AIPcS<sub>2a</sub> was monitored by subsequent measurements of the supernatants. The resulting spectra were compared with the standard MSN after AIPcS<sub>2a</sub>-functionalization (Figure 6.10). The obtained results are similar, therefore the washing of LP-MSN-AIPcS<sub>2a</sub> is assumed to be sufficient.

## 10 Outlook: Modifications of surface coated MSN

Nevertheless in all following cell experiments a spreading of the photosensitizer (AIPcS<sub>2a</sub>) occurred after photo-activation (639 nm). As free photosensitizer was eliminated as cause, another possibility could be photochemical cleavage of the sulfonamide bonds. [354] In cell tests performed with standard-MSN this cleavage couldn't be observed [15], but the attachment was slightly different (additional PEG-spacer). Another possibility would be the ending of the SLB@LP-MSN-AIPcS<sub>2a</sub> inside lysosomes (pH around 4) resulting in a degradation.

The cause of this side effect has to be cleared, as free photosensitizer spreading inside the cell is unfavorable and causes immediate cell death.

### 10.1.3 Delivery of different sized cargos with LP-MSN

#### Fluorescence live cell imaging of photo-activable supported lipid bilayer capped LP-MSN

After the successful characterization of LP-MSN-AIPcS<sub>2a</sub>, cargo loaded SLB@LP-MSN-AIPcS<sub>2a</sub> were incubated on HeLa cells. The first cargo was calcein. Therefore, calcein loaded SLB@LP-MSN-AIPcS<sub>2a</sub> were incubated for 21 h to allow an sufficient cell uptake via endocytosis. With spinning disc confocal fluorescence microscopy confocal cuts through the cells were recorded before and after activation of AIPcS<sub>2a</sub> with 639 nm light (Figure 10.7).

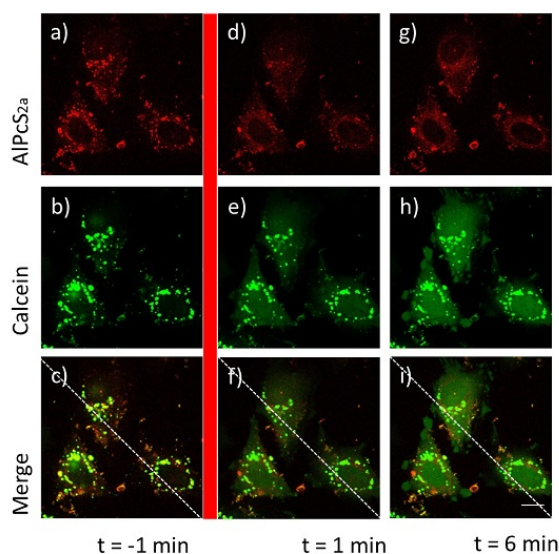


**Figure 10.7:** Fluorescence microscopy of SLB@LP-MSN-AIPcS<sub>2a</sub> loaded with calcein after 21h incubation on HeLa cells. (a-c) AIPcS<sub>2a</sub> (red) and calcein (green) are mainly co-localized (yellow) prior to photoactivation. The red line indicates photoactivation with 0.6 W/mm<sup>2</sup> of red light (639 nm). (d-f) 1 min after photoactivation, (g-i) 6 min after photoactivation. The scale bar represents 10 μm.

Before activation of the PS (Figure 10.7 a-c) the fluorescence of AIPcS<sub>2a</sub> (red) and calcein (green) are co-localized to a good amount and exhibit a dot-like pattern. This indicates, that the cargo calcein is still enclosed inside the mesopores and internalized by photoactivation. In the red channel a small

amount of photosensitizer is already spread inside the cells, which could be attributed to activation by daylight and out-of-focus fluorescence. After activation of the photosensitizer spreading of calcein inside the cell could be detected. Through the photoactivation singlet oxygen was produced, which caused disintegration of the SLB and the endosomal membrane and subsequent release of calcein out of the mesopores into the cytosol.

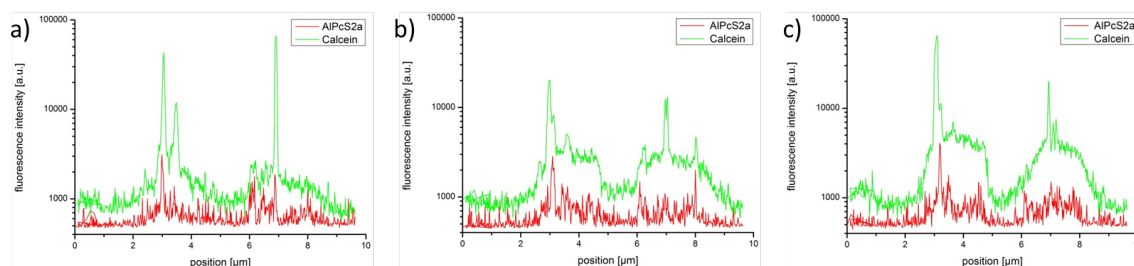


**Figure 10.8:** Intensity profiles of the calcein (green) and AIPcS<sub>2a</sub> (red) fluorescence along the dashed white lines in the activation series of calcein loaded SLB@LP-MSN-AIPcS<sub>2a</sub> (see Figure 10.7) for  $t = -1$  min,  $t = 1$  min and  $t = 6$  min with  $t = 0$  min denoting the point of photosensitizer activation.

Along the dashed white line inside Figure 10.7 c/f/i the intensity-profiles for AIPcS<sub>2a</sub> and calcein were determined. As a result an increase in calcein intensity could be observed over a distinct time, as calcein de-quenches through the dilution inside the cell compartments. The intensity of AIPcS<sub>2a</sub> stays more or less the same, but it could be observed, that not only calcein spreads over the whole cell but also AIPcS<sub>2a</sub>. This spreading leads to a damage of the cell, which can already be seen after 6 min in the formation of bubbles on the cell membrane. The formation is an indication for cell death. In a next set of experiments the delivery of the cargo propidium iodide (PI) was investigated. Propidium iodide was already tested with the dendrimeric system in this work and was successfully delivered by our groups before. [1] PI is a fluorescent, cell-membrane impermeable dye to stain nucleoli, as it interacts with the nucleic acids of ribosomal RNA. The particles were incubated for 21 h on HeLa cells. After that time period they were imaged. In this case the pictures do not show single confocal planes but an average of the intensity over multiple slices to improve the signal-to-noise ratio. Before photoactivation no staining of the nucleoli is visible (Figure 10.9 a/c). Due to the photoactivation a strong decrease in fluorescence occurs because of photobleaching (Figure 10.9 d-f). 10 min after the activation the nucleoli are visible (Figure 10.9 j/l). In the region of the six clearly visible nuclei (white boxes in Figure 10.9 a/d/g/j) the fluorescence intensity was measured and plotted, setting the fluorescence intensity at time point -1 min to 100 % (Figure 10.10).

In the plot depicting the intensity's of the nucleoli it can be seen, that the fluorescence is increasing with increasing time after activation with a strong photo-bleaching derived fluorescence-decrease (Figure 10.10). Again a spreading of AIPcS<sub>2a</sub> could be observed. The obtained measurements suggest a successful encapsulation and delivery of the small sized cargo's calcein and propidium iodide. As model for a bigger cargo Alexa-Fluor-Dextran 488 (AFD488, MW 10.000) citeAFD488 was tested. The hydrodynamic radius of this molecule is roughly 2.3 nm. Again HeLa cells were

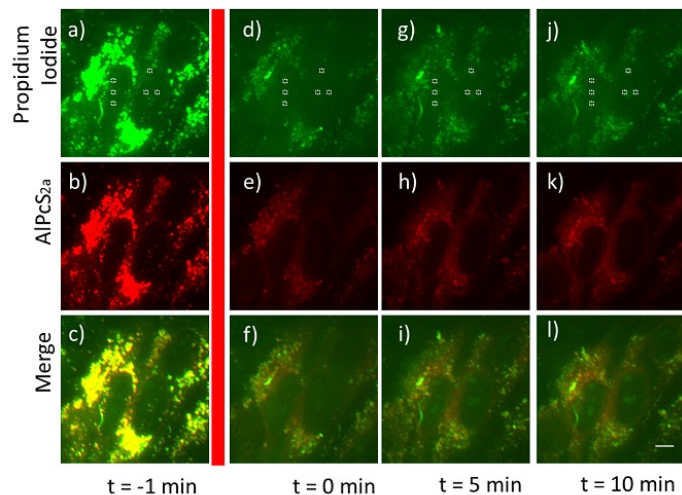


**Figure 10.9:** Fluorescence microscopy of SLB@LP-MSN-AIPcS<sub>2a</sub> loaded with propidium iodide after 21 h of incubation on HeLa cells. Several z-planes were averaged for each image in order to improve the signal-to-noise ratio, especially for the propidium iodide fluorescence. (a-c) Propidium Iodide (green) and AIPcS<sub>2a</sub> (red) before photoactivation. The red line indicates photoactivation with 1.2 W/mm<sup>2</sup> of red light (639 nm). (d-f) after photoactivation, (g-i) 5 min and (j-k) 10 min after photoactivation. Fluorescence intensity for the nucleoli indicated with white circles was measured, after photoactivation strong photobleaching effects. The scale bar represents 10  $\mu$ m.

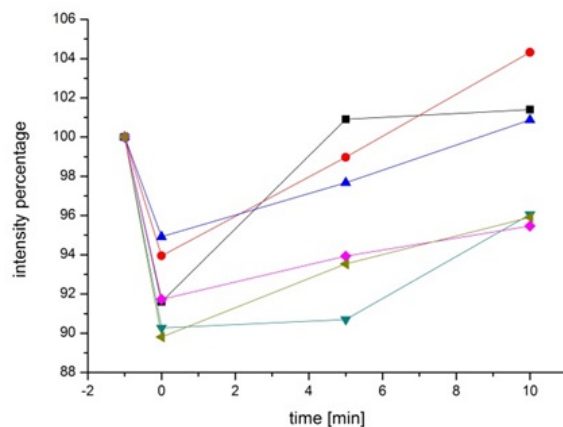


**Figure 10.10:** Propidium iodide intensities for the time points -1, 0, 5 and 10 min for the six different nucleoli. They are measured in the region of the nucleoli (within the outlined squares in Figure 10.9). The intensity at time point -1 min was normalized to 100 %. The decrease in intensity percentage at 0 min is caused by photo-bleaching due to photoactivation.

incubated with particles for 23 h, in this case AFD488 loaded SLB@LP-MSN-AIPcS<sub>2a</sub>, and an activation series comparable to the PI loaded SLB@LP-MSN-AIPcS<sub>2a</sub> was performed. Again not single confocal cuts but z-projections of the entire height of the cells out of confocal cuts are depicted

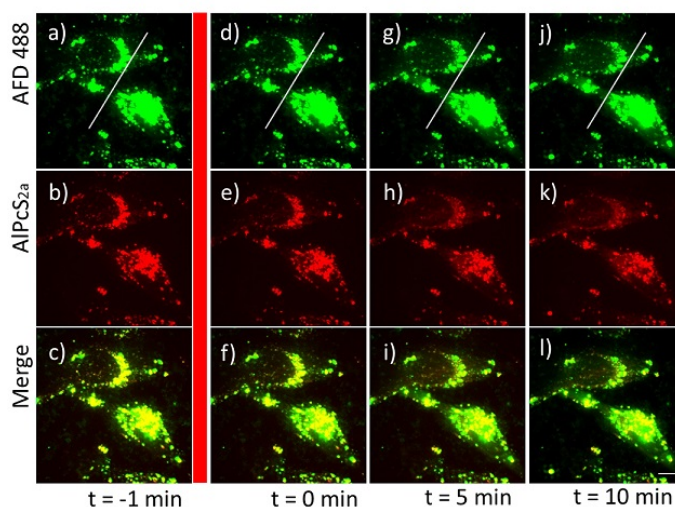


**Figure 10.11:** Fluorescence microscopy of SLB@LP-MSN-AlPcS<sub>2a</sub> loaded with AFD488 after 23 h incubation of HeLa cells. The channels represent z-projections of the entire height of the cells out of confocal cuts. (a-c) AFD488 (green) and AlPcS<sub>2a</sub> (red) are in the same regions (yellow) prior to photoactivation. The red line indicates photoactivation with 1.2 W/mm<sup>2</sup> of red light (639 nm). (d-f) after photoactivation, (g-i) 5 min and (j-l) 10 min after photoactivation. Along the white lines intensity profiles were measured. The scale bar represents 10  $\mu$ m.

(Figure 10.11). The scaling was chosen in order to visualize the spreading of dextrans in the cytoplasm in regions without particles. Therefore the particle fluorescence seems to be overexposed. The spreading of the dextran is not easy to visualize, due to the lack of self-quenching, also no de-quenching effect can be observed and the Alexa dye is bleaching relatively fast compared to other dyes which were used in this thesis.

Again the signal of the cargo (AFD488) and AlPcS<sub>2a</sub> is located in the same region which suggest a packing of the cargo inside the endosomes (Figure 10.11 a-c). After photoactivation a slight spreading of the cargo inside the cytoplasm could be observed (Figure 10.11 c/g/j). For a clearer demonstration the intensity profile through two cells in a region without big particles was measured along the dashed white line and plotted in Figure 10.12. For a greater visibility a black line was drawn in the region of the main fluorescence in the beginning.

Only a slight increase in AFD488-dextran fluorescence could be detected, which can be also seen in the intensity profiles plotted along the dashed white lines (Figure 10.12). Compared to the intensity of the particles a low amount of cargo seemed to be release inside the cell. We assume that the diffusion of the large cargo needs more time for diffusing out of the pore, due to steric or charge effects.

We also tried to deliver fluorescent-labeled phalloidin. But although it was already shown with even smaller pores in the MSN [1] it was not possible in our case. It seems that already the loading isn't efficient enough, as the fluorescence of the phalloidin labeling inside the particles was very weak.

But taken together we were able to demonstrate the release and delivery of small to large cargo

## 10 Outlook: Modifications of surface coated MSN

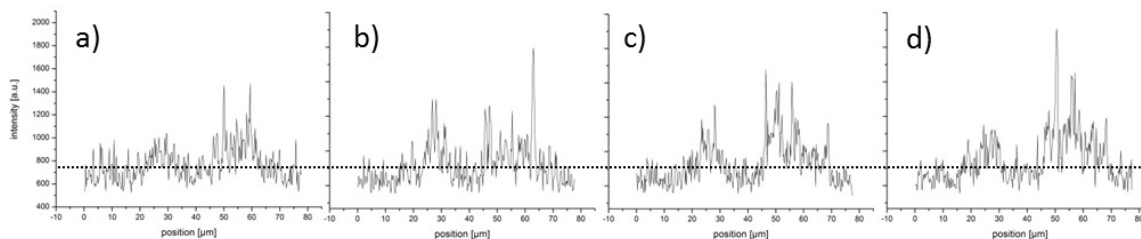


**Figure 10.12:** Intensity profiles of AFD488 fluorescence along the dashed white lines in the activation series of AFD488 loaded SLB@LP-MSN-AIPcS<sub>2a</sub> (see Figure 10.11) for  $t = -1$  min,  $t = 0$  min,  $t = 5$  min and  $t = 10$  min with  $t = 0$  min denoting the point after photosensitizer activation. A slight fluorescence increase in the region of the cytosol was observed.

molecules out of SLB@LP-MSN-AIPcS<sub>2a</sub>. This opens new application areas for the particles as now also small proteins can be delivered. In addition to the above observations, the spread of free photosensitizer was detected in the channel of AIPcS<sub>2a</sub>. As mentioned above, the cause of the formation of free photosensitizer has to be investigated in more detail in future studies.

### Photoinduced cargo release from post-synthesis modified LP-MSN with PVP capping

Also the functionality of LP-MSN-PVP-PEG-AIPcS<sub>2a</sub> particles was tested *in vitro*. As cargo again calcein was used and the red light photosensitizer AIPcS<sub>2a</sub> was attached to enable endosomal escape. HeLa cells were incubated with calcein-loaded LP-MSN-PVP-PEG-AIPcS<sub>2a</sub> for 21 h. After 21 h the cells were imaged with constant activation and monitoring. In Figure 10.13 a-c a confocal cut through the cells is depicted and a high degree of co-localization between calcein (green) and AIPcS<sub>2a</sub> (red) is visible (yellow). With increased activation time the cargo is released out of the endosomes. After the incubation time of 21 h the particles should have ended up in acidic cell compartments and the cargo calcein set free inside the endosome. Due to the acidification PVP was already protonated inside the endosome and calcein released. So that the photosensitizer only has to open endosomal membranes. After 5.5 min of activation (Figure 10.13 d-f) calcein is clearly visible inside the cytoplasm and nucleus. The fluorescence intensity inside the nucleus was measured over the whole activation time and plotted in Figure 10.14. In the fluorescence images as well as in the plotted intensities it can be seen that the calcein intensity decreases again after an increase over around 5.5 min. This decrease is attributed to photobleaching effects, as calcein is not very photostable. But the strong increase until 5.5 min is attributed to de-quenching effects as the dye is diluted out of the mesoporous system into the cell.

The constant but slow increase of AIPcS<sub>2a</sub>, in the plotted intensity over time, can be attributed to spreading of the photosensitizer as the fluorescence is measured inside the nucleus region, an area which could not be entered by the whole MSNs. This spreading is also visible in the cell pictures themselves. Beside the problem of AIPcS<sub>2a</sub> de-attachment the functionalization with PVP-PEG moieties was successful.

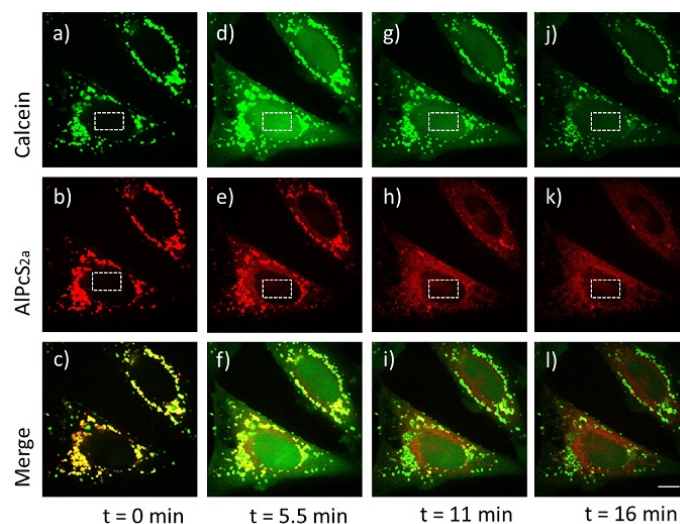


**Figure 10.13:** Fluorescence microscopy of LP-MSN-PVP-PEG-AIPcS<sub>2a</sub> loaded with calcein after 21 h incubation of HeLa cells. Constant monitoring and therefore activation of the cells with 0.6 W/mm<sup>2</sup> of red light (639 nm). (a-c) calcein (green) and AIPcS<sub>2a</sub> (red) are co-localized (yellow) in the beginning of the measurement. With increasing time the AIPcS<sub>2a</sub> gets activated and calcein is released (d-f) 5.5 min, (g-i) 11 min and (j-l) 16 min after the start of the measurement. The intensities inside the nucleus was measured for calcein and AIPcS<sub>2a</sub> (white box). The scale bar represents 10  $\mu$ m.

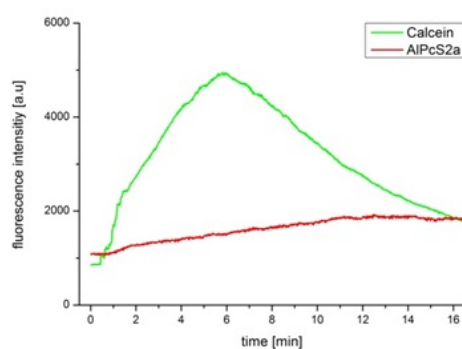


**Figure 10.14:** Fluorescence intensity of calcein (green) and AIPcS<sub>2a</sub> (red) inside the dashed white square in the activation series of calcein loaded LP-MSN-PVP-PEG-AIPcS<sub>2a</sub> (see Figure 10.13) with constant but lower laser intensity (0.6 W/mm<sup>2</sup>; 639 nm) photosensitizer activation. Decrease of calcein fluorescence is due to photobleaching.

## 10.2 Membrane-fusion inducing peptides - reduced SNARE peptides

This Chapter is based on the work in cooperation with: Alexandra Schmidt, Katharina Braunger, Thomas Bein, Christoph Bräuchle and with Harshal Zope and Alexander Kros. The synthesis of MSN for fusionogenic applications was mainly performed by Alexandra Schmidt and the reduced SNARE peptides were provided by the group of A. Kros.

In order to increase the application area of our supported lipid bilayer MSNs we wanted to include other possibilities to overcome the endosomal entrapment. One possible solution could be the incorporation of fusion inducing proteins inside the SLB. In the group of Prof. Kros a reduced SNARE (soluble N-ethyl-maleimide-sensitive fusion (NSF) protein) attachment protein model for membrane fusion was developed. [277]

In all living system membrane fusion is a key process for facilitating transport between and within cells, for example in vesicle transport, cell division and chemical synaptic transmission. [355] SNARE proteins play an important role in this processes as they mediate the fusion process. [355, 356] The interaction between two membrane bound SNAREs and a cytoplasmic SNARE leads to the formation of a four-helical bundle complex, which zip up and simultaneously induces bilayer fusion. [277, 355] As the exact mechanism is still unclear, reduced SNARE proteins were developed. The complex designed in the Kros group consists of a lipid, a short PEG-linker and the oligopeptide hybrids (LPK/LPE, see also Figure 10.15). This peptides are able to induce fusion between liposomes. In order to demonstrate this ability, they used liposomes with incorporated reduced SNARE peptides, either LPE or LPK. After mixing of these two liposomes an increase in the size could be observed and a content mixing between the different liposomes has been shown. Figure 10.15 shows a schematic

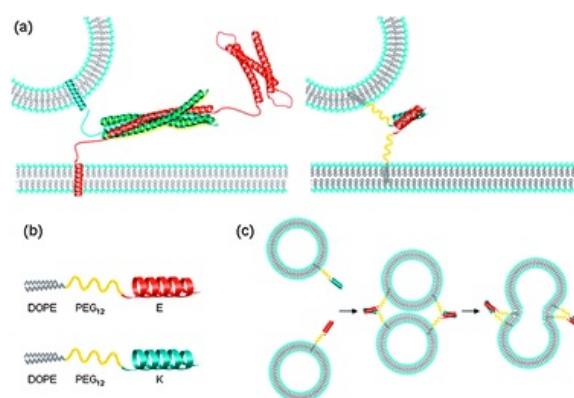


**Figure 10.15:** (a) Model of the natural SNARE-protein (left) and of the the minimal model (right). Both systems are based on the same principle, in the minimal model only the key features were adopted (b) Schematic illustrations of  $G(EIAALEK)_3-NH_2-PEG_{12}-DOPE$  (LPE) and  $(KIAALKE)_3GW-NH_2-PEG_{12}-DOPE$  (LPK). (c) After mixing of Liposomes with either LPE or LPK, coiled-coil formation occurs, which induces close proximity and thus fusion. Figure was taken from Ref [357].

## 10.2 Membrane-fusion inducing peptides - reduced SNARE peptides

representation of the the natural SNARE-protein-based model in comparison to the minimal model. The minimal model mimics the coiled-coil forming motif and consist of a DOPE (or a cholesterol) tail, a PEG<sub>12</sub> linker and the amino acid sequence. For LPE the sequence is G(EIAALEK)<sub>3</sub>-NH<sub>2</sub> (peptide E) and for LPK (KIAALKE)<sub>3</sub>GW-NH<sub>2</sub> (peptide K). Between peptide E and K the formation of coiled coil motives leads to membrane fusion. [277] The lipid (or cholesterol) tail can be diffused into membranes, the PEG<sub>12</sub> linker has the function of a spacer and the amino acid sequence for forming coiled-coil-motives. [358] Besides the PEG<sub>12</sub>-linker, the usage of PEGylation should be avoided, since it can inhibit the fusion process as it prevents close proximity of the membranes. [359]

To combine these two projects, the fusion peptide and SLB coated MSNs, a collaboration between the groups of Prof. Bein, Prof. Bräuchle and Prof. Kros was started. In this collaboration, we wanted to show in real time and on a single nanoparticle level the fusion process between MSN with an SLB and one reduced SNARE-peptide and giant vesicles or cells functionalized with the other reduced SNARE-peptide.

**Table 10.3:** Various synthesis approaches for introducing SNARE-peptides into the SLB of MSN. With dioleoyl-sn-glycero-3-phosphocholine (DOPC), dioleoyl-trimethylammonium propane (DOTAP), dioleoyl-phosphatidylethanolamine (DOPE), cholesterol-PEG-peptide E/K (CPE/CPK), DOPE-PEG-peptide K (LPK), carboxyfluorescein (cf).

#	SLB-composition	SNARE-peptide	method
1	DOPC/DOTAP 70/30 $w_i$	CPE-cf	diffusion, 2/6 h
2	DOPC/DOTAP 70/30 $w_i$	CPE-cf	mixing
3	DOPC/DOTAP/cholesterol 80/10/10 $w_i$	CPE-cf	diffusion, 2 h
4	DOPC/DOTAP/cholesterol 80/10/10 $w_i$	CPK+E-cf	diffusion, 2 h
5	DOPC/DOTAP/cholesterol 80/10/10 $w_i$	CPE-cf, 1 %	mixing
6	DOPC/DOTAP/cholesterol 80/10/10 $x_i$	CPE-cf, 1 %	mixing
7	DOPC/DOTAP 70/30 $w_i$	DOPE-lr, 1 %	diffusion, 4/24 h
8	DOPC/DOTAP 70/30 $w_i$	LPK + E-cf	diffusion, 37°C, 24 h
9	DOPC/DOTAP 70/30 $w_i$	LPK + E-cf	diffusion, 23°C, 24 h

The incorporation of the reduced SNARE peptide into the SLB was performed analogous to the diffusion of DSPE-PEG-TL into the SLB (Chapter 6). In first attempts we used cholesterol as tail, which was proved to incorporate into cell membranes and liposomes in the Kros group. [360] In Table 10.3 the different approaches are listed. The incorporation of the cholesterol tail was not successful, neither the diffusion approach, nor mixing of the lipids with the construct before SLB-formation. Also changes in the SLB composition did not succeed. The incorporation of the according construct was proved by cover-slip measurements with fluorescent labeled MSN and addition of fluorescent labeled (corresponding) peptide to the particles after synthesis. If the incorporation would have worked out co-localization would be visible.

## 10 Outlook: Modifications of surface coated MSN

As the cholesterol-tail could not be successfully incorporated into the SLB we tested the incorporation of fluorescent labeled DOPE into the SLB by the diffusion method. Since this approach was successful, we subsequently used DOPE as tail for the reduced SNARE motive. For the incorporation of the reduced SNARE motive into cell membranes further on cholesterol was utilized. The best

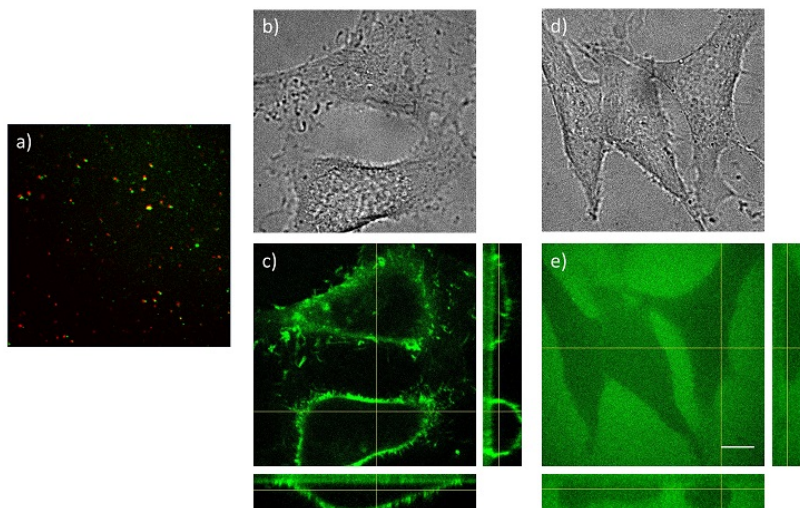


**Figure 10.16:** (a) SLB@MSN-SH<sub>in</sub>-Atto633<sub>out</sub> (red) with LPK-Ecf (green) diffused into the SLB. Co-localization (yellow) results from successful incorporation. (b) Brightfield image and (c) fluorescence image of HeLa cells incubated for 1 min with CPE and K-cf (green) each, staining the cell membranes. (d) Brightfield image and (e) fluorescence image of HeLa cells incubated for 1 min with K-cf (green), no staining of the cell membranes but fluorescence in the cell medium. The scale bar represents 10  $\mu\text{m}$ .

attempt for incorporation of the reduced SNARE peptide into SLB@MSN-SH<sub>in</sub>-Atto633<sub>out</sub> was using LPK and diffusion on a shaker at room temperature for 24 h. In Figure 10.16 the co-localization (yellow) between MSN-SH<sub>in</sub>-Atto633<sub>out</sub> (red) and carboxy-fluorescein labeled peptide E bound to LPK is depicted. After the incorporation of LPK into the SLB was achieved, the incorporation of CPE into HeLa cells was tested. Firstly the cell membrane was functionalized with the reduced SNARE motive (CPE) by incubation for 1 min. Afterwards, the corresponding labeled peptide K-cf was added and the cells were washed. The cell-membrane staining demonstrates a successful incorporation of the construct into the membrane (Figure 10.16 c). As control experiment we also incubated the fluorescent K-cf with the cells, according to the staining step. Here again we washed the cells after incubation, but in this case no staining of the cell membrane could be observed. The cell boundaries are nevertheless visible, because K-cf is still present in the cell medium (Figure 10.16 e).

We already observed during the creation of the SLB around the NPs that the temperature in the diffusion step seems to play a role for the functionality of LPK. Hence we stored a small amount of LPK at 37°C and one at RT, the normal storage is at -20°C, to prove our assumption. After one day, comparable to the diffusion time in the synthesis, we incubated HeLa cells with this LPKs and E-cf for subsequent staining. In Figure 10.17 the result is depicted. The cell membrane staining in

## 10.2 Membrane-fusion inducing peptides - reduced SNARE peptides

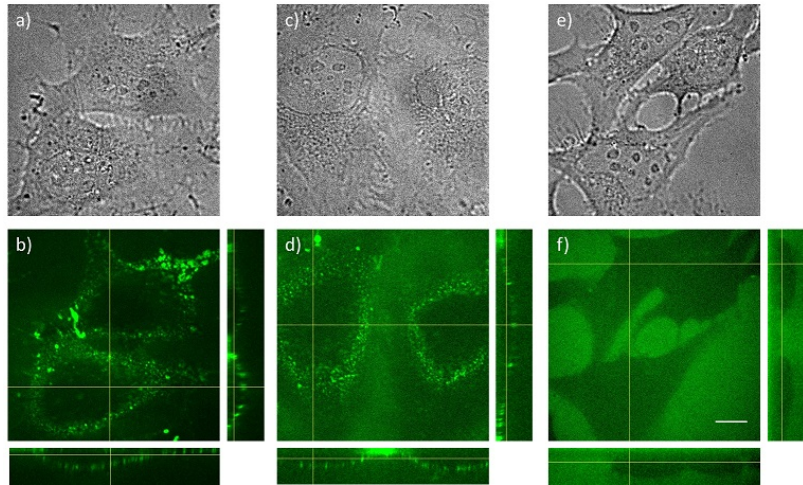


**Figure 10.17:** HeLa cell incubated with LPK-E-cf and E-cf as functionality test. (a) Brightfield image and (b) fluorescence image of HeLa cells incubated for 1 min with LPK (stored for 1 d at RT) and E-cf (green) each, staining the cell membrane. (c) Brightfield image and (d) fluorescence image of HeLa cells incubated for 1 min with LPK (stored for 1 d at 37°C) and E-cf (green) each, staining the cell membrane less than RT-stored LPK. (e) Brightfield image and (f) fluorescence image of HeLa cells incubated for 1 min with E-cf (green), no staining of the cell membrane but fluorescence in the cell medium. The scale bar represents 10  $\mu\text{m}$ .

the case of LPK (RT) was stronger than with LPK (37°C), but both constructs exhibit a weaker staining than the cholesterol-construct. This result suggest a temperature-dependence of peptides. Also it could be concluded, that it is useful to use different anchor groups for SLB and cell membrane incorporation.

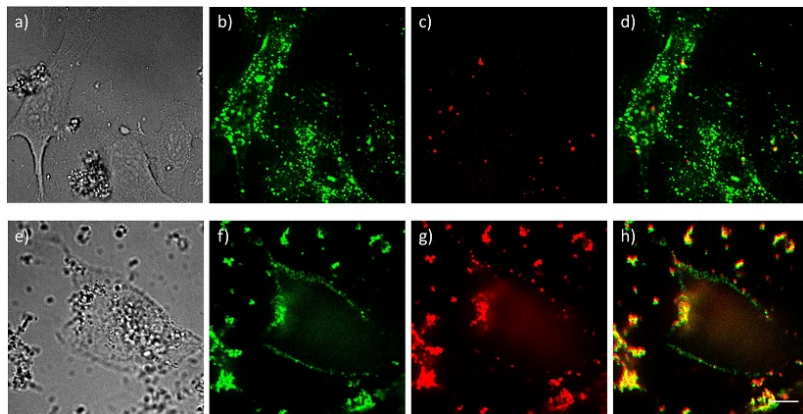


**Figure 10.18:** HeLa cell incubated with CPE and LPK-SLB@MSN-SH<sub>in</sub>-Atto633<sub>out</sub>. (a-d) LPK-SLB@MSN-SH<sub>in</sub>-Atto633<sub>out</sub> loaded with calcein and incubated for 2 h. (e-h) LPK-SLB@MSN-SH<sub>in</sub>-Atto633<sub>out</sub>, SLB stained with bodipy and incubated for 6 h. The scale bar represents 10  $\mu\text{m}$ .

The last step was to investigate if fusion could be observed for reduced SNARE motive functionalized

## *10 Outlook: Modifications of surface coated MSN*

HeLa cells and MSN. For visualization we used two different approaches. First the incorporation of a membrane-impermeable cargo (calcein), which should be able to diffuse into the cell after fusion of the MSN with the cell (Figure 10.18 a-d). Second we used a bodipy-labeled lipid, mixed into the SLB (Figure 10.18 e-h). In the case of fusion on the cell membrane the cell membrane should be stained. If the fusion needs a pH change and the fusion takes place inside the endosomes a separation between the endosome and the particles should be observable. The cell experiments revealed problems with the incorporation of calcein, as can be seen only a few particles were internalized (Figure 10.18 c), but many calcein-filled endosomes can be detected which do not contain MSN (Figure 10.18 b). Nevertheless also no release of the cargo was detectable. The fusion process was believed to take place within a few minutes, but even after several hours no release of calcein or fusion detectable with bodipy was observed. As the pH, temperature, serum proteins or the used cell line can influence the fusion behavior, it has to be investigated which factor is the determining one.

## 10.3 Membrane-fusion inducing peptides - fusion peptide H5WYG

### H5WYG

This Chapter is based on the work in cooperation with: Alexandra Schmidt, Katharina Braunger, Thomas Bein, and Christoph Bräuchle. The synthesis of MSN for fusiongenic applications was mainly performed by Alexandra Schmidt.

In nature, membrane-fusion is not only used within one organism, but also for virus entry. To induce fusion the natural distance between membranes, caused by electrostatic repulsion and steric interactions, of 10 - 20 nm has to be overcome. Viruses overcome this hurdle by using fusion proteins. [357] One example is the influenza virus, the envelope of the virus particles consists to a large extent of the glycoprotein hemagglutinin. Hemagglutinin possesses two domains, one is responsible for membrane binding (HA1) and the other to induce the fusion process (HA2). [361] In Figure 10.19 a the general principle of the fusion process is shown. After binding of subunit HA1 to sialic acid receptors (not shown) the protein undergoes a conformational change in the acidic environment of the endosomes. The illustration displays the pre-fusion conformation in the first step, in a second step at low pH the extended intermediate is forming, and the fusion peptide (green) interacts with the target bilayer. In the next two steps the intermediate collapses and therefore brings the membranes together. [357]

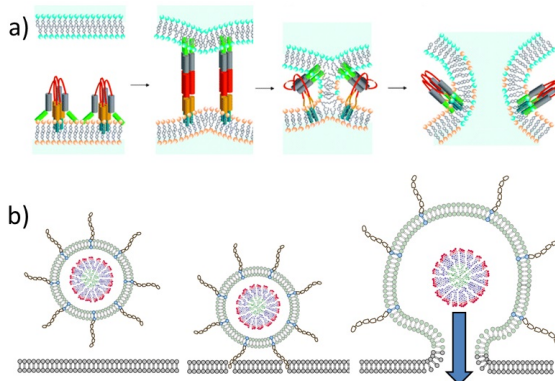


**Figure 10.19:** a) Schematic representation of full fusion protein hemagglutinin. First the pre-fusion state, second formation of an extended intermediate (fusion peptide (green) inside target membrane), and finally collapse of the intermediate and fusion of the membranes. [357] b) Schematic representation of the possible mechanism for fusion induced by a fusion peptide incorporated into the SLB of MSN.

As the full fusion protein would induce an immune response [362], much effort was put into mimicking this system in order to circumvent endosomal entrapment. The fusion domain on the N-terminus of HA2 was identified to be a good candidate to overcome the endosomal entrapment. The fusion domain forms an  $\alpha$ -helix structure which is capable of insertion into membranes. [363] Based on the sequence of this fusion domain (23 N-terminal amino acids) the so-called fusion peptides were developed. Besides the peptide with HA2-analogous structure, peptides with slightly improved amino-acid sequences were developed, for example INF1-4, INF7, E5 or H5WYG. They all vary in a few amino acids from

## 10 Outlook: Modifications of surface coated MSN

the original amino acid structure, the sequences for the original segment and H5WYG, which we used, are listed in Table 10.4. H5WYG performs a conformational change from random coil to  $\alpha$

**Table 10.4:** Sequence of fusion peptide H5WYG and N-terminal segment of the subunit HA2. [364]

	amino acid sequence
H5WYG	GLFHAI AHFIHGGWHGLIHGWYG
HA2, N-terminal	GLFGAIAGFIEGGWTGMIDGWYG

helix in a pH range between 5 -6.5 due to protonation of the histidines, finally leading to membrane rupture. [364, 365] But, because of the protonation capacities mainly of the histidines, there is also the hypothesis, that H5WYG is buffering the pH inside the endosomes, similar to PEI, causing osmotic swelling and finally leading to endosomal destabilization. [365] The goal of experiments with this so called fusion peptide was to investigate the working mechanism.

To incorporate the fusion peptide into SLB@MSN-SH<sub>in</sub>-NH<sub>2out</sub> we used amino-functionalized H5WYG (H<sub>2</sub>N-H5WYG-GGC-COOH) and either DSPE-PEG<sub>2000</sub>-Mal or DOPE-PEG<sub>4</sub>-Mal to obtain DSPE-PEG<sub>2000</sub>-H5WYG / DOPE-PEG<sub>4</sub>-H5WYG. We tested two different linkers and lipids, because these factor can influence the incorporation into the SLB, especially because of the poor water solubility of H5WYG. The lipid constructs then were incorporated similar to targeting ligands or reduced SNARE constructs into the SLB by simple diffusion. In Figure 10.20 the co-localization (yellow) between FITC-labeled H5WYG (green) and Atto633 (red) labeled MSN is displayed. In both cases the incorporation should have worked, but with DOPE-PEG<sub>4</sub>-H5WYG we obtained the more reproducible results and so it was chosen over DSPE-PEG<sub>2000</sub>-H5WYG, also because the co-localization is slightly better.

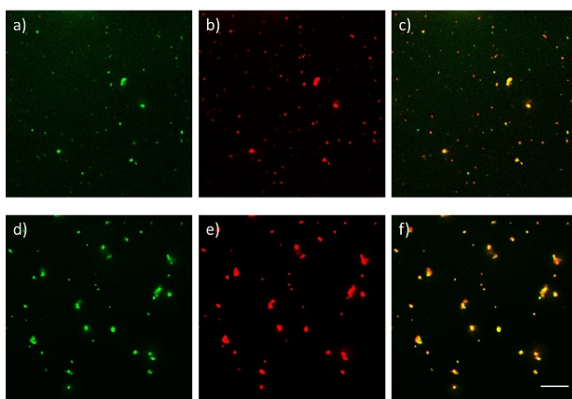


**Figure 10.20:** Co-localization (yellow) between FITC-labeled H5WYG (green) and Atto633 (red) labeled MSN (a-c) FITC-H5WYG-PEG<sub>2000</sub>-DSPE-SLB@MSN (d-f) FITC-H5WYG-PEG<sub>4</sub>-DOPE-SLB@MSN. (a/d) FITC fluorescence, (b/e) Atto633 fluorescence, (c/f) merge of FITC and Atto633 fluorescence. Scale bar represents 10  $\mu$ m.

### 10.3 Membrane-fusion inducing peptides - fusion peptide H5WYG

In a first attempt the functionality of the entire process should be tested. For this purpose, we loaded calcein into the pores of covalently Atto633 labeled MSN and incubated the SLB-sealed and H5WYG-functionalized particles on HeLa cells. But as can be seen in Figure 10.21, neither after 4 h, nor after 22 or 65 h any release of calcein into the cells could be observed. On the contrary, free calcein could be detected, as only fluorescence derived from calcein could be detected in several endosomes (green, especially in Figure 10.21 a).

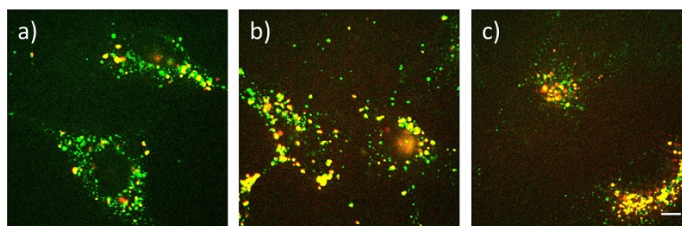


**Figure 10.21:** HeLa cells incubated with calcein (green) loaded H5WYG-PEG<sub>4</sub>-DOPE-SLB@MSN (red) for (a) 4 h (b) 22 h (c) 65 h. Especially after 4 h a high amount of calcein without MSN fluorescence was detected. Scale bar represents 10  $\mu\text{m}$ .

It was also observed, that the co-localization between the particles and the cargo seems to increase over time. This effect is attributed to fusion of endosomes among themselves on their way to become lysosomes at the end. The greater aggregation behavior of the particles could possibly arise from an unstable SLB formation, which would also explain the high amount of free calcein, which was not observed without incorporation of fusion peptides (see also Figure 6.7 where the co-localization was almost 100 %).

The influence of serum proteins on the fusion behavior of these kind of peptides is also discussed in the literature. It is stated, that for H5WYG the presence of serum proteins inside the cell culture medium has no influence. [364] But as the binding to PEG reduces the activity to more acidic environments [365] it was also considered to influence the system. But also measurements in serum free environments has not resulted in better co-localization between calcein and MSN or release of calcein inside cells.

In a different approach, we did not use adsorbed calcein, but tested the integrity of the SLB with bodipy-labeled lipid (DOPC) during the experiment (Figure 10.22). As can be seen a high amount of free bodipy is visible already on the coverslip (Figure 10.22 a). In case of H5WYG-free particles less unbound bodipy is visible, but also fewer particles are available (Figure 10.22 d). The cell experiments revealed a slight staining of the cell membrane especially in the case of H5WYG containing MSN (Figure 10.22 c/f), but free bodipy is also able to incorporate into cell membranes. A conclusion on the mechanism of fusion therefore was not yet possible.

Additionally, we tested the combination of the pH-dependent polymer PVP (see Chapter 7) and fusion peptides. The fusion peptide hereby was covalently attached to a PEG to the NH<sub>2</sub> group of H5WYG. The MSN in this case were only loaded with calcein. On the coverslip many evenly distributed particles were observed (Figure 10.23 a). Incubation on cells didn't show any release of calcein into the cytosol, even after 41 h of incubation (Figure 10.23 c). Co-localization experiments

## 10 Outlook: Modifications of surface coated MSN

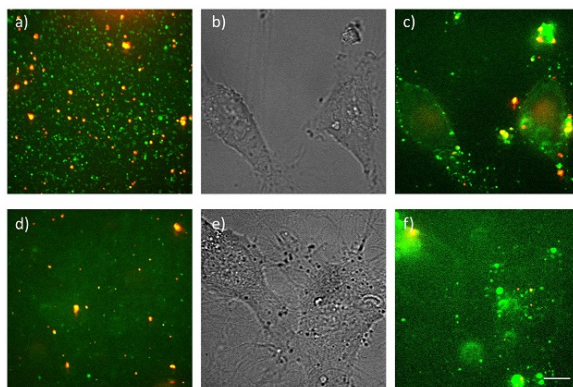


**Figure 10.22:** (a) Bodipy (green) labeled H5WYG-PEG<sub>4</sub>-DOPE-SLB@MSN (red) (d) Bodipy (green) labeled SLB@MSN. (b) Brightfield and (c) fluorescence image of HeLas cells incubated for 1.5 h with H5WYG-PEG<sub>4</sub>-DOPE-SLB@MSN. (e) Brightfield and (f) fluorescence image of HeLas cells incubated for 1.5 h with SLB@MSN. Scale bar represents 10  $\mu\text{m}$ .

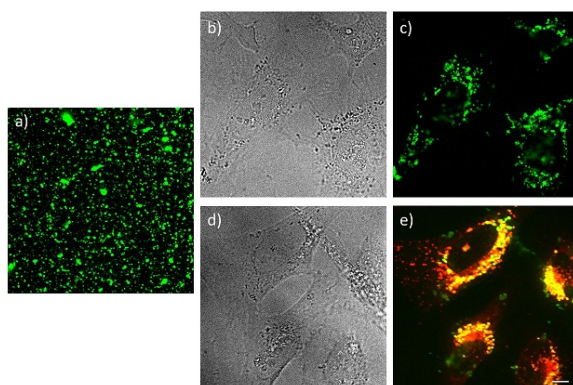


**Figure 10.23:** (a) MSN-PVP-PEG-H5WYG loaded with calcein imaged on a coverslip. (b) Brightfield and (c) fluorescent image of HeLa cells incubated for 4 h with MSN-Calcein-PVP-PEG-H5WYG. and (d) Brightfield and (e) fluorescent image of HeLa cells incubated for 41 h with MSN-Calcein-PVP-PEG-H5WYG (green) and Lysotraker Red (red). High amount of co-localization can be detected (yellow). Scale bar represents 10  $\mu\text{m}$ .

with a lysosome staining (Figure 10.23 e) dye revealed that the particles were already transported to the lysosomes and therefore were transported to acidic compartments, but the lysosome membrane seems to stay intact despite the presence of the fusion peptide. This could be either an indication for a buffering capacity of the fusion peptide, as the polymer needs an acidic pH in order to release cargo, or the need of two lipid membranes to induce fusion.

## 10.4 Summary

In this thesis it was demonstrated, that mesoporous silica nanoparticles exhibit a great platform for targeted drug delivery applications. Various different capping and release systems were investigated and their functionality *in vitro* (including live-cell experiments) was proven. Drug delivery systems are desired in order to safely hide non-membrane-permeable cargos as well as membrane-permeable cargos inside the nanoparticle in order to prevent the cargo or the body from damage.

The **first system** (chapter 6) presented a combination of the high loading capacity of MSN, the supported lipid bilayer for controlled release, the addition of targeting ligands, and overcoming of endosomal entrapment by photoactivation. This system exhibits an ideal platform as cargo molecules, targeting ligands and the photosensitizer can be varied easily.

In the **second system** (chapter 7), the pH-responsive polymer PVP was investigated as drug delivery platform. Beside supported lipid bilayers, the employment of stimuli-responsive polymers is a new promising capping approach for MSN. In addition to its ability to encapsulate membrane-permeable cargos within the mesopores, the features of our previous developed system (attachment of photosensitizer and targeting ligands) could be successfully employed to this approach. Additionally, the biocompatibility of our novel drug delivery platform was investigated *in vivo* (mouse model) and proved to be nontoxic.

The **third system** (chapter 8) is an example for internal pore modifications. In contrast to the systems presented so far, the mechanism to overcome endosomal entrapment is not relied on a photosensitizer, but on inducing the proton sponge effect. For this purpose the shell of the MSN is modified with a dendrimeric polymer which is known to induce a proton sponge effect. Osmotic swelling finally leads to membrane rupture and subsequent cargo release. Cytotoxicity tests suggest a very good bio-tolerability of these kind of particles. Targeting could be achieved by binding targeting ligands to the outer periphery of the MSNs.

A **fourth system** (chapter 9) was an example of particle pore gating, as we used a bulky enzyme to close the pores. The release trigger in this case was internally as we attached an enzyme inhibitor on the particle surface which binds pH-dependent to the enzyme. By incorporating unnatural amino acids into the enzyme we were also able to incorporate targeting moieties. Again we achieved a versatile drug delivery platform.

Increasing the pore size of the MSN (**fifth system**) in order to gain greater variation possibilities for cargo loading is one important point, in order to further enhance the surface coating approach we discussed in this work. We demonstrated the release of different sized cargos out of large pore MSNs with two different, but for standard pore sizes already established, capping systems. The used capping systems were the supported lipid bilayer and the pH-dependent polymer PVP. In both cases successful release was demonstrated. Nevertheless, the systems raised new questions, as the binding of a photosensitizer to the large pore system is not as straight forward as the addition of capping systems and the delivery of cargos of different sizes.

Furthermore we incorporated fusogenic peptides into the SLB (**sixth and seventh system**) in order to expand our platform presented in the first system to an internal trigger. Especially for membrane-impermeable cargos the supported lipid bilayer offers an easy method to cap MSNs,

## 10 Outlook: Modifications of surface coated MSN

and the systems can be simply modified afterward, e.g. with targeting moieties. The first step, the successful incorporation of fusion inducing peptides into the SLB was demonstrated. Two different fusigenic peptides were investigated. First a influenza virus-derived peptide (H5WYG) was examined with the aim to clarify the working mechanism. And second a minimal model of the cellular “SNARE” proteins was applied to the SLB coated MSN and the cells. The successful incorporation of the peptides into the cell membrane could be demonstrated and the working direction outlined. After the successful implementation of targeting ligands and stimuli responsive pore and endour some opening mechanisms the next step now should be testing the particle behavior *in vivo* with real chemotherapeutica. Our studies demonstrate various drug delivery platforms, in which the particles can be modified in many parameters. Therefore good chances exist to adapt the system to the challenges arising in *in vivo* studies.

# 11 Perspective

This chapter is adapted from the publication “Multifunctional Mesoporous Silica Nanoparticles as a Universal Platform for Drug Delivery”, published in *Chemistry of Materials*, written in collaboration with C. Argyo from the group of T. Bein. [14]

Colloidal MSNs have attracted great attention as potential drug delivery systems for cancer cell targeting and as bioimaging devices. In addition to their biocompatibility and biodegradability, they can be selectively modified at their inner and outer surface. Guest molecules can be efficiently encapsulated in their tunable pore system. Furthermore, it is possible to functionalize their outer surface with targeting ligands, biomimetic and other pore gating molecules, fluorescent dyes, and biocompatible polymers. Compared to most other prominent organic carriers, such as liposomes and polyplexes, MSNs offer several advantages including high loading capacity, high stability, and the ability to protect the guest molecules from various biochemical attacks causing degradation of the bioactive cargo molecules. Extensive *in vitro* studies on the controlled release of therapeutics and the evaluation of cytotoxicity have proven the feasibility of multifunctional MSNs for a sustainable and efficient drug delivery to cancer cells.

Today’s challenge is the investigation of pharmacokinetics and pharmacodynamics of mesoporous silica nanoconstructs for *in vivo* diagnostic and therapeutic applications. Issues and opportunities have been recently reviewed by several groups. [184, 186, 366, 367] The biological effects of MSNs at different levels ranging from molecules, cells, and blood to tissue and organs, involving cytotoxicity, biodegradability, blood compatibility, biodistribution, and excretion, are currently under investigation. Oral administration and injection into the bloodstream of such nanocarriers require specific properties for long-term stability during circulation in the organism, specific targeting of the desired location, and controllable release of the loaded drugs to obtain the desired therapeutic outcome.

Controlling all these requirements is important to avoid side effects harming healthy tissue. Researchers are still faced with many challenges, especially *in vivo* applicable stimuli-responsive release mechanisms, targeting specificity, and biosafety issues, which need to be fully understood to achieve efficient and safe drug delivery. A complete understanding of the mechanisms for intracellular uptake, trafficking, and the fate of multifunctional MSNs in the body would be highly desirable. Up to now, only a few *in vivo* studies of the pharmacokinetics of multifunctional MSNs including biodistribution, biodegradation, and excretion and clearance have been performed, and additional work in this area is clearly needed. [228, 368–371] Additional functional groups such as PEG chains on the external surface of MSNs seem to be important for achieving the EPR effect; they were shown to decrease the clearance through the RES. [47, 228] Selected strategies and model systems are needed to gain insights into such complex processes before reaching the stage of clinical trials.

## 11 Perspective

Comprehensive reviews address the state of the art regarding preclinical studies. [184, 367] Model systems for investigations on the way to clinical trials are being discussed, including chorioallantoic membrane, zebrafish embryo, and mouse, among others. [372–374]

The pharmacokinetics of nanomaterials are closely related to *in vivo* toxicity, biocompatibility, and retention. The issue of potential toxicity to cells or organisms caused by nanocarriers seems to be strongly influenced by several particle properties including size, morphology, and surface functionality. [215] Studies on the dissolution of silica nanoparticles concerning retention and clearance in the body showed that the silica was adsorbed or excreted in the urine in the form of silicic acid or organic silica species. [228]

Finally, recent studies focus on the ultimate combination of diagnostic and therapeutic capabilities in the multifunctional mesoporous nanoparticles, such that the nanocarrier uses diagnostic information to control or tune its therapeutic actions. One such approach could be the detection of the presence of multiple receptors indicating specific target tissue, where the logical combination of this information leads to release of drug only at this location. And another one could be the detection of several enzymes that together constitute the signature of a target tissue. Therefore the future is bright for multifunctional mesoporous nanoparticles in diagnostics and therapy.

## List of abbreviations

abbreviation	explanation
AFD	alexa fluor dextran
AlPcS <sub>2a</sub>	Al(III)phthalocyanine chloride disulfonic acid
ALT	alanine transaminase
AOTF	acousto-optical tunable filter
AST	aspartate transaminase
ATP	adenosine triphosphate
BET	brunauer-emmett-teller
BP	band pass
BUN	blood urea nitrogen
(H)CA	(human) carbonic anhydrases
CAPS	3-(Cyclohexylamino)-1-propanesulfonic acid
CD	cyclodextrin
CPE	cholesterol - PEG <sub>12</sub> - peptide K
CTAC	cetyltrimethylammonium chloride
DAPI	4',6-diamidino-2-phenylindole
DFT	density functional theory
DLS	dynamic light scattering
DMEM	dulbecco's modified eagle's medium
(ss)DNA	(single-stranded) desoxyribonucleic acid
DOPC	dioleoyl-sn-glycero-3-phosphocholine
DOPE	dioleoyl-phosphatidylethanolamine
DOTAP	dioleoyl-trimethylammonium propane
DOX	doxorubicin
DPBS	dulbecco's phosphate-buffered saline
DSPE	1,2distearoyl-sn-glycero-3-phosphoethanolamine
DTT	dithiothreitol
D3	PAMAM dendron 3rd generation
EDC	1-ethyl-3-(3-dimethylaminopropyl)carbodiimide

*List of abbreviations*

abbreviation	explanation
E-cf	peptide E - carboxyfluorescein
EGF(R)	epidermal growth factor (receptor)
EPR	enhanced permeability and retention effect
EMCCD	electron-multiplying charge-coupled device
FA	folic acid
FBS	fetal bovine serum
FC-4	fluorocarbon Surfactant
FITC	fluorescein isothiocyanate
FRET	fluorescence resonance energy transfer
(E)GFP	(enhanced) green fluorescent protein
GSH	glutathion
HBG	HEPES with 5% glucose
HBSS	hank's balanced salt solution
HeLa	cervix adenocarcinoma cell line
HEPES	4-(2-hydroxyethyl)-1-piperazineethanesulfonic acid
(poly)HIS	(poly)histidine
HMEC-1	immortalized human microvascular endothelial cells
HuH7	human hepato cellular carcinoma cell line
H5WYG	endosomolytic peptide
ICG	indocyanine green
IEP	isoelectric point
IR	infrared
KB	HeLa derived cell line
K-cf	peptide K - carboxyfluorescein
LDH	layered double hydroxides
LPE	DOPE - PEG <sub>4</sub> - peptide E
LPK	DOPE - PEG <sub>4</sub> - peptide K
LP-MSN	large-pore mesoporous silica nanoparticles
MCM-41	Mobil Crystalline Materials
MDR	multiple drug resistance
MPTES	(3-mercaptopropyl)-triethoxysilane
MSN	mesoporous silica nanoparticles

abbreviation	explanation
MTS	methanethiosulfonate
NA	numerical aperture
(P)NIPAM	(poly)N-isopropylacrylamide
NIR	near-infrared
(ss)NMR	(solid state) nuclear magnetic resonance
NSF	N-ethyl-maleimide-sensitive fusion
PAMAM	poly(amidoamine)
(D)PBS	(dulbecco's) phosphate buffered saline
PCI	photochemical internalization
PDT	photodynamic therapy
PEG	polyethylene glycol
PEI	polyethyleneimine
PFA	paraformaldehyde
PI	propidium iodide
PMO	periodic mesoporous organosilicas
PS	photosensitizer
PVP	poly(2-vinylpyridine)
QD	quantum dot
RD	5(6)-carboxy-X-rhodamine
(r/si/t)RNA	(ribosomal/small interfering/transfer) ribonucleic acid
RGD	Arg-Gly-Asp amino acid sequence
RES	reticuloendothelial system
phSA	benzene sulfonamide
rcDH	relative cellular dehydrogenase activity
ROI	region of interest
ROS	reactive oxygen species
ROX	5(6)- carboxy-X- rhodamine
RPMI	roswell park memorial institute 16440 medium
RTES	organotriethoxysilane (R represents an organic moiety)
SBA-15	Santa Barbara Amorphous type material
SKBr3	breast carcinoma cells
SD	spinning disc

*List of abbreviations*

abbreviation	explanation
SD	standard deviation
SLB	supported lipid bilayer
SNARE	soluble N-ethylmaleimide-sensitive factor attachment protein receptor
SPION	superparamagnetic iron oxide nanoparticle
SP94	targeting peptide
TEA	triethanolamine
TEM	transmission electron microscopy
TEOS	tetraethyl orthosilicate
TFA	trifluoroacetic acid
TGA	thermogravimetric analysis
TL	targeting ligand
TRIS	tris(hydroxymethyl)-aminomethan
UV-VIS	ultraviolet-visible spectroscopy
WGA	wheat germ agglutinin
XRD	Xray diffraction

## Bibliography

- [1] Axel Schlossbauer, Anna M. Sauer, Valentina Cauda, Alexandra Schmidt, Hanna Engelke, Ulrich Rothbauer, Kourosh Zolghadr, Heinrich Leonhardt, Christoph Braeuchle, and Thomas Bein. Cascaded photoinduced drug delivery to cells from multifunctional core-shell mesoporous silica. *Adv Healthc Mater*, 1:316–320, 2012.
- [2] Deutsches Krebsforschungszentrum. Krebsmortalität im Überblick - verlgleich mit anderen todesursachen. [http://www.dkfz.de/de/krebsatlas/gesamt/mort\\_2.html](http://www.dkfz.de/de/krebsatlas/gesamt/mort_2.html), 2010.
- [3] National Cancer Insitute. Cancer topics - type of treatment. <http://www.cancer.gov/cancertopics/factsheet/Therapy>, 2014.
- [4] Lauren Gravitz. Cancer immunotherapy. *Nature*, 504:S1–S1, 2013.
- [5] Jennifer Couzin-Frankel. Cancer immunotherapy. *Science*, 342:1432–1433, 2013.
- [6] National Cancer Institute. Targeted cancer therapy. <http://www.cancer.gov/cancertopics/factsheet/Therapy/targeted>, 2014.
- [7] Eugene W.M. Ng and Anthony P. Adamis. Targeting angiogenesis, the underlying disorder in neovascular age-related macular degeneration. *Canadian Journal of Ophthalmology / Journal Canadien d’Ophtalmologie*, 40:352 – 368, 2005.
- [8] P Wust, B Hildebrandt, G Sreenivasa, B Rau, J Gellermann, H Riess, R Felix, and PM Schlag. Hyperthermia in combined treatment of cancer. *The Lancet Oncology*, 3:487 – 497, 2002.
- [9] Stanley B Brown, Elizabeth A Brown, and Ian Walker. The present and future role of photodynamic therapy in cancer treatment. *The Lancet Oncology*, 5:497 – 508, 2004.
- [10] Ranjita Misra, Sarbari Acharya, and Sanjeeb K. Sahoo. Cancer nanotechnology: application of nanotechnology in cancer therapy. *Drug Discovery Today*, 15:842–850, 2010.
- [11] James H. Adair, Mylisa P. Parette, Erhan I. Altinoglu, and Mark Kester. Nanoparticulate alternatives for drug delivery. *ACS Nano*, 4:4967–4970, 2010.
- [12] Michelle Longmire, Peter L. Choyke, and Hisataka Kobayashi. Clearance properties of nano-sized particles and molecules as imaging agents: Considerations and caveats. *Nanomedicine*, 3:703–717, 2008.
- [13] Neil Desai. Challenges in development of nanoparticle-based therapeutics. *The AAPS Journal*, 14:282–295, 2012.

## Bibliography

- [14] Christian Argyo, Veronika Weiss, Christoph Braeuchle, and Thomas Bein. Multifunctional mesoporous silica nanoparticles as a universal platform for drug delivery. *Chem. Mater.*, 26:435–451, 2014.
- [15] Stephan A. Mackowiak, Alexandra Schmidt, Veronika Weiss, Christian Argyo, Constantin von Schirnding, Thomas Bein, and Christoph Braeuchle. Targeted drug delivery in cancer cells with red-light photoactivated mesoporous silica nanoparticles. *Nano Lett.*, 13:2576–2583, 2013.
- [16] Monty Liong, Jie Lu, Michael Kovoichich, Tian Xia, Stefan G. Ruehm, Andre E. Nel, Fuyuhiko Tamanoi, and Jeffrey I. Zink. Multifunctional inorganic nanoparticles for imaging, targeting, and drug delivery. *ACS Nano*, 2:889–896, 2008.
- [17] Ji Eun Lee, Nohyun Lee, Taeho Kim, Jaeyun Kim, and Taeghwan Hyeon. Multifunctional mesoporous silica nanocomposite nanoparticles for theranostic applications. *Acc. Chem. Res.*, 44:893–902, 2011.
- [18] Igor I. Slowing, Brian G. Trewyn, S. Giri, and Victor S.-Y. Lin. Mesoporous silica nanoparticles for drug delivery and biosensing applications. *Adv. Funct. Mater.*, 17:1225–1236, 2007.
- [19] Jinliang Liu, Chunyan Li, and Fuyou Li. Fluorescence turn-on chemodosimeter-functionalized mesoporous silica nanoparticles and their application in cell imaging. *J. Mater. Chem.*, 21:7175–7181, 2011.
- [20] B. F.G. Johnson. Nanoparticles in catalysis. *Top. Catal.*, 24:147–159, 2003.
- [21] Amirali Popat, Sandy Budi Hartono, Frances Stahr, Jian Liu, Shi Zhang Qiao, and Gao Qing (Max) Lu. Mesoporous silica nanoparticles for bioadsorption, enzyme immobilisation, and delivery carriers. *Nanoscale*, 3:2801–2818, 2011.
- [22] Katsuhiko Ariga, Qingmin Ji, Taizo Mori, Masanobu Naito, Yusuke Yamauchi, Hideki Abe, and Jonathan P. Hill. Enzyme nanoarchitectonics: organization and device application. *Chem. Soc. Rev.*, 42:6322–6345, 2013.
- [23] Antonio J. Salinas, Pedro Esbrit, and Maria Vallet-Regi. A tissue engineering approach based on the use of bioceramics for bone repair. *Biomater. Sci.*, 1:40–51, 2013.
- [24] Nina Ehlert, Peter P. Mueller, Martin Stieve, Thomas Lenarz, and Peter Behrens. Mesoporous silica films as a novel biomaterial: applications in the middle ear. *Chem. Soc. Rev.*, 42:3847–3861, 2013.
- [25] Chiara Vitale-Brovarone, Francesco Baino, Marta Miola, Renato Mortera, Barbara Onida, and Enrica Vernae. Glass-ceramic scaffolds containing silica mesophases for bone grafting and drug delivery. *J. Mater. Sci.: Mater. Med.*, 20:809–820, 2009.

- [26] Zongxi Li, Jonathan C. Barnes, Aleksandr Bosoy, J. Fraser Stoddart, and Jeffrey I. Zink. Mesoporous silica nanoparticles in biomedical applications. *Chem. Soc. Rev.*, 41:2590–2605, 2012.
- [27] Juan L. Vivero-Escoto, Igor I. Slowing, Brian G. Trewyn, and Victor S.-Y. Lin. Mesoporous silica nanoparticles for intracellular controlled drug delivery. *Small*, 6:1952–1967, 2010.
- [28] Piaoping Yang, Shili Gai, and Jun Lin. Functionalized mesoporous silica materials for controlled drug delivery. *Chem. Soc. Rev.*, 41:3679–3698, 2012.
- [29] Yajun Wang, Aimin Yu, and Frank Caruso. Nanoporous polyelectrolyte spheres prepared by sequentially coating sacrificial mesoporous silica spheres. *Angew Chem Int Ed*, 44:2888–2892, 2005.
- [30] Yajun Wang, Yan Yan, Jiwei Cui, Leticia Hosta-Rigau, Joan K. Heath, Edouard C. Nice, and Frank Caruso. Encapsulation of water-insoluble drugs in polymer capsules prepared using mesoporous silica templates for intracellular drug delivery. *Adv Mater*, 22:4293–4297, 2010.
- [31] Jiwei Cui, Yan Yan, Yajun Wang, and Frank Caruso. Templated assembly of pH-labile polymer-drug particles for intracellular drug delivery. *Adv. Funct. Mater.*, 22:4718–4723, 2012.
- [32] J. S. Beck, J. C. Vartuli, W. J. Roth, M. E. Leonowicz, C. T. Kresge, K. D. Schmitt, C. T. W. Chu, D. H. Olson, and E. W. Sheppard. A new family of mesoporous molecular sieves prepared with liquid crystal templates. *J. Am. Chem. Soc.*, 114:10834–10843, 1992.
- [33] C. T. Kresge, M. E. Leonowicz, W. J. Roth, J. C. Vartuli, and J. S. Beck. Ordered mesoporous molecular sieves synthesized by a liquid-crystal template mechanism. *Nature*, 359:710–712, 1992.
- [34] M. Vallet-Regi, A. Ramila, R. P. del Real, and J. Perez-Pariente. A new property of mcm-41: Drug delivery system. *Chem. Mater.*, 13:308–311, 2001.
- [35] Si-Han Wu, Yann Hung, and Chung-Yuan Mou. Mesoporous silica nanoparticles as nanocarriers. *Chem. Commun.*, 47:9972–9985, 2011.
- [36] Karin Moeller, Johannes Kobler, and Thomas Bein. Colloidal suspensions of nanometer-sized mesoporous silica. *Adv. Funct. Mater.*, 17:605–612, 2007.
- [37] Valentina Cauda, Axel Schlossbauer, Johann Kecht, Andreas Zuerner, and Thomas Bein. Multiple core-shell functionalized colloidal mesoporous silica nanoparticles. *J. Am. Chem. Soc.*, 131:11361–11370, 2009.
- [38] Valentina Cauda, Christian Argyo, and Thomas Bein. Impact of different pegylation patterns on the long-term bio-stability of colloidal mesoporous silica nanoparticles. *J. Mater. Chem.*, 20:8693–8699, 2010.

## Bibliography

- [39] Valentina Cauda, Hanna Engelke, Anna Sauer, Delphine Arcizet, Christoph Braeuchle, Joachim Raedler, and Thomas Bein. Colchicine-loaded lipid bilayer-coated 50 nm mesoporous nanoparticles efficiently induce microtubule depolymerization upon cell uptake. *Nano Lett.*, 10:2484–2492, 2010.
- [40] Axel Schlossbauer, Johann Kecht, and Thomas Bein. Biotin-avidin as a protease-responsive cap system for controlled guest release from colloidal mesoporous silica. *Angew Chem Int Ed*, 48:3092–3095, 2009.
- [41] Valentina Cauda, Christian Argyo, Axel Schlossbauer, and Thomas Bein. Controlling the delivery kinetics from colloidal mesoporous silica nanoparticles with ph-sensitive gates. *J. Mater. Chem.*, 20:4305–4311, 2010.
- [42] Dan Peer, Jeffrey M. Karp, Seungpyo Hong, Omid C. Farokhzad, Rimona Margalit, and Robert Langer. Nanocarriers as an emerging platform for cancer therapy. *Nat Nano*, 2:751–760, 2007.
- [43] Robby A. Petros and Joseph M. DeSimone. Strategies in the design of nanoparticles for therapeutic applications. *Nat. Rev. Drug Discov.*, 9:615–627, 2010.
- [44] Volker Wagner, Anwyn Dullaart, Anne-Katrin Bock, and Axel Zweck. The emerging nanomedicine landscape. *Nat Biotech*, 24:1211–1217, 2006.
- [45] Andre E. Nel, Lutz Madler, Darrell Velegol, Tian Xia, Eric M. V. Hoek, Ponisseril Somasundaran, Fred Klaessig, Vince Castranova, and Mike Thompson. Understanding biophysicochemical interactions at the nano-bio interface. *Nat. Mater.*, 8:543–557, 2009.
- [46] Mauro Ferrari. Cancer nanotechnology: opportunities and challenges. *Nat. Rev. Cancer*, 5:161–171, 2005.
- [47] Huan Meng, Min Xue, Tian Xia, Zhaoxia Ji, Derrick Y. Tarn, Jeffrey I. Zink, and Andre E. Nel. Use of size and a copolymer design feature to improve the biodistribution and the enhanced permeability and retention effect of doxorubicin-loaded mesoporous silica nanoparticles in a murine xenograft tumor model. *ACS Nano*, 5:4131–4144, 2011.
- [48] Ji Eun Lee, Nohyun Lee, Hyoungsu Kim, Jaeyun Kim, Seung Hong Choi, Jeong Hyun Kim, Taeho Kim, In Chan Song, Seung Pyo Park, Woo Kyung Moon, and Taeghwan Hyeon. Uniform mesoporous dye-doped silica nanoparticles decorated with multiple magnetite nanocrystals for simultaneous enhanced magnetic resonance imaging, fluorescence imaging, and drug delivery. *J. Am. Chem. Soc.*, 132:552–557, 2010.
- [49] H Maeda, J Wu, T Sawa, Y Matsumura, and K Hori. Tumor vascular permeability and the epr effect in macromolecular therapeutics: a review. *J Control Release*, 65:271 – 284, 2000.
- [50] Derrick Tarn, Carlee E. Ashley, Min Xue, Eric C. Carnes, Jeffrey I. Zink, and C. Jeffrey Brinker. Mesoporous silica nanoparticle nanocarriers: Biofunctionality and biocompatibility. *Acc. Chem. Res.*, 46:792–801, 2013.

- [51] Carlee E. Ashley, Eric C. Carnes, Genevieve K. Phillips, David Padilla, Paul N. Durfee, Page A. Brown, Tracey N. Hanna, Juewen Liu, Brandy Phillips, Mark B. Carter, Nick J. Carroll, Xingmao Jiang, Darren R. Dunphy, Cheryl L. Willman, Dimiter N. Petsev, Deborah G. Evans, Atul N. Parikh, Bryce Chackerian, Walker Wharton, David S. Peabody, and C. Jeffrey Brinker. The targeted delivery of multicomponent cargos to cancer cells by nanoporous particle-supported lipid bilayers. *Nat. Mater.*, 10:389–397, 2011.
- [52] Michael M. Gottesman, Tito Fojo, and Susan E. Bates. Multidrug resistance in cancer: role of atp-dependent transporters. *Nat. Rev. Cancer*, 2:48–58, 2002.
- [53] Li-Sheng Wang, Li-Chen Wu, Shin-Yi Lu, Li-Ling Chang, I-Ting Teng, Chia-Min Yang, and Ja-an Annie Ho. Biofunctionalized phospholipid-capped mesoporous silica nanoshuttles for targeted drug delivery: Improved water suspensibility and decreased nonspecific protein binding. *ACS Nano*, 4:4371–4379, 2010.
- [54] Jessica M. Rosenholm, Annika Meinander, Emilia Peuhu, Rasmus Niemi, John E. Eriksson, Cecilia Sahlgren, and Mika Linden. Targeting of porous hybrid silica nanoparticles to cancer cells. *ACS Nano*, 3:197–206, 2009.
- [55] Quan Zhang, Fang Liu, Kim Truc Nguyen, Xing Ma, Xiaojun Wang, Bengang Xing, and Yanli Zhao. Multifunctional mesoporous silica nanoparticles for cancer-targeted and controlled drug delivery. *Adv. Funct. Mater.*, 22:5144–5156, 2012.
- [56] Jianmei Pang, Lanxia Zhao, Longlong Zhang, Zhonghao Li, and Yuxia Luan. Folate-conjugated hybrid sba-15 particles for targeted anticancer drug delivery. *J Colloid Interface Sci*, 395:31 – 39, 2013.
- [57] Dongyun Chen, Mengjun Jiang, Najun Li, Hongwei Gu, Qingfeng Xu, Jianfeng Ge, Xuewei Xia, and Jianmei Lu. Modification of magnetic silica/iron oxide nanocomposites with fluorescent polymethacrylic acid for cancer targeting and drug delivery. *J. Mater. Chem.*, 20:6422–6429, 2010.
- [58] Fang Wang, Xiaolan Chen, Zengxia Zhao, Shaoheng Tang, Xiaoqing Huang, Chenghong Lin, Congbo Cai, and Nanfeng Zheng. Synthesis of magnetic, fluorescent and mesoporous core-shell-structured nanoparticles for imaging, targeting and photodynamic therapy. *J. Mater. Chem.*, 21:11244–11252, 2011.
- [59] Veronika Mamaeva, Jessica M Rosenholm, Laurel Tabe Bate-Eya, Lotta Bergman, Emilia Peuhu, Alain Duchanoy, Lina E Fortelius, Sebastian Landor, Diana M Toivola, Mika Linden, and Cecilia Sahlgren. Mesoporous silica nanoparticles as drug delivery systems for targeted inhibition of notch signaling in cancer. *Mol. Ther.*, 19:1538–1546, 2011.
- [60] Chunfang Zhou, Andrea Kunzmann, Marija Rakonjac, Bengt Fadeel, and Alfonso Garcia-Bennett. Morphological properties of nanoporous folic acid materials and in vitro assessment of their biocompatibility. *Nanomedicine*, 7:327–334, 2011.

## Bibliography

- [61] Jianquan Fan, Gang Fang, Xiaodan Wang, Fang Zeng, Yufei Xiang, and Shuizhu Wu. Targeted anticancer prodrug with mesoporous silica nanoparticles as vehicles. *Nanotechnology*, 22:455102, 2011.
- [62] Yufang Zhu, Ying Fang, and Stefan Kaskel. Folate-conjugated  $\text{Fe}_3\text{O}_4/\text{SiO}_2$  hollow mesoporous spheres for targeted anticancer drug delivery. *J Phys Chem C*, 114:16382–16388, 2010.
- [63] Georgette Thumshirn, Ulrich Hersel, Simon L. Goodman, and Horst Kessler. Multimeric cyclic rgd peptides as potential tools for tumor targeting: Solid-phase peptide synthesis and chemoselective oxime ligation. *Chemistry*, 9:2717–2725, 2003.
- [64] I-Ju Fang, Igor I. Slowing, Kevin C.-W. Wu, Victor S.-Y. Lin, and Brian G. Trewyn. Ligand conformation dictates membrane and endosomal trafficking of arginine-glycine-aspartate (rgd)-functionalized mesoporous silica nanoparticles. *Chem. Eur. J.*, 18:7787–7792, 2012.
- [65] Shih-Hsun Cheng, Chia-Hung Lee, Meng-Chi Chen, Jeffrey S. Souris, Fan-Gang Tseng, Chung-Shi Yang, Chung-Yuan Mou, Chin-Tu Chen, and Leu-Wei Lo. Tri-functionalization of mesoporous silica nanoparticles for comprehensive cancer theranostics-the trio of imaging, targeting and therapy. *J. Mater. Chem.*, 20:6149–6157, 2010.
- [66] Jing Zhang, Zhe-Fan Yuan, Ya Wang, Wei-Hai Chen, Guo-Feng Luo, Si-Xue Cheng, Ren-Xi Zhuo, and Xian-Zheng Zhang. Multifunctional envelope-type mesoporous silica nanoparticles for tumor-triggered targeting drug delivery. *J. Am. Chem. Soc.*, 135:5068–5073, 2013.
- [67] Kai Cheng, Steven R. Blumen, Maximilian B. MacPherson, Jeremy L. Steinbacher, Brooke T. Mossman, and Christopher C. Landry. Enhanced uptake of porous silica microparticles by bifunctional surface modification with a targeting antibody and a biocompatible polymer. *ACS Appl Mater Interfaces*, 2:2489–2495, 2010.
- [68] Ziwei Deng, Zipeng Zhen, Xiaoxi Hu, Shuilin Wu, Zushun Xu, and Paul K. Chu. Hollow chitosan-silica nanospheres as pH-sensitive targeted delivery carriers in breast cancer therapy. *Biomaterials*, 32:4976 – 4986, 2011.
- [69] Chih-Pin Tsai, Chao-Yu Chen, Yann Hung, Fu-Hsiung Chang, and Chung-Yuan Mou. Monoclonal antibody-functionalized mesoporous silica nanoparticles (msn) for selective targeting breast cancer cells. *J. Mater. Chem.*, 19:5737–5743, 2009.
- [70] Le-Le Li, Qian Yin, Jianjun Cheng, and Yi Lu. Polyvalent mesoporous silica nanoparticle-aptamer bioconjugates target breast cancer cells. *Adv Healthc Mater*, 1:567–572, 2012.
- [71] David Brevet, Magali Gary-Bobo, Laurence Raehm, Sebastien Richeter, Ouahiba Hocine, Kassem Amro, Bernard Loock, Pierre Couleaud, Celine Frochot, Alain Morere, Philippe Mailhard, Marcel Garcia, and Jean-Olivier Durand. Mannose-targeted mesoporous silica nanoparticles for photodynamic therapy. *Chem. Commun.*, 12:1475–1477, 2009.

- [72] Magali Gary-Bobo, Ouahiba Hocine, David Brevet, Marie Maynadier, Laurence Raehm, Sebastien Richeter, Virginie Charasson, Bernard Looock, Alain Morere, Philippe Maillard, Marcel Garcia, and Jean-Olivier Durand. Cancer therapy improvement with mesoporous silica nanoparticles combining targeting, drug delivery and pdt. *Int J Pharm*, 423:509 – 515, 2012.
- [73] Zhaowei Chen, Zhenhua Li, Youhui Lin, Meili Yin, Jinsong Ren, and Xiaogang Qu. Bioreponsive hyaluronic acid-capped mesoporous silica nanoparticles for targeted drug delivery. *Chem. Eur. J.*, 19:1778–1783, 2013.
- [74] Juan L. Vivero-Escoto, Kathryn M. L. Taylor-Pashow, Rachel C. Huxford, Joseph Della Rocca, Christie Okoruwa, Hongyu An, Weili Lin, and Wenbin Lin. Multifunctional mesoporous silica nanospheres with cleavable gd(iii) chelates as mri contrast agents: Synthesis, characterization, target-specificity, and renal clearance. *Small*, 7:3519–3528, 2011.
- [75] Srivani Veerananarayanan, Aby Cheruvathoor Poulouse, M. Sheikh Mohamed, Saino Hanna Varghese, Yutaka Nagaoka, Yasuhiko Yoshida, Toru Maekawa, and D. Sakthi Kumar. Synergistic targeting of cancer and associated angiogenesis using triple-targeted dual-drug silica nanoformulations for theragnostics. *Small*, 8:3476–3489, 2012.
- [76] Sean D. Conner and Sandra L. Schmid. Regulated portals of entry into the cell. *Nature*, 422:37–44, 2003.
- [77] Huan Meng, Sui Yang, Zongxi Li, Tian Xia, Justin Chen, Zhaoxia Ji, Haiyuan Zhang, Xiang Wang, Sijie Lin, Connie Huang, Z. Hong Zhou, Jeffrey I. Zink, and Andre E. Nel. Aspect ratio determines the quantity of mesoporous silica nanoparticle uptake by a small gtpase-dependent macropinocytosis mechanism. *ACS Nano*, 5:4434–4447, 2011.
- [78] Zhimin Tao, Bonnie B. Toms, Jerry Goodisman, and Tewodros Asefa. Mesoporosity and functional group dependent endocytosis and cytotoxicity of silica nanomaterials. *Chem. Res. Toxicol.*, 22:1869–1880, 2009.
- [79] Gousia Begum, Shashi Singh, Nandini Rangaraj, G. Srinivas, and Rohit K. Rana. Cellular permeation with nuclear infiltration capability of biomimetically synthesised fluorescent monodisperse mesoporous silica nanospheres in hela and human stem cells. *J. Mater. Chem.*, 20:8563–8570, 2010.
- [80] Jingxian Yu, Huanying Zhao, Ling Ye, Hui Yang, Shuting Ku, Nan Yang, and Ning Xiao. Effect of surface functionality of magnetic silica nanoparticles on the cellular uptake by glioma cells in vitro. *J. Mater. Chem.*, 19:1265–1270, 2009.
- [81] Jie Zhu, Jiawei Tang, Lingzhi Zhao, Xufeng Zhou, Yunhua Wang, and Chengzhong Yu. Ultra-small, well-dispersed, hollow siliceous spheres with enhanced endocytosis properties. *Small*, 6:276–282, 2010.

## Bibliography

- [82] Tsai-Hua Chung, Si-Han Wu, Ming Yao, Chen-Wen Lu, Yu-Shen Lin, Yann Hung, Chung-Yuan Mou, Yao-Chang Chen, and Dong-Ming Huang. The effect of surface charge on the uptake and biological function of mesoporous silica nanoparticles in 3t3-l1 cells and human mesenchymal stem cells. *Biomaterials*, 28:2959 – 2966, 2007.
- [83] Igor Slowing, Brian G. Trewyn, and Victor S.-Y. Lin. Effect of surface functionalization of mcm-41-type mesoporous silica nanoparticles on the endocytosis by human cancer cells. *J. Am. Chem. Soc.*, 128:14792–14793, 2006.
- [84] Matthieu Fisichella, Hinda Dabboue, Sanjib Bhattacharyya, Gérald Lelong, Marie-Louise Saboungi, Fabienne Warmont, Patrick Midoux, Chantal Pichon, Martine Guerin, Tobias Hevor, and Jean-Paul Salvetat. Uptake of functionalized mesoporous silica nanoparticles by human cancer cells. *Journal of Nanoscience and Nanotechnology*, 10:2314–2324, 2010.
- [85] Wei Sun, Ning Fang, Brian G. Trewyn, Makoto Tsunoda, Igor I. Slowing, Victor S.Y. Lin, and Edward S. Yeung. Endocytosis of a single mesoporous silica nanoparticle into a human lung cancer cell observed by differential interference contrast microscopy. *Anal. Bioanal. Chem.*, 391:2119–2125, 2008.
- [86] Anna M. Sauer, Axel Schlossbauer, Nadia Ruthardt, Valentina Cauda, Thomas Bein, and Christoph Braeuchle. Role of endosomal escape for disulfide-based drug delivery from colloidal mesoporous silica evaluated by live-cell imaging. *Nano Lett.*, 10:3684–3691, 2010.
- [87] Amir K. Varkouhi, Marije Scholte, Gert Storm, and Hidde J. Haisma. Endosomal escape pathways for delivery of biologicals. *J. Controlled Release*, 151:220–228, 2011.
- [88] K.G. de Bruin, C. Fella, M. Ogris, E. Wagner, N. Ruthardt, and C. Bräuchle. Dynamics of photoinduced endosomal release of polyplexes. *J Control Release*, 130:175 – 182, 2008.
- [89] Jean-Paul Behr. The proton sponge: a trick to enter cells the viruses did not exploit. *Chimia*, 51:34–36, 1997.
- [90] Jean Gruenberg and Frederick R Maxfield. Membrane transport in the endocytic pathway. *Curr Opin Cell Biol*, 7:552 – 563, 1995.
- [91] O Boussif, F Lezoualch, M A Zanta, M D Mergny, D Scherman, B Demeneix, and J P Behr. A versatile vector for gene and oligonucleotide transfer into cells in culture and in vivo: polyethylenimine. *Proceedings of the National Academy of Sciences*, 92:7297–7301, 1995.
- [92] Akin Akinc, Mini Thomas, Alexander M. Klibanov, and Robert Langer. Exploring polyethylenimine-mediated dna transfection and the proton sponge hypothesis. *J. Gene Med.*, 7:657–663, 2005.
- [93] J. Suh, H.J. Paik, and B.K. Hwang. Ionization of poly(ethylenimine) and poly(allylamine) at various ph's. *Bioorg. Chem.*, 22:318 – 327, 1994.

- [94] Sabrina Oliveira, Inge van Rooy, Onno Kranenburg, Gert Storm, and Raymond M. Schiffelers. Fusogenic peptides enhance endosomal escape improving sirna-induced silencing of oncogenes. *Int J Pharm*, 331:211 – 214, 2007.
- [95] Rui Liu, Puhong Liao, Jikai Liu, and Pingyun Feng. Responsive polymer-coated mesoporous silica as a ph-sensitive nanocarrier for controlled release. *Langmuir*, 27:3095–3099, 2011.
- [96] Eun Seong Lee, Hyun Joon Shin, Kun Na, and You Han Bae. Poly(l-histidine)-peg block copolymer micelles and ph-induced destabilization. *J Control Release*, 90:363 – 374, 2003.
- [97] Yuma Yamada, Yasuo Shinohara, Tomoyuki Kakudo, Shinji Chaki, Shiroh Futaki, Hiroyuki Kamiya, and Hideyoshi Harashima. Mitochondrial delivery of mastoparan with transferrin liposomes equipped with a ph-sensitive fusogenic peptide for selective cancer therapy. *Int J Pharm*, 303:1 – 7, 2005.
- [98] Tomoyuki Kakudo, Shinji Chaki, Shiroh Futaki, Ikuhiko Nakase, Kenichi Akaji, Toru Kawakami, Kazuo Maruyama, Hiroyuki Kamiya, and Hideyoshi Harashima. Transferrin-modified liposomes equipped with a ph-sensitive fusogenic peptide: An artificial viral-like delivery system. *Biochemistry (Mosc.)*, 43:5618 – 5628, 2004.
- [99] Carlee E. Ashley, Eric C. Carnes, Katharine E. Epler, David P. Padilla, Genevieve K. Phillips, Robert E. Castillo, Dan C. Wilkinson, Brian S. Wilkinson, Cameron A. Burgard, Robin M. Kalinich, Jason L. Townson, Bryce Chackerian, Cheryl L. Willman, David S. Peabody, Walker Wharton, and C. Jeffrey Brinker. Delivery of small interfering rna by peptide-targeted mesoporous silica nanoparticle-supported lipid bilayers. *ACS Nano*, 6:2174–2188, 2012.
- [100] Dinggeng He, Xiaoxiao He, Kemin Wang, Jie Cao, and Yingxiang Zhao. A light-responsive reversible molecule-gated system using thymine-modified mesoporous silica nanoparticles. *Langmuir*, 28:4003–4008, 2012.
- [101] Daniel P. Ferris, Yan-Li Zhao, Niveen M. Khashab, Hussam A. Khatib, J. Fraser Stoddart, and Jeffrey I. Zink. Light-operated mechanized nanoparticles. *J. Am. Chem. Soc.*, 131:1686–1688, 2009.
- [102] Jonas Croissant and Jeffrey I. Zink. Nanovalve-controlled cargo release activated by plasmonic heating. *J. Am. Chem. Soc.*, 134:7628–7631, 2012.
- [103] Nikola Z. Knezevic, Brian G. Trewyn, and Victor S.-Y. Lin. Light- and ph-responsive release of doxorubicin from a mesoporous silica-based nanocarrier. *Chem. Eur. J.*, 17:3338–3342, 2011.
- [104] Jinping Lai, Xue Mu, Yunyan Xu, Xiaoli Wu, Chuanliu Wu, Chong Li, Jianbin Chen, and Yibing Zhao. Light-responsive nanogated ensemble based on polymer grafted mesoporous silica hybrid nanoparticles. *Chem. Commun.*, 46:7370–7372, 2010.

## Bibliography

- [105] Rui Liu, Ying Zhang, and Pingyun Feng. Multiresponsive supramolecular nanogated ensembles. *J. Am. Chem. Soc.*, 131:15128–15129, 2009.
- [106] Maria Pamela Dobay, Alexandra Schmidt, Eduardo Mendoza, Thomas Bein, and Joachim O. Raedler. Cell type determines the light-induced endosomal escape kinetics of multifunctional mesoporous silica nanoparticles. *Nano Lett.*, 13:1047–1052, 2013.
- [107] Nikola Z. Knezevic, Brian G. Trewyn, and Victor S.-Y. Lin. Functionalized mesoporous silica nanoparticle-based visible light responsive controlled release delivery system. *Chem. Commun.*, 47:2817–2819, 2011.
- [108] Xinjian Yang, Xia Liu, Zhen Liu, Fang Pu, Jinsong Ren, and Xiaogang Qu. Near-infrared light-triggered, targeted drug delivery to cancer cells by aptamer gated nanovehicles. *Adv Mater*, 24:2890–2895, 2012.
- [109] Weijun Fang, Jing Yang, Jiawei Gong, and Nanfeng Zheng. Photo- and ph-triggered release of anticancer drugs from mesoporous silica-coated pdag nanoparticles. *Adv. Funct. Mater.*, 22:842–848, 2012.
- [110] Eduardo Ruiz-Hernandez, Alejandro Baeza, and Maria Vallet-Regi. Smart drug delivery through dna/magnetic nanoparticle gates. *ACS Nano*, 5:1259–1266, 2011.
- [111] Supratim Giri, Brian G. Trewyn, Michael P. Stellmaker, and Victor S.-Y. Lin. Stimuli-responsive controlled-release delivery system based on mesoporous silica nanorods capped with magnetic nanoparticles. *Angew Chem Int Ed*, 44:5038–5044, 2005.
- [112] Elena Aznar, Ma Dolores Marcos, Ramon Martinez-Manez, Felix Sancenon, Juan Soto, Pedro Amoros, and Carmen Guillem. ph- and photo-switched release of guest molecules from mesoporous silica supports. *J. Am. Chem. Soc.*, 131:6833–6843, 2009.
- [113] A. Baeza, E. Guisasola, Eduardo Ruiz-Hernandez, E., and M. Vallet-Regi. Magnetically triggered multidrug release by hybrid mesoporous silica nanoparticles. *Chem. Mater.*, 24:517–524, 2012.
- [114] Axel Schlossbauer, Simon Warncke, Philipp M. E. Gramlich, Johann Kecht, Antonio Manetto, Thomas Carell, and Thomas Bein. A programmable dna-based molecular valve for colloidal mesoporous silica. *Angew Chem Int Ed*, 49:4734–4737, 2010.
- [115] Yongqiang Wen, Liping Xu, Chuanbao Li, Hongwu Du, Linfeng Chen, Bin Su, Zhiliang Zhang, Xueji Zhang, and Yanlin Song. Dna-based intelligent logic controlled release systems. *Chem. Commun.*, 48:8410–8412, 2012.
- [116] Elena Aznar, Laura Mondragon, L.n, Jose V. Ros-Lis, Felix Sancenon, M. Dolores Marcos, Ramon Martinez-Manez, Juan Soto, Enrique Perez-Paya, and Pedro Amoros. Finely tuned temperature-controlled cargo release using paraffin-capped mesoporous silica nanoparticles. *Angewandte Chemie International Edition*, 50:11172–11175, 2011.

- [117] Xixue Hu, Xiaohong Hao, Yan Wu, Jinchao Zhang, Xiaoning Zhang, Paul C. Wang, Guozhang Zou, and Xing-Jie Liang. Multifunctional hybrid silica nanoparticles for controlled doxorubicin loading and release with thermal and ph dual response. *J. Mater. Chem. B*, 1:1109–1118, 2013.
- [118] Ye-Zi You, Kennedy K. Kalebaila, Stephanie L. Brock, and David Oupicky . Temperature-controlled uptake and release in pnipam-modified porous silica nanoparticles. *Chem. Mater.*, 20:3354–3359, 2008.
- [119] Yufang Zhu, Stefan Kaskel, Toshiyuki Ikoma, and Nobutaka Hanagata. Magnetic sba-15/poly(n-isopropylacrylamide) composite: Preparation, characterization and temperature-responsive drug release property. *Microporous Mesoporous Mater*, 123:107 – 112, 2009.
- [120] Estela Climent, Andrea Bernardos, Ramon Martinez-Manez, Angel Maquieira, Maria Dolores Marcos, Nuria Pastor-Navarro, Rosa Puchades, Felix Sancenon, Juan Soto, and Pedro Amoros. Controlled delivery systems using antibody-capped mesoporous nanocontainers. *J. Am. Chem. Soc.*, 131:14075–14080, 2009.
- [121] Dinggeng He, Xiaoxiao He, Kemin Wang, Mian Chen, Jie Cao, and Yingxiang Zhao. Reversible stimuli-responsive controlled release using mesoporous silica nanoparticles functionalized with a smart dna molecule-gated switch. *J. Mater. Chem.*, 22:14715–14721, 2012.
- [122] Estela Climent, Ramon Martinez-Manez, Felix Sancenon, Maria D. Marcos, Juan Soto, Angel Maquieira, and Pedro Amoros. Controlled delivery using oligonucleotide-capped mesoporous silica nanoparticles. *Angew Chem Int Ed*, 49:7281–7283, 2010.
- [123] Jie Geng, Meng Li, Li Wu, Cuie Chen, and Xiaogang Qu. Mesoporous silica nanoparticle-based h<sub>2</sub>o<sub>2</sub> responsive controlled-release system used for alzheimer’s disease treatment. *Adv Healthc Mater*, 1:332–336, 2012.
- [124] Young Lan Choi, Justyn Jaworski, Moo Lyong Seo, Soo Jin Lee, and Jong Hwa Jung. Controlled release using mesoporous silica nanoparticles functionalized with 18-crown-6 derivative. *J. Mater. Chem.*, 21:7882–7885, 2011.
- [125] Qi Gan, Xunyu Lu, Yuan Yuan, Jiangchao Qian, Huanjun Zhou, Xun Lu, Jianlin Shi, and Changsheng Liu. A magnetic, reversible ph-responsive nanogated ensemble based on fe<sub>3</sub>o<sub>4</sub> nanoparticles-capped mesoporous silica. *Biomaterials*, 32:1932 – 1942, 2011.
- [126] Rui Liu, Ying Zhang, Xiang Zhao, Arun Agarwal, Leonard J. Mueller, and Pingyun Feng. ph-responsive nanogated ensemble based on gold-capped mesoporous silica through an acid-labile acetal linker. *J. Am. Chem. Soc.*, 132:1500–1501, 2010.
- [127] Yan-Li Zhao, Zongxi Li, Sanaz Kabehie, Youssry Y. Botros, J. Fraser Stoddart, and Jeffrey I. Zink. ph-operated nanopistons on the surfaces of mesoporous silica nanoparticles. *J. Am. Chem. Soc.*, 132:13016–13025, 2010.

## Bibliography

- [128] Huan Meng, Monty Liong, Tian Xia, Zongxi Li, Zhaoxia Ji, Jeffrey I. Zink, and Andre E. Nel. Engineered design of mesoporous silica nanoparticles to deliver doxorubicin and p-glycoprotein sirna to overcome drug resistance in a cancer cell line. *ACS Nano*, 4:4539–4550, 2010.
- [129] Li Du, Shijun Liao, Hussam A. Khatib, J. Fraser Stoddart, and Jeffrey I. Zink. Controlled-access hollow mechanized silica nanocontainers. *J. Am. Chem. Soc.*, 131:15136–15142, 2009.
- [130] Cheng Wang, Zongxi Li, Dennis Cao, Yan-Li Zhao, Justin W. Gaines, O. Altan Bozdemir, Michael W. Ambrogio, Marco Frascioni, Youssry Y. Botros, Jeffrey I. Zink, and J. Fraser Stoddart. Stimulated release of size-selected cargos in succession from mesoporous silica nanoparticles. *Angew Chem Int Ed*, 51:5460–5465, 2012.
- [131] Niveen M. Khashab, Matthew E. Belowich, Ali Trabolsi, Douglas C. Friedman, Cory Valente, Yuen Lau, Hussam A. Khatib, Jeffrey I. Zink, and J. Fraser Stoddart. ph-responsive mechanised nanoparticles gated by semirotaxanes. *Chem. Commun.*, 36:5371–5373, 2009.
- [132] Sarah Angelos, Niveen M. Khashab, Ying-Wei Yang, Ali Trabolsi, Hussam A. Khatib, J. Fraser Stoddart, and Jeffrey I. Zink. ph clock-operated mechanized nanoparticles. *J. Am. Chem. Soc.*, 131:12912–12914, 2009.
- [133] Jinshui Liu and Xuezhong Du. ph- and competitor-driven nanovalves of cucurbit[7]uril pseudorotaxanes based on mesoporous silica supports for controlled release. *J. Mater. Chem.*, 20:3642–3649, 2010.
- [134] Elena Aznar, Carmen Coll, M. Dolores Marcos, Ramon Martinez-Manez, Felix Sancenon, Juan Soto, Pedro Amoros, Joan Cano, and Eliseo Ruiz. Borate-driven gate-like scaffolding using mesoporous materials functionalised with saccharides. *Chem. Eur. J.*, 15:6877–6888, 2009.
- [135] Qishan Zheng, Yanli Hao, Peirong Ye, Liangqia Guo, Hanyin Wu, Qingquan Guo, Jinzhi Jiang, Fengfu Fu, and Guonan Chen. A ph-responsive controlled release system using layered double hydroxide (ldh)-capped mesoporous silica nanoparticles. *J. Mater. Chem. B*, 1:1644–1648, 2013.
- [136] Qing Yang, Shichao Wang, Peiwei Fan, Lifeng Wang, Yan Di, Kaifeng Lin, and Feng-Shou Xiao. ph-responsive carrier system based on carboxylic acid modified mesoporous silica and polyelectrolyte for drug delivery. *Chem. Mater.*, 17:5999–6003, 2005.
- [137] Faqi Yu, Xinde Tang, and Meishan Pei. Facile synthesis of pdmaema-coated hollow mesoporous silica nanoparticles and their ph-responsive controlled release. *Microporous Mesoporous Mater*, 173:64 – 69, 2013.
- [138] Lei Sun, Xinge Zhang, Chao Zheng, Zhongming Wu, and Chaoxing Li. A ph gated, glucose-sensitive nanoparticle based on worm-like mesoporous silica for controlled insulin release. *J. Phys. Chem. B*, 117:3852–3860, 2013.

- [139] Young Lan Choi, Ji Ha Lee, Justyn Jaworski, and Jong Hwa Jung. Mesoporous silica nanoparticles functionalized with a thymidine derivative for controlled release. *J. Mater. Chem.*, 22:9455–9457, 2012.
- [140] Baisong Chang, Dan Chen, Yang Wang, Yanzuo Chen, Yunfeng Jiao, Xianyi Sha, and Wuli Yang. Bioresponsive controlled drug release based on mesoporous silica nanoparticles coated with reductively sheddable polymer shell. *Chem. Mater.*, 25:574–585, 2013.
- [141] Lei Xing, Haoquan Zheng, Yuanyuan Cao, and Shunai Che. Coordination polymer coated mesoporous silica nanoparticles for ph-responsive drug release. *Adv Mater*, 24:6433–6437, 2012.
- [142] Amirali Papat, Jian Liu, Gao Qing Lu, and Shi Zhang Qiao. A ph-responsive drug delivery system based on chitosan coated mesoporous silica nanoparticles. *J. Mater. Chem.*, 22:11173–11178, 2012.
- [143] Fang Chen and Yingchun Zhu. Chitosan enclosed mesoporous silica nanoparticles as drug nano-carriers: Sensitive response to the narrow ph range. *Microporous Mesoporous Mater*, 150:83 – 89, 2012.
- [144] Chuanbo Gao, Haoquan Zheng, Lei Xing, Mouhai Shu, and Shunai Che. Designable coordination bonding in mesopores as a ph-responsive release system. *Chem. Mater.*, 22:5437–5444, 2010.
- [145] Axel Schlossbauer, Christian Dohmen, David Schaffert, Ernst Wagner, and Thomas Bein. ph-responsive release of acetal-linked melittin from sba-15 mesoporous silica. *Angew. Chem. Int. Ed.*, 50:6828–6830, 2011.
- [146] Yanhang Ma, Lin Zhou, Haoquan Zheng, Lei Xing, Chenguang Li, Jinghao Cui, and Shunai Che. ph-responsive mitoxantrone (mx) delivery using mesoporous silica nanoparticles (msn). *J. Mater. Chem.*, 21:9483–9486, 2011.
- [147] Qianjun He, Yu Gao, Lingxia Zhang, Zhiwen Zhang, Fang Gao, Xiufeng Ji, Yaping Li, and Jianlin Shi. A ph-responsive mesoporous silica nanoparticles-based multi-drug delivery system for overcoming multi-drug resistance. *Biomaterials*, 32:7711 – 7720, 2011.
- [148] Shih-Hsun Cheng, Wei-Neng Liao, Li-Ming Chen, and Chia-Hung Lee. ph-controllable release using functionalized mesoporous silica nanoparticles as an oral drug delivery system. *J. Mater. Chem.*, 21:7130–7137, 2011.
- [149] Remy Guillet-Nicolas, Amirali Papat, Jean-Luc Bridot, Gregory Monteith, Shi Zhang Qiao, and Freddy Kleitz. ph-responsive nutraceutical-mesoporous silica nanoconjugates with enhanced colloidal stability. *Angew Chem Int Ed*, 52:2318–2322, 2013.
- [150] Mengjun Xue and Gerhard H. Findenegg. Lysozyme as a ph-responsive valve for the controlled release of guest molecules from mesoporous silica. *Langmuir*, 28:17578–17584, 2012.

## Bibliography

- [151] Nuria Mas, Alessandro Agostini, Laura Mondragon, Andrea Bernardos, Felix Sancenon, M. Dolores Marcos, Ramon Martinez-Manez, Ana M. Costero, Salvador Gil, Matilde Merino-Sanjuan, Pedro Amoros, Mar Orzaez, and Enrique Perez-Paya. Enzyme-responsive silica mesoporous supports capped with azopyridinium salts for controlled delivery applications. *Chem. Eur. J.*, 19:1346–1356, 2013.
- [152] Jinshui Liu, Xuezhong Du, and Xianfeng Zhang. Enzyme-inspired controlled release of cucurbit[7]uril nanovalves by using magnetic mesoporous silica. *Chemistry*, 17:810–815, 2011.
- [153] Kaushik Patel, Sarah Angelos, William R. Dichtel, Ali Coskun, Ying-Wei Yang, Jeffrey I. Zink, and J. Fraser Stoddart. Enzyme-responsive snap-top covered silica nanocontainers. *J. Am. Chem. Soc.*, 130:2382–2383, 2008.
- [154] Alessandro Agostini, Laura Mondragon, Lluís Pascual, Elena Aznar, Carmen Coll, Ramon Martinez-Manez, Felix Sancenon, Juan Soto, M. Dolores Marcos, Pedro Amoros, Ana M. Costero, Margarita Parra, and Salvador Gil. Design of enzyme-mediated controlled release systems based on silica mesoporous supports capped with ester-glycol groups. *Langmuir*, 28:14766–14776, 2012.
- [155] Carmen Coll, Laura Mondragon, Ramon Martinez-Manez, Felix Sancenon, M. Dolores Marcos, Juan Soto, Pedro Amoros, and Enrique Perez-Paya. Enzyme-mediated controlled release systems by anchoring peptide sequences on mesoporous silica supports. *Angew Chem Int Ed*, 50:2138–2140, 2011.
- [156] Andrea Bernardos, Laura Mondragon, Elena Aznar, M. Dolores Marcos, Ramon Martinez-Manez, Felix Sancenon, Juan Soto, Jose Manuel Barat, Enrique Perez-Paya, Carmen Guillem, and Pedro Amoros. Enzyme-responsive intracellular controlled release using nanometric silica mesoporous supports capped with "saccharides". *ACS Nano*, 4:6353–6368, 2010.
- [157] Andrea Bernardos, Elena Aznar, Maria Dolores Marcos, Ramon Martinez-Manez, Felix Sancenon, Juan Soto, Jose Manuel Barat, and Pedro Amoros. Enzyme-responsive controlled release using mesoporous silica supports capped with lactose. *Angew. Chem., Int. Ed.*, 48:5884–5887, 2009.
- [158] Xing Ma, Kim Truc Nguyen, Parijat Borah, Chung Yen Ang, and Yanli Zhao. Functional silica nanoparticles for redox-triggered drug/ssdna co-delivery. *Adv Healthc Mater*, 1:690–697, 2012.
- [159] Zhong Luo, Kaiyong Cai, Yan Hu, Li Zhao, Peng Liu, Lin Duan, and Weihua Yang. Mesoporous silica nanoparticles end-capped with collagen: Redox-responsive nanoreservoirs for targeted drug delivery. *Angew Chem Int Ed*, 50:640–643, 2011.
- [160] Rui Liu, Xiang Zhao, Tao Wu, and Pingyun Feng. Tunable redox-responsive hybrid nanogated ensembles. *J. Am. Chem. Soc.*, 130:14418–14419, 2008.

- [161] Jessica Mendez, Alina Monteagudo, and Kai Griebenow. Stimulus-responsive controlled release system by covalent immobilization of an enzyme into mesoporous silica nanoparticles. *Bioconjug. Chem.*, 23:698–704, 2012.
- [162] Xiaoxiao He, Yingxiang Zhao, Dinggeng He, Kemin Wang, Fengzhou Xu, and Jinlu Tang. Atp-responsive controlled release system using aptamer-functionalized mesoporous silica nanoparticles. *Langmuir*, 28:12909–12915, 2012.
- [163] Chun-Ling Zhu, Chun-Hua Lu, Xue-Yuan Song, Huang-Hao Yang, and Xiao-Ru Wang. Bioreponsive controlled release using mesoporous silica nanoparticles capped with aptamer-based molecular gate. *J. Am. Chem. Soc.*, 133:1278–1281, 2011.
- [164] Veli C. Oezalp and Thomas Schaefer. Aptamer-based switchable nanovalves for stimuli-responsive drug delivery. *Chem. Eur. J.*, 17:9893–9896, 2011.
- [165] Yannan Zhao, Brian G. Trewyn, Igor I. Slowing, and Victor S.-Y. Lin. Mesoporous silica nanoparticle-based double drug delivery system for glucose-responsive controlled release of insulin and cyclic amp. *J. Am. Chem. Soc.*, 131:8398–8400, 2009.
- [166] Linfeng Chen, Yongqiang Wen, Bin Su, Jiancheng Di, Yanlin Song, and Lei Jiang. Programmable dna switch for bioresponsive controlled release. *J. Mater. Chem.*, 21:13811–13816, 2011.
- [167] Wenru Zhao, Hongti Zhang, Qianjun He, Yongsheng Li, Jinlou Gu, Liang Li, Hua Li, and Jianlin Shi. A glucose-responsive controlled release of insulin system based on enzyme multilayers-coated mesoporous silica particles. *Chem. Commun.*, 47:9459–9461, 2011.
- [168] Lejiao Jia, Jingyi Shen, Zhenyu Li, Dianrui Zhang, Qiang Zhang, Guangpu Liu, Dandan Zheng, and Xiaona Tian. In vitro and in vivo evaluation of paclitaxel-loaded mesoporous silica nanoparticles with three pore sizes. *Int J Pharm*, 445:12 – 19, 2013.
- [169] Hee-Kyung Na, Mi-Hee Kim, Kihyun Park, Soo-Ryoon Ryoo, Kyung Eun Lee, Hyesung Jeon, Ryong Ryoo, Changbong Hyeon, and Dal-Hee Min. Efficient functional delivery of sirna using mesoporous silica nanoparticles with ultralarge pores. *Small*, 8:1752–1761, 2012.
- [170] Alessandro Agostini, Laura Mondragon, Andrea Bernardos, Ramon Martinez-Manez, M. Dolores Marcos, Felix Sancenon, Juan Soto, Ana Costero, Cristina Manguan-Garcia, Rosario Perona, Marta Moreno-Torres, Rafael Aparicio-Sanchis, and Jose Ramon Murguia. Targeted cargo delivery in senescent cells using capped mesoporous silica nanoparticles. *Angew. Chem. Int. Ed.*, 51:10556–10560, 2012.
- [171] Pascale Changenet-Barret, Thomas Gustavsson, Dimitra Markovitsi, Ilse Manet, and Sandra Monti. Unravelling molecular mechanisms in the fluorescence spectra of doxorubicin in aqueous solution by femtosecond fluorescence spectroscopy. *Phys. Chem. Chem. Phys.*, 15:2937–2944, 2013.

## Bibliography

- [172] Yu Chen, Hangrong Chen, Deping Zeng, Yunbo Tian, Feng Chen, Jingwei Feng, and Jianlin Shi. Core/shell structured hollow mesoporous nanocapsules: A potential platform for simultaneous cell imaging and anticancer drug delivery. *ACS Nano*, 4:6001–6013, 2010.
- [173] Tingting Wang, Fang Chai, Qin Fu, Lingyu Zhang, Haiyan Liu, Lu Li, Yi Liao, Zhongmin Su, Chungang Wang, Beiye Duan, and Dongxue Ren. Uniform hollow mesoporous silica nanocages for drug delivery in vitro and in vivo for liver cancer therapy. *J. Mater. Chem.*, 21:5299–5306, 2011.
- [174] Yu Gao, Yu Chen, Xiufeng Ji, Xinyu He, Qi Yin, Zhiwen Zhang, Jianlin Shi, and Yaping Li. Controlled intracellular release of doxorubicin in multidrug-resistant cancer cells by tuning the shell-pore sizes of mesoporous silica nanoparticles. *ACS Nano*, 5:9788–9798, 2011.
- [175] Yu Chen, Qi Yin, Xiufeng Ji, Shengjian Zhang, Hangrong Chen, Yuanyi Zheng, Yang Sun, Haiyun Qu, Zheng Wang, Yaping Li, Xia Wang, Kun Zhang, Linlin Zhang, and Jianlin Shi. Manganese oxide-based multifunctionalized mesoporous silica nanoparticles for ph-responsive mri, ultrasonography and circumvention of mdr in cancer cells. *Biomaterials*, 33:7126 – 7137, 2012.
- [176] Ellen C. Dengler, Juewen Liu, Audra Kerwin, Sergio Torres, Clara M. Olcott, Brandi N. Bowman, Leisha Armijo, Katherine Gentry, Jenny Wilkerson, James Wallace, Xingmao Jiang, Eric C. Carnes, C. Jeffrey Brinker, and Erin D. Milligan. Mesoporous silica-supported lipid bilayers (protocells) for dna cargo delivery to the spinal cord. *J Control Release*, 168:209 – 224, 2013.
- [177] Juewen Liu, Alison Stace-Naughton, Xingmao Jiang, and C. Jeffrey Brinker. Porous nanoparticle supported lipid bilayers (protocells) as delivery vehicles. *J. Am. Chem. Soc.*, 131:1354–1355, 2009.
- [178] Christopher Hom, Jie Lu, Monty Liong, Hanzhi Luo, Zongxi Li, Jeffrey I. Zink, and Fuyuhiko Tamanoi. Mesoporous silica nanoparticles facilitate delivery of sirna to shutdown signaling pathways in mammalian cells. *Small*, 6:1185–1190, 2010.
- [179] Si-Han Wu, Yu-Shen Lin, Yann Hung, Yi-Hsin Chou, Yi-Hua Hsu, Chen Chang, and Chung-Yuan Mou. Multifunctional mesoporous silica nanoparticles for intracellular labeling and animal magnetic resonance imaging studies. *Chembiochem*, 9:53–57, 2008.
- [180] Huan Meng, Wilson X. Mai, Haiyuan Zhang, Min Xue, Tian Xia, Sijie Lin, Xiang Wang, Yang Zhao, Zhaoxia Ji, Jeffrey I. Zink, and Andre E. Nel. Codelivery of an optimal drug/sirna combination using mesoporous silica nanoparticles to overcome drug resistance in breast cancer in vitro and in vivo. *ACS Nano*, 7:994–1005, 2013.
- [181] Jie Lu, Monty Liong, Jeffrey I. Zink, and Fuyuhiko Tamanoi. Mesoporous silica nanoparticles as a delivery system for hydrophobic anticancer drugs. *Small*, 3:1341–1346, 2007.

- [182] Linlin Li, Fangqiong Tang, Huiyu Liu, Tianlong Liu, Nanjing Hao, Dong Chen, Xu Teng, and Junqi He. In vivo delivery of silica nanorattle encapsulated docetaxel for liver cancer therapy with low toxicity and high efficacy. *ACS Nano*, 4:6874–6882, 2010.
- [183] F Sharif, F Porta, A H Meijer, A Kros, and M K Richardson. Mesoporous silica nanoparticles as a compound delivery system in zebrafish embryos. *Int J Nanomedicine*, 7:1875–1890, 2012.
- [184] Yu Chen, Hangrong Chen, and Jianlin Shi. In vivo bio-safety evaluations and diagnostic/therapeutic applications of chemically designed mesoporous silica nanoparticles. *Adv Mater*, 25:3144–3176, 2013.
- [185] Si-Han Wu, Chung-Yuan Mou, and Hong-Ping Lin. Synthesis of mesoporous silica nanoparticles. *Chem. Soc. Rev.*, 42:3862–3875, 2013.
- [186] Yu-Shen Lin, Katie R. Hurley, and Christy L. Haynes. Critical considerations in the biomedical use of mesoporous silica nanoparticles. *J Phys Chem Lett*, 3:364–374, 2012.
- [187] Igor I. Slowing, Juan L. Vivero-Escoto, Brian G. Trewyn, and Victor S.-Y. Lin. Mesoporous silica nanoparticles: structural design and applications. *J. Mater. Chem.*, 20:7924–7937, 2010.
- [188] Fangqiong Tang, Linlin Li, and Dong Chen. Mesoporous silica nanoparticles: Synthesis, biocompatibility and drug delivery. *Adv. Mater.*, 24:1504–1534, 2012.
- [189] Frank Hoffmann, Maximilian Cornelius, Jürgen Morell, and Michael Fröba. Silica-based mesoporous organic-inorganic hybrid materials. *Angew Chem Int Ed Engl*, 45:3216–3251, 2006.
- [190] Dongyuan Zhao, Jianglin Feng, Qisheng Huo, Nicholas Melosh, Glenn H. Fredrickson, Bradley F. Chmelka, and Galen D. Stucky. Triblock copolymer syntheses of mesoporous silica with periodic 50 to 300 angstrom pores. *Science*, 279:548–552, 1998.
- [191] J. C. Vartuli, K. D. Schmitt, C. T. Kresge, W. J. Roth, M. E. Leonowicz, S. B. McCullen, S. D. Hellring, J. S. Beck, and J. L. and Schlenker. Effect of surfactant/silica molar ratios on the formation of mesoporous molecular sieves: Inorganic mimicry of surfactant liquid-crystal phases and mechanistic implications. *Chem. Mater.*, 6:2317–2326, 1994.
- [192] Peter T. Tanev and Thomas J. Pinnavaia. A neutral templating route to mesoporous molecular sieves. *Science*, 267:865–867, 1995.
- [193] Gontran Herrier, Jean-Luc Blin, and Bao-Lian Su. Mso-type mesoporous silicas with well-tailored pore sizes synthesized via an assembly of deca(ethylene oxide) oleyl ether surfactant and tetramethoxysilane silica precursor. *Langmuir*, 17:4422–4430, 2001.
- [194] B. Devika Chithrani, Arezou A. Ghazani, and Warren C. W. Chan. Determining the size and shape dependence of gold nanoparticle uptake into mammalian cells. *Nano Lett.*, 6:662–668, 2006.

## Bibliography

- [195] C. E. Fowler, D. Khushalani, B. Lebeau, and S. Mann. Nanoscale materials with mesostructured interiors. *Adv Mater*, 13:649–652, 2001.
- [196] Yunfeng Lu, Hongyou Fan, Aaron Stump, Timothy L. Ward, Thomas Rieker, and C. Jeffrey Brinker. Aerosol-assisted self-assembly of mesostructured spherical nanoparticles. *Nature*, 398:223–226, 1999.
- [197] Keisei Suzuki, Kenichi Ikari, and Hiroaki Imai. Synthesis of silica nanoparticles having a well-ordered mesostructure using a double surfactant system. *J. Am. Chem. Soc.*, 126:462–463, 2004.
- [198] Michael Grun, Iris Lauer, and Klaus K. Unger. The synthesis of micrometer- and submicrometer-size spheres of ordered mesoporous oxide mcm-41. *Adv Mater*, 9:254–257, 1997.
- [199] C. Jeffrey Brinker, Yunfeng Lu, Alan Sellinger, and Hongyou Fan. Evaporation-induced self-assembly: Nanostructures made easy. *Adv Mater.*, 11:579–585, 1999.
- [200] Seong Huh, Jerzy W. Wiench, Ji-Chul Yoo, Marek Pruski, and Victor S.-Y. Lin. Organic functionalization and morphology control of mesoporous silicas via a co-condensation synthesis method. *Chem. Mater.*, 15:4247–4256, 2003.
- [201] Qiang Cai, Zhong-Sheng Luo, Wen-Qin Pang, Yu-Wei Fan, Xi-Hua Chen, and Fu-Zhai Cui. Dilute solution routes to various controllable morphologies of mcm-41 silica with a basic medium. *Chem. Mater.*, 13:258–263, 2001.
- [202] Yu-Shen Lin, Nardine Abadeer, Katie R. Hurley, and Christy L. Haynes. Ultrastable, redispersible, small, and highly organomodified mesoporous silica nanotherapeutics. *J. Am. Chem. Soc.*, 133:20444–20457, 2011.
- [203] Kai Ma, Ulrike Werner-Zwanziger, Josef Zwanziger, and Ulrich Wiesner. Controlling growth of ultrasmall sub-10 nm fluorescent mesoporous silica nanoparticles. *Chem. Mater.*, 25:677–691, 2013.
- [204] Johannes Kobler, Karin Moeller, and Thomas Bein. Colloidal suspensions of functionalized mesoporous silica nanoparticles. *ACS Nano*, 2:791–799, 2008.
- [205] Mi-Hee Kim, Hee-Kyung Na, Young-Kwan Kim, Soo-Ryoon Ryoo, Hae Sung Cho, Kyung Eun Lee, Hyesung Jeon, Ryong Ryoo, and Dal-Hee Min. Facile synthesis of monodispersed mesoporous silica nanoparticles with ultralarge pores and their application in gene delivery. *ACS Nano*, 5:3568–3576, 2011.
- [206] Kun Zhang, Lang-Lang Xu, Jin-Gang Jiang, Nathalie Calin, Koon-Fung Lam, San-Jun Zhang, Hai-Hong Wu, Guang-Dong Wu, B len Albela, Laurent Bonneviot, and Peng Wu. Facile large-scale synthesis of monodisperse mesoporous silica nanospheres with tunable pore structure. *J. Am. Chem. Soc.*, 135:2427–2430, 2013.

- [207] Xiaoxing Sun, Yannan Zhao, Victor S.-Y. Lin, Igor I. Slowing, and Brian G. Trewyn. Luciferase and luciferin co-immobilized mesoporous silica nanoparticle materials for intracellular biocatalysis. *J. Am. Chem. Soc.*, 133:18554–18557, 2011.
- [208] Helen Vallhov, Natalia Kupferschmidt, Susanne Gabrielsson, Staffan Paulie, Maria StrÅ, mme, Alfonso E. Garcia-Bennett, and Annika Scheynius. Adjuvant properties of mesoporous silica particles tune the development of effector t cells. *Small*, 8:2116–2124, 2012.
- [209] Valentina Cauda, Christian Argyo, Davin G. Piercey, and Thomas Bein. Liquid-phase calcination of colloidal mesoporous silica nanoparticles in high-boiling solvents. *J. Am. Chem. Soc.*, 133:6484–6486, 2011.
- [210] A. Stein, B. J. Melde, and R. C. Schrodén. Hybrid inorganic-organic mesoporous silicates-nanoscope reactors coming of age. *Adv Mater*, 12:1403–1419, 2000.
- [211] David M Ford, Eric E Simanek, and Daniel F Shantz. Engineering nanospaces: ordered mesoporous silicas as model substrates for building complex hybrid materials. *Nanotechnology*, 16:S458, 2005.
- [212] Chiyong Park, Kyoungoh Oh, Cheon Lee, and Chulhee Kim. Controlled release of guest molecules from mesoporous silica particles based on a ph-responsive polypseudorotaxane motif. *Angew Chem Int Ed*, 46:1455–1457, 2007.
- [213] Yu-Shen Lin, Chih-Pin Tsai, Hsing-Yi Huang, Chieh-Ti Kuo, Yann Hung, Dong-Ming Huang, Yao-Chang Chen, and Chung-Yuan Mou. Well-ordered mesoporous silica nanoparticles as cell markers. *Chem. Mater.*, 17:4570–4573, 2005.
- [214] Cheng-Yu Lai, Brian G. Trewyn, Dusan M. Jeftinija, Ksenija Jeftinija, Shu Xu, Srdija Jeftinija, and Victor S.-Y. Lin. A mesoporous silica nanosphere-based carrier system with chemically removable cds nanoparticle caps for stimuli-responsive controlled release of neurotransmitters and drug molecules. *J. Am. Chem. Soc.*, 125:4451–4459, 2003.
- [215] Xinglu Huang, Linlin Li, Tianlong Liu, Nanjing Hao, Huiyu Liu, Dong Chen, and Fangqiong Tang. The shape effect of mesoporous silica nanoparticles on biodistribution, clearance, and biocompatibility in vivo. *ACS Nano*, 5:5390–5399, 2011.
- [216] M. Manzano, V. Aina, C.O. Arean, F. Balas, V. Cauda, M. Colilla, M.R. Delgado, and M. Vallet-Regi. Studies on mcm-41 mesoporous silica for drug delivery: Effect of particle morphology and amine functionalization. *Chem. Eng. J.*, 137:30 – 37, 2008.
- [217] Jessica M. Rosenholm and Mika Linden. Towards establishing structure-activity relationships for mesoporous silica in drug delivery applications. *J Control Release*, 128:157 – 164, 2008.
- [218] Katsutoshi Yamamoto and Takashi Tatsumi. Remarkable improvement in hydrothermal stability of mcm-41 by surface modification with grignard reagents. *Chem. Lett.*, 29:624–625, 2000.

## Bibliography

- [219] Jung Eun Lim, Chang Bo Shim, Ji Man Kim, Bun Yeoul Lee, and Jae Eui Yie. Dehydroxylation route to surface modification of mesoporous silicas by using grignard reagents. *Angew Chem Int Ed*, 43:3839–3842, 2004.
- [220] Johann Kecht and Thomas Bein. Functionalization of colloidal mesoporous silica by metalorganic reagents. *Langmuir*, 24:14209–14214, 2008.
- [221] Johann Kecht, Axel Schlossbauer, and Thomas Bein. Selective functionalization of the outer and inner surfaces in mesoporous silica nanoparticles. *Chem. Mater.*, 20:7207–7214, 2008.
- [222] Jie Lu, Eunshil Choi, Fuyuhiko Tamanoi, and Jeffrey I. Zink. Light-activated nanoimpeller-controlled drug release in cancer cells. *Small*, 4:421–426, 2008.
- [223] Gustav Nordlund, Jovice Boon Sing Ng, Lennart Bergstroem, and Peter Brzezinski. A membrane-reconstituted multisubunit functional proton pump on mesoporous silica particles. *ACS Nano*, 3:2639–2646, 2009.
- [224] Juewen Liu, Xingmao Jiang, Carlee Ashley, and C. Jeffrey Brinker. Electrostatically mediated liposome fusion and lipid exchange with a nanoparticle-supported bilayer for control of surface charge, drug containment, and delivery. *J. Am. Chem. Soc.*, 131:7567–7569, 2009.
- [225] Abdul M. Mumin, John W. Barrett, Gregory A. Dekaban, and Jin Zhang. Dendritic cell internalization of foam-structured fluorescent mesoporous silica nanoparticles. *J Colloid Interface Sci*, 353:156 – 162, 2011.
- [226] Qianjun He, Jianlin Shi, Min Zhu, Yu Chen, and Feng Chen. The three-stage in vitro degradation behavior of mesoporous silica in simulated body fluid. *Microporous Mesoporous Mater*, 131:314 – 320, 2010.
- [227] Valentina Cauda, Axel Schlossbauer, and Thomas Bein. Bio-degradation study of colloidal mesoporous silica nanoparticles: Effect of surface functionalization with organo-silanes and poly(ethylene glycol). *Microporous Mesoporous Mater*, 132:60 – 71, 2010.
- [228] Qianjun He, Zhiwen Zhang, Fang Gao, Yaping Li, and Jianlin Shi. In vivo biodistribution and urinary excretion of mesoporous silica nanoparticles: Effects of particle size and pegylation. *Small*, 7:271–280, 2011.
- [229] Yu-Shen Lin and Christy L. Haynes. Impacts of mesoporous silica nanoparticle size, pore ordering, and pore integrity on hemolytic activity. *J. Am. Chem. Soc.*, 132:4834–4842, 2010.
- [230] Adem Yildirim, Erol Ozgur, and Mehmet Bayindir. Impact of mesoporous silica nanoparticle surface functionality on hemolytic activity, thrombogenicity and non-specific protein adsorption. *J. Mater. Chem. B*, 1:1909–1920, 2013.
- [231] Christian Argyo, Valentina Cauda, Hanna Engelke, Joachim Raedler, Gregor Bein, and Thomas Bein. Heparin-coated colloidal mesoporous silica nanoparticles efficiently bind to antithrombin as an anticoagulant drug-delivery system. *Chem. Eur. J.*, 18:428–432, 2012.

- [232] Invitrogen. Cell and tissue analysis. <http://www.b2b.invitrogen.com/site/us/en/home/Products-and-Services/Applications/Cell-and-Tissue-Analysis/Cell-Structure.html>, 2014.
- [233] Timo Lebold, Christophe Jung, Jens Michaelis, and Christoph Braeuchle. Nanostructured silica materials as drug-delivery systems for doxorubicin: Single molecule and cellular studies. *Nano Lett.*, 9:2877–2883, 2009.
- [234] Jeff W Lichtman and Jose-Angel Conchello. Fluorescence microscopy. *Nat Meth*, 2:910–919, 2005.
- [235] Peter Jomo Walla. *Modern Biophysical Chemistry*. Wiley-VCH, 2009.
- [236] L. Song, E.J. Hennink, I.T. Young, and H.J. Tanke. Photobleaching kinetics of fluorescein in quantitative fluorescence microscopy. *Biophys J*, 68:2588–2600, 1995.
- [237] Raymond Bonnett. Photosensitizers of the porphyrin and phthalocyanine series for photodynamic therapy. *Chem. Soc. Rev.*, 24:19–33, 1995.
- [238] Rudiger Rudolf, Marco Mongillo, Rosario Rizzuto, and Tullio Pozzan. Looking forward to seeing calcium. *Nat Rev Mol Cell Biol*, 4:579–586, 2003.
- [239] Roger Y. Tsien. Chapter 5 fluorescent indicators of ion concentrations. *Methods in Cell Biology*, Volume 30:127–156, 1989.
- [240] M.L. Barcellona, G. Cardiel, and E. Gratton. Time-resolved fluorescence of dapi in solution and bound to polydeoxynucleotides. *Biochem. Biophys. Res. Commun.*, 170:270 – 280, 1990.
- [241] August Andersson, Jens Danielsson, Astrid Graeslund, and Lena Maeler. Kinetic models for peptide-induced leakage from vesicles and cells. *Eur. Biophys. J.*, 36:621–635, 2007.
- [242] Anthony S. Stender, Kyle Marchuk, Chang Liu, Suzanne Sander, Matthew W. Meyer, Emily A. Smith, Bhanu Neupane, Gufeng Wang, Junjie Li, Ji-Xin Cheng, Bo Huang, and Ning Fang. Single cell optical imaging and spectroscopy. *Chem. Rev.*, 113:2469–2527, 2013.
- [243] Zeiss. Fluorescence imaging modes in live-cell microscopy. <http://zeiss-campus.magnet.fsu.edu/articles/livecellimaging/techniques.html>, 2014.
- [244] Juan L. Vivero-Escoto, Rachel C. Huxford-Phillips, and Wenbin Lin. Silica-based nanoprobe for biomedical imaging and theranostic applications. *Chem. Soc. Rev.*, 41:2673–2685, 2012.
- [245] Tennyson L. Doane and Clemens Burda. The unique role of nanoparticles in nanomedicine: imaging, drug delivery and therapy. *Chem. Soc. Rev.*, 41:2885–2911, 2012.
- [246] Giuseppe Bardi, Maria Ada Malvindi, Lisa Gherardini, Mario Costa, Pier Paolo Pompa, Roberto Cingolani, and Tommaso Pizzorusso. The biocompatibility of amino functionalized cdse/zns quantum-dot-doped sio2 nanoparticles with primary neural cells and their gene carrying performance. *Biomaterials*, 31:6555 – 6566, 2010.

## Bibliography

- [247] Bastian Rühle, Melari Davies, Timo Lebold, Christoph Braeuchle, and Thomas Bein. Highly oriented mesoporous silica channels synthesized in microgrooves and visualized with single-molecule diffusion. *ACS Nano*, 6:1948–1960, 2012.
- [248] Andreas Zuerner, Johanna Kirstein, Markus Doblinger, Christoph Braeuchle, and Thomas Bein. Visualizing single-molecule diffusion in mesoporous materials. *Nature*, 450:705–708, 2007.
- [249] J. Kirstein, B. Platschek, C. Jung, R. Brown, T. Bein, and C. Braeuchle. Exploration of nanostructured channel systems with single-molecule probes. *Nat. Mater.*, 6:303–10, 2007.
- [250] Timo Lebold, Axel Schlossbauer, Katrin Schneider, Lothar Schermelleh, Heinrich Leonhardt, Thomas Bein, and Christoph Braeuchle. Controlling the mobility of oligonucleotides in the nanochannels of mesoporous silica. *Adv. Funct. Mater.*, 22:106–112, 2012.
- [251] Florian Feil, Valentina Cauda, Thomas Bein, and Christoph Braeuchle. Direct visualization of dye and oligonucleotide diffusion in silica filaments with collinear mesopores. *Nano Lett.*, 12:1354–1361, 2012.
- [252] Jinping Lai, Birju P. Shah, Eric Garfunkel, and Ki-Bum Lee. Versatile fluorescence resonance energy transfer-based mesoporous silica nanoparticles for real-time monitoring of drug release. *ACS Nano*, 7:2741–2750, 2013.
- [253] Veronika Weiss. Single particle tracking von egf-rezeptor gerichteten mesoporösen silica-nanopartikeln mit lipiddoppelschicht. Master’s thesis, University of Munich (LMU), 2011.
- [254] Karla de Bruin, Nadia Ruthardt, Katharina von Gersdorff, Ralf Bausinger, Ernst Wagner, Manfred Ogris, and Christoph Braeuchle. Cellular dynamics of egf receptor-targeted synthetic viruses. *Mol. Ther.*, 15:1297–1305, 2007.
- [255] W.J. Godinez, M. Lampe, S. Woerz, B. Mueller, R. Eils, and K. Rohr. Deterministic and probabilistic approaches for tracking virus particles in time-lapse fluorescence microscopy image sequences. *Med Image Anal*, 13:325 – 342, 2009.
- [256] Delphine Arcizet, Boern Meier, Erich Sackmann, Joachim O. Raedler, and Doris Heinrich. Temporal analysis of active and passive transport in living cells. *Phys. Rev. Lett.*, 101:248103–248107, 2008.
- [257] Georg Seisenberger, Martin U. Ried, Thomas Endreß, Hildegard Buening, Michael Hallek, and Christoph Braeuchle. Real-time single-molecule imaging of the infection pathway of an adeno-associated virus. *Science*, 294:1929–1932, 2001.
- [258] Frauke M. Mickler, Leonhard Moeckl, Nadia Ruthardt, Manfred Ogris, Ernst Wagner, and Christoph Braeuchle. Tuning nanoparticle uptake: Live-cell imaging reveals two distinct endocytosis mechanisms mediated by natural and artificial egfr targeting ligand. *Nano Lett.*, 12:3417–3423, 2012.

- [259] Nadia Ruthardt, Don C Lamb, and Christoph Brauchle. Single-particle tracking as a quantitative microscopy-based approach to unravel cell entry mechanisms of viruses and pharmaceutical nanoparticles. *Mol. Ther.*, 19:1199–1211, 2011.
- [260] Chia-Hung Lee, Shih-Hsun Cheng, Yu-Jing Wang, Yu-Ching Chen, Nai-Tzu Chen, Jeffrey Souris, Chin-Tu Chen, Chung-Yuan Mou, Chung-Shi Yang, and Leu-Wei Lo. Near-infrared mesoporous silica nanoparticles for optical imaging: Characterization and in vivo biodistribution. *Adv. Funct. Mater.*, 19:215–222, 2009.
- [261] Qianjun He, Jiamin Zhang, Jianlin Shi, Ziyang Zhu, Linxia Zhang, Wenbo Bu, Limin Guo, and Yu Chen. The effect of pegylation of mesoporous silica nanoparticles on nonspecific binding of serum proteins and cellular responses. *Biomaterials*, 31:1085 – 1092, 2010.
- [262] Invitrogen. Dapi nucleic acid stain - productinformation. <http://tools.lifetechnologies.com/content/sfs/manuals/mp01306.pdf>, 2014.
- [263] Invitrogen. Dextran conjugates - productinformation. <http://tools.lifetechnologies.com/content/sfs/manuals/mp01800.pdf>, 2014.
- [264] Invitrogen. Bodipy @lipid probes - productinformation. <http://tools.lifetechnologies.com/content/sfs/manuals/mp03792.pdf>, 2014.
- [265] Sigma-Aldrich. Calcein - productinformation. <http://www.sigmaaldrich.com/catalog/product/sigma/c0875?lang=de&region=DE>, 2014.
- [266] Sigma-Aldrich. 5(6)-carboxyfluorecein - productinformation. <http://www.sigmaaldrich.com/catalog/product/sigma/21877?lang=de&region=DE>, 2014.
- [267] Sigma-Aldrich. Fluorescein isothiocyanate-dextran - productinformation. [http://www.sigmaaldrich.com/content/dam/sigma-aldrich/docs/Sigma/Product\\_Information\\_Sheet/1/fd4pis.pdf](http://www.sigmaaldrich.com/content/dam/sigma-aldrich/docs/Sigma/Product_Information_Sheet/1/fd4pis.pdf), 03 2014.
- [268] Invitrogen. Green fluorescent protein (gfp) - productinformation. [www.lifetechnologies.com/de/de/home/life-science/cell-analysis/fluorophores/green-fluorescent-protein.html?icid=fr-gfp-main](http://www.lifetechnologies.com/de/de/home/life-science/cell-analysis/fluorophores/green-fluorescent-protein.html?icid=fr-gfp-main), 2014.
- [269] Invitrogen. Wga488 - productinformation. <http://tools.lifetechnologies.com/content/sfs/manuals/mp00831.pdf>, 2014.
- [270] Invitrogen. LysoTracker red dnd-99 - productinformation. <http://tools.lifetechnologies.com/content/sfs/manuals/mp07525.pdf>, 2014.
- [271] Invitrogen. Propidium iodide nucleic acid stain - productinformation. <http://tools.lifetechnologies.com/content/sfs/manuals/mp01304.pdf>, 2014.
- [272] Sigma-Aldrich. 5(6)-carboxy-x-rhodamine - productinformation. <http://www.sigmaaldrich.com/catalog/product/sigma/21965?lang=de&region=DE>, 03 2014.

## Bibliography

- [273] Claudia C. Lee, Brian W. Pouge, Rendy R. Strawbridge, Karen L. Moodie, Luanna R. Bartholomew, Gregory C. Burke, and P. Jack Hoopes. Comparison of photosensitizer (alpcs2) quantification techniques: In situ fluorescence microsampling versus tissue chemical extraction's. *Photochem. Photobiol.*, 74:453–460, 2001.
- [274] ATTO-TECGmbH. Atto633 - productinformation. [https://www.atto-tec.com/attotecshop/product\\_info.php?info=p110\\_atto-633.html&XTCsid=c34954b3452254b8fa8964d16d3d914f](https://www.atto-tec.com/attotecshop/product_info.php?info=p110_atto-633.html&XTCsid=c34954b3452254b8fa8964d16d3d914f), 2014.
- [275] Invitrogen. Bacmam gfp - productinformation. <http://tools.lifetechnologies.com/content/sfs/manuals/mp10383.pdf>, 2014.
- [276] N. D. Sonawane, Francis C. Szoka, and A. S. Verkman. Chloride accumulation and swelling in endosomes enhances dna transfer by polyamine-dna polyplexes. *J. Biol. Chem.*, 278:44826–44831, 2003.
- [277] Robson Marsden, Hana, Nina A. Elbers, Paul H. H. Bomans, Nico A. J. M. Sommerdijk, and Alexander Kros. A reduced snare model for membrane fusion. *Angew Chem Int Ed*, 48:2330–2333, 2009.
- [278] Martin Meyer, Christian Dohmen, Alexander Philipp, Daniel Kiener, Gelja Maiwald, Christina Scheu, Manfred Ogris, and Ernst Wagner. Synthesis and biological evaluation of a bioresponsive and endosomolytic sirna-polymer conjugate. *Mol. Pharm.*, 6:752–762, 2009.
- [279] R Rox Anderson and Parrish John A. The optics of human skin. *J. Invest. Dermatol.*, 77:13–19, 1981.
- [280] Nobuhiro Nishiyama, Aya Iriyama, Woo-Dong Jang, Kanjiro Miyata, Keiji Itaka, Yuji Inoue, Hidenori Takahashi, Yasuo Yanagi, Yasuhiro Tamaki, Hiroyuki Koyama, and Kazunori Kataoka. Light-induced gene transfer from packaged dna enveloped in a dendrimeric photosensitizer. *Nat. Mater.*, 4:934–941, 2005.
- [281] Sebastien Febvay, Davide M. Marini, Angela M. Belcher, and David E. Clapham. Targeted cytosolic delivery of cell-impermeable compounds by nanoparticle-mediated, light-triggered endosome disruption. *Nano Lett.*, 10:2211–2219, 2010.
- [282] Yang Yang, Weixing Song, Anhe Wang, Pengli Zhu, Jinbo Fei, and Junbai Li. Lipid coated mesoporous silica nanoparticles as photosensitive drug carriers. *Phys. Chem. Chem. Phys.*, 12:4418–4422, 2010.
- [283] Junseok Lee, Juhee Park, Kaushik Singha, and Won Jong Kim. Mesoporous silica nanoparticle facilitated drug release through cascade photosensitizer activation and cleavage of singlet oxygen sensitive linker. *Chem. Commun.*, 49:1545–1547, 2013.
- [284] Cynthia A. Ladino, Ravi V.J. Chari, Elizabeth A. Bourret, Nancy L. Kedersha, and Victor S. Goldmacher. Folate-maytansinoids: Target-selective drugs of low molecular weight. *Int. J. Cancer*, 73:859–864, 1997.

- [285] Y H Xu, N Richert, S Ito, G T Merlino, and I Pastan. Characterization of epidermal growth factor receptor gene expression in malignant and normal human cell lines. *Proc. Natl. Acad. Sci. USA*, 81:7308–7312, 1984.
- [286] Halina Mojzisova, Stephanie Bonneau, and Daniel Brault. Structural and physico-chemical determinants of the interactions of macrocyclic photosensitizers with cells. *Eur. Biophys. J.*, 36:943–953, 2007.
- [287] K.I. Salokhiddinov, I.M. Byteva, and G.P. Gurinovich. Lifetime of singlet oxygen in various solvents. *J. Appl. Spectrosc.*, 34:561–564–, 1981.
- [288] Erik Brewer, Jason Coleman, and Anthony Lowman. Emerging technologies of polymeric nanoparticles in cancer drug delivery. *J Nanomater.*, 2011:1–10, 2011.
- [289] Jessica Y. Shu, Brian Panganiban, and Ting Xu. Peptide-polymer conjugates: From fundamental science to application. *Annu. Rev. Phys. Chem.*, 64:631–657, 2013.
- [290] G. Wilhelmina de Groot, M. Gabriella Santonicola, Kaori Sugihara, Tomaso Zambelli, Erik Reimhult, Janos Voeroes, and G. Julius Vancso. Switching transport through nanopores with ph-responsive polymer brushes for controlled ion permeability. *ACS Appl Mater Interfaces*, 5:1400–1407, 2013.
- [291] Lorenzo Albertazzi, Frauke M. Mickler, Giovanni M. Pavan, Fabrizio Salomone, Giuseppe Bardi, Mariangela Panniello, Elizabeth Amir, Taegon Kang, Kato L. Killops, Christoph Braeuchle, Roey J. Amir, and Craig J. Hawker. Enhanced bioactivity of internally functionalized cationic dendrimers with peg cores. *Biomacromolecules*, 13:4089–4097, 2012.
- [292] A Vetter, KS Viridi, S Espenlaub, W Roedl, E Wagner, PS Holm, C Scheu, F Kreppel, C Spitzweg, and M Ogris. Adenoviral vectors coated with pamam dendrimer conjugates allow car independent virus uptake and targeting to the egf receptor. *Mol. Pharm.*, 10:606–618, 2013.
- [293] Claire Minard-Basquin, Tanja Weil, Andreas Hohner, Joachim O. Raedler, and Klaus Muellen. A polyphenylene dendrimer-detergent complex as a highly fluorescent probe for bioassays. *J. Am. Chem. Soc.*, 125:5832–5838, 2003.
- [294] Silvia Arpicco, Barbara Stella, Oddone Schiavon, Paola Milla, Daniele Zonari, and Luigi Cattel. Preparation and characterization of novel poly(ethylene glycol) paclitaxel derivatives. *Int. J. Pharm.*, 454:653–659, 2013.
- [295] Zhuxian Zhou, Xinpeng Ma, Erlei Jin, Jianbin Tang, Meihua Sui, Youqing Shen, Edward A. Van Kirk, William J. Murdoch, and Maciej Radosz. Linear-dendritic drug conjugates forming long-circulating nanorods for cancer-drug delivery. *Biomaterials*, 34:5722–5735, 2013.
- [296] Oshrat Harush-Frenkel, Nir Debotton, Simon Benita, and Yoram Altschuler. Targeting of nanoparticles to the clathrin-mediated endocytic pathway. *Biochem. Biophys. Res. Commun.*, 353:26–32, 2007.

## Bibliography

- [297] Melike Lakadamyali, Michael J. Rust, Hazen P. Babcock, and Xiaowei Zhuang. Visualizing infection of individual influenza viruses. *Proceedings of the National Academy of Sciences*, 100:9280–9285, 2003.
- [298] Chun-Yan Hong, Xin Li, and Cai-Yuan Pan. Fabrication of smart nanocontainers with a mesoporous core and a ph-responsive shell for controlled uptake and release. *J. Mater. Chem.*, 19:5155–5160, 2009.
- [299] Jiao-Tong Sun, Chun-Yan Hong, and Cai-Yuan Pan. Fabrication of pdeama-coated mesoporous silica nanoparticles and ph-responsive controlled release. *J. Phys. Chem. C*, 114:12481–12486, 2010.
- [300] Rui Liu, Puhong Liao, Jikai Liu, and Pingyun Feng. Responsive polymer-coated mesoporous silica as a ph-sensitive nanocarrier for controlled release. *Langmuir*, 27:3095–3099, 2011.
- [301] Alla Synytska, Manfred Stamm, Stefan Diez, and Leonid Ionov. Simple and fast method for the fabrication of switchable bicomponent micropatterned polymer surfaces. *Langmuir*, 23:5205–5209, 2007.
- [302] Marcela D’Alincourt Salazar and Manohar Ratnam. The folate receptor: What does it promise in tissue-targeted therapeutics? *J. Appl. Spectrosc.*, 26:141–152–, 2007.
- [303] Jatta Huotari and Ari Helenius. Endosome maturation. *EMBO J*, 30:3481–3500, 2011.
- [304] N Brasseur, R Ouellet, C La Madeleine, and J E van Lier. Water-soluble aluminium phthalocyanine-polymer conjugates for pdt: photodynamic activities and pharmacokinetics in tumour-bearing mice. *Br. J. Cancer*, 80:1533–1541, 1999.
- [305] Daniele Zink, Nicolas Sadoni, and Ernst Stelzer. Visualizing chromatin and chromosomes in living cells. *Methods*, 29:42–50, 2003.
- [306] ME Lalande, V Ling, and RG Miller. Hoechst 33342 dye uptake as a probe of membrane permeability changes in mammalian cells. *Proc. Natl. Acad. Sci. U. S. A.*, 78:363–367–, 1981.
- [307] J Kapuscinski. Interactions of nucleic acids with fluorescent dyes: spectral properties of condensed complexes. *J Histochem Cytochem*, 38:1323–1329, 1990.
- [308] Lingling Shan, Sisi Cui, Changli Du, Shunan Wan, Zhiyu Qian, Samuel Achilefu, and Yueqing Gu. A paclitaxel-conjugated adenovirus vector for targeted drug delivery for tumor therapy. *Biomaterials*, 33:146–162, 2012.
- [309] Yung-Chu Chen, Wen-Hsiang Chang, Shian-Jy Wang, and Wen-Yuan Hsieh. Fluorescent magnetic nanoparticles with specific targeting functions for combined targeting, optical imaging and magnetic resonance imaging. *Journal of Biomaterials Science, Polymer Edition*, 23:1903–1922, 2012.

- [310] Stefan Andersson-Engels and Brian C Wilson. In vivo fluorescence in clinical oncology: fundamental and practical issues. *Journal of Cellular Pharmacology*, 3:66–79, 1992.
- [311] Christian Argyo. *Tailoring Properties of Multifunctional Mesoporous Silica Nanoparticles for Controlled Drug Delivery Applications*. PhD thesis, LMU Munich, 2014.
- [312] D A Tomalia, H Baker, J Dewald, M Hall, G Kallos, S Martin, J Roeck, J Ryder, and P Smith. A new class of polymers: Starburst-dendritic macromolecules. *Polym J*, 17:117–132, 1985.
- [313] Roseita Esfand and Donald A. Tomalia. Poly(amidoamine) (pamam) dendrimers: from biomimicry to drug delivery and biomedical applications. *Drug Discovery Today*, 6:427 – 436, 2001.
- [314] A.R. Menjoge, R.M. Kannan, and D.A. Tomalia. Dendrimer-based drug and imaging conjugates: design considerations for nanomedical applications. *Drug Discov Today*, 15:171–185, 2010.
- [315] Anna Carlmark, Craig Hawker, Anders Hult, and Michael Malkoch. New methodologies in the construction of dendritic materials. *Chem. Soc. Rev.*, 38:352–362, 2009.
- [316] J F Kukowska-Latallo, A U Bielinska, J Johnson, R Spindler, D A Tomalia, and J R Baker. Efficient transfer of genetic material into mammalian cells using starburst polyamidoamine dendrimers. *Proc Natl Acad Sci*, 93:4897–4902, 1996.
- [317] Jiehua Zhou, Jiangyu Wu, Nadia Hafdi, Jean-Paul Behr, Patrick Erbacher, and Ling Peng. Pamam dendrimers for efficient sirna delivery and potent gene silencing. *Chem. Commun.*, 22:2362–2364, 2006.
- [318] Bi-feng Pan, Da-xiang Cui, Ping Xu, Hao Chen, Feng-tao Liu, Qing Li, Tuo Huang, Xiao-gang You, Jun Shao, Chen-chen Bao, Feng Gao, Rong He, Meng-jun Shu, and Yong-jie Ma. Design of dendrimer modified carbon nanotubes for gene delivery. *Chin J Cancer Res*, 19:1–6, 2007.
- [319] Daniela R. Radu, Cheng-Yu Lai, Ksenija Jeftinija, Eric W. Rowe, Srdija Jeftinija, and Victor S.-Y. Lin. A polyamidoamine dendrimer-capped mesoporous silica nanosphere-based gene transfection reagent. *J Am Chem Soc*, 126:13216–13217, 2004.
- [320] Jae Wook Lee, Byung-Ku Kim, Hee Joo Kim, Seung Choul Han, Won Suk Shin, and Sung-Ho Jin. Convergent synthesis of symmetrical and unsymmetrical pamam dendrimers. *Macromolecules*, 39:2418–2422, 2006.
- [321] Jun Nakazawa and T. Daniel P. Stack. Controlled loadings in a mesoporous material: Click-on silica. *J Am Chem Soc*, 130:14360–14361, 2008.
- [322] Ute Boehme, Anja Klenge, Brigitte Haenel, and Ulrich Scheler. Counterion condensation and effective charge of pamam dendrimers. *Polymers*, 3:812–819, 2011.

## Bibliography

- [323] Neha Shah, Raymond J. Steptoe, and Harendra S. Parekh. Low-generation asymmetric dendrimers exhibit minimal toxicity and effectively complex dna. *J Pept Sci*, 17:470–478, 2011.
- [324] Adriano A Torrano, Julia Blechinger, Christian Osseforth, Christian Argyo, Armin Reller, Thomas Bein, Jens Michaelis, and Christoph Braeuchle. A fast analysis method to quantify nanoparticle uptake on a single cell level. *Nanomedicine*, 8:1815–1828, 2013.
- [325] Jong Ah Kim, Christoffer Aberg, Anna Salvati, and Kenneth A. Dawson. Role of cell cycle on the cellular uptake and dilution of nanoparticles in a cell population. *Nat Nano*, 7:62–68, 2012.
- [326] Danyel Hermes Tacker and Anthony O Okorodudu. Evidence for injurious effect of cocaethylene in human microvascular endothelial cells. *Clinica Chimica Acta*, 345:69 – 77, 2004.
- [327] Raimond B.G. Ravelli, Benoit Gigant, Patrick A. Curmi, Isabelle Jourdain, Sylvie Lachkar, Andre Sobel, and Marcel Knossow. Insight into tubulin regulation from a complex with colchicine and a stathmin-like domain. *Nature*, 428:198–202, 2004.
- [328] Bhabatarak Bhattacharyya, Dulal Panda, Suvroma Gupta, and Mithu Banerjee. Anti-mitotic activity of colchicine and the structural basis for its interaction with tubulin. *Medicinal Research Reviews*, 28:155–183, 2008.
- [329] Young-Mi Go and Dean P. Jones. Redox compartmentalization in eukaryotic cells. *Biochim Biophys Acta*, 1780:1273 – 1290, 2008.
- [330] Jun Yang, Hongtao Chen, Iontcho R. Vlahov, Ji-Xin Cheng, and Philip S. Low. Evaluation of disulfide reduction during receptor-mediated endocytosis by using fret imaging. *Proc. Natl. Acad. Sci. USA*, 103:13872–13877, 2006.
- [331] Cary D. Austin, Xiaohui Wen, Lewis Gazzard, Christopher Nelson, Richard H. Scheller, and Suzie J. Scales. Oxidizing potential of endosomes and lysosomes limits intracellular cleavage of disulfide-based antibody-drug conjugates. *Proc. Natl. Acad. Sci. U. S. A.*, 102:17987–17992, 2005.
- [332] Balasubramanian Arunachalam, Uyen T. Phan, Hans J. Geuze, and Peter Cresswell. Enzymatic reduction of disulfide bonds in lysosomes: Characterization of a gamma-interferon-inducible lysosomal thiol reductase (gilt). *Proc. Natl. Acad. Sci. U. S. A.*, 97:745–750, 2000.
- [333] Dimitrios A. Skoufias and Leslie Wilson. Mechanism of inhibition of microtubule polymerization by colchicine: inhibitory potencies of unliganded colchicine and tubulin-colchicine complexes. *Biochemistry*, 31:738–746, 1992.
- [334] Kosuke Morikawa and Mitsushiro Yanagida. Visualization of individual dna molecules in solution by light microscopy: Dapi staining method. *J Biochem*, 89:693–696, 1981.

- [335] Mahesh L. Patil, Min Zhang, and Tamara Minko. Multifunctional triblock nanocarrier (pamam-peg-pll) for the efficient intracellular sirna delivery and gene silencing. *ACS Nano*, 5:1877–1887, 2011.
- [336] Mahesh L. Patil, Min Zhang, Oleh Taratula, Olga B. Garbuzenko, Huixin He, and Tamara Minko. Internally cationic polyamidoamine pamam-oh dendrimers for sirna delivery: Effect of the degree of quaternization and cancer targeting. *Biomacromolecules*, 10:258–266, 2009.
- [337] Toshinari Takahashi, Eiji Yuba, Chie Kojima, Atsushi Harada, and Kenji Kono. Synthesis of a polyamidoamine dendron-bearing lipid having sugar moieties and its use for preparation of nonviral gene vectors. *Res. Chem. Intermed.*, 35:1005–1014, 2009.
- [338] Olimpia Gamucci, Alice Bertero, Mariacristina Gagliardi, and Giuseppe Bardi. Biomedical nanoparticles: Overview of their surface immune-compatibility. *Coatings*, 4:139–159, 2014.
- [339] Vijay M. Krishnamurthy, George K. Kaufman, Adam R. Urbach, Irina Gitlin, Katherine L. Gudiksen, Douglas B. Weibel, and George M. Whitesides. Carbonic anhydrase as a model for biophysical and physical-organic studies of proteins and protein-ligand binding. *Chemical Reviews*, 108:946–1051, 2008.
- [340] Emine Kaya, Milan Vrabel, Christian Deiml, Stefan Prill, Viviana S. Fluxa, and Thomas Carell. A genetically encoded norbornene amino acid for the mild and selective modification of proteins in a copper-free click reaction. *Angew Chem Int Ed*, 51:4466–4469, 2012.
- [341] Sabine Schneider, Michael J. Gattner, Milan Vrabel, Veronika Fluegel, Veronica Lopez-Carrillo, Stefan Prill, and Thomas Carell. Structural insights into incorporation of norbornene amino acids for click modification of proteins. *ChemBioChem*, 14:2114–2118, 2013.
- [342] Alexander T. Bauer, Elwira A. Strozyk, Christian Gorzelanny, Christoph Westerhausen, Anna Desch, Matthias F. Schneider, and Stefan W. Schneider. Cytotoxicity of silica nanoparticles through exocytosis of von willebrand factor and necrotic cell death in primary human endothelial cells. *Biomaterials*, 32:8385 – 8393, 2011.
- [343] Joanna Rejman, Volker Oberle, Inge S Zuhorn, and Dick Hoekstra. Size-dependent internalization of particles via the pathways of clathrin- and caveolae-mediated endocytosis. *Biochem. J.*, 377:159–169, 2004.
- [344] Martina Lichtnecker. Mesoporous silica nanoparticles with large pores for advanced drug delivery applications and enzyme immobilization. Master’s thesis, University of Munich (LMU), 2013.
- [345] Sandy B. Hartono, Wenyi Gu, Freddy Kleitz, Jian Liu, Lizhong He, Anton P. J. Middelberg, Chengzhong Yu, Gao Qing (Max) Lu, and Shi Zhang Qiao. Poly-l-lysine functionalized large pore cubic mesostructured silica nanoparticles as biocompatible carriers for gene delivery. *ACS Nano*, 6:2104–2117, 2012.

## Bibliography

- [346] Dongyuan Zhao, Qisheng Huo, Jianglin Feng, Bradley F. Chmelka, and Galen D. Stucky. Nonionic triblock and star diblock copolymer and oligomeric surfactant syntheses of highly ordered, hydrothermally stable, mesoporous silica structures. *J. Am. Chem. Soc.*, 120:6024–6036, 1998.
- [347] Hoang Vinh-Thang, Qinglin Huang, Mladen Eic, Do Trong-On, and Serge Kaliaguine. Adsorption of *c*7 hydrocarbons on biporous sba-15 mesoporous silica. *Langmuir*, 21:5094–5101, 2005.
- [348] N.K. Kala Raj, S.S. Deshpande, RohitH. Ingle, T. Raja, and P. Manikandan. Heterogenized molybdovanadophosphoric acid on amine-functionalized sba-15 for selective oxidation of alkenes. *Catalysis Letters*, 98:217–224–, 2004.
- [349] Christian Hess. Nanostructured vanadium oxide model catalysts for selective oxidation reactions. *ChemPhysChem*, 10:319–326, 2009.
- [350] Brian J. Scott, Gernot Wirnsberger, and Galen D. Stucky. Mesoporous and mesostructured materials for optical applications. *Chem. Mater.*, 13:3140–3150, 2001.
- [351] Ukmar Tina and Planinsek Odon. Ordered mesoporous silicates as matrices for controlled release of drugs. *Acta Pharmaceutica*, 60:373–, 2010.
- [352] Maria Vallet-Regi, Francisco Balas, and Daniel Arcos. Mesoporous materials for drug delivery. *Angewandte Chemie International Edition*, 46:7548–7558, 2007.
- [353] Fei Gao, Pablo Botella, Avelino Corma, Jose Blesa, and Lin Dong. Monodispersed mesoporous silica nanoparticles with very large pores for enhanced adsorption and release of dna. *J. Phys. Chem. B*, 113:1796–1804, 2009.
- [354] Monica W. Lam and Scott A. Mabury. Photodegradation of the pharmaceuticals atorvastatin, carbamazepine, levofloxacin, and sulfamethoxazole in natural waters. *Aquatic Sciences*, 67:177–188, 2005.
- [355] Yu A. Chen and Richard H. Scheller. Snare-mediated membrane fusion. *Nat Rev Mol Cell Biol*, 2:98–106, 2001.
- [356] Leonid V Chernomordik and Michael M Kozlov. Mechanics of membrane fusion. *Nat Struct Mol Biol*, 15:675–683, 2008.
- [357] Hana Robson Marsden, Itsuro Tomatsu, and Alexander Kros. Model systems for membrane fusion. *Chem. Soc. Rev.*, 40:1572–1585, 2011.
- [358] Hana Robson Marsden, Alexander V. Korobko, Tingting Zheng, Jens Voskuhl, and Alexander Kros. Controlled liposome fusion mediated by snare protein mimics. *Biomater. Sci.*, 1:1046–1054, 2013.

- [359] Itsuro Tomatsu, Hana Robson Marsden, Martin Rabe, Frank Versluis, Tingting Zheng, Harshal Zope, and Alexander Kros. Influence of pegylation on peptide-mediated liposome fusion. *J. Mater. Chem.*, 21:18927–18933, 2011.
- [360] Harshal R. Zope, Frank Versluis, Anita Ordas, Jens Voskuhl, Herman P. Spalink, and Alexander Kros. In vitro and in vivo supramolecular modification of biomembranes using a lipidated coiled-coil motif. *Angew. Chem. Int. Ed.*, 52:14247–14251, 2013.
- [361] Stephen C Harrison. Viral membrane fusion. *Nat Struct Mol Biol*, 15:690–698, 2008.
- [362] Alan R. Davis, Timothy Bos, Masahiro Ueda, Debi P. Nayak, Donald Dowbenko, and Richard W. Compans. Immune response to human influenza virus hemagglutinin expressed in escherichia coli. *Gene*, 21:273–284, 1983.
- [363] Ayman El-Sayed, Shiroh Futaki, and Hideyoshi Harashima. Delivery of macromolecules using arginine-rich cell-penetrating peptides: Ways to overcome endosomal entrapment. *The AAPS Journal*, 11:13–22–, 2009.
- [364] Patrick Midoux, Eric LeCam, Dominique Coulaud, Etienne Delain, and Chantal Pichon. Histidine containing peptides and polypeptides as nucleic acid vectors. *Somat Cell Mol Genet*, 27:27–47–, 2002.
- [365] Nicole M. Moore, Clayton L. Sheppard, Tiffany R. Barbour, and Shelly E. Sakiyama-Elbert. The effect of endosomal escape peptides on in vitro gene delivery of polyethylene glycol-based vehicles. *J. Gene Med.*, 10:1134–1149, 2008.
- [366] Veronika Mamaeva, Cecilia Sahlgren, and Mika Linden. Mesoporous silica nanoparticles in medicine - recent advances. *Adv Drug Deliv Rev*, 65:689 – 702, 2013.
- [367] Jessica M Rosenholm, Veronika Mamaeva, Cecilia Sahlgren, and Mika Linden. Nanoparticles in targeted cancer therapy: mesoporous silica nanoparticles entering preclinical development stage. *Nanomedicine*, 7:111–120, 2012.
- [368] Jie Lu, Monty Liong, Zongxi Li, Jeffrey I. Zink, and Fuyuhiko Tamanoi. Biocompatibility, biodistribution, and drug-delivery efficiency of mesoporous silica nanoparticles for cancer therapy in animals. *Small*, 6:1794–1805, 2010.
- [369] Bengt Fadeel and Alfonso E. Garcia-Bennett. Better safe than sorry: Understanding the toxicological properties of inorganic nanoparticles manufactured for biomedical applications. *Adv Drug Deliv Rev*, 62:362 – 374, 2010.
- [370] Qianjun He, Zhiwen Zhang, Yu Gao, Jianlin Shi, and Yaping Li. Intracellular localization and cytotoxicity of spherical mesoporous silica nano- and microparticles. *Small*, 5:2722–2729, 2009.

## Bibliography

- [371] Zhimin Tao, Matthew P. Morrow, Tewodros Asefa, Krishna K. Sharma, Cole Duncan, Abhishek Anan, Harvey S. Penefsky, Jerry Goodisman, and Abdul-Kader Souid. Mesoporous silica nanoparticles inhibit cellular respiration. *Nano Lett.*, 8:1517–1526, 2008.
- [372] Rainer Wittig, Jessica M Rosenholm, Eva von Haartman, Jarl Hemming, Felicitas Genze, Lotta Bergman, Thomas Simmet, Mika Linden, and Cecilia Sahlgren. Active targeting of mesoporous silica drug carriers enhances  $\gamma$ -secretase inhibitor efficacy in an in vivo model for breast cancer. *Nanomedicine*, 0:1–17, 2013.
- [373] Junchao Duan, Yongbo Yu, Yang Li, Yang Yu, and Zhiwei Sun. Cardiovascular toxicity evaluation of silica nanoparticles in endothelial cells and zebrafish model. *Biomaterials*, 34:5853 – 5862, 2013.
- [374] Harm HogenEsch and Alexander Yu Nikitin. Challenges in pre-clinical testing of anti-cancer drugs in cell culture and in animal models. *J Control Release*, 164:183 – 186, 2012.
- [375] Liang Cao and Michal Kruk. Synthesis of large-pore sba-15 silica from tetramethyl orthosilicate using triisopropylbenzene as micelle expander. *Colloids Surf A Physicochem Eng Asp*, 357:91 – 96, 2010.
- [376] Jolanta F. Kukowska-Latallo, Kimberly A. Candido, Zhengyi Cao, Shraddha S. Nigavekar, Istvan J. Majoros, Thommey P. Thomas, Lajos P. Balogh, Mohamed K. Khan, and James R. Baker. Nanoparticle targeting of anticancer drug improves therapeutic response in animal model of human epithelial cancer. *Cancer Res*, 65:5317–5324, 2005.
- [377] Li-Yan Qiu, Lu Yan, Lu Zhang, Yang-Min Jin, and Qing-He Zhao. Folate-modified poly(2-ethyl-2-oxazoline) as hydrophilic corona in polymeric micelles for enhanced intracellular doxorubicin delivery. *Int J Pharm*, 456:315 – 324, 2013.
- [378] Ying Li, Yang Lei, Ernst Wagner, Cao Xie, Weiyue Lu, Jianhua Zhu, Jie Shen, Jing Wang, and Min Liu. Potent retro-inverso d-peptide for simultaneous targeting of angiogenic blood vasculature and tumor cells. *Bioconjug Chem*, 24:133–143, 2013.
- [379] B Smrekar, L Wightman, M F Wolschek, C Lichtenberger, R Ruzicka, M Ogris, W Rodl, M Kursal, E Wagner, and R Kircheis. Tissue-dependent factors affect gene delivery to tumors in vivo. *Gene Ther.*, 10:1079–1088, 2003.
- [380] Jaehong Lim, Su Seong Lee, and Jackie Y. Ying. Mesoporous silica-supported catalysts for metathesis: application to a circulating flow reactor. *Chem. Commun.*, 46:806–808, 2010.

# Appendix

## 1 Synthesis details for Chapter 6: Targeted drug delivery in cancer cells with red light photoactivated mesoporous silica nanoparticles

### Experimental procedure for the shell reactions shown in Scheme 6.2

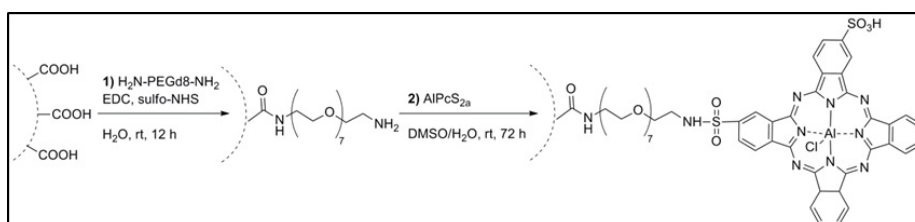


**Figure 1:** Shell reactions of MSN-SH<sub>in</sub>COOH<sub>out</sub> nanoparticles. 1) PEGylation reaction and 2) covalent attachment of photosensitizer AlPcS<sub>2a</sub>.

The carboxylic acid moieties of the colloidal mesoporous silica nanoparticles (MSN) obtained through hydrolysis of the cyano groups of the sample MSN-SH<sub>in</sub>-CN<sub>out</sub> (II) are PEGylated with a short bisamino polyethylene glycol linker via an EDC amidation. To avoid crosslinking of the nanoparticles an excess of the PEG-spacer was used. In a second reaction step, the Al(III) phthalocyanine chloride disulfonic acid (AlPcS<sub>2a</sub>) photosensitizer was covalently attached to the outer surface of the particle via a sulfonamide bond.

### Experimental procedure for Lipid-EGF construct

To utilize EGF as another targeting ligand beside folic acid, we synthesized a lipid-EGF construct, where the EGF (50  $\mu$ g) is covalently attached to the lipid DSPE-PEG<sub>2000</sub>-maleimide (Scheme 2). In a first step, the N-terminus of the targeting peptide was modified via the Traut's reagent (2-Iminothiolane, 2 equiv., 16 nmol) in an aqueous solution by stirring for 1 h at room temperature. This resulted in a terminal thiol group which can be used for further functionalization. Subsequently, the modified EGF was covalently attached to the lipid DSPE-PEG<sub>2000</sub>-maleimide (3.5  $\mu$ L of a 10 mg/mL 60/40 H<sub>2</sub>O/EtOH v%). The final DSPE-PEG<sub>2000</sub>-EGF construct can be further utilized to use as targeting ligand on the nanoparticle as described below.

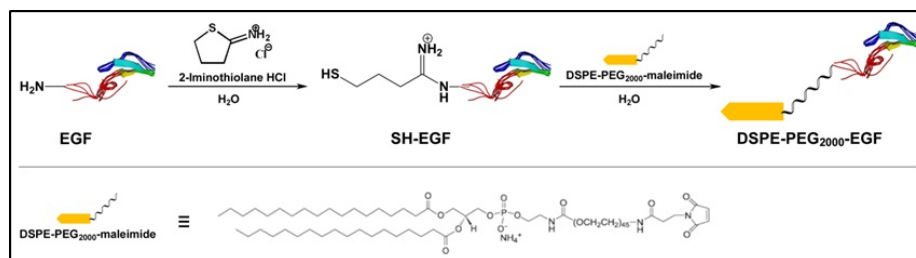


**Figure 2:** Chemical modification of the EGF targeting ligand via the Traut's reagent (2-iminothiolane) to achieve thiolation of the N-terminus of EGF. In a second step the lipid DSPE-PEG<sub>2000</sub>-maleimide covalently binds to the modified EGF

### Transmission electron microscopy

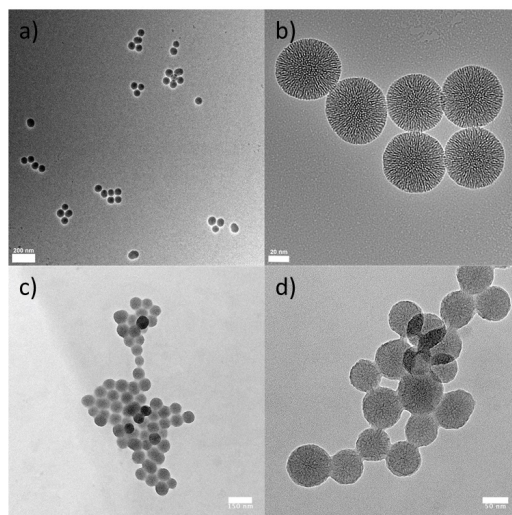


**Figure 3:** a-b)TEM images of the template-extracted core-shell MSN-SH<sub>in</sub>-CN<sub>out</sub> (I). c-d)TEM micrographs of the sample MSN-SH<sub>in</sub>-PEGd8NH<sub>2out</sub> (III).

All samples were investigated with a FEI Titan 80-300 operating at 300 kV with a high-angle annular dark field detector. A droplet of the diluted MSN solution in ethanol absolute was dried on a carbon-coated copper grid. The TEM micrographs in Figure 3 show template-extracted mesoporous core-shell silica particles of the type MSN-SH<sub>in</sub>-CN<sub>out</sub>. All nanoparticles are of perfect spherical shape, highly monodisperse and uniform with a size of around 70 nm, which is consistent with the dynamic light scattering data (see Figure 6.3 b). Furthermore, the worm-like mesoporous network is clearly visible in the micrographs, indicating a radial growth of the MSN.

Figure 3 c/d shows TEM images of the sample MSN-SH<sub>in</sub>-PEGd8NH<sub>2</sub> (III). The homogeneity of the sample and the meso-structure of the MSN are preserved during the hydrolysis of the cyano-groups and the PEGylation step. The size of around 70 nm is in good agreement with the results from the

dynamic light scattering experiments. In comparison to Figure 3a/b, the mesoporous structure of the nanoparticles is hardly detectable due to the additional organic layer attached to the MSN shell. The mild white-greyish halo is a focus artifact caused by electron beam exposure and ultrahigh vacuum.

## Nitrogen Sorption measurements

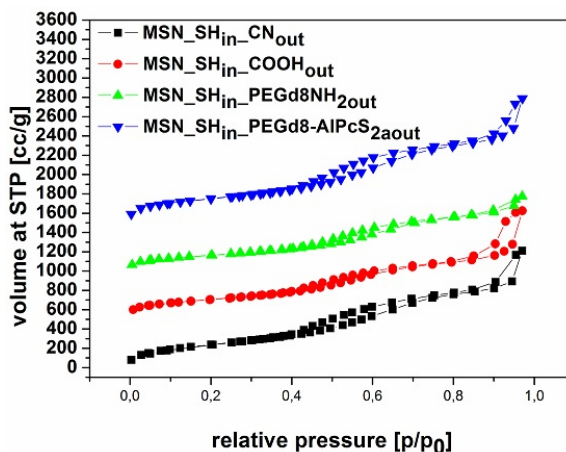


**Figure 4:** Nitrogen sorption isotherms for the samples MSN-SH<sub>in</sub>-CN<sub>out</sub> (black squares), MSN-SH<sub>in</sub>-COOH<sub>out</sub> (red circles), MSN-SH<sub>in</sub>-PEGd8NH<sub>2out</sub> (green up triangles) and MSN-SH<sub>in</sub>-PEGd8-AIPcS<sub>2aout</sub> (blue down triangles). For clarity reasons curves for MSN-SH<sub>in</sub>-COOH<sub>out</sub>, MSN-SH<sub>in</sub>-PEGd8NH<sub>2out</sub>, and MSN-SH<sub>in</sub>-PEGd8-AIPcS<sub>2aout</sub> are shifted along the y-axis by a value of 500 each.

Nitrogen sorption measurements were performed on a Quantachrome Instruments NOVA 4000e. All four samples (15 mg each) were heated to 393 K for 12 h in vacuo (10 mTorr) to outgas the samples before nitrogen sorption was measured at 77 K. For calculations of pore sizes and volumes a non-local density functional theory (NLDFT) equilibrium model of nitrogen on silica was used. The nitrogen sorption isotherms of the samples MSN-SH<sub>in</sub>-CN<sub>out</sub> (I, black squares), MSN-SH<sub>in</sub>-COOH<sub>out</sub> (II, red circles), MSN-SH<sub>in</sub>-PEGd8NH<sub>2out</sub> (III, green up triangles), and MSN-SH<sub>in</sub>-PEGd8-AIPcS<sub>2aout</sub> (IV, blue inverted triangles) can be seen in Figure 4a, exhibiting a typical type IV isotherms for mesoporous materials.

The Brunauer-Emmett-Teller (BET) surface areas for each sample are calculated from the corresponding nitrogen sorption isotherm in the range  $p/p_0 = 0.05 - 0.2$  and are summarized in Table 4b. All samples feature a high specific surface area typical for our MSN. We assume that the reduced BET surface area in the sample MSN-SH<sub>in</sub>-COOH<sub>out</sub> (II) in comparison with MSN-SH<sub>in</sub>-CN<sub>out</sub> (I) comes from the more condensed silica network and pore shrinkage resulting from the hydrolysis of the cyano-moiety in hydrochloric acid. The decrease of the specific surface area in the sample MSN-SH<sub>in</sub>-PEGd8NH<sub>2out</sub> (III) can be explained by the addition of non-porous PEG and the blocking of some pores by frozen PEG-linker in the surface layer of the MSN.

**Table 2:** Particle size, specific BET surface area, pore size and relative mass loss derived from Figure 6.3 b, Figure 4 and Figure 6.4 b

Sample	Particle size [nm]	BET surface area [m <sup>2</sup> *g <sup>-1</sup> ]	Pore size [nm]	Relative mass loss [%]
MSN-SH <sub>in</sub> -CN <sub>out</sub>	69	934	5.2	17
MSN-SH <sub>in</sub> -COOH <sub>out</sub>	125	746	5.1	12
MSN-SH <sub>in</sub> -PEGd8-NH <sub>2</sub>	98	615	5.6	18
MSN-SH <sub>in</sub> -PEGd8-NH <sub>2</sub>	98	615	5.6	18
MSN-SH <sub>in</sub> -PEGd8-AIPcS <sub>2aout</sub>	294	918	5.5	31
DOPC/DOTAP-SLB@MSN	160	n.a.	n.a.	n.a.

This effect is relatively small due to the short length of the flexible spacer. In contrast, the BET surface area of the sample MSN-SH<sub>in</sub>-PEGd8-AIPcS<sub>2aout</sub> is with 918 m<sup>2</sup>/g significantly higher than the BET surface area for MSN-SH<sub>in</sub>-COOH<sub>out</sub> (II) and MSN-SH<sub>in</sub>-PEGd8NH<sub>2out</sub> (III). We suppose that this effect comes from interstitial pore volume occurring upon attachment of AIPcS<sub>2a</sub> onto the particle shell. Considering phthalocyanines are large, sterically hindered molecules that lack the flexibility of a PEG-linker, a covalent attachment of them to the MSN surface will result in voids at liquid nitrogen temperatures. The pore size distributions derived from NLDFT calculations are given in Figure 6.2 and are summarized in Table 2. The pore size changes little upon PEGylation and photosensitizer attachment, indicating that the mesopores are still accessible for guest molecules. Furthermore, it proves the selective functionalization of the particle shell.

## Dynamic Light Scattering

Dynamic light scattering (DLS) measurements were performed on a Malvern Zetasizer-Nano instrument equipped with a 4 mW He-Ne laser (633 nm) and an avalanche photodiode. The hydrodynamic radius of the particles was determined by dynamic light scattering in ethanolic suspension. For this purpose, 100  $\mu$ L of an ethanolic suspension of MSN particles (ca. 10 mg/ml) was diluted with 3 mL of ethanol prior to the measurement. The data for the samples MSN-SH<sub>in</sub>-CN<sub>out</sub>, MSN-SH<sub>in</sub>-COOH<sub>out</sub>, MSN-SH<sub>in</sub>-PEGd8NH<sub>2out</sub>, MSN-SH<sub>in</sub>-PEGd8-AIPcS<sub>2aout</sub>, and DOPC/DOTAP@MSN-CARGO<sub>in</sub>-PEGd8-AIPcS<sub>2aout</sub> can be seen in Figure 6.3 and are summarized in Table 2. A shorter measurement time was used for the samples MSN-SH<sub>in</sub>-PEGd8-AIPcS<sub>2aout</sub> and DOPC/DOTAP@MSN-CARGO<sub>in</sub>-PEGd8-AIPcS<sub>2aout</sub> in order to avoid generation of singlet oxygen.

## Zeta potential measurements

Zeta potential measurements of the samples were performed on a Malvern Zetasizer-Nano instrument equipped with a 4 mW He-Ne laser (633 nm) and an avalanche photodiode. For determination of

the zeta potential curves, two drops of the ethanolic MSN suspension ( 3 % wt.) was mixed with 1 mL commercial Hydrion Buffer solution of the appropriate pH prior to measurement. The

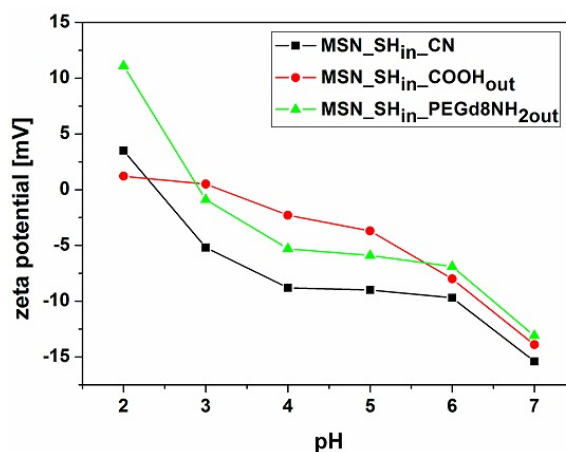


**Figure 5:** Zeta potential measurements of the samples MSN-SH<sub>in</sub>-CN<sub>out</sub> (black squares), MSN-SH<sub>in</sub>-COOH<sub>out</sub> (red circles), MSN-SH<sub>in</sub>-PEGd8NH<sub>2</sub><sub>out</sub> (green up triangles).

cyanopropyl groups of the sample MSN-SH<sub>in</sub>-CN<sub>out</sub> (I, black squares) are uncharged at high or low pH values, resulting in a zeta potential curve that is similar to the one of unfunctionalized MSN. The successful attachment of NH<sub>2</sub>-PEGd8-NH<sub>2</sub> to the sample MSN-SH<sub>in</sub>-COOH<sub>out</sub> results in a higher zeta potential value due to protonation of the amino groups at low pH values (green). The sample MSN-SH<sub>in</sub>-PEGd8-AIPcS-2a<sub>out</sub> (IV) couldn't be measured because the laser wavelength of 633 nm leads to an excitation of the photosensitizer, resulting in oxygen production with bubble formation on the electrode. Shorter measurement times did not lead to sufficient results.

## IR Spectroscopy

All measurements were performed on a Bruker Equinox 55 FTIR/FTNIR Spectrometer in absorbance mode (spectra were background subtracted). The CH<sub>2</sub> stretching vibrations from the organic functionality (mercaptopropyl- and cyanopropyl) are visible between 2800 cm<sup>-1</sup> and 2850 cm<sup>-1</sup>. Furthermore, several peaks at 2900 cm<sup>-1</sup> (C-H stretching vibrations) and at 1400 cm<sup>-1</sup> (C-H bending vibrations) are visible. The intensity of these vibrations decreases after the carboxylation of the cyanide groups. Further condensation of the silica framework was achieved through the hydrolysis of the cyano-moiety and therefore the content of ethoxygroups was reduced. The cyanide vibration at 2253 cm<sup>-1</sup> for the species I disappears completely after hydrolysis while the new -COOH vibration at 1707 cm<sup>-1</sup> (MSN-SH<sub>in</sub>-COOH<sub>out</sub>) arises. After PEGylation by EDC amidation the C=O stretching vibration mode is moved to higher vibrational energies (1616 cm<sup>-1</sup>) resulting from the newly formed amide bond. Also the N-H bending vibrations appear at 1530 cm<sup>-1</sup>. The band between 1300 cm<sup>-1</sup> and 900 cm<sup>-1</sup> can be attributed to silica framework vibrations and is visible in all spectra. The peak at 1332 cm<sup>-1</sup> represents the asymmetric stretching of the -SO<sub>2</sub> group in AIPcS<sub>2a</sub>.

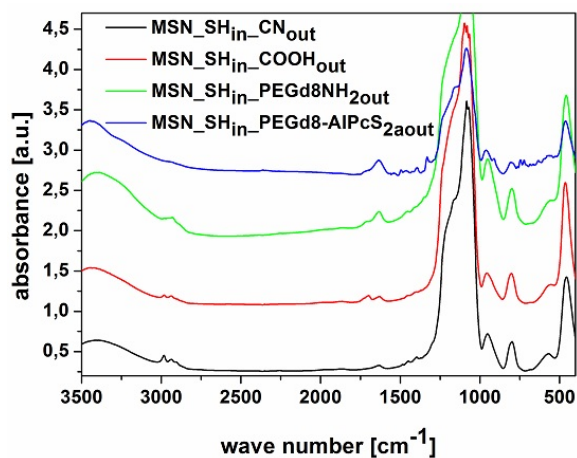


**Figure 6:** IR spectra of MSN-SH-*in*-CN<sub>out</sub> (black), MSN-SH<sub>in</sub>-COOH<sub>out</sub> (red), MSN-SH<sub>in</sub>-PEGd8NH<sub>2out</sub> (green) and MSN-SH<sub>in</sub>-PEGd8-AIPcS<sub>2aout</sub> (blue). For clarity reasons curves for MSN-SH<sub>in</sub>-COOH<sub>out</sub> (red), MSN-SH<sub>in</sub>-PEGd8NH<sub>2out</sub> (green) and MSN-SH<sub>in</sub>-PEGd8-AIPcS<sub>2aout</sub> (blue) were shifted along the y-axis by a value of 0.8 each.

The peak arising at  $904\text{ cm}^{-1}$  in the spectra of MSN-SH<sub>in</sub>-PEGd8-AIPcS<sub>2aout</sub> can be assigned to the stretching vibration of the newly formed N-S bond between the terminal amino-group of the PEG-linker and AIPcS<sub>2a</sub>. The two peaks at  $743\text{ cm}^{-1}$  and  $720\text{ cm}^{-1}$  correspond to the non-planar deformation vibrations of the C-H bonds of benzene rings.

### Uptake of MSN-PS-SLB-FA particles with folic acid ligand by KB cells, imaging after fixation of cells

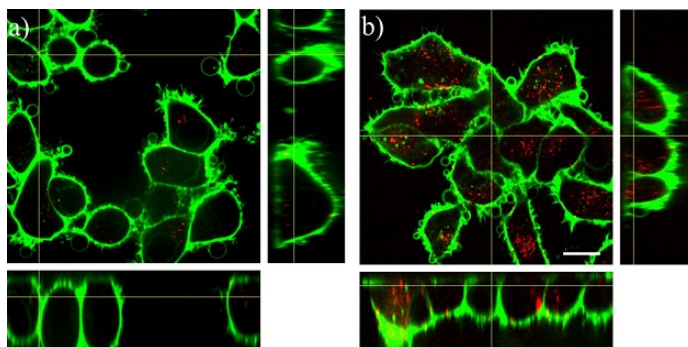


**Figure 7:** Unspecific and receptor mediated endocytosis of MSN-PS-SLB-FA particles with folic acid ligand by KB cells. Cells are fixed with paraformaldehyde after an incubation of 3 h and the cell membrane is stained with a cell membrane stain (WGA488). (a) Incubation of MSN-PS-SLB-FA particles with FA pre-incubated KB cells for 3h at 37°C . b) Incubation of MSN-PS-SLB-FA particles with KB cells, not FA pre-incubated, 3h at 37°C . For both a) and b) the orthogonal view in xz and yz plane is shown on the bottom and right side of the main image. The KB cell membrane is shown in green and the particles in red. The particles are imaged over the Photosensitizer, and even after fixation one can see the particles in a dot-like structure which indicates that the photosensitizer is not separated from the particles. The scale bar represents 10  $\mu\text{m}$ .

### Uptake of MSN-PS-SLB-EGF particles with folic acid ligand by HuH7 cells

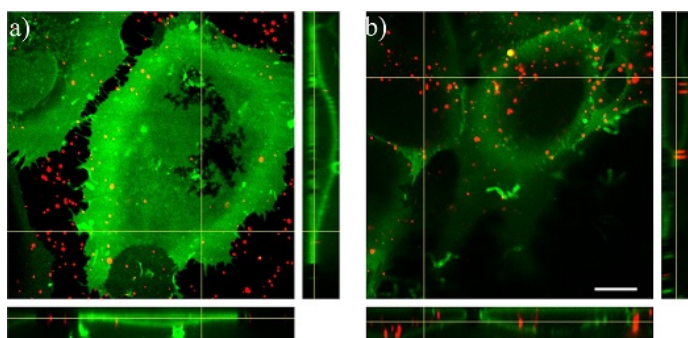


**Figure 8:** Unspecific and receptor mediated endocytosis of MSN-PS-SLB-FA particles with EGF ligand by HuH7 cells. Cells are incubated for 3h and the cell membrane is stained with a cell membrane stain (WGA 633). A) Incubation of MSN-PS-SLB-EGF particles with EGF pre-incubated HuH7 cells for 3 h at 37°C . b) Incubation of MSN-PS-SLB-EGF particles with EGF cells, not EGF pre-incubated, 3 h at 37°C . For both a) and b) the orthogonal view in xz and yz plane is shown on the bottom and right side of the main image. The HuH7 cell membrane is shown in green and the particles in red. The scale bar represents 10  $\mu\text{m}$ .

## Chemicals

Tetraethylorthosilicate (TEOS, Fluka, > 99 %), (3-mercaptopropyl)- triethoxysilane (MPTES, Gelest, 95 %), (3cyanopropyl)- triethoxysilane (CN-TES, ABCR, 98 %), cetyltrimethylammonium chloride (CTAC, Fluka, 25 wt% in H<sub>2</sub>O), triethanolamine (TEA, Aldrich, 98 %), ammonium fluoride (NH<sub>4</sub>F, Sigma, > 98 %),  $\alpha,\omega$ - bis- amino octa (ethylene glycol) (NH<sub>2</sub>-PEGd8-NH<sub>2</sub>, Iris Biotech), Al(III) phthalocyanine chloride disulfonic acid (AlPcS<sub>2a</sub>, Frontier Scientific), ammonium nitrate (Sigma, 99 %), conc. hydrochloric acid (Aldrich, > 95 %, 37 wt%), 1,3,5- triisopropylbenzene (TiPB, Fluka, 96 %), sulfo-N- hydroxysuccinimide (sulfo-NHS, Aldrich, 98 %), N-(3- dimethylaminopropyl)-N'-ethylcarbodiimide (EDC, Sigma, 97 %), calcein (CAL, Sigma), dimethyl sulfoxide (DMSO, Sigma, >99.5 %), ethanol (EtOH, Aldrich, > 99.5 %), 1,2- dioleoyl-sn- glycerol-3- phosphocholine (DOPC, Avanti Polar Lipids), 1,2- distearoyl-sn-glycerol-3- phosphoethanolamine-N- [folate (polyethylene glycol)-2000] (ammonium salt) (DSPE-PEG<sub>2000</sub>-FA, Avanti Polar Lipids), 1,2- distearoyl-sn- glycerol-3- phosphoethanolamine -N- [maleimide (polyethylene glycol) - 2000] (ammonium salt) (DSPE-PEG<sub>2000</sub>-maleimide, Avanti Polar Lipids), 2-Iminothiolane hydrochloride (Traut's reagent, Sigma-Aldrich), 5(6)-Carboxy-X- rhodamine (RD, Sigma), Wheat germ agglutinin (WGA) Alexa Fluor 488 conjugate (Invitrogen), epidermal growth factor (EGF, PeproTech, > 98 %), Folic acid (FA, Sigma, > 97 %). All chemicals were used as received without further purification. Doubly distilled water from a Millipore system (Milli-Q Academic A10) was used for all synthesis and purification steps.

## Synthesis of core-shell MSN-SH<sub>in</sub>-CN<sub>out</sub>

Bi-functional core-shell colloidal mesoporous silica nanoparticles were synthesized according to a slightly modified published method. [221, 375] A mixture of TEOS (1.63 g, 9.22 mmol), MPTES (112 mg, 0.48 mmol) and TEA (14.3 g, 95.6 mmol) was heated under static conditions at 90°C for 20 min in a polypropylene reactor. Then a solution of CTAC (25 wt% in water, 2.41 mL, 1.83 mmol), NH<sub>4</sub>F (100 mg, 2.70 mmol) and TiPB (2.54 g, 12.4 mmol) in water (21.7 g, 1.21 mol) was preheated to 60°C and added quickly. The reaction mixture was stirred vigorously (1000 rpm) at room temperature for 20 min. Subsequently TEOS (138.2 mg, 0.922 mmol) was added in four equal increments every three minutes. This step was followed by 30 min of stirring at RT. For the shell functionalization a mixture of TEOS (19.3 mg, 92.5  $\mu$ mol) and CN-TES (21.4 mg, 92.5  $\mu$ mol) was added to the reaction. The resulting mixture was then allowed to stir at room temperature for 12 h. After the addition of 100 mL ethanol, the MSN were collected by centrifugation, re-dispersed in 100 mL of ethanol and extracted according to the procedure described below.

## Extraction of MSN-SH<sub>in</sub>-CN<sub>out</sub>

Extraction of the surfactant was performed by heating 250 mg of MSN for 45 min under reflux at 90°C in a solution containing 2 g ammonium nitrate in 100 mL ethanol. This extraction step was performed twice. The template-free MSN were separated by centrifugation and washed with ethanol after each extraction step. MSN-SH<sub>in</sub>-CN<sub>out</sub> were obtained as colloidal suspension in EtOH.

### **Conversion of MSN-SH<sub>in</sub>-CN<sub>out</sub> to MSN-SH<sub>in</sub>-COOH<sub>out</sub>**

250 mg of MSN-SH<sub>in</sub>-CN<sub>out</sub> in EtOH were collected by centrifugation and washed with H<sub>2</sub>O once. The particles were re-dispersed in 10 mL H<sub>2</sub>O and 30 mL hydrochloric acid (37 wt%) was added carefully. The reaction mixture was heated to reflux for 3 h. After cooling down, 20 mL H<sub>2</sub>O were added and the synthesis was stirred at room temperature overnight. The resulting colloidal suspension of MSN-SH<sub>in</sub>-COOH<sub>out</sub> was diluted further with 100 mL H<sub>2</sub>O, collected by centrifugation, and re-dispersed in 100 mL of water. This washing step was repeated twice with both water and ethanol. MSN-SH<sub>in</sub>-COOH<sub>out</sub> were obtained as an ethanolic suspension.

### **PEGylation of MSN-SH<sub>in</sub>-COOH<sub>out</sub> with bi-functional NH<sub>2</sub>-PEGd8-NH<sub>2</sub> to the sample MSN-SH<sub>in</sub>-PEGd8-NH<sub>2out</sub>**

An ethanolic suspension containing 20 mg of MSN-SH<sub>in</sub>-COOH<sub>out</sub> was centrifuged and re-dispersed in 60 mL of water. This washing step was repeated twice. EDC (0.85  $\mu$ L, 4.6  $\mu$ mol, 1.2 eq) was added at RT to a diluted suspension of MSN-SH<sub>in</sub>-COOH<sub>out</sub> in 40 mL of water. The reaction mixture was stirred for 5 min before sulfo-NHS (1 mg, 4.6  $\mu$ mol, 1.2 eq) was added. A second solution, containing bi-functional NH<sub>2</sub>-PEGd8-NH<sub>2</sub> (7.05 mg, 19.2  $\mu$ mol, 5 eq.) dissolved in 2 mL water was prepared. The EDC-activated MSN-SH<sub>in</sub>-COOH<sub>out</sub> were added dropwise to the PEG-containing solution. Afterwards, the pH was adjusted with two drops of hydrochloric acid (37 wt%) to a value pH < 7 and the reaction mixture was stirred for 12 h at ambient temperature. In order to remove the excess of the PEG-linker, the reaction mixture was washed five times with 30 mL of water to remove unbound PEG. All washing steps were followed by centrifugation. Finally, the sample MSN-SH<sub>in</sub>-PEGd8-NH<sub>2out</sub> was re-dispersed in 10 mL ethanol.

### **Attachment of the photosensitizer AIPcS<sub>2a</sub> to MSN-SH<sub>in</sub>-PEGd8-NH<sub>2out</sub> yielding the sample MSN-SH<sub>in</sub>-PEGd8-AIPcS<sub>2aout</sub>**

1 mg of MSN-SH<sub>in</sub>-PEGd8-NH<sub>2out</sub> in ethanolic solution was centrifuged and re-suspended in a 500  $\mu$ L water/DMSO mixture (2:1). Subsequently, 40  $\mu$ L of an AIPcS<sub>2a</sub> stock solution (2 mg in 1 mL DMSO) were added to the MSN. The reaction mixture was stirred in the dark at room temperature for 72 h. The resulting MSN-SH<sub>in</sub>-PEGd8-AIPcS<sub>2aout</sub> were extensively washed by centrifugation with water/DMSO (1:1) in order to remove excess photosensitizer. All supernatants were investigated with a Nanodrop UV-VIS in order to monitor the content of free photosensitizer. Results of these measurements can be seen in Figure 6.10 a. In order to remove DMSO from the mesopores the sample was washed three times with water after no free PS could be detected (Figure 6.10 b and 6.10 a). The colloidal solution of sample MSN-SH<sub>in</sub>-PEGd8-AIPcS<sub>2aout</sub> was used for further experiments immediately.

### **Adsorption of the the dyes calcein and a rhodamine derivative (RD) into the mesopores of MSN-SH<sub>in</sub>-PEGd8-AIPcS<sub>2aout</sub>**

0.5 mg of the sample MSN-SH<sub>in</sub>-PEGd84-AIPcS<sub>2aout</sub> in ethanol were centrifuged and re-dispersed in 1 mL water. This washing step was repeated twice. Then, the suspension was centrifuged again and re-dispersed in 500  $\mu$ L calcein in water (1 mM stock solution in water) or RD (1 mM stock solution in water), respectively. The mixture was stirred over night in the dark yielding the sample MSN-CARGO<sub>in</sub>-PEGd8-AIPcS<sub>2aout</sub>.

### **Supported DOPC/DOTAP lipid bilayer (SLB) around MSN-CARGO<sub>in</sub>-PEGd8-AIPcS<sub>2aout</sub>**

0.5 mg of MSN-CARGO<sub>in</sub>-PEGd8-AIPcS<sub>2aout</sub> in 1 mL dye solution were centrifuged (14000 rpm, 16873 rcf, 4 min) and the supernatant discarded. Afterwards, a mixture of 70  $\mu$ L DOPC and 30  $\mu$ L DOTAP (each 2.5 mg/mL in 60:40 H<sub>2</sub>O:EtOH) were added to the resulting pellet, mixed extensively, and sonicated for 10 s. To form the supported lipid bilayer around the MSN via solvent exchange method, 700  $\mu$ L of water were added. The resulting suspension was mixed and sonicated for 10 s, yielding DOPC/DOTAP@MSN-Cargo<sub>in</sub>-PEGd8-AIPcS<sub>2aout</sub>.

### **Diffusion of the targeting ligand (TL) construct, DSPE-PEG<sub>2000</sub>-TL, into the SLB of DOPC/DOTAP@MSN-CARGO<sub>in</sub>-PEGd8-AIPcS<sub>2aout</sub>**

0.5 mg of DOPC/DOTAP@MSN-CARGO<sub>in</sub>-PEGd8-AIPcS<sub>2aout</sub> in 800  $\mu$ L water were incubated with 6  $\mu$ L of DSPE-PEG<sub>2000</sub>-TL for 3 h (for DSPE-PEG<sub>2000</sub>-Folate) and 12 h respectively (for DSPE-PEG<sub>2000</sub>-EGF) at 37°C . The resulting sample DOPC/DOTAP@MSN-CARGO<sub>in</sub>-PEGd8-AIPcS<sub>2aout</sub>-TL was used without further purification for confocal microscopy studies.

### **Time-based fluorescence release experiments of the sample DOPC/DOTAP@MSN-CARGO<sub>in</sub>-PEGd8-AIPcS<sub>2aout</sub>**

Fluorescence time-based release experiments were recorded on a PTI fluorescence system featuring a PTI 814 photomultiplier detector and a PTI A1010B Xenon arclamp driven by a PTI LPS4220B lamp power supply. For temperature settings, a Quantum Northwest TC 125 sample holder was used. Our previously described custom-made release cuvette system was used for all experiments. [40] All samples were measured at a temperature of 37°C. For RD an excitation wavelength of 575 nm was used (emission maximum at 597 nm), whereas calcein was excited with 495 nm and with an emission maximum at 516 nm. Results are given in Figure 6.5. For all experiments, 0.5 mg of DOPC/DOTAP@MSN-Cargo<sub>in</sub>-PEGd8-AIPcS<sub>2aout</sub> were used. 200  $\mu$ L of the particle suspension was filled into the reservoir cap sealed with a dialysis membrane (Molecular weight cut-off 14000 g/mol) allowing released dye molecules to pass into the fluorescence cuvette. In order to monitor the release of adsorbed dyes upon membrane rupture with singlet oxygen, the sample was

excited with  $0,56 \text{ W/mm}^2$  of 633 nm light for 1 min prior the measurement. For triton-mediated release, 5  $\mu\text{L}$  of a 1 mM stock solution of TritonX-100 was added to the particle solution.

### **Thermogravimetric analysis**

Thermogravimetric analysis of the bulk samples MSN-SH<sub>in</sub>-CN<sub>out</sub>, MSN-SH<sub>in</sub>-COOH<sub>out</sub>, MSN-SH<sub>in</sub>-PEGd8-NH<sub>2out</sub> and MSN-SH<sub>in</sub>-PEGd8-ALPcS<sub>2aout</sub> was performed on a Netzsch STA 440 C TG/DSC with a heating rate of 10 K/min in a stream of synthetic air of about 25 mL/min. The mass was normalized to 100 % at 133.8°C for all samples and the resulting data is presented in Figure 6.4.

### **<sup>13</sup>C solid state NMR**

Cross-polarized <sup>13</sup>C solid-state NMR (ssNMR) measurements were performed on a Bruker DSX Avance500 FT spectrometer in a 4 mm ZrO<sub>2</sub> rotor. The spinning rate was 10 kHz and a total number of up to 8000 scans were recorded. Spectra are shown in Figure

## 2 Synthesis details for Chapter 7: Polymer pore closing with pH depended polymer and photoinduced opening mechanism

Further *in vitro* and *in vivo* experiments.

Photoactivated release experiments.

With additional attachment of the photosensitizer AlPcS<sub>2a</sub> the release and therefore the increase of the cargo fluorescence inside the cell could be detected.

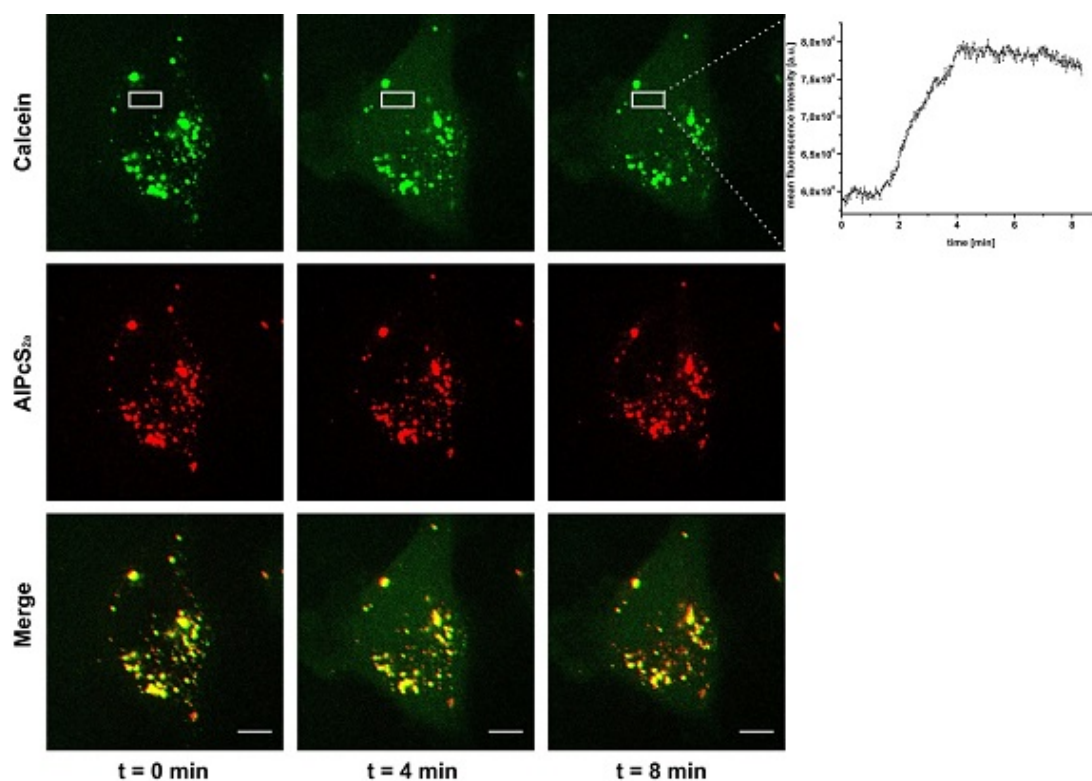


**Figure 9:** Fluorescence microscopy of MSN-PVP-PEG-AlPcS<sub>2a</sub>-FA (25  $\mu\text{g}/\text{mL}$ ) nanoparticles loaded with calcein inside HeLa cells after 24 h incubation. a-c) Calcein (green) and AlPcS<sub>2a</sub> (red) are co-localized (yellow) prior to photoactivation. The cell was constantly monitored with a frame rate of 1 frame/s and 0.6 W/mm<sup>2</sup> of red light (639 nm). d-i) example images after different time points; spreading of calcein can be clearly seen over time, whereas AlPcS<sub>2a</sub> stays at the same location. j) Intensity of calcein fluorescence inside the cytosol over time in the indicated rectangle, after approximately 2 min an increase can be monitored. The scale bar represents 10  $\mu\text{m}$ .

In comparison to Figure Appendix 9, the incubation of cells with free photosensitizer and free calcein (Figure Appendix 10) does not lead to the same effect. It is possible to detect calcein in the beginning of the experiment, but the endocytosed amount is too low to be detected after

some time and therefore no spreading could be observed. In contrast to the dot-like pattern of the particle-bound photosensitizer in Figure Appendix 9, the spreading of the free photosensitizer can be detected in Figure Appendix 10.

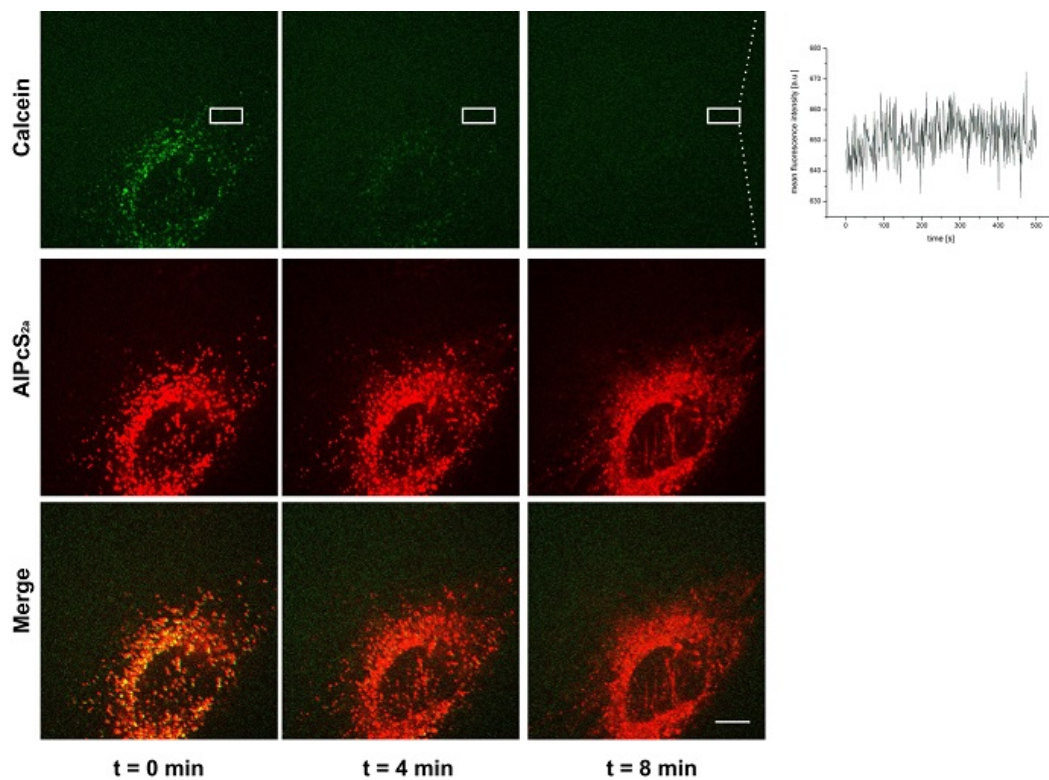


**Figure 10:** Fluorescence microscopy of free calcein and free AIPcS<sub>2a</sub> (each 2.5  $\mu\text{g}/\text{mL}$ ) inside HeLa cells after 24 h incubation. a-c) Calcein (green) and AIPcS<sub>2a</sub> (red) are co-localized (yellow) prior to photoactivation. The cell was constantly monitored with a frame rate of 1 frame/s and 0.6  $\text{W}/\text{mm}^2$  of red light (639 nm). d-i) example images after different time points, spreading of AIPcS<sub>2a</sub> can be clearly seen over time, whereas the calcein fluorescence is too weak to be detected after some time. j) Intensity of calcein fluorescence inside the cytosol over time in the indicated rectangle; no increase inside the cytosol can be detected. The scale bar represents 10  $\mu\text{m}$ .

## Targeting.

## Prolonged retention in (subcutaneous) tumors of mice.

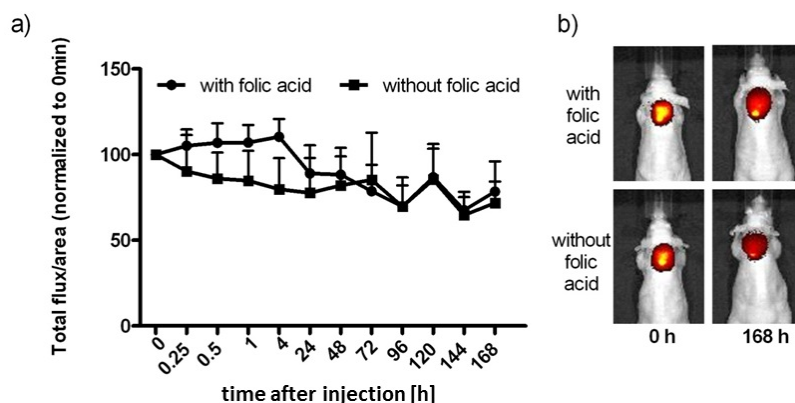


**Figure 11:** Intratumoral administration of MSN. a) Retention of MSN in subcutaneous KB-tumors in mice after intratumoral injection of FA-targeted or untargeted MSN over 168 h. Retention was determined by fluorescent signal for the Cy7-labeled MSN and normalized to 0 min (3 mice per group). b) Representative pictures of NIR fluorescence imaging of FA-targeted MSN (top) and untargeted MSN (bottom).

Cy7-labeled targeted and untargeted MSN with cap were also tested in mice bearing subcutaneously growing human KB carcinomas (Figure 11). Near infrared fluorescence imaging after intratumoral injection revealed, that for the first hours the folic acid modification results in slightly increased retention in the tumor tissue compared to untargeted particles (Figure 11a). After more than 24 h no difference between targeted and untargeted particles is observable. Interestingly, both types of particles show a prolonged retention in tumors for the whole observation period of 7 d (Figure 11a and b). This retention in tumors differs from lower persistence upon intravenous administration (Figure 7.12). The slightly enhanced retention of receptor-targeted over untargeted MSN particles with cap in the initial phase can be explained by a pronounced washout of non-receptor bound particles into the blood vessel system.

A bad signal to noise ratio in a similar experiment, but with a slightly different MSN labeling procedure, prevented a statement on the prolonged retention of these MSN in *in vivo* KB tumor. But we also assume that the targeting effect in this tumor model is not that easy traceable for large MSN as it was already observed for (smaller) polypexes. [376–378] The KB tumor model is known to poorly form blood vessels [379] and thus we suppose that the blood flow isn't effective enough to remove the large particles (over 100 nm) out of the tumor tissue and hence the targeting effect is negligible.

## Chemicals

All reagents were purchased from commercial suppliers: tetraethyl orthosilicate (TEOS, Fluka, > 98 %), cetyltrimethylammonium bromide (CTAB, Aldrich, 95 %), (3-aminopropyl)triethoxysilane

(APTES, Fluka, 95 %), (3-mercaptopropyl)triethoxysilane (ABCRCR), *N*-(3-dimethylaminopropyl)-*N*-ethylcarbodiimide hydrochloride (EDC, Fluka, 97 %),  $\alpha$ -amino- $\omega$ -carboxy terminated poly(2-vinylpyridine) (NH<sub>2</sub>-PVP-COOH, Polymer source,  $M_n = 10000$ , PDI = 1.08),  $\alpha,\omega$ -polyethylene-glycolbisamine (NH<sub>2</sub>-PEG-NH<sub>2</sub>, Aldrich,  $M_n = 2000$ ), Boc anhydride (Aldrich, 95 %), folic acid (Sigma, 99 %), aluminum (III) Phthalocyanine chloride tetrasulfonic acid (AlPcS<sub>2a</sub>, Frontier Scientific), *N*-hydroxy-sulfosuccinimide sodium salt (Sulfo-NHS, Aldrich, 98 %), 4,6-diamidino-2-phenylindole dihydrochloride (DAPI,  $\geq 98$  %), Bis[N,N'-bis(carboxymethyl)aminomethyl] fluorescein (calcein), Folic Acid (FA,  $> 97$  %). Doubly distilled water from a Millipore system (Milli-Q academie A-10) was used for all syntheses and purification steps. All solvents and buffer contents above were purchased from Sigma-Aldrich. Wheat germ agglutinin (WGA) Alexa Fluor 488 conjugate (Invitrogen), Atto 633 maleimide (ATTO-TEC). Unless otherwise noted, all reagents were used without further purification.

### Characterization.

All samples were investigated with a FEI Titan 80-300 operating at 300 kV with a high-angle annular dark field detector. A droplet of the diluted MSN solution in absolute ethanol was dried on a carbon-coated copper grid. Nitrogen sorption measurements were performed on a Quantachrome Instruments NOVA 4000e. All samples (15 mg each) were heated to 60°C for 12 h in vacuum (10 mTorr) to outgas the samples before nitrogen sorption was measured at 77 K. Pore size and pore volume were calculated by a NLDFT equilibrium model of N<sub>2</sub> on silica, based on the desorption branch of the isotherms. In order to remove the contribution of the interparticle textural porosity, pore volumes were calculated only up to a pore size of 8 nm. A BET model was applied in the range of 0.05 - 0.20 p/p<sub>0</sub> to evaluate the specific surface area of the samples. Centrifugation was performed using a Sorvall Evolution RC equipped with a SS-34 rotor or an Eppendorf centrifuge 5418 for small volumes. Raman spectra were recorded on a Jobin Yvon Horiba HR800 UV Raman microscope using a He Ne laser emitting at  $\lambda = 633$  nm. Dynamic light scattering (DLS) measurements were performed on a Malvern Zetasizer-Nano instrument equipped with a 4 mW He-Ne laser (633 nm) and an avalanche photodiode. The hydrodynamic radius of the particles was determined by dynamic light scattering in ethanolic suspension. For this purpose, 100  $\mu$ L of an ethanolic suspension of MSN particles (ca. 10 mg/mL) was diluted with 3 mL of ethanol prior to the measurement. Zeta potential measurements of the samples were performed on a Malvern Zetasizer-Nano instrument equipped with a 4 mW He-Ne laser (633 nm) and an avalanche photodiode. Zeta potential measurements were performed using the add-on Zetasizer titration system (MPT-2) based on diluted NaOH and HCl as titrants. For this purpose, 1 mg of the particles was diluted in 10 mL bi-distilled water. IR measurements were performed on a Bruker Equinox 55 FTIR/FTNIR Spectrometer in absorbance mode (spectra were background subtracted). Thermogravimetric analysis was performed on a Netzsch STA 440 C TG/DSC with a heating rate of 10 K / min in a stream of synthetic air of about 25 mL/min. The mass was normalized to 100% at 150°C for all samples. UV-VIS spectra were recorded with a NanoDrop ND 1000 spectrometer. Usually, 2  $\mu$ L of sample were used and all presented spectra are background corrected for water absorption.

## Preparation of shell-functionalized colloidal mesoporous silica nanoparticles (MSN-NH<sub>2</sub>).

MSN nanoparticles were prepared by a delayed co-condensation approach as described earlier by Cauda *et al.* [37] In detail, a two phase mixture of TEA (14.3 g) and TEOS (1.9 g, 9.12 mmol) was heated at 90°C for 20 min without stirring. After removal of the oil bath, a preheated (60°C) solution of CTAC (2.14 mL, 1.62 mmol, 25 wt% in H<sub>2</sub>O) and water (21.7 g) was added and stirred afterwards at 500 rpm for 30 min at room temperature. Subsequently, a mixture of 3-aminopropyltriethoxysilane (22.5 μL, 96 μmol) and TEOS (20.5 μL, 92 μmol) was added. The resulting solution was stirred overnight at room temperature at 500 rpm. Extraction of the organic template was achieved by heating the ethanol-suspended sample (10 mg/mL) under reflux at 90°C for 1 h in a mixture of 2 g ammonium nitrate and 100 mL ethanol. Afterwards, the sample was centrifuged for 20 min at 19000 rpm (43146 rcf), redispersed in ethanol and heated under reflux at 90°C in a solution of 8 mL concentrated HCl and 32 mL ethanol for 45 min. After centrifugation, the particles were redispersed in ethanol, resulting in a colloidal suspension.

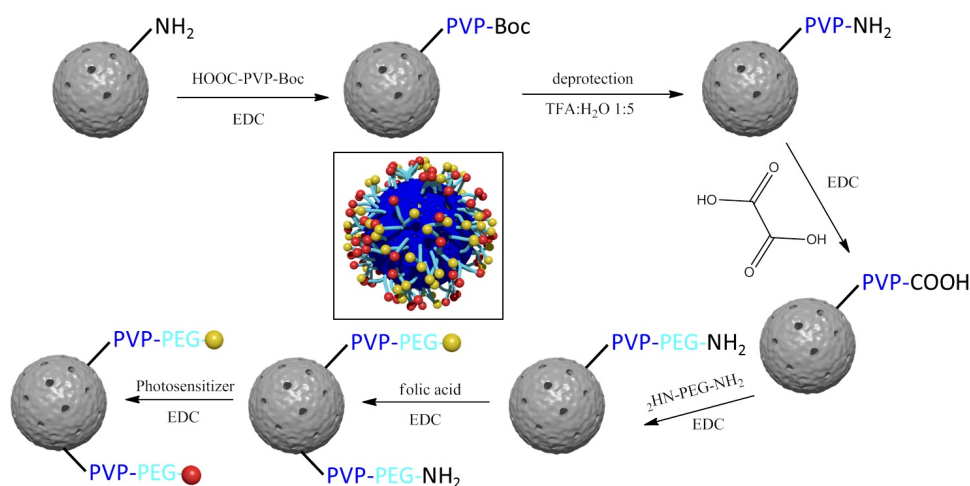


**Figure 12:** Synthesis scheme of a fully functionalized MSN particle.

## Protection of NH<sub>2</sub>-PVP-COOH (Boc-PVP-COOH).

To a solution of 500 mg (50 μmol) NH<sub>2</sub>-PVP-COOH in 10 mL dry dichloromethane, 15 μL (0.11 mmol) triethylamine and 15 mg (69 μmol) Boc anhydride were added. The solution was stirred overnight and extracted several times with brine. The organic phase was dried over MgSO<sub>4</sub> and evaporated to dryness to afford the Boc protected polymer. The polymer was used without further purification.

### **General procedure for the attachment of poly(2-vinyl pyridine) to MSN-NH<sub>2</sub> (MSN-PVP-Boc).**

To a dispersion of 50 mg MSN-NH<sub>2</sub> in 10 mL tetrahydrofuran (THF), 60 mg (5.6  $\mu$ mol) polymer dissolved in 1.5 mL THF were added. The amidation was activated by the addition of 10  $\mu$ L (57.2  $\mu$ mol) EDC and 1.3 mg (6  $\mu$ mol) Sulfo-NHS. The mixture was stirred at room temperature for 12 h. Afterwards the particles were separated by centrifugation (19000 rpm, 43146 rcf, 20 min) and washed 3 times by repeated centrifugation and redispersion in 30 mL THF.

### **Deprotection of MSN-PVP-Boc (MSN-PVP-NH<sub>2</sub>).**

Deprotection of the polymer was achieved through stirring 10 mg polymer functionalized particles in a mixture of 2 mL trifluoroacetic acid and 8 mL water for 24 h. After deprotection, the particles were extensively washed by centrifugation (19000 rpm, 43146 rcf, 20 min) and redispersion in a mixture of 0.01 M HCl and EtOH.

### **Conversion of MSN-PVP-NH<sub>2</sub> to MSN-PVP-COOH.**

10 mg MSN-PVP-NH<sub>2</sub> in 2 mL EtOH were reacted with a large excess of oxalic acid (5 mg, 55  $\mu$ mol) and EDC (9  $\mu$ L, 51  $\mu$ mol) for 1 h. Afterwards the particles were extensively washed by centrifugation (19000 rpm, 43146 rcf, 20 min) and redispersion in a mixture of 0.01 M HCl and EtOH.

### **PEGylation of MSN-PVP-COOH (MSN-PVP-PEG-NH<sub>2</sub>).**

To a dispersion 1 mg MSN-PVP-COOH in 500  $\mu$ L EtOH, 2 mg (100 nmol) NH<sub>2</sub>-PEG-NH<sub>2</sub> in 500  $\mu$ L bidistilled water was added and the reaction was started through the addition of 0.5  $\mu$ L (2.8  $\mu$ mol) EDC. After stirring for 1 h at room temperature, the sample was washed 3 times by centrifugation with a mixture of EtOH:water 1:1.

### **Attachment of folic acid to MSN-PVP-PEG-NH<sub>2</sub> (MSN-PVP-PEG-NH<sub>2</sub>-FA).**

The amino functionalities of 1 mg MSN-PVP-PEG-NH<sub>2</sub> in 1 mL EtOH:water 1:1 were partially reacted with 0.44  $\mu$ g (1 nmol) folic acid. To start the reaction, 0.5  $\mu$ L (2.8  $\mu$ mol) EDC and a catalytic amount (approx. 1 mg) of Sulfo-NHS were added. After 1 h, the sample was washed 3 time by centrifugation with a mixture of EtOH:water 1:1.

### **Attachment of AIPcS<sub>2a</sub> to residual amino groups of MSN-PVP-PEG-NH<sub>2</sub>-FA (MSN-PVP-PEG-FA- AIPcS<sub>2a</sub>).**

To the sample MSN-PVP-PEG-NH<sub>2</sub>-FA in 1 mL DMSO:water 1:1 was added 20  $\mu$ L of AIPcS<sub>2a</sub> (1 mg/mL in DMSO). The resulting mixture was stirred at room temperature in the dark for 24 h. Subsequently, the sample was washed extensively with DMSO:water 1:1 until there was no photosensitizer in the supernatant.

### **Drug/dye loading.**

1 mg MSN-PVP-PEG-NH<sub>2</sub> were dispersed in 500  $\mu\text{L}$  of a 1 mM drug/dye solution in water. To open the pores and enable the uptake, 50  $\mu\text{L}$  of citrate buffer (pH 2) were added. The particles were stirred overnight, centrifuged, and redispersed in 1 mL SSC buffer (pH 7) to trigger closure of the polymer shell. The particles were washed extensively with SSC buffer until no fluorescence was detected in the supernatant.

### ***In vitro* fluorescein release.**

1 mg fluorescein loaded MSN-PVP-NH<sub>2</sub> or MSN-PVP-PEG-NH<sub>2</sub> were redispersed in 200  $\mu\text{L}$  SSC buffer and transferred to the cap of the fluorescence cuvette. This cap is sealed with a dialysis membrane (molecular weight cutoff of 16000 g/mol) and placed on top of the fluorescence cuvette, which is also filled with SSC buffer. The “release” of fluorescein out of the closed particles was monitored for 2 h ( $\lambda_{ex} = 490$  nm,  $\lambda_{em} = 512$  nm). Subsequently, the cap was removed and the particles were centrifuged and redispersed in 200  $\mu\text{L}$  citrate-phosphate buffer (pH 5), before being put into the cap of the release setup. The fluorescence cuvette was also filled with citrate-phosphate buffer (pH 5). After reassembling of the release setup, the release of fluorescein was measured for 10 h continuously. For comparison of the obtained curves, calibration curves of fluorescein in SSC buffer (pH 7) and in citrate-phosphate buffer (pH 5) were recorded.

**Experimental Setup.** Fluorescence experiments were performed to show the time-dependent release of fluorescein from the mesopores of colloidal mesoporous silica spheres. The measurements were recorded on a PTI fluorescence system featuring a PTI 814 photomultiplier detector and an PTI A1010B Xenon arclamp driven by a PTI LPS-220B lamp power supply. For temperature settings, a Quantum Northwest TC 125 sample holder was used. Fluorescein was excited with 490 nm and emission was detected at 512 nm (excitation slit 1.0 mm, emission slit 1.0 mm, 1 point per 30 min). For the release experiment, a ROTH Visking Typ 8/32 dialysis membrane with a molecular cut-off of 14000 g/mol was used. An image of this custom made Teflon container can be seen in Figure 13a.

1 mg MSN were loaded by redispersing them in 500  $\mu\text{L}$  of a 1 mM fluorescein solution that was acidified with 50  $\mu\text{L}$  of a citrate/phosphate buffer of pH 2. After 12 h, the particles were washed by centrifugation and redispersion in SSC buffer pH 7 until no fluorescence was observed in the supernatant. For the release experiment, the particles were redispersed in 200  $\mu\text{L}$  SSC buffer pH 7 and put into a container, that was subsequently closed by a dialysis membrane. The closed container was then put onto a fluorescence cuvette, which was completely filled with SSC buffer pH 7. The released dye is able to pass through the applied membrane while the relatively larger particles are retained. After 16 h, the particles were centrifuged and redispersed in 200  $\mu\text{L}$  Mc Ilvaine’s buffer pH 5, put into the container and closed by the dialysis membrane. The closed container was then put onto the fluorescence cuvette, which was completely filled with Mc Ilvaine’s buffer pH 5. The release was measured every 30 min until no further release was observed (Figure 13 c).

As the fluorescence of fluorescein is strongly dependent on the pH, calibration curves at pH 7 and

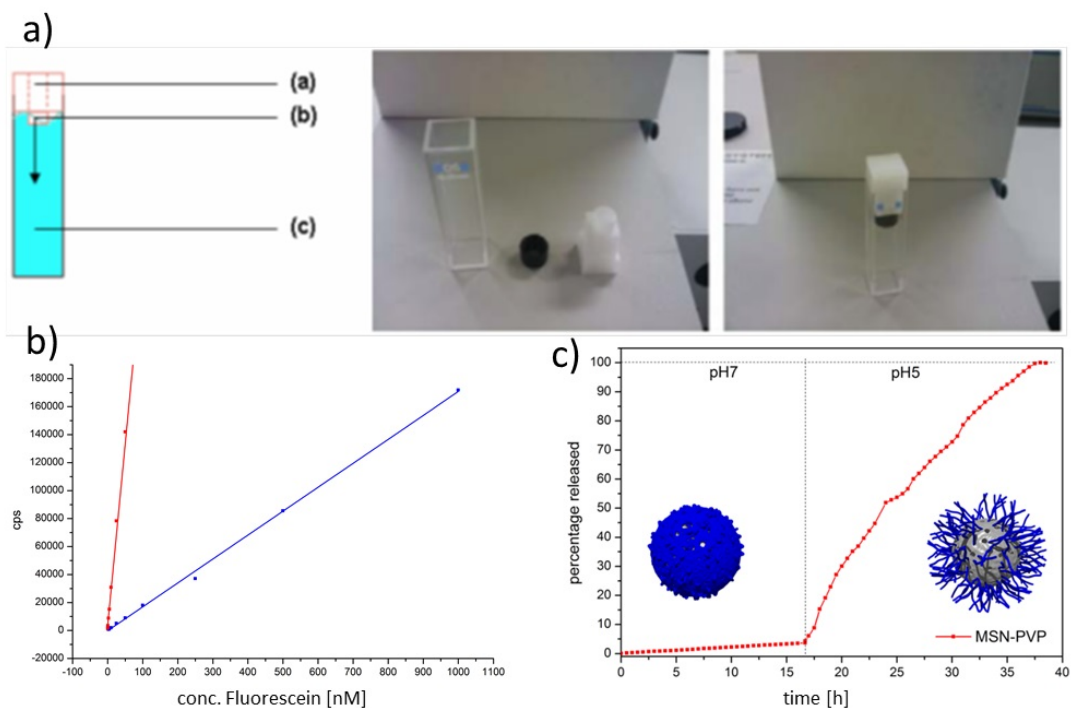


**Figure 13:** a) Custom made release experiment setup featuring a 200  $\mu\text{L}$  Teflon tube (a) which is closed by a dialysis membrane (b). This setup is put onto a fluorescence cuvette filled with the desired buffer (c). b) Calibration curves of fluorescein at pH 7 (red) and pH 5 (blue). c) Longterm release curve (normalized fluorescence intensity).

pH 5 were recorded (Figure 13 b) to be able to compare fluorescence signals in the closed and open state.

## UV-VIS Spectroscopy

The loading capacity of the particles was quantified with UV-Vis spectroscopy. 1 mg of particles were loaded with 500  $\mu\text{g}$  calcein and washed as described above. The absorption of the supernatants was measured on a Thermo Scientific PeQLab Nanodrop 2000c. Afterwards the particles were stirred for 48 h in 1 mL Mc Ilvaine's buffer pH 5, centrifuged and the absorption of the supernatant was measured again. For determination of the calcein concentration, calibration curves of calcein in Mc Ilvaine's buffer pH 5 and SSC buffer pH 7 at 495 nm were recorded (Figure 14)

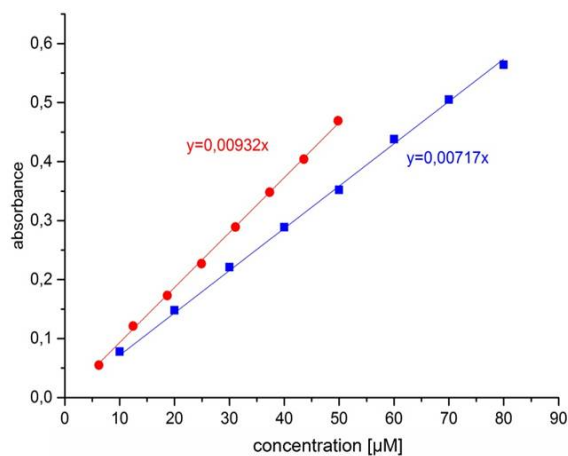


**Figure 14:** Calcein calibration curves for determination of loading and release capacity at pH 7 (red) and pH 5 (blue).

The calcein supernatant solution after loading was diluted by the factor of 20. The measured absorbance at 495 nm for the loading capacity of 0.155 leads to an amount of 432  $\mu\text{g}$  by using the calibration curve's linear regression. After several washing steps with SSC buffer to close the pore system, the supernatants were collected and measured. The measured absorbance of 0.151 leads to an additional amount of 16  $\mu\text{g}$ . Consequently, the total amount of calcein loaded in 1 mg MSN was 0.052 mg.

Loading capacity: 0.05 mg/mg MSN

The released amount of calcein was then measured as described above. The measured absorbance at 495 nm of 0.147 leads to an amount of 21  $\mu\text{g}$  by using the calibration curve's linear regression. The total amount of calcein released from 1 mg MSN was 0.021 mg.

Release capacity: 0.02 mg/mg MSN

## Stability tests

After immersion of the particles in DMEM for different times at different pH, they were extensively washed and dried from an acidified (several droplets of 0.01 M HCl) aqueous solution at 60°C obtain opened particles for sorption experiments. Nitrogen sorption measurements were performed on a Quantachrome Instruments NOVA 4000e at 77 K. It can be seen that all isotherms maintain the shape of a type IV isotherm. Additionally, no changes in the NLDFT pore size distribution are observed, which shows that the pore structure is not affected by the medium.

## *In vivo* experiments with MSN-PVP-PEG-NH<sub>2</sub>-FA

All *in vivo* experiments from Chapter 7 were performed by Annika Hermann (group of Prof. Wagner).

## 2 Details for Chapter 7: Polymer-Capped Mesoporous Silica Nanoparticles

For *in vivo* experiments female Rj:NMRI-nu (nu/nu) (Janvier, Le Genest-St-Isle, France) mice were housed in isolated ventilated cages with a 12 h day/night cycle and food and water ad libitum. Animal experiments were performed according to guidelines of the German law of protection of animal life and were approved by the local animal experiments ethical committee.

### MSN biodistribution

MSN were prepared in 20mM HEPES (Biomol GmbH, Hamburg, Germany) with 5 % glucose (Merck, Darmstadt, Germany) (HBG). For analysis of MSN, mice were anesthetized with 3 % isoflurane in oxygen. A 100  $\mu\text{g}$  (5 mg/kg) dose of Cy-7 loaded MSN-PVP-PEG-NH<sub>2</sub>-FA or unfunctionalized MSN dispersed in 200  $\mu\text{L}$  (HBG) was injected intravenously into the tail vein of tumor-free mice. Near-infrared fluorescence imaging by a CCD camera using the IVIS Lumina system with Living Image software 3.2 (Caliper Life Sciences, Hopkinton, MA, USA) was started immediately after injection and was repeated after 0.25, 0.5, 1, 4, 24 and 48 h.

### Clinical chemistry and histopathology

Mice (n=9) were sacrificed with isoflurane (Isofluran CP<sup>®</sup>, CP-Pharma Handelsgesellschaft mbH, Burgdorf, Germany) 48 h after intravenous injection of pure HBG or a 100  $\mu\text{g}$  (5 mg/kg) dose of Cy-7 loaded MSN-PVP-PEG-NH<sub>2</sub>-FA or unfunctionalized MSN. Blood was collected in serum tubes (Multivette, Sarstedt, Nuembrecht, Germany) and clinical chemistry parameters (alanine transaminase/aspartate transaminase, creatinine levels and blood urea nitrogen) were analyzed. Organs were dissected and fixed in formalin, embedded into paraffin and stained with eosin and hematoxylin. Results were documented using an Olympus BX41 microscope (Olympus, Germany).

### MSN retention in tumors

Human cervix carcinoma cells (KB wild-type) were cultured as described above. Mice were injected with  $5 \times 10^6$  cells subcutaneously into the nape and tumors were allowed to grow for 14 days. At day 14, mice were anesthetized with 3 % isoflurane in oxygen and 100  $\mu\text{g}$  (5 mg/kg) of Cy-7 labeled MSN-PVP-PEG-NH<sub>2</sub> with and without folic acid ligand solved in 50  $\mu\text{L}$  (HBG) were injected intratumorally to test for differential retention in tumors. The near infrared fluorescence signals were recorded by a CCD camera immediately after injection and repeated after 0.25, 0.5, 1, 4, 24 h and daily for one week using the IVIS Lumina system. Data interpretation was done with equalized color bar scales for each trial and pictures were analyzed using the Living Image software 3.2 (Caliper Life Sciences, Hopkinton, MA, USA).

Human breast cancer cells (MDA-MB-231) were cultured in DMEM-medium. Mice were injected subcutaneously into the left flank with  $5 \times 10^6$  cells suspended in 50 % Matrigel (BD Biosciences) in PBS. At day 42, mice were injected intravenously via tail vein with 100  $\mu\text{g}$  (5 mg/kg) of Atto633-labeled MSN-PVP-PEG-NH<sub>2</sub> with and without folic acid ligand solved in 100  $\mu\text{L}$  HBG. Mice were sacrificed by cervical dislocation under isoflurane anesthesia 3 h after injection of MSN. Tumors and organs (liver, spleen, kidneys and lungs) were harvested and embedded in Tissue Tek (Sakura

## *Appendix*

Finetek, Heppenheim, Germany) and immediately stored at  $-20^{\circ}\text{C}$  Celsius. For preparation of cryosections with a thickness of  $5\ \mu\text{m}$  a cryotom was used. The cryosections were fixed in 4 % paraformaldehyde, stained with 4',6-Diamidino-2- phenylindol (DAPI) and results were documented with Zeiss Cell Observer SD (recording z-stacks).

### 3 Synthesis details for Chapter 8: Dendrimeric shell and disulfide binding of cargo - proton sponge effect

#### IR spectra

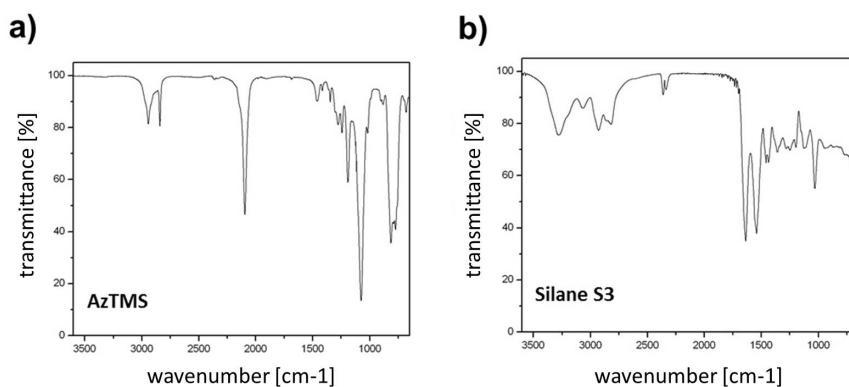


Figure 15: IR spectroscopy data of a) AzTMS, b) dendron-silane S1, c) dendron-silane S2, and d) dendron-silane S3.

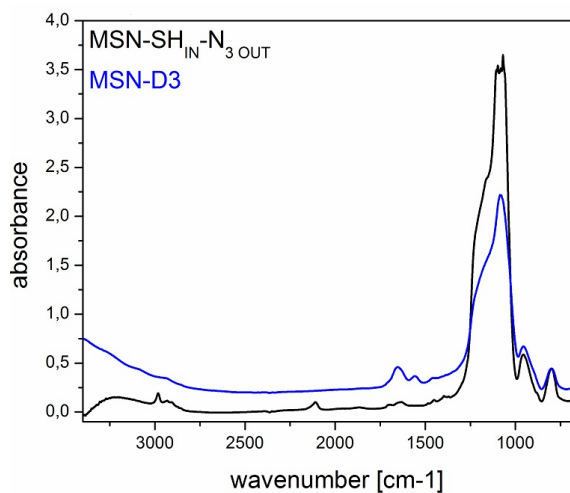


Figure 16: IR spectroscopy data of functionalized MSNs.

NMR spectra

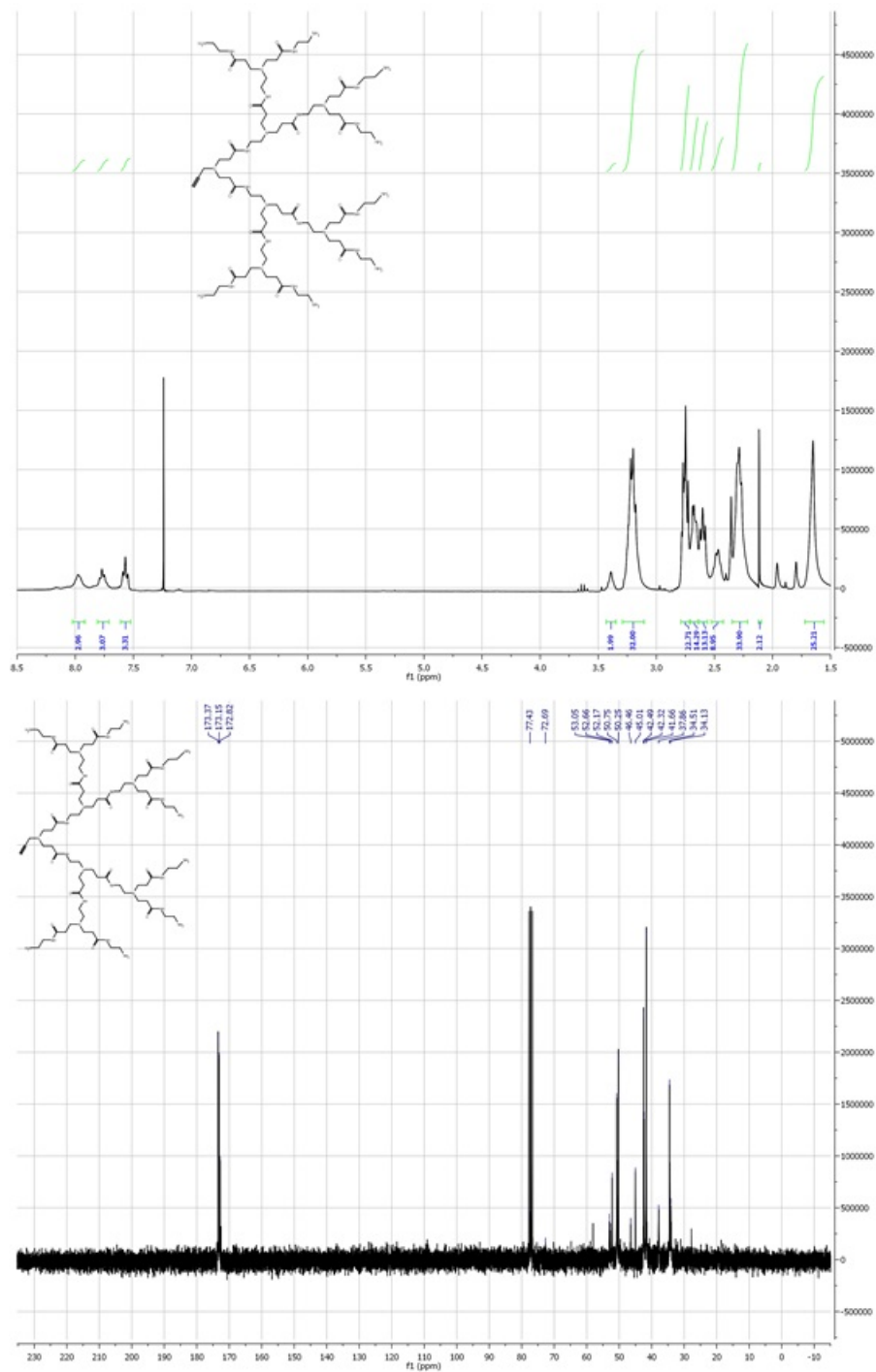
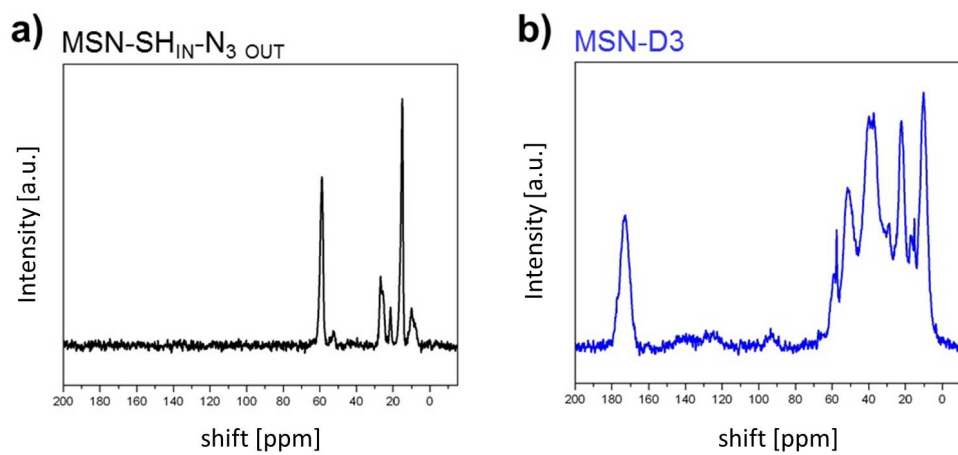


Figure 17: <sup>1</sup>H and <sup>13</sup>C NMR spectrum of propargyl-dendron D3.

$^{13}\text{C}$  solid state NMR



**Figure 18:**  $^{13}\text{C}$  solid state NMR spectra of functionalized MSNs. a) MSN-SH<sub>IN</sub>-N<sub>3</sub><sub>OUT</sub> (black), b) MSN-D<sub>3</sub> (blue)

## DAPI release

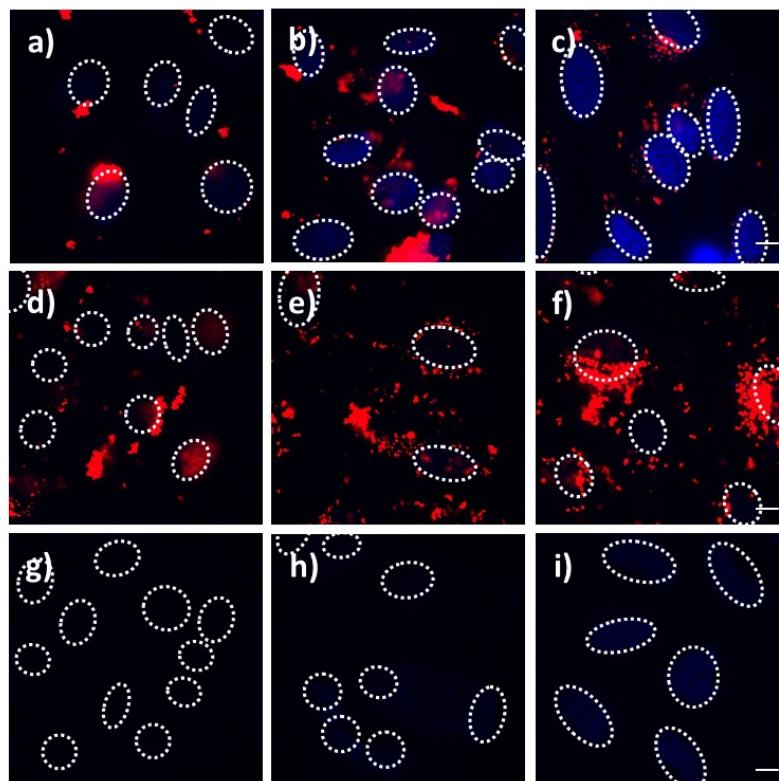


**Figure 19:** Fluorescence microscopy of HeLa cells incubated with MSN-D3-MTS-DAPI (a, b, c), MSN-NH<sub>2</sub>-MTS-DAPI (d, e, f), and the supernatant of MSN-D3-MTS-DAPI (g, h, i). The nanoparticles have been loaded with covalently attached DAPI (MTS-DAPI, blue) and labeled with Atto633 (red). The cells have been incubated with the samples for 5 h (a, d, g), 24 h (b, e, h) and 61 h (c, f, i). The nuclei are indicated with dashed circles. A time-dependent nuclei staining can be observed for MSN-D3-MTS-DAPI, suggesting triggered release of the cargo molecules from the nanocarriers after endosomal escape via the proton sponge effect and excess to the cytosol. For MSN-NH<sub>2</sub>-MTS-DAPI and the supernatant incubation almost no nucleic staining can be detected which implies that no DAPI has been release form the particles or has been present in the solution, respectively. The scale bars represent 10  $\mu\text{m}$ .

## Cytotoxicity studies

The cytotoxic impact of the PAMAM dendron-coated MSNs was determined by using immortalized human microvascular endothelial cells (HMEC-1; Centers for Disease Control and Prevention, USA). HMEC-1 were cultivated in Gibco<sup>®</sup> MCDB 131 medium (Life Technologies GmbH, Germany) supplemented with 10 % (v/v) fetal bovine serum (FBS, Life Technologies GmbH, Germany), 1 % (v/v) GlutaMAX<sup>™</sup> I 100X (Life Technologies GmbH, Germany), 1  $\mu\text{g}/\text{ml}$  hydrocortisone (Sigma-Aldrich Chemie GmbH, Germany) and 10 ng/ml epidermal growth factor (Life Technologies GmbH,

Germany) at 37°C in a 5 % CO<sub>2</sub> humidified environment by changing the growth medium every 2-3 days. Subcultivation was performed after reaching cellular confluency of 70-85 % using GIBCO® trypsin (Life Technologies GmbH, Germany) for cell detachment. PCR was routinely performed to test that the cells were free of mycoplasma infection. For cytotoxicity evaluation, 12.000 cells/cm<sup>2</sup> were seeded in a 96 well cell culture plate. 24 h after seeding they were exposed to PAMAM dendron-coated MSNs of different concentrations (10 fg/ml to 100 µg/ml) for 3 to 72 h. After the defined incubation times, the cells were washed with Hank's BSS and freshly cell culture medium and 20 µl Cell titer 96 Aqueous One Solution Reagent (Promega GmbH, Germany) per well were added. The absorbance of the supernatants was measured at 492 nm via a microplate reader (Sunrise™ Tecan Group Ltd., Switzerland) and the relative cellular dehydrogenase activity of endothelial cells was calculated by normalizing the values to untreated control cells. For evaluation of nanoparticle uptake kinetics, 12.000 cells/cm<sup>2</sup> were seeded in 8-well LabTek-II slides (Nunc). Cells were exposed to 100 µg/ml of PAMAM dendron-coated MSNs 24 h after seeding for 3, 24 and 48 h. After that, cells were washed twice with phosphate buffered and plasma membrane was stained with a 10 µg/ml wheat germ agglutinin Alexa Fluor 488 conjugate (WGA488, Invitrogen) solution in cell medium during 1 min. Staining solution was removed and cells were washed twice with cell medium. Fresh cell medium was added and cells were imaged immediately by spinning disc confocal microscopy with a Z-spacing of 0.25 µm (63x objective). Calibration experiments were carried out with PAMAM dendron-coated MSNs deposited on a cover slip and covered with cell medium. The images were evaluated with the subroutine *Calibration* of Particle\_in\_Cell-3D and the mean intensity value showed a Gaussian distribution with the mean at 64632 pixel intensities per nanoparticle.

## Chemicals.

Propargylamine (Aldrich, 98 %), N,N- diisopropylethylamine (DIPEA, Sigma-Aldrich, ≥ 99 %), copper(I) iodide (Aldrich, 99.999 %), (3- aminopropyl) triethoxysilane (APTES, Aldrich, 99 %), tetraethyl orthosilicate (TEOS, Fluka, > 98 %), triethanolamine (TEA, Aldrich, 98 %), cetyltrimethylammonium chloride (CTAC, Fluka, 25 % in H<sub>2</sub>O), (3-mercaptopropyl) trimethoxysilane (MPTMS, Gelest, 95 %), methanethiosulfonate 5(6)- carboxy-X- rhodamine (MTS-ROX, Biotium), colchicine methanethiosulfonate (MTS-Col, Santa Cruz Biotechnology), 4,6- diamidino-2- phenylindole dihydrochloride (DAPI, Sigma Aldrich), folic acid (FA, Sigma), Atto633 maleimide (ATTO-TEC), 1-ethyl-3-(3- dimethylaminopropyl) carbodiimide hydrochloride (EDC, Fluka, 97 %), N-hydroxysulfosuccinimide (sulfo-NHS, Sigma Aldrich, > 98.5 %), poly (ethylene glycol) bisamine (PEG<sub>2000</sub>-bisNH<sub>2</sub>, MW2000, Sigma Aldrich), N-succinimidyl oxycarbonylethyl methanethiosulfonate (NHS-3-MTS, Santa Cruz Biotechnology), and oxalic acid were used as received. Methyl acrylate (Aldrich, 99 %) and 1,2-ethylenediamine (Aldrich, 99.5 %) were freshly distilled prior to use. Ethanol (EtOH, absolute), N,N-dimethyl formamide (DMF, Sigma Aldrich, anhydrous) and methanol (MeOH, anhydrous, Sigma) were used as solvents without further purification. Bidistilled water was obtained from a Millipore system (Milli-Q Academic A10). (3-Azidopropyl) trimethoxy silane (AzTMS) was freshly prepared as previously reported. [219]

## Synthesis of propargyl-PAMAM dendrons.

Starting with propargylamine, the synthesis of PAMAM dendrons employs a Michael addition with methyl acrylate and amidation with 1,2-ethyldiamine in an alternating fashion. The methodology was developed by Lee *et al.* [320]

### General procedure for Michael addition.

A solution of the amino-terminal compound in anhydrous methanol (80 mL) was added drop-wise to a stirring solution of freshly distilled methyl acrylate in methanol over a period of approx. 1 h at 0°C. The resulting solution was allowed to warm up to room temperature and stirred for 48 h. The reaction progress was monitored by NMR spectroscopy and stopped when the N-H signal had disappeared. Solvent and methyl acrylate were removed in vacuo, traces of methyl acrylate were removed by redissolving the residue in methanol and repeated removal of the solvent. Drying under high vacuum gave the desired pure product as orange viscous oil.

### General procedure for amidation.

A solution of the ester-terminal compound in methanol (80 mL) was added drop-wise to a stirring solution of freshly distilled 1,2-ethyldiamine in methanol over a period of approx. 1 h at 0°C. The resulting solution was allowed to warm up to room temperature and stirred for 48 h. The reaction was monitored by NMR spectroscopy and stopped when no methyl ester signal could be detected anymore. Solvent was removed in vacuo, the excess of 1,2-ethyldiamine was removed successively by adding 100 mL of an azeotropic toluene/methanol mixture (9:1) and removal of the volatiles in vacuo. This procedure needed to be repeated four to six times with a final pressure after removal of < 10 mbar. Remaining toluene was removed by azeotropic distillation using methanol. Drying under high vacuum gave the desired pure product as orange viscous oil.

### Dendron D3:

**Dendron D0.5:** Starting material: Propargylamine (1.50 g, 1.74 mL, 27.2 mmol, 1+eq.); Reagents: methyl acrylate (17.0 g, 17.9 mL, 197 mmol, 7.3 eq.) in 20 mL methanol; Yield: 5.74 g (25.3 mmol, 93 %);

**Dendron D1:** Starting material: D0.5 (4.90 g, 21.6 mmol, 1 eq.); Reagents: 1,2-ethyldiamine (111 g, 100 mL, 1.85 mol, 86 eq.) in 30 mL methanol; Yield: 6.23 g (21.2 mmol, 98 %);

**Dendron D1.5:** Starting material: D1 (5.78 g, 20.4 mmol, 1 eq.); Reagents: methyl acrylate (28.5 g, 30.0 mL, 331 mmol, 16 eq.) in 40 mL methanol; Yield: 12.3 g (19.6 mmol, 96 %);

**Dendron D2:** Starting material: D1.5 (10.5 g, 16.7 mmol, 1 eq.); Reagents: 1,2-ethyldiamine (111 g, 100 mL, 1.85 mol, 110 eq.) in 20 mL methanol; Yield: 12.1 g (16.4 mmol, 98 %);

**Dendron D2.5:** Starting material: D2 (6.7 g, 10.4 mmol, 1 eq.); Reagents: methyl acrylate (85.5 g, 90.0 mL, 0.99 mol, 96 eq.) in 30 mL methanol; Yield: 14.5 g (10.2 mmol, 98 %);

**Dendron D3:** Starting material: D2.5 (6.42 g, 4.50 mmol, 1 eq.); Reagents: 1,2-ethyldiamine (122 g, 110 mL, 2.0 mol, 452 eq.) in 10 mL methanol; Yield: 6.5 g (3.91 mmol, 87 %);

**IR (film):** 3271, 3074, 2933, 2863, 1636, 1540, 1436, 1359, 1197, 1127, 935  $\text{cm}^{-1}$ ;

**$^1\text{H}$  NMR** (270 MHz,  $\text{CDCl}_3$ )  $\delta$  = 7.98 (s, 2H, NHCO), 7.77 (s, 4H, NHCO), 7.57 (s, 8H, NHCO), 3.39 (d, 4J = 2.0 Hz, 2H, N-CH<sub>2</sub>-C(CH<sub>2</sub>)<sub>2</sub>), 3.29-3.11 (m, 32H), 2.79-2.72 (m, 24H), 2.70-2.64 (m, 12H), 2.63-2.56 (m, 12H), 2.51-2.42 (m, 8H), 2.38-2.21 (m, 24H), 2.12 (t, J = 2.0 Hz, 1H, CH<sub>2</sub>-C(CH<sub>2</sub>)<sub>2</sub>-H), 1.65 (br s, 16H, NH<sub>2</sub>);

**$^{13}\text{C}$  NMR** (68 MHz,  $\text{CDCl}_3$ )  $\delta$  = 173.37 (C=O), 173.15 (C=O), 172.82 (C=O), 77.43 (CH<sub>2</sub>-C(CH<sub>2</sub>)<sub>2</sub>), 72.69 (CH<sub>2</sub>-C(CH<sub>2</sub>)<sub>2</sub>), 53.05, 52.66, 52.17, 50.75, 50.25, 46.46, 45.01, 42.49, 42.32, 41.66, 37.86, 34.51, 34.13 (NMR spectra are shown in Figure Appendix 17/18);

**HRMS (ESI)** ( $\text{C}_{73}\text{H}_{145}\text{N}_{29}\text{O}_{14}$ ):  $m/z$  (%) = 827.0835 (24)  $[\text{M}+2\text{H}]^{2+}$ , 1653.1595 (9)  $[\text{M}+\text{H}]^+$ .

### Synthesis of PAMAM Silanes.

Huisgen azide-alkyne 1,3-dipolar cycloaddition with amino-terminated propargyl-PAMAM dendrons and AzTMS was performed based on a similar reaction of AzTMS with an alkyne compound reported by Lim *et al.* [380]

General procedure: The amino-terminated propargyl-PAMAM dendron D1-3 (1 eq.) was dissolved in a suspension of molecular sieves (3 Å) in anhydrous methanol (15 mL) and DIPEA (2 eq.). The resulting suspension was degassed afterwards. Under an atmosphere of nitrogen, copper(I) iodide (10 mol%), as catalyst, and AzTMS (0.25 eq.) were added. The reaction was stirred for 24 h at room temperature and subsequently filtered using a syringe filter. After exposure to air the solution turned purple-blue very quickly. The solvent was removed in vacuo, drying of the crude product at high vacuum yielded a blue gum which was used without further purification.

S3 Starting material: D3 (3.31 g, 2.00 mmol); Reagents: AzTMS (103 mg, 103 mL, 0.500 mmol), DIPEA (517 mg, 697 mL, 4.00 mmol), CuI (38.1 mg, 0.200 mmol); Crude product: 3.5 g containing 836 mg (450 mmol) of S3.

### Synthesis of dendron-functionalized MSNs (MSN-SH<sub>IN</sub>-D<sub>3OUT</sub>).

Colloidal mesoporous silica nanoparticles (MSN-SH<sub>IN</sub>-D<sub>3OUT</sub>) were prepared according to a synthesis procedure published by Cauda *et al.* [37] The amount of functionalized silane was calculated to be 1 % of total silica. A mixture of TEA (14.3 g, 95.6 mmol), TEOS (1.56 g, 7.48 mmol) and MPTMS (92.3 mg, 87.3 mL, 0.47 mmol) was heated for 20 min at 90°C without stirring in a polypropylene reactor. Afterwards, a preheated mixture of CTAC (2.41 mL, 7.29 mmol) and H<sub>2</sub>O (21.7 g, 1.21 mol) to 60°C was added to the first solution and stirred for 20 min at room temperature. Then, every 3 min 37.2  $\mu\text{L}$  TEOS (34.6 mg) was added to the stirring suspension four times in total. The reaction was stirred for further 30 min. After this time, a mixture of TEOS (19.2 mg, 92.2 mmol) and functionalized trialkoxysilane (RTMS: AzTMS, S3) (92.2 mmol) was added. In the case of the PAMAM silanes S3, the amount of crude product to be used for particle functionalization was calculated from the percental mass of the silane in the crude product. Furthermore, the mixture of TEOS and PAMAM silane was dissolved in a solution of 2 mL methanol and 1 mL water briefly before the addition. The reaction was stirred at room temperature over night. The suspension was

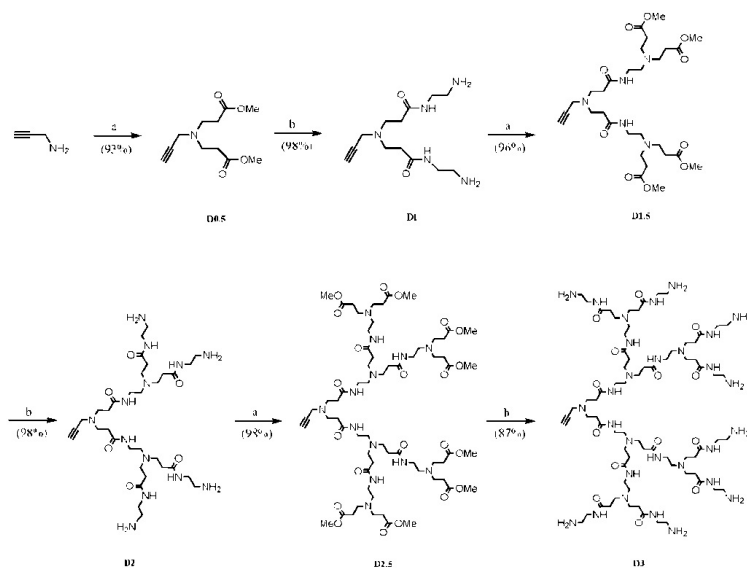


**Figure 20:** Synthesis of propargyl-PAMAM dendrons (D0.5 - D3). Reagents and reaction conditions: a) methyl acrylate (large excess), MeOH, 0  $\rightarrow$  25°C, 48 h and b) 1,2-ethylenediamine (large excess), MeOH, 0  $\rightarrow$  25°C, 48 h.

diluted 1:1 with absolute ethanol, the colloidal MSNs were separated by centrifugation (19,000 rpm, 43,146 rcf, 20 min) and redispersed in absolute ethanol. The template extraction was performed by heating the samples under reflux at 90°C (oil bath) for 45 min in a solution of ammonium nitrate (2 wt% in ethanol) followed by 45 min under reflux at 90°C in a solution of 10 mL conc. HCl (37 %) in 90 mL ethanol. The extracted MSNs were collected by centrifugation after each extraction step and finally washed with 100 mL absolute ethanol. The resulting MSNs were stored in an ethanol/water solution (2:1).

### Cargo loading.

MSN-D3 (1 mg) was incubated for 2 h at room temperature in the dark with MTS-ROX (5  $\mu$ L, 5 mg/mL in DMF), MTS-Col (50  $\mu$ L, 5 mg/mL in DMF), or MTS-DAPI for a one-step covalent attachment of the cargo molecules to the internal surface of the mesopores via disulfide bridges. MTS-DAPI was prepared in-situ by mixing DAPI (10  $\mu$ L, 5 mg/mL in DMF) and NHS-3-MTS (100  $\mu$ g) in an aqueous solution for 1 h at room temperature in the dark. This reaction mixture was subsequently added to MSN-D3. The particles were washed five times (centrifugation, 4 min, 14,000 rpm, 16,837 rcf) with water and were finally redispersed in 1 mL H<sub>2</sub>O.

### MSN labeling.

MSN-D3 (0.5 mg) were mixed with Atto633 maleimide (1  $\mu$ L, 2 mg/mL in DMF). After 2 h of stirring at room temperature in the dark the labeled particles were washed three times with water

by subsequent centrifugation (4 min, 14,000 rpm, 16,837 rcf) and redispersed in H<sub>2</sub>O.

### **Attachment of the targeting ligand folate.**

Oxalic acid, EDC, and sulfoNHS (each 5 mg) were successively added to an aqueous dispersion of MSN-D3 (0.5 mg) and the resulting reaction mixture was stirred at room temperature in the dark for another 2 h. Subsequently, the particles were washed three times (centrifugation, 4 min, 14,000 rpm, 16,837 rcf) and redispersed in 300  $\mu$ L H<sub>2</sub>O. The PEG linker was attached via EDC amidation. EDC, sulfoNHS and PEG<sub>2000</sub>-bisNH<sub>2</sub> (each 5 mg) were consecutively added to the particle dispersion and stirred for another 2 h at room temperature in the dark. The particles were washed three times by centrifugation (4 min, 14,000 rpm) and redispersed in 100  $\mu$ L water. Then 400  $\mu$ L of a folate stock solution (0.75  $\mu$ M in H<sub>2</sub>O), EDC (5 mg), and sulfoNHS (5 mg) were added. The reaction mixture was stirred over night at room temperature in the dark. After washing the particle three times with water (centrifugation, 4 min, 14,000 rpm, 16,837 rcf) the MSN-D3-FA sample was finally redispersed in 1 mL H<sub>2</sub>O.

### **Characterization.**

IR spectra were recorded on a Bruker Equinox 55. The dried powder of the silica nanoparticles (1.5 mg) was mixed with KBr (200 mg) to produce pressed, transparent pellets to be measured in absorbance mode. For background measurements a neat KBr pellet (200 mg) was used. IR spectra of the organic compounds were recorded in the attenuated total reflectance (ATR) mode on the same device or on a Perkin-Elmer FT-IR Spektrum BXII spectrometer with Schmith Dura SampIIR II ATR-Unit.

Acid-base titrations were performed on a Metrohm 905 Titrando potentiometric titrator combined with the software tiamo. The titration method met the following parameters: monotonic equivalence point titration (MET); stirring speed 5; measurement value drift 20.0 mV/min; min. delay 0 s; max. delay 300 s; volume increment 0.025 mL; dosing speed maximal; stop value pH 10.2. The samples were prepared as follows: A volume containing 13.7 mg particles from the suspensions was added to 30.0 mL H<sub>2</sub>O. The starting pH was set to 3.000 using HCl (0.1 M) and NaOH (0.01 M) from the dosing unit. The samples were titrated against NaOH (0.01 M).

TGA of the bulk extracted samples (about 10 mg of dried powder) were performed on a Netzsch STA 440 Jupiter thermobalance (heating rate of 10 K/min in a stream of synthetic air of about 25 mL/min).

Nitrogen sorption measurements were performed on a Quantachrome Instruments NOVA 4000e at -196°C. Sample out-gassing was performed at 120°C for 12 h at a pressure of 10 mTorr. Pore size and pore volume were calculated using a NLDFT equilibrium model of N<sub>2</sub> on silica, based on the desorption branch of the isotherm. The BET model was used in the range of 0.05  $\hat{a}$ €“ 0.20 p/p<sub>0</sub> to estimate the specific surface area.

DLS and zeta potential measurements were performed on a Malvern Zetasizer-Nano instrument equipped with a 4 mW He-Ne laser (633 nm) and avalanche photodiode detector. DLS measurements

## *Appendix*

were directly recorded on aqueous colloidal suspension at a constant concentration for all sample solutions of 1 mg/mL. For determination of the zeta potential profiles, one to three drop of the ethanolic suspension (ca. 3 wt%) was mixed with 1 mL of commercial Hydrion Buffer solution of the appropriate pH prior to measurement. Hückel's approximation was used for interpretation.

For TEM (using a Titan 80-300 kV microscope operating at 300 kV), samples were prepared by dispersing MSNs (1 mg) in 4 mL absolute ethanol, by means of an ultrasonic bath, and drying a drop of the resulting diluted suspension on a carbon-coated copper grid.

## 4 Synthesis details for Chapter 9: Enzyme based pH-sensitive cap system for MSNs.

### Chemicals.

Tetraethyl orthosilicate (TEOS, Fluka, > 99 %), triethanolamine (TEA, Aldrich, 98 %), cetyltrimethylammonium chloride (CTAC, Fluka, 25 % in H<sub>2</sub>O), (3-mercaptopropyl)-triethoxysilane (MPTES, Sigma Aldrich, > 80 %), 6-maleimidohexanoic acid N-hydroxysuccinimide ester (Fluka, > 98 %), bovine carbonic anhydrase (bCA, Sigma, > 95 %), 4-(2-aminoethyl) benzenesulfonic acid (Aldrich, 98 %), ammonium nitrate (NH<sub>4</sub>NO<sub>3</sub>, Aldrich), ammonium fluoride (NH<sub>4</sub>F, Aldrich), hydrochloric acid (37 %), fluorescein disodium salt dihydrate (Aldrich, 90 %), and Hank's balanced salt solution (HBSS-buffer, Sigma Aldrich) were used as received. Ethanol (EtOH, absolute, Aldrich) and dimethylformamide (DMF, dry, Aldrich) were used as solvent without further purification. Bidistilled water was obtained from a millipore system (Milli-Q Academic A10). Citric-acid phosphate buffer (CAP-buffer, pH 5.5) was freshly prepared by carefully mixing a certain amount of disodium hydrogen phosphate (Na<sub>2</sub>HPO<sub>4</sub>, 0.2 M in H<sub>2</sub>O) and citric acid (0.2 M in H<sub>2</sub>O) to adjust a pH value of 5.5. Subsequently, the solution was diluted with bidistilled H<sub>2</sub>O to a total volume of 500 mL.

### Synthesis of thiol-functionalized MSNs (MSN-SH).

A mixture of TEOS (1.92 g, 9.22 mol) and TEA (14.3 g, 95.6 mmol) was heated to 90°C for 20 min at static conditions in a polypropylene reactor. Then, a preheated (60°C) mixture of CTAC (2.41 mL, 1.83 mmol, 25 % in H<sub>2</sub>O) and NH<sub>4</sub>F (100 mg, 0.37 mmol) in bidistilled H<sub>2</sub>O (21.7 g, 1.21 mol) was added and the resulting reaction mixture was stirred vigorously (700 rpm) for 30 min while cooling down to room temperature. Afterwards, TEOS (18.2 mg, 92 μmol) and MPTES (18.1 mg, 92 μmol) were added as a 1:1 solution premixed to allow premature condensation. The final reaction mixture was stirred over night at room temperature. After dilution with absolute ethanol (100 mL), the nanoparticles were collected by centrifugation (19,000 rpm, 43,146 rcf, 20 min) and redispersed in absolute ethanol. Template extraction was performed in an ethanolic solution of MSNs (100 mL) containing NH<sub>4</sub>NO<sub>3</sub> (2 g) which was heated at reflux conditions (90°C oil bath) for 45 min. Followed by a second extraction step (90 mL absolute ethanol and 10 mL hydrochloric acid (37 %)) under reflux conditions for 45 min (the material was washed with absolute ethanol after each extraction step and collected by centrifugation), the particles were finally redispersed in absolute ethanol and stored as colloidal suspension.

### Synthesis of sulfonamide-functionalized MSNs (MSN-phSA).

For the covalent attachment of a sulfonamide derivative to the external particle surface, a thiol-reactive linker was synthesized. 6-maleimidohexanoic acid N-hydroxysuccinimide ester (mal-C6-NHS, 10 mg, 33 μmol) was dissolved in DMF (500 μL, dry) and was added to an ethanolic solution (15 mL) containing 4-(2-aminoethyl)benzene sulfonamide (6.7 mg, 33 μmol). The resulting reaction mixture was stirred for 1 h at room temperature. Afterwards, thiol-functionalized silica nanoparticles

## Appendix

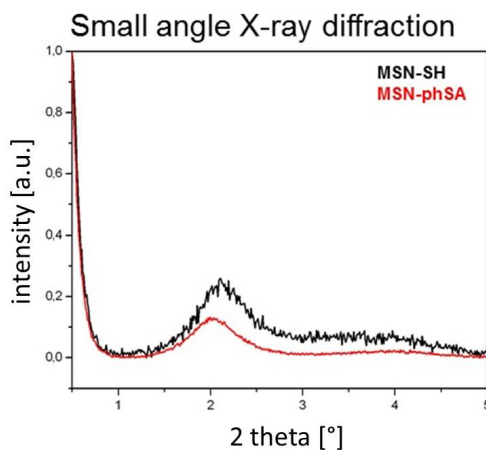
(MSN-SH, 100 mg) in absolute ethanol (10 mL) were added and the mixture was stirred over night at room temperature. Subsequently, the particles were collected by centrifugation (19,000 rpm, 41,146 rcf, 20 min), washed twice with absolute ethanol and were finally redispersed in ethanol (15 mL) to obtain a colloidal suspension.

### **Cargo loading and particle capping.**

MSNs (MSN-phSA, 1 mg) were immersed in an aqueous solution of fluorescein (1 mL, 1 mM) or DAPI (500  $\mu$ L, 14.3 mM) and stirred over night or for 1 h, respectively. After collection by centrifugation (14,000 rpm, 16,837 rcf, 4 min), the loaded particles were redispersed in a HBSS buffer solution (1 mL) containing carbonic anhydrase (1 mg) and the resulting mixture was allowed to react for 1 h at room temperature under static conditions. The particles were thoroughly washed with HBSS buffer (4 times), collected by centrifugation (5,000 rpm, 2,200 rcf, 4 min, 15°C), and finally redispersed in HBSS buffered solution.

### **Characterization.**

DLS and zeta potential measurements were performed on a Malvern Zetasizer Nano instrument equipped with a 4 mW He-Ne-Laser (633 nm) and an avalanche photodiode detector. DLS measurements were directly recorded in diluted colloidal suspensions of the particles at a concentration of 1 mg/mL. Zeta potential measurements were performed using the add-on Zetasizer titration system (MPT-2) based on diluted NaOH and HCl as titrants. For this purpose, 1 mg of the particles was diluted in 10 mL bi-distilled water. Nitrogen sorption measurements were performed on a Quantachrome Instrument NOVA 4000e at  $-196^{\circ}\text{C}$ . Sample outgassing was performed for 12 hours at a vacuum of 10 mTorr at  $60^{\circ}\text{C}$ . Pore size and pore volume were calculated by a NLDFT equilibrium model of  $\text{N}_2$  on silica, based on the desorption branch of the isotherms. In order to remove the contribution of the interparticle textural porosity, pore volumes were calculated only up to a pore size of 8 nm. A BET model was applied in the range of  $0.05 \leq p/p_0 \leq 0.20$  to evaluate the specific surface area. Infrared spectra of dried sample powder were recorded on a ThermoScientific Nicolet iN10 IR-microscope in reflexion-absorption mode with a liquid- $\text{N}_2$  cooled MCT-A detector. Raman spectroscopy measurements were performed on a confocal LabRAM HR UV/VIS (HORIBA Jobin Yvon) Raman microscope (Olympus BX 41) with a SYMPHONY CCD detection system. Dried sample powder was directly measured on a coverslip. UV/VIS measurements were performed on a Perkin Elmer Lambda 1050 spectrophotometer equipped with a deuterium arc lamp (UV region) and a tungsten filament (visible range). The detector was an InGaAs integrating sphere. Fluorescence spectra were recorded on a PTI spectrofluorometer equipped with a xenon short arc lamp (UXL-75XE USHIO) and a photomultiplier detection system (model 810/814). The measurements were performed in HBSS buffer solution at  $37^{\circ}\text{C}$  to simulate human body temperature. For time-based release experiments of fluorescein a custom made container consisting of a Teflon tube, a dialysis membrane (ROTH Visking type 8/32, MWCO 14,000 g/mol) and a fluorescence cuvette was used. The excitation wavelength was set to  $\lambda = 495$  nm for fluorescein-loaded MSNs. Emission scans (505 - 650 nm) were performed every 5 min. All slits were adjusted to 1.0 mm, bandwidth 8 nm).

**Small-angle X-ray diffraction.**

**Figure 21:** Small-angle X-ray diffraction pattern of MSN-SH (black) and MSN-phSA (red).

**Raman spectra.**

Full range of Raman spectra in Figure 22. Various additional bands (\*) can be observed for the benzene sulfonamide-functionalized particles. A sharp band at  $1780\text{ cm}^{-1}$  can be assigned to the carbonyl stretching vibration of the diacylamine group of the maleimide residue that is covalently attached to the thiol groups of the MSN surface. The presence of phenyl groups is confirmed by characteristic bands of aromatic C=C stretching vibrations ( $1600\text{ cm}^{-1}$  and  $1055\text{ cm}^{-1}$ ) and aromatic =C-H out-of-plane deformation vibrations ( $693\text{ cm}^{-1}$ ). The broadening of the signal at  $1600\text{ cm}^{-1}$  can be assigned to the partial overlap by amide II vibration modes. The bands at  $1326$  and  $1156\text{ cm}^{-1}$  are related to the characteristic asymmetric and symmetric stretching vibrations of the sulfonamide group, respectively.

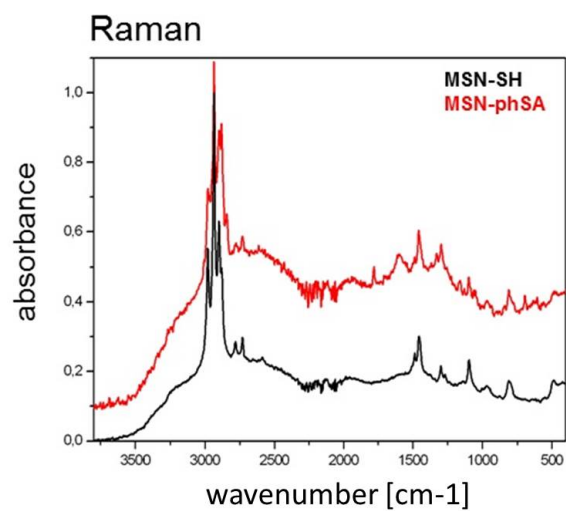


**Figure 22:** Raman spectroscopy data of functionalized MSNs. MSN-SH (black) and MSN-phSA (red). For clarity reasons, the curves are shifted along the y-axis by 0.1 units.

**Fluorescein calibration curve.**

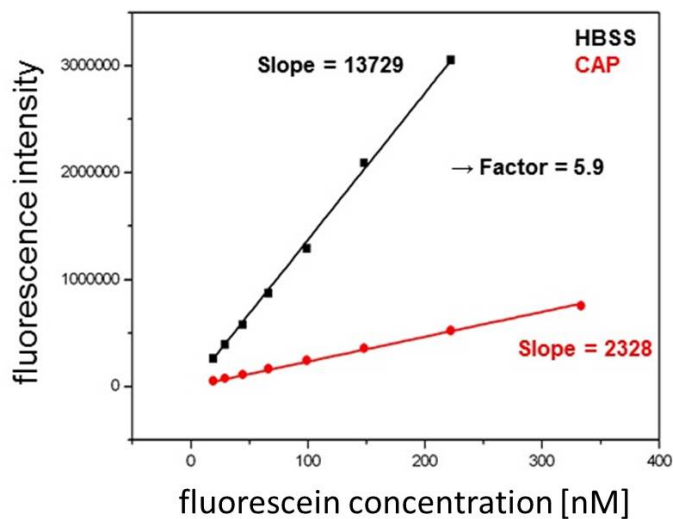


**Figure 23:** Calibration curves of fluorescein at pH 7.4 (HBSS buffer, black curve) and pH 5.5 (CAP buffer, red curve)

## 5 Synthesis details for Chapter 10: Modifications for supported lipid bilayer coated MSN

### 5.1 Chapter 10.1: Large pore MSN

#### Synthesis of unfunctionalized LP-MSN with the dual surfactant system F127 and FC-4 and the swelling agent TiPB at 30°C

Pluronic<sup>®</sup> F127 (0.25 g, 19.8  $\mu$ mol) and FC-4 (0.70 g) were dissolved in hydrochloric acid (HCl, 30 mL, 0.02 M), followed by the addition of the swelling agent TiPB (0.34 g, 1.66 mmol). The reaction mixture was stirred in a polypropylene reactor for 2 h at 30°C before TEOS (1.5 g, 7.2 mmol) was added dropwise. The resulting suspension was vigorously stirred over night at 30°C.

#### Synthesis of LP-MSN-NH<sub>2</sub>/Ph via co-condensation

The applied amounts of TEOS, APTES/PTES, FC-4 and the amount of the swelling agent TiPB (30°C) or TMB (10°C) for the synthesis of LP-MSN-NH<sub>2</sub>/Ph are summarized in Table 3. (3-azidopropyl)triethoxysilane was used as synthesized according to a procedure published by Nakazawa *et al.* [321] Pluronic<sup>®</sup> F127 (0.25 g, 19.8  $\mu$ mol) and fluorocarbon surfactant FC-4 were dissolved in hydrochloric acid (HCl, 30 mL, 0.02 M), followed by the addition of the swelling agent 1,3,5-triisopropylbenzene (TiPB) or 1,3,5-trimethylbenzene (TMB) respectively. The reaction mixture was stirred in a polypropylene reactor for 2 h at 10°C/30°C before a mixture of TEOS and organotriethoxysilane (APTES/PTES) was added dropwise. The resulting suspension was vigorously stirred over night at 10°C/30°C.

**Table 3:** List of synthesized LP MSN

sample name	TEOS [mmol]	amount of functionalization	FC-4 [g]	swelling agent [g]	T[°C]	Hydrothermal treatment T[°C]/days
MLA-004	7.12	0.036 mmol APTES (0.5%) + 0.036 mmol PTES (0.5%)	0.70	0.2 TMB	10	150/1; 140/2
MLA-004	7.20 7.20	0.036 mmol APTES (0.5%) + 0.036 mmol PTES (0.5%)	1.40	0.34 TiPB	30	150/2; 140/2

**Hydrothermal treatment of LP-MSN** The as-synthesized particles were transferred to an autoclave and heated at 150°C for 1-2 d under static conditions. The mixture was centrifuged (15 min, 20500 rpm, 50228 rcf), re-suspended in hydrochloric acid (HCl, 30 mL, 0.2 M) and heated under static conditions at 140°C for two days. The resulting precipitate was centrifuged (15 min, 20500 rpm, 50228 rcf) and re-suspended in absolute ethanol.

**Template removal of LP-MSN** The organic template was removed via extraction. For this

## Appendix

purpose, the particles were refluxed for 2 h at 75°C in a mixture of absolute ethanol, acetone and hydrochloric acid (HCl, 37 wt%; ethanol:acetone:HCl: 50:50:10 vol %). Afterwards, the particles were collected by centrifugation (15 min, 20500 rpm, 50228 rcf). This procedure was repeated once. The particles were stored in tightly sealed glass vials.

**Size separation centrifugation** In order to separate large agglomerates from the synthesized nanoparticles, a size separation centrifugation was performed (15 sec, 3.000 rpm, 775 rcf). The resulting supernatant comprising a nanoparticle yield of 50 % (relative to the synthesis yield) was employed for all further applications. The obtained particles in ethanol were stored in tightly sealed glass vials.

### Synthesis of SLB@LP-MSN<sub>cargo</sub> and SLB@LP-MSN-AIPcS<sub>2a</sub>-cargo for drug delivery

#### Attachment of the red light photosensitizer AIPcS<sub>2a</sub> to LP-MSN-NH<sub>2</sub>/-Ph

2 mg of size separated LP-MSN-Ph/NH<sub>2</sub> in EtOH were centrifuged, washed three times with 500 μL of water and finally resuspended in 500 μL of water. After the addition of 50 μL of an AIPcS<sub>2a</sub> stock solution (2 mg AIPcS<sub>2a</sub> in 1 mL DMSO), the mixture was stirred in the dark at room temperature for 72 h. The obtained LP-MSN-AIPcS<sub>2a</sub> particles were washed by repeated centrifugation and redispersion in water/DMSO (1:1 vol%) to remove excess photosensitizer. To investigate the content of free photosensitizer in all supernatants, the absorbance at 680 nm was measured by NanoDrop UV-Vis. Subsequently, the sample was washed three times with Millipore water to remove DMSO from the mesopores.

**Adsorption of differently sized cargos into the pores of LP-MSN-AIPcS<sub>2a</sub>** An ethanolic solution of LP-MSN-AIPcS<sub>2a</sub>, was washed three times by repeated centrifugation (5 min, 14.000 rpm, 16873 rcf) and redispersion in H<sub>2</sub>O. After the last centrifugation step the received pellet was dispersed in 500 μL cargo solution (Table 4) (in case of Alexa Fluor dextran 488 in 110 μL cargo-solution). The mixture was stirred over night in the dark yielding the sample LP-MSN-AIPcS<sub>2a</sub>-cargo.

**Table 4:** Loading of LP-MSN-AIPcS<sub>2a</sub> with differently sized cargos.

sample name	amount of applied NP [mg]	cargo	composition of cargo solution
MLA-014	1	calcein	500μL solution-1mM in H <sub>2</sub> O
MLA-034/71.1	0.5	PI	500μL solution-0.5mM in H <sub>2</sub> O
MLA-030	0.5	Alexa Fluor Dextran 488 (10000Da)	10μL solution - 2 mg/mL in PBS + 100μL H <sub>2</sub> O

**Supported DOPC/DOTAP lipid bilayer (SLB) around LP-MSN-AIPcS<sub>2a</sub>-cargo (SLB @ LP-MSN-AIPcS<sub>2a</sub>-cargo)** The amount of 0.5 mg of LP-MSN-AIPcS<sub>2a</sub>-cargo was separated by centrifugation (4 min, 14000 rpm, 16873 rcf). The supernatant was discarded and the obtained pellet was re-dispersed in a mixture containing 70  $\mu$ L DOPC and 30  $\mu$ L DOTAP (each 2.5 mg/mL in 60:40 H<sub>2</sub>O:EtOH). The suspension was mixed extensively and sonicated for 2 s. To form the supported lipid bilayer around the LP-MSN via a solvent exchange method, 700  $\mu$ L of millipore water was added. The resulting suspension was mixed and sonicated for 2 s, yielding SLB@LP-MSN-AIPcS<sub>2a</sub>-cargoSLB@LP-MSN-cargo and was used without further purification.

### Synthesis of polyvinylpyridine-capped large pore MSN

**Attachment of a Boc protecting group to poly(2-vinyl-pyridine)**  $\alpha$  amino-,  $\omega$  carboxy-terminated poly(2-vinyl-pyridine) (PVP, Mn:10 000, 474 mg, 4.7  $\mu$ mol, 1 eq) was dissolved in 10 mL anhydrous dichloromethane. Triethylamine (14.5  $\mu$ L 0.10 mmol, 21.3 eq) and di-tert-butyl-dicarbonate (Boc) anhydride (14.2 mg, 6.5  $\mu$ mol, 1.4 eq) were added subsequently to the polymer solution. The reaction mixture was stirred over night at ambient temperature. After removal of CH<sub>2</sub>Cl<sub>2</sub> in vacuo the crude product was dissolved in toluene. The organic phase was washed several times with brine and dried over anhydrous MgSO<sub>4</sub>. Toluene was removed and the product was dissolved in EtOH. The obtained HOOC PVP Boc in ethanol was used without further purification.

**Attachment of HOOC-PVP-Boc to LP-MSN -NH<sub>2</sub>/-Ph (LP-MSN-PVP-Boc)** 250 mg of LP MSN NH<sub>2</sub>/Ph were collected by centrifugation (15 min, 20500 rpm, 50228 rcf) and re-dispersed in 30 mL THF. 250 mg HOOC-PVP-Boc (2.5 mL of a 1 g/10 mL ethanolic solution, 19  $\mu$ mol, 1 eq) were added to the particle suspension. Subsequently, EDC (50  $\mu$ L, 286  $\mu$ mol, 15 eq) and sulfo-NHS (6.5 mg, 30  $\mu$ mol, 1.6 eq) added. The mixture was stirred at room temperature for 12 h. The particles were collected by centrifugation (15 min, 20500 rpm, 50228 rcf) and re-dispersed in 30 mL THF. This purification step was repeated three times. The obtained LP-MSN-PVP-Boc were stored in ethanolic solution.

**Deprotection of LP-MSN-PVP-Boc (LP-MSN-PVP-NH<sub>2</sub>)** Selective removal of the N-Boc protection group from LP-MSN-PVP-Boc was achieved by stirring 225 mg LP-MSN-PVP-Boc in 5 mL TFA and in 20 mL Millipore water for 24 h at ambient temperature. Afterwards, the LP-MSN were collected by centrifugation (15 min, 20500 rpm, 50228 rcf) and redispersed in 30 mL EtOH : 0.01 M HCl mixture (1:1 vol%). This washing step was repeated three times.

**Attachment of oxalic acid to LP-MSN-PVP-NH<sub>2</sub> (LP-MSN-PVP-Ox)** To 20 mL of an ethanolic solution containing 120 mg LP MSN-PVP-NH<sub>2</sub> oxalic acid (100 mg, 1.1 mmol, 47.8 eq), EDC (40  $\mu$ L, 228.8  $\mu$ mol, 9.9 eq) and sulfo-NHS (5 mg, 23  $\mu$ mol, 1 eq) were added. The resulting reaction mixture was stirred for 2 h at ambient temperature. Afterwards, the mixture was centrifuged (15 min, 20500 rpm, 50228 rcf) and washed 3 times by repeated centrifugation and redispersion in a 1:1 vol% mixture of 0.01 M HCl and EtOH (30 mL).

**PEGylation of LP-MSN-PVP-Ox with bi-functional H<sub>2</sub>N-PEG<sub>44</sub>-NH<sub>2</sub> of the sample LP-MSN-PVP-Ox (LP-MSN-PVP-PEG-NH<sub>2</sub>)** To a suspension of 80 mg LP-MSN-PVP-Ox in 20 mL H<sub>2</sub>O:EtOH (1:1 vol%) EDC (50  $\mu$ L, 286  $\mu$ mol, 12.4 eq) and sulfo-NHS (5 mg, 23  $\mu$ mol,

## Appendix

1 eq) were added at room temperature. The mixture was stirred for 10 min, followed by the addition of 20 mg bi-functional H<sub>2</sub>N-PEG<sub>44</sub>-NH<sub>2</sub> (Mw: 2000 g/mol, 448.3 μmol, 21.2 eq) and stirring 24 h at ambient temperature. In order to remove unreacted PEG-linker, the resulting sample LP-MSN-PVP-PEG-NH<sub>2</sub> was washed three times with 30 mL H<sub>2</sub>O/EtOH. All washing steps were followed by centrifugation (15 min, 20500 rpm, 50228 rcf).

**Attachment of the red light photosensitizer AlPcS<sub>2a</sub> to LP-MSN-PVP-PEG-NH<sub>2</sub> (LP-MSN-PVP-PEG-AlPcS<sub>2a</sub>)** 4 mg of LP-MSN-PVP-PEG-NH<sub>2</sub> in ethanolic solution were centrifuged and re-suspended in 1 mL DMSO in an Eppendorf tube. Subsequently, 100 μL of an AlPcS<sub>2a</sub> stock solution (2 mg in 1 mL DMSO) was added to the LP-MSN. The reaction mixture was stirred in the dark at room temperature for 12 h. Afterwards, the suspension was extensively washed by centrifugation (5 min, 14000 rpm, 16873 rcf) with DMSO to remove excess photosensitizer. In order to monitor the content of free photosensitizer, all supernatants were investigated with a NanoDrop UV-Vis. Subsequently, the sample was washed three times with water to remove DMSO from the mesopores. The colloidal suspension of sample LP-MSN-PVP-PEG-AlPcS<sub>2a</sub> was stored in ethanolic solution and used for further experiments.

**Loading of LP-MSN-PVP-NH<sub>2</sub> / LP-MSN-PVP-PEG-AlPcS<sub>2a</sub> with calcein and capping of the pores** 0.5 mg of LP-MSN-PVP-NH<sub>2</sub> were centrifuged (5 min, 14000 rpm, 16873 rcf) and the received pellet was redispersed in a mixture of a calcein solution (500 μL of a 1 mM solution in H<sub>2</sub>O) and citrate/HCl buffer (50 μL, pH 2). The suspension was stirred for 12 h in the dark. To seal the pores, the particles were centrifuged (5 min, 14000 rpm, 16873 rcf) and the pellet was redispersed in SSC-buffer. The sample was extensively washed by subsequent centrifugation (5 min, 14000 rpm, 16873 rcf), until no free calcein could be detected in the supernatant. This was monitored by UV-Vis measurements. After the last centrifugation step, the particles were redispersed in 200 μL SSC buffer (for cuvette-release test) or in 500 μL (for cell test). The sample LP-MSN-PVP-PEG-AlPcS<sub>2a</sub> was loaded with calcein identically to the above described procedure.

## Characterization

### Time-based fluorescence release experiments for SLB-capped samples

In order to show the time-dependent release of different cargos out of the mesopores of LP-MSN, fluorescence spectroscopy was carried out. For all experiments the temperature was set at 37°C using a Quantum Northwest TC 125 sample holder. 200 μL of the applied nanoparticle suspension was transferred into a specially designed Teflon cap, as described in the literature. The container was closed by a holey lid lined with a ROTH Visking Typ 8/32 dialysis membrane (MWCO = 14.000 g/mol). For release tests with SLB@LP-MSN-AlPcS<sub>2a</sub>-cargo particles, the cuvette was filled with water. The released cargo is able to pass through the membrane while the MSN are held back. First, release experiments were performed with nanoparticles in the closed state (with intact SLB) for 3 h. Afterwards, the nanoparticles were transferred from the Teflon cap into an Eppendorf tube. In case of SLB@LP-MSN-AlPcS<sub>2a</sub>-cargo the red light photosensitizer AlPcS<sub>2a</sub> was activated by laser light (639 nm, 1 min, 5.4 W/cm<sup>2</sup>). This way, the SLB was disrupted, resulting in the release of the cargo. Immediately, the opened nanoparticles were transferred back into the Teflon cap and a

second release experiment was performed for 8-13 h.

#### **Time-based fluorescence release experiments for poly(2-vinylpyridine)-capped samples**

For the release experiments using LP-MSN-PVP-NH<sub>2</sub>-particles, the cuvette was filled with SSC buffer solution (1:40, pH 7.34) for the closed-state test in neutral medium. After 3 h, the nanoparticles were transferred from the Teflon cap into an Eppendorf tube. The suspension was separated by centrifugation and re-dispersed in McIlvaine buffer (pH 5.0) leading to a protonation of the polymer chains and the opening of the pores. Immediately, the opened nanoparticles were transferred back into the Teflon cap and the cuvette was likewise filled with McIlvaine buffer (pH 5.0). A second release experiment was performed for 13 h. The emission maxima of calcein at 5115 nm and excitation maxima at 495 nm were used.

## **5.2 Chapter 10.2: Fusion-SNARE**

**MSN-SH<sub>in</sub>-NH<sub>2out</sub>.** The inner functionalization was obtained by adding a mixture of TEOS (83 mol%, 1.74 mL, 7.8 mmol) and MPTES (5 mol%, 123.5  $\mu$ L, 0.50 mmol) slowly to TEA (14.3 g, 95.6 mmol) and heating the solution for 20 min at 90°C under static conditions. A mixture of CTAC (25 wt% in water, 2.41 mL, 1.83 mmol) and ammonium fluoride (NH<sub>4</sub>F, 100 mg, 2.70 mmol) in water (21.7 g, 1.21 mol) heated to 60°C was quickly added to solution A. After stirring the resulting reaction mixture for 20 min at room temperature TEOS (10 mol%, 206  $\mu$ L, 0.922 mmol) was added in four equal steps every three minutes followed by 30 min of stirring at room temperature. The outer functionalization was created by adding a mixture of TEOS (1 mol%, 20.5  $\mu$ L, 92.5  $\mu$ mol) and APTES (1 mol%, 21.5  $\mu$ L, 92.5  $\mu$ mol) and stirring the solution overnight at room temperature. The obtained particles were centrifuged (15 min, 19000 rpm, 43146 rcf), resuspended in EtOH and extracted in a solution containing ammonium nitrate (NH<sub>4</sub>NO<sub>3</sub>, 2 g) in absolute ethanol (100 mL). The second extraction step was performed in an ethanolic solution of hydrochloric acid (37 wt%, 10 mL). MSN-SH<sub>in</sub>-NH<sub>2out</sub> were obtained as a colloidal suspension in ethanol.

**SLB@MSN-SH<sub>in</sub>-Atto633<sub>out</sub> labeled with Atto633-Mal** In order to create SLB@MSN-Atto633 MSN-SH<sub>in</sub>-NH<sub>2out</sub> (0.5 mg, 15.4 mg/mL) were washed with EtOH by centrifugation (4 min, 14000 rpm, 16873 rcf). The particles were resuspended in absolute ethanol (500  $\mu$ L) and labeled with a Atto633-Mal stock solution (1 mg Atto in 500  $\mu$ L DMF, 5  $\mu$ L). The solution was stirred for 5 h at room temperature in the dark before the NPs were washed three times with absolute ethanol and once with water. After centrifugation (4 min, 14000 rpm, 16873 rcf) the SLB was formed by adding a mixture of DOPC (70  $\mu$ L) and DOTAP (30  $\mu$ L) (each 2.5 mg/mL in 60:40 H<sub>2</sub>O:EtOH) subsequently followed by adding water (700  $\mu$ L) and treatment in an ultrasonic bath.

**Diffusion of LPK into the SLB** After formation of the SLB 50  $\mu$ L of LPK (50  $\mu$ M) were added and the mixture was incubated on a shaker at room temperature for 48 h to form SLB@MSN-LPK.

## **5.3 Chapter 10.3: Fusion-H5WYG**

**MSN-SH<sub>in</sub>-NH<sub>2out</sub>.** The Particle Synthesis and labeling is analog to the synthesis described in Chapter 5.2.

**Synthesis of SLB@MSN-SH<sub>in</sub>-NH<sub>2out</sub> modified with lipid-PEG-H5WYG moieties.** In order to create H5WYG-modified MSN the fusion peptide was attached to a lipid via a PEG (polyethylene glycol) linker in a first step. Therefore the employed PEG-linker possessed both NHS and maleimide as terminal groups. The bi-functional PEG-linker was connected to the lipids by amide formation with the NHS group and with the maleimide group to a terminal cystein group of H5WYG. Two different combinations of lipids and PEG linkers were tested: DOPE-PEG<sub>4</sub> and DSPE-PEG<sub>2000</sub>. MSN-SH<sub>in</sub>-NH<sub>2out</sub> were coated with a DOPC/DOTAP-SLB.

**DSPE-PEG<sub>2000</sub>-H5WYG.** DSPE-PEG<sub>2000</sub>-H5WYG was synthesized by adding the fusiogenic peptide H5WYG labeled with FITC (fluorescein isothiocyanat) (5  $\mu$ L) to DSPE-PEG<sub>2000</sub>-Mal stock solution (5  $\mu$ L) solved in water (50  $\mu$ L). The reaction mixture was shaken for 3 h at room temperature.

**DOPE-PEG<sub>4</sub>-H5WYG.** DOPE-PEG<sub>4</sub>-H5WYG was obtained by adding DOPE (5  $\mu$ L; 2.5 mg/mL in 60:40 H<sub>2</sub>O: EtOH) to NHS-PEG<sub>4</sub>-Mal solved in water (50  $\mu$ L) and stirring the solution for 3 h at room temperature. Afterwards, FITC-H5WYG (5  $\mu$ L) was added and stirred for 3 h at room temperature.

**Integration of DSPE-PEG<sub>2000</sub>-H5WYG/ DOPE-PEG<sub>4</sub>-H5WYG into SLB@MSN-SH<sub>in</sub>-NH<sub>2out</sub>-Atto633.** In order to diffuse the lipid-PEG-H5WYG to the SLB@MSN the complete solution containing the SLB@MSN-SH<sub>in</sub>-NH<sub>2out</sub>-Atto633 was added to the solution with the DSPE-PEG<sub>2000</sub>-H5WYG or DOPE-PEG<sub>4</sub>-H5WYG. The reaction mixture was treated in an ultrasonic bath and incubated overnight at 37°C in the dark.

# Acknowledgments

Lieber Herr Prof. Christoph Bräuchle, vielen Dank für die herzliche Aufnahme in Ihre Gruppe und die Möglichkeit, diese Arbeit zu schreiben. Dank Ihres Forschungsdrangs habe ich meine Leidenschaft für wissenschaftliches Arbeiten entdeckt. Danke für die vielen Freiheiten, die wir unter Ihrer Führung genießen durften.

Prof. Thomas Bein möchte ich insbesondere für die Übernahme der Zweitkorrektur danken. Vielen Dank auch für die vielen Kooperationen mit seiner Gruppe und für die vielen Anregungen, die unsere Arbeit immer auf den Punkt gebracht haben.

Es war mir eine große Freude mit Dr. Stephan Mackowiak zusammenarbeiten und auf diese Weise so manches Projekt schneller zum Ziel zu führen. Stephan, vielen Dank, dass du mich unter deine Fittiche genommen hast. Du hast nicht nur so manch langweiligen Messtag deutlich unterhaltsamer gestaltet.

Alexandra Schmidt, Christian Argyo, Stefan Niedermayer, Martina Lichtenecker danke ich natürlich für die Synthese der Partikel. Danke, dass ihr nie die Geduld verloren habt, auch wenn die Zellen mal wieder nicht so wollten, wie sie sollten. Immer gerne werde ich mich an die schönen (Konferenz-)Reisen und lustigen Runden mit euch zurückerinnern, besonders Japan und San Francisco. Es war mir eine Freude, mit euch zusammenzuarbeiten!

Vielen Dank auch für das fleißige Korrekturlesen meiner Arbeit!

Annika, vielen Dank für den Einblick in die Welt der Tierexperimente, es hat viel Spaß gemacht mit dir zu messen.

Monika Franke danke ich für ihre gründliche Einführung in die Welt des sterilen Arbeitens und ihre liebevolle Pflege unserer Zellkultur. Ohne dich war es nicht mehr dasselbe.

Basti Rühle danke ich für viele coole POF-Ray-Bilder, die unsere Systeme so schön anschaulich gemacht haben.

Anna Sauer hat mich in meinem F-Praktikum für die Thematik begeistert und mir in der Masterarbeit geholfen, ein rundes Projekt zu schaffen. Vielen Dank für den guten Start!

Moritz Ehrl danke ich für seine unerschöpflichen Bemühungen, uns beim Überwinden bürokratischer Hürden zu helfen, und seinen Versuchen, uns mit den neuesten Artikeln der *Zeit* eine andere Sichtweise auf die Welt zu geben.

Meinen (Büro-)Kollegen/innen Ellen, Julia, Frauke, Adriano, Meli und Leonhard danke ich für die angenehme gemeinsame Zeit und die Hilfe in Rat oder Tat.

### *Acknowledgments*

Besonders Daniela, Jens, Giulia, Fabian, Niko, und Lena möchte ich für viele Mittags- und Kaffeepausen und so manch erheiternden Abend danken.

Danke auch für die neuen Sichtweisen und Ideen, die mir meine F-Praktikanten Sebastian Siegl und Katharina Braunger gebracht haben.

Nicht zu vergessen: Ein herzliches Dankeschön an alle Mitglieder der Arbeitskreise Bräuchle, Lamb und Michaelis, die ich im Laufe der Zeit kennenlernen durfte.

Susi danke ich ebenfalls fürs Korrekturlesen und für viele Diskussionen, die mich immer weiter gebracht haben.

An Anna geht ein großer Dank für Hilfe in jeder Lebenslage, viele Ausflüge und Entspannung im spannenden Unialltag.

Der größte Dank geht an meine Eltern Christa und Jakob. Ohne eure Unterstützung wäre diese Arbeit nicht entstanden. Vielen Dank für viele aufbauende Telefonate, wenn es in der Chemie mal wieder nicht so lief, wie es sollte. Danke, dass ihr immer an mich geglaubt habt! Natürlich auch an Ecki, der mich immer wieder auf den Boden der Realität holt mit vielen Alltags-Chemiefragen.

# List of publications

## Publications related to the thesis

### Peer reviewed journals

- Mackowiak S.A\*., Schmidt A.\*., Weiss V.\*., Argyo C., von Schirnding C., Bein T., Bräuchle C.  
Targeted Drug Delivery in Cancer Cells with Red Light Photoactivated Mesoporous Silica Nanoparticles.  
*Nano Lett.* 13(6): 2576-83, 2013.
- Argyo C\*., Weiss V\*., Bräuchle C., Bein T.  
Multifunctional Mesoporous Silica Nanoparticles as a Universal Platform for Drug Delivery  
*Chem. Mater.* 26(1): 435-51, 2014.

### Manuscripts in preparation

- Niedermayer S\*., Weiss V\*., Herrmann A\*., Schmidt A., Datz S., Wagner E., Bräuchle C., Bein T.  
Multifunctional Polymer-Capped Mesoporous Silica Nanoparticles for pH-responsive Targeted Drug Delivery  
*submitted*
- Weiss V\*., Argyo C\*., de Andrade Torrano A., Strobel C., Mackowiak S.A., Gattenmeier T., Hilger I., Bräuchle C., Bein T.  
Investigation of the Endosomal Escape via the Proton Sponge Effect with Dendron-Functionnalized Mesoporous Silica Nanoparticles  
*in preparation*
- Argyo C., Gattner M., Weiss V., Datz S., Carell T., Bräuchle C., Bein T.  
Carbonic Anhydrase-Based pH-Responsive Cap System for Mesoporous Silica Nanoparticles  
*in preparation*

\* contributed equally.

## Posters

- Niedermayer S., Schmidt A., Argyo C., Weiss V., Bein T., Bräuchle T.  
*Nanopartikel zur lokalen Bekämpfung von Krebszellen.*,  
11. Münchner Wissenschaftstage – Herausforderung Gesundheit, 2011, Munich, Germany.
- Weiss V., Sauer A. M., Argyo C., Bein T., Bräuchle C.  
*Single particle tracking of EGF receptor-targeted mesoporous silica nanoparticles with supported lipid bilayer.*,  
Summer Retreat of the Nanosystems Initiative Munich (NIM) 2011, Kampenwand, Germany.
- Weiss V., Mackowiak S.A., Argyo C., Schmidt A., Bein T., Bräuchle C.  
*Colloidal mesoporous silica (CMS) nanoparticles with supported lipid bilayer for targeted drug delivery.*,  
Summer Retreat of the Nanosystems Initiative Munich (NIM) 2012, Garmisch-Partenkirchen, Germany.
- Weiss V., Niedermayer S., Schmidt A., Argyo C., Mackowiak S.A., Bein T., Bräuchle C.  
*High-resolution live-cell imaging of photoinduced drug delivery from multifunctional mesoporous silica nanoparticles.*,  
CeNS Workshop “Nanosciences: Soft, Solid, Alive and Kicking”, 2012, Venice International University (VIU), San Servolo, Italy.
- Weiss V., Schmidt A., Mackowiack S.A., Argyo C., von Schirnding C., Bräuchle C., Bein T.  
*High-resolution live-cell imaging of cascaded photoinduced drug delivery from lipid bilayer coated mesoporous silica nanoparticles*  
CIPSM- Bayer HealthCare-Symposium 2012, Munich, Germany.  
6th Annual Symposium on Nanobiotechnology Kyoto Cell-Material Integration, 2012, Kyoto, Japan.  
Summer Retreat of the Nanosystems Initiative Munich (NIM) 2013, Sylvensteinstausee, Germany.  
CeNS Workshop “Nanosciences: Great Adventures on Small Scales”, 2013, Venice International University (VIU), San Servolo, Italy.  
NIM-Workshop "Young Ideas in Nanoscience" 2013, Munich, Germany.
- Weiss V., Schmidt A., Mackowiack S.A., Argyo C., von Schirnding C., Bräuchle C., Bein T.  
*Targeted Drug Delivery in Cancer Cells with Red Light Photoactivated Mesoporous Silica Nanoparticles*  
Annual SFB 749-Symposium at Wildbad Kreuth, March 2013, Germany.
- Weiss V., Niedermayer S., Argyo C., Bräuchle C., Bein T.  
*Mesoporous silica nanoparticles with pH-responsive Polymershells for Drug Delivery Applications*  
Annual SFB 749-Symposium at Wildbad Kreuth, March 2013, Germany.

- Weiss V., Niedermayer S., Herrmann A., Schmidt A., Edinger D., Wagner E., Bräuchle C., Bein T.  
*Multifunctional polymer-capped mesoporous silica nanoparticles for targeted drug delivery*  
NIM-Workshop "Young Ideas in Nanoscience" 2013, Munich, Germany.

### Oral presentations

- Weiss V., Schmidt A., Mackowiack S.A., Argyo C., von Schirnding C., Bräuchle C., Bein T.  
*Targeted Drug Delivery in Cancer Cells with Red Light Photoactivated Mesoporous Silica Nanoparticles.*,  
Annual SFB 749-Symposium at Wildbad Kreuth, March 2013, Germany.

### Publications not related to the thesis

- Tegel M., Johansson S., Weiß V., Schellenberg I., Hermes W., Pöttgen R., Johrendt D.  
Synthesis, crystal structure and spin-density-wave anomaly of the iron arsenide-fluoride Sr-FeAsF  
*EPL*, 84 (67007), 2008.
- Tegel M., Rotter M., Weiß V., Schappacher F. M., Pöttgen R., Johrendt D.  
Structural and magnetic phase transitions in the ternary iron arsenides SrFe<sub>2</sub>As<sub>2</sub> and EuFe<sub>2</sub>As<sub>2</sub>  
*J. Phys.: Condens. Matter* 20 (452201), 2008.

